Multiscale study of the calcium sulfate hemihydrate-gypsum transformation with diffraction and tomography techniques

Michela La Bella

THÈSE

Pour obtenir le grade de

DOCTEUR DE L'UNIVERSITÉ GRENOBLE ALPES

École doctorale : STEP - Sciences de la Terre de lEnvironnement et des Planètes
Spécialité : Sciences de la Terre et de lEnvironnement
Unité de recherche : Institut des Sciences de la Terre

Étude multi-échelle de la transformation du sulfate de calcium hémihydraté en gypse par diffraction des rayons-X et tomographie

Multiscale study of the calcium sulfate hemihydrate-gypsum transformation with diffraction and tomography techniques

Présentée par :

Michela LA BELLA

Direction de thèse :

Alejandro FERNANDEZ-MARTINEZ CHARGE DE RECHERCHE, Université Grenoble Alpes	Directeur de thèse
Carlotta Giacobbe ESRF-EBS (European Synchrotron Radiation Facility)	Co-encadrant de thèse

Rapporteurs :

Maria Chiara DALCONI
PROFESSEUR ASSOCIE, Università degli studi di Padova
Giuseppe CRUCIANI
PROFESSEUR, Università degli studi di Ferrara

Thèse soutenue publiquement le **26 avril 2023**, devant le jury composé de :

Alejandro FERNANDEZ-MARTINEZ CHARGE DE RECHERCHE, CNRS	Directeur de thèse
Maria Chiara DALCONI PROFESSEUR ASSOCIE, Università degli studi di Padova	Rapporteure
Francois RENARD PROFESSEUR, University of Oslo	Examinateur
Giuseppe CRUCIANI PROFESSEUR, Università degli studi di Ferrara	Rapporteur
Pierre BORDET DIRECTEUR DE RECHERCHE, CNRS	Examinateur
Laurent TRUCHE PROFESSEUR DES UNIVERSITES, Université Grenoble Alpes	Président
Tomasz STAWSKI CHARGE DE RECHERCHE, Federal Institute for Materials Research and Testing	Examinateur

Invités :

Carlotta Giacobbe
DOCTEUR EN SCIENCES, ESRF-EBS (European Synchrotron Radiation Facility)

Abstract

Calcium sulfate hemihydrate –bassanite and calcium sulfate dehydrate –gypsum are two mineral phases of geological and industrial significance. They are widely present in the Earth's crust and used in various industrial processes due to their low cost and availability. Gypsum plaster, which is produced from the hydration of calcium sulfate hemihydrate to gypsum, is an important construction material made of calcium sulfate. In this Ph.D. thesis, a detailed multiscale characterization of the hydration process of gypsum plaster and all its sub-processes has been performed. The application of synchrotron hard X-ray diffraction and tomography techniques at a 4th generation synchrotron light source such as the ESRF-EBS has allowed *in situ* investigations of the system, gaining complementary morphologic and crystallographic insights. The thesis focuses on three main research chapters. The first one contains a detailed crystallographic study of calcium sulfate hemihydrate samples synthesized following different methods, and answering some long-standing questions about the polymorphism of bassanite. In the second chapter, the spatial and crystallographic relationships between calcium sulfate hemihydrate and gypsum have been investigated using an *in situ* approach. Lastly, the dissolution mechanisms of calcium sulfate hemihydrate have been probed at different spatial scales. The results of this comprehensive multiscale study of the processes involved in the hydration reaction of calcium sulfate demonstrates the suitability and potentiality of unconventional powerful techniques in characterizing heterogeneous complex systems.

Résumé

Le sulfate de calcium hémihydraté -bassanite et le gypse sont deux phases minérales d'importance géologique et industrielle. Ils sont largement présents dans la croûte terrestre et sont utilisés dans divers processus industriels en raison de leur faible coût et de leur disponibilité. Le plâtre de Paris, qui est produit à partir de l'hydratation du sulfate de calcium hémihydraté en gypse, est un important matériau de construction à base de sulfate de calcium. Dans cette thèse de doctorat, une caractérisation multi-échelle détaillée du processus d'hydratation du plâtre de Paris et de tous ses sous-processus a été réalisée. L'application de techniques de diffraction des rayons-X durs et de tomographie au synchrotron à une source de lumière synchrotron de 4ème génération telle que l'ESRF-EBS a permis d'étudier le système *in situ* et d'obtenir des informations morphologiques et cristallographiques complémentaires. La thèse se concentre sur trois principaux chapitres de recherche. Le premier contient une étude cristallographique détaillée d'échantillons de sulfate de calcium hémihydraté synthétisés selon différentes méthodes, et répond à certaines questions de longue date sur le polymorphisme de la bassanite. Dans le deuxième chapitre, les relations spatiales et cristallographiques entre le sulfate de calcium hémihydraté et le gypse ont été étudiées en utilisant une approche in situ. Enfin, les mécanismes de dissolution du sulfate de calcium hémihydraté ont été étudiés à différentes échelles spatiales. Les résultats de cette étude multi-échelle complète des processus impliqués dans la réaction d'hydratation du sulfate de calcium démontrent la pertinence et le potentiel des techniques puissantes non conventionnelles dans la caractérisation des systèmes complexes hétérogènes.

Acknowledgments

At the end of this journey, there is a long list of people whom I would like to thank.

My major acknowledgment goes to my two supervisors Carlotta and Alejandro. Not only they gave me the opportunity to do what I like the most, they also encouraged me in every situation. They have been a constant guide throughout these years and it has been a pleasure working with them.

A special acknowledgment goes to my colleagues from both ID11 and ISTerre. I was very lucky to have the opportunity to collaborate with such dynamic and enthusiastic teams. I have enjoyed a lot my time spent at ID11, even the nights of measurements during beamtime. For this, I woud like to thank Carlotta, Jon, Pierre-Olivier, Ellie, and Pedro.

I also would like to thank Sander, Rogier, Alicia, Carlos, Pierre-Olivier, Marta, Jon, Ellie, Cathy, and Raquel for collaborating with me on various projects.

The final acknowledgment is for my friends, old and new, Lorenzo and my family for their infinite support.

Étude multi-échelle de la transformation du sulfate de calcium hémihydraté en gypse par diffraction des rayons-X et tomographie

Introduction

Le sulfate de calcium hémihydraté, ou bassanite, ou encore hémihydrate ($CaSO_4 \cdot 0.5H_2O$) et le gypse ($CaSO_4 \cdot 2H_2O$) sont deux phases appartenant à la famille des sulfates de calcium. Cette famille de minéraux et leurs équivalents synthétiques est bien connue des communautés scientifiques géologiques et industrielles et a suscité une activité de recherche florissante pendant de nombreuses années. L'intérêt pour ces minéraux d'un point de vue géologique est principalement dû à leur présence répandue dans la croûte terrestre et aux paléoenvironnements dans lesquels ils se sont formés. D'un point de vue industriel, les composés de sulfate de calcium sont parmi les matériaux les plus produits par l'homme. L'utilisation des sulfates de calcium, du sulfate de calcium hémihydraté et du gypse en particulier, est largement favorisée par leurs faibles coûts et leur grande disponibilité pour des applications dans de nombreux secteurs industriels. Parmi ces matériaux, le plâtre de Paris, produit à partir de sulfates de calcium, représente le plus gros tonnage [1] [2]. Le plâtre de Paris est obtenu par l'hydratation de $CaSO_4 \cdot 0.5H_2O$ pour former $CaSO_4 \cdot 2H_2O$. L'utilisation du plâtre dans l'industrie du bâtiment, la médecine et la pharmacologie est une pratique ancienne et bien établie, quand bien même, plusieurs questions fondamentales bénéficieraient d'investigations supplémentaires. De nos jours, la communauté scientifique a accès à des instruments de caractérisation de pointe qui permettent d'obtenir des informations avec un niveau de détail sans précédent. La récente amélioration de l'Installation Européenne de Rayonnement Synchrotron (ESRF) vers la nouvelle Source Extrêmement Brillante (EBS) a ouvert la voie à de nouveaux types d'expériences dans lesquelles nous pouvons suivre des processus *in situ* avec une excellente résolution temporelle et spatiale. Dans cette thèse de doctorat, nous allons explorer certaines des nouvelles possibilités qu'un grand instrument tel que le synchrotron, peut offrir pour réaliser une caractérisation multi-échelle du processus d'hydratation du plâtre *in-situ*. Dans la première partie du projet, nous nous sommes concentrés sur la caractérisation cristallographique de l'hémihydrate synthétisé par différentes méthodes. La ligne de lumière ID22 de l'ESRF, grâce à son instrument de diffraction de poudre haute résolution, permet de discerner des caractéristiques structurelles qui restent indétectable pour tout instrument conventionnel. Pour cette raison, une expérience a été réalisée sur la ligne de lumière afin d'étudier la présence éventuelle de différences cristallographiques entre des échantillons de sulfate de calcium hémihydraté synthétisés de différentes manières. Pour la deuxième partie de la thèse, nous avons réalisé des expériences *insitu* sur la ligne de lumière ID11 de l'ESRF en combinant des techniques d'imagerie (tomographie assistée par ordinateur, en contraste de phase) et d'imagerie basée sur la diffraction (3DXRD par balayage) pour observer la transformation de l'hémihydrate en gypse pendant l'hydratation. ID11 est une ligne de lumière polyvalente spécialisée dans la caractérisation des matériaux. L'un des principaux avantages de cette ligne de lumière réside dans la possibilité de focaliser le faisceau de rayons-X jusqu'à des tailles submicroniques, ce qui permet des analyses hiérarchiques. Cette fonctionnalité, associée à l'application de techniques complémentaires, constitue une approche prometteuse pour étudier le lien entre les propriétés cristallographiques et texturales du processus de l'hydratation du plâtre. Dans la dernière partie du projet de doctorat, nous nous sommes consacrés à l'observation de la dissolution de l'hémihydrate *in situ* à l'échelle de la surface et dans la masse. Certaines problématiques expérimentales et pratiques liées aux

propriétés et à la morphologie du matériau compliquent l'observation et l'interprétation de la dissolution des cristaux d'hémihydrate de sulfate de calcium. Avec une approche expérimentale précautionneuse, par l'utilisation de la microscopie à force atomique aux laboratoires ISterre et de la tomographie en contraste de phase à ID11, avec l'aide d'outils sophistiqués de traitement de données par apprentissage profond, ces problèmes ont pu être surmontés.

La structure cristalline du sulfate de calcium hémihydraté synthétisé de différentes manières

Le sulfate de calcium hémihydraté synthétique, peut être produit de différentes manières, ce qui entraîne la formation de deux types d'hémihydrate appelés α et β. Pour les applications industrielles, l'hémihydrate est généralement produit via la déshydratation du gypse. La déshydratation sous air sec ou sous vide (calcination), conduit à la production du β-hémihydrate. Chauffé en solution ou sous haute pression d'eau le gypse se transforme en α-hémihydrate. Dans l'état actuel des connaissances, ces deux types d'hémihydrate diffèrent principalement par la taille et la morphologie des cristaux, qui influencent leur comportement lors de l'hydratation [2]. Grâce à l'important travail d'investigation de la cristallographie du sulfate de calcium hémihydraté [3] [4] [5] [6] [7] [8] [9] [10], les principales complexités résultant du jumelage pseudo-méroédrique et de la distribution de l'eau dans la structure ont été décrites. Néanmoins, un point reste obscur. En particulier, nous ne savons toujours pas avec certitude comment les différentes méthodes de production telles que la précipitation directe du sulfate de calcium à partir de la solution (α-hémihydrate) ou la calcination du gypse (β-hémihydrate) influencent la structure cristalline et l'incorporation des molécules d'eau de l'hémihydrate. C'est pourquoi des mesures de diffraction de poudre à haute résolution (HR-XRPD) ont été réalisées afin de mettre en lumière la présence éventuelle de différences entre l'α et le β-hémihydrate. Des échantillons d'α-hémihydrate ont également été caractérisés par µSXRD pour étudier leur mésostructure et la présence éventuelle de défauts cristallins.

Trois échantillons d'hémihydrate ont été mesurés sur la ligne de lumière ID22 de l'ESRF en utilisant la HR-XRPD. Deux échantillons étaient de l'α-hemihydrate et un était du β-hemihydrate. Les diagrammes de de diffraction de poudre des trois échantillons ont révélé la présence de différences entre l'α et le β-hémihydrate. La Figure 1 montre un tracé des trois diffractogrammes avec les deux échantillons d'α-hémihydrate en rouge et bleu, et le β-hémihydrate en vert.

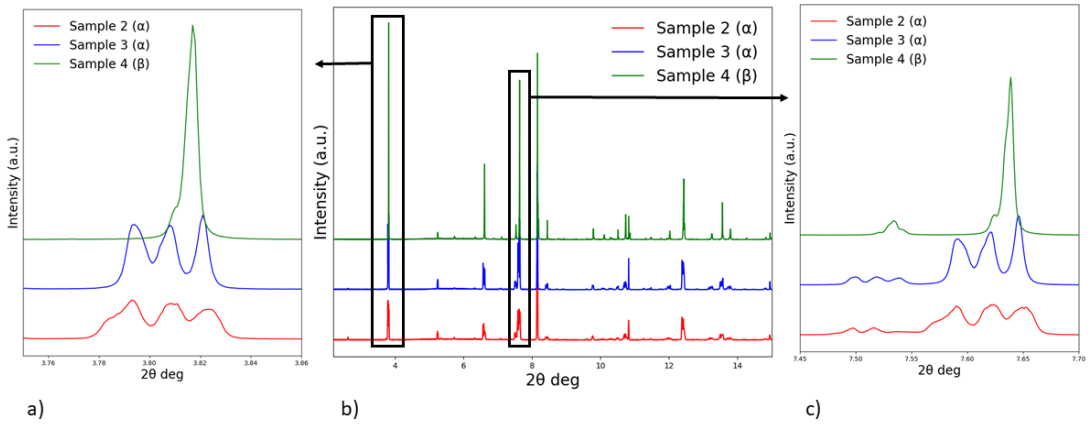

Figure 1. Tracé des diagrammes de diffraction de poudre haute résolution de l'α-hémihydrate (en rouge et bleu) et du β-hémihydrate (en vert).

D'après les diagrammes de diffraction de la Figure 1, il est évident que l'α-hémihydrate présente un fractionnement du pic qui n'est pas présent dans le β-hémihydrate. Les trois diagrammes ont été affinés par la méthode de Rietveld. Les résultats des affinements de Rietveld ont révélé que dans le cas de l'α-hémihydrate, les échantillons pouvaient être affinés avec trois phases I2 hémihydratées [8] avec des paramètres de maille légèrement différents. Dans le cas de l'échantillon de β-hémihydrate, l'affinement a pu être effectué avec un seul hémihydrate I2 [8]. Les résultats de l'affinement de Rietveld des deux α-hémihydrate et β-hémihydrate relatifs aux mêmes régions des diffractogrammes mis en évidence dans la Figure 1a sont rapportés dans la Figure 2. Dans le cas de l'α-hemihydrate (Figure 2a et b), la division du pic en trois pics distincts s'explique par les trois composants de l'hémihydrate.

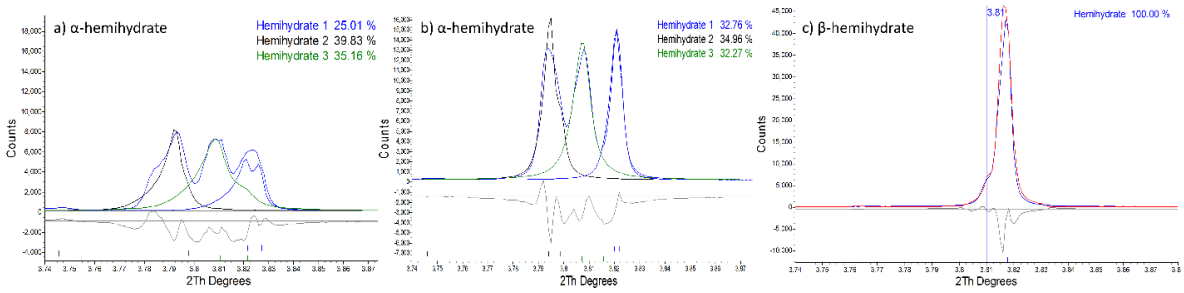

Figure 2. Résultats de l'affinement de Rietveld pour les échantillons d'α-hémihydrate (a et b) et de β-hémihydrate (c). Les diagrammes observés sont tracés en bleu, le diagramme somme calculé est reporté en rouge, et les contributions individuelles au diagramme calculé sont reportées en noir, vert et bleu. Les différences entre les modèles calculés et observés sont indiquées en gris.

Les deux échantillons d'α-hemihydrate ont également été mesurés par µSXRD sur la ligne de lumière ID11. De leurs analyses il résulte la présence de mosaïcité et, dans un cas, la preuve de défauts cristallins dans des directions cristallographiques spécifiques.

Grâce à l'application de la HR-XRPD couplée à des outils de caractérisation préliminaires (analyse thermogravimétrique, microscopie électronique à balayage et spectroscopie infrarouge transformée par Fourier), il a été possible de démontrer pour la première fois les différences entre l'α et le β-hémihydrate. La séparation des pics de l'α-hémihydrate est une caractéristique qui n'avait jamais été observée auparavant, car la résolution d'un instrument de diffraction des rayons-X de laboratoire ou d'une ligne de lumière de diffraction synchrotron avec une installation conventionnelle n'est pas assez élevée pour les révéler.

L'hydratation du sulfate de calcium hémihydraté pour former du gypse

Parmi toutes les études qui ont été réalisées pour décrire la transformation de l'hémihydrate en gypse qui a lieu au cours de son processus d'hydratation, deux scénarios prédominants ont été proposés. Dans un cas, il a été proposé que l'hémihydrate se dissolve dès qu'il entre en contact avec l'eau, déclenchant la nucléation et la cristallisation du gypse à partir de la solution sursaturée [11] [12] [13] [14] [15]. Dans un autre cas, il a été proposé que le gypse se nucléise de manière hétérogène à partir de cristaux d'hémihydrate, suggérant des relations épitaxiales entre les deux phases [16]. Dans certaines de ces études, les relations entre l'hémihydrate en dissolution et le gypse en croissance ont été suivies à l'aide de techniques d'imagerie et de microscopie [17] [13] [14] [15] [16]. Cependant, aucune analyse cristallographique détaillée *in situ* basée sur la diffraction

des rayons-X n'a jamais été réalisée. Ceci pourrait fournir des preuves des relations cristallographiques entre l'hémihydrate et le gypse. Ici, nous avons appliqué, pour la première fois dans le domaine des matériaux de construction, des mesures semi-simultanées de 3DXRD par balayage (s3DXRD) et de tomographie en contraste de phase (PCT) pour suivre le développement de l'hydratation du plâtre *in situ*. À partir des mesures de s3DXRD, nous avons pu identifier les phases, obtenir les paramètres de maille et les orientations des grains d'hémihydrate et de gypse qui étaient présents dans l'échantillon pendant l'hydratation. À partir des mesures de PCT, nous avons pu reconstruire la forme et la morphologie complète des grains et suivre l'évolution de la microstructure de la pâte de gypse. Pour les expériences couplées de s3DXRD et de PCT *in situ* effectuées sur la ligne de lumière ID11, des cristaux d'α-hemihydrate contenus dans un capillaire ont été hydratés avec une solution saturée en sulfate de calcium. Une représentation du montage expérimental utilisé pour cette expérience est présentée dans la Figure 3.

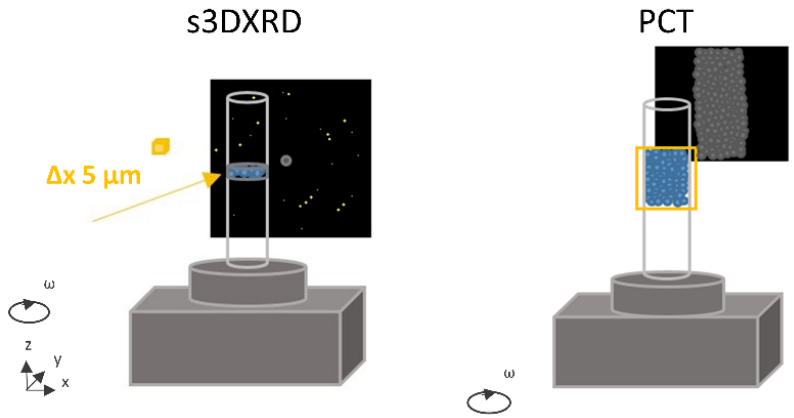

Figure 3. Montages expérimentaux utilisés pour les expériences semi-simultanées de s3DXRD et de FPCT. Les deux montages ne diffèrent que par le type de détecteur utilisé pour collecter les données et la taille du faisceau. Pour les mesures de s3DXRD, le faisceau de rayons-X a été focalisé à une taille de 5 µm.

Les informations morphologiques et cristallographiques complémentaires obtenues lors de cette expérience ont permis de démontrer que dans nos conditions il n'y a aucune trace de relations épitaxiales entre l'hémihydrate en dissolution et le gypse en précipitation. Ces résultats soutiennent l'hypothèse selon laquelle la dissolution de l'hémihydrate crée des environnements locaux de solution sursaturée qui déclenchent la nucléation et la croissance des cristaux de gypse. La Figure 4 explique le mécanisme du processus couplé de dissolution-précipitation de l'hémihydrate et du gypse à partir des résultats complémentaires obtenus par s3DXRD et PCT. La particule d'hémihydrate, allongée le long de la direction [001], montre une dissolution préférentielle à partir du centre du cristal, suggérant une réactivité différente entre les différents plans cristallographiques [18].

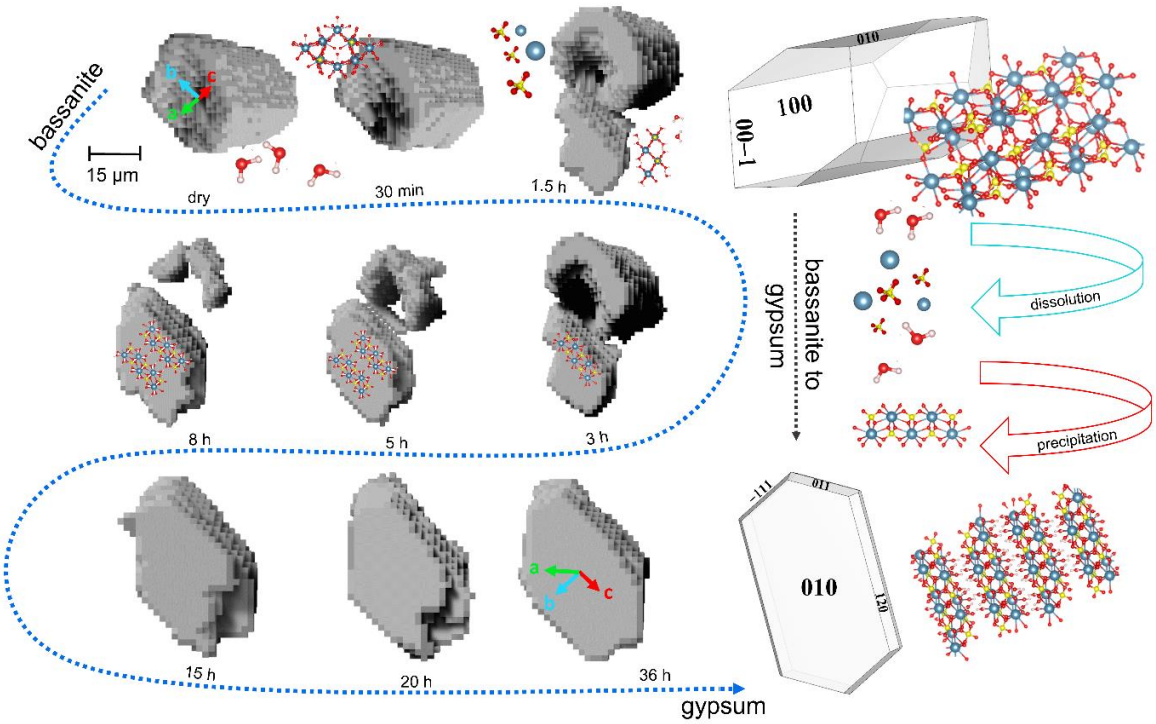

Figure 4. Reconstructions 3D de l'évolution d'une particule d'hémihydrate et d'une particule de gypse pendant le processus d'hydratation. Les reconstructions ont été réalisées à partir des données de PCT tandis que l'orientation cristallographique des cristaux a été calculée à partir des données s3DXRD. À droite est reporté un modèle du processus de dissolution-précipitation proposé pour le processus d'hydratation de l'hémihydrate.

Dissolution de l'hémihydrate de sulfate de calcium à différentes échelles d'observation

La dissolution minérale est un processus fondamental dans la nature et dans les milieux industriels, associé aux processus naturels d'altération, de corrosion et de modification au sens large. La dissolution minérale est généralement associée à la reprécipitation interfaciale, en raison des concentrations élevées de solutés aux interfaces minéral-eau, qui contrôlent souvent le transfert de matière à travers ces interfaces [19]. En raison du grand intérêt que représentent ces processus de dissolution-précipitation, ils ont souvent été étudiés à différentes échelles (du kilomètre jusqu'à l'angstrom comme rapporté par Luttge et al. (2019) [20]). La dissolution de l'hémihydrate de sulfate de calcium n'a cependant jamais été observée ni à l'échelle atomique ni à l'échelle globale en raison des complications liées à la haute solubilité et à la forme des cristaux d'hémihydrate. Ici, nous avons préparé des solutions avec des additifs couramment utilisés dans l'industrie qui nous ont permis d'observer la dissolution des surfaces cristallographiques de l'hémihydrate grâce à la microscopie à force atomique (AFM), et de calculer le taux de dissolution de l'hémihydrate dans sa globalité avec la PCT. Grâce à l'utilisation d'acide polyacrylique (PAA), nous avons réussi à ralentir suffisamment la dissolution de l'hémihydrate pour obtenir des images des surfaces cristallographiques par AFM. Au cours de l'expérience de PCT *in situ* menée à ID11, un échantillon composé de cristaux d'hémihydrate a été hydraté avec une solution préparée avec du bêta-naphtalène sulfonate (BNS). L'utilisation du BNS a permis de précipiter des cristaux de gypse de forme régulière, clairement distingués des cristaux d'hémihydrate. Cette caractéristique a permis d'extrapoler l'hémihydrate se dissolvant en globalité à partir de l'échantillon hydraté complet (hémihydrate + gypse) dans les ensembles de données de PCT. L'extrapolation de la fraction d'hémihydrate de l'échantillon à partir

des volumes de PCT a été réalisée à l'aide d'un réseau neuronal convolutif par apprentissage profond (CNN U-Net 2.5D) implémenté dans le logiciel Dragonfly. Un exemple de la séparation de la fraction d'hémihydrate (en vert) de la fraction de gypse (en violet) dans une portion du capillaire après hydratation est présenté sur la Figure 5.

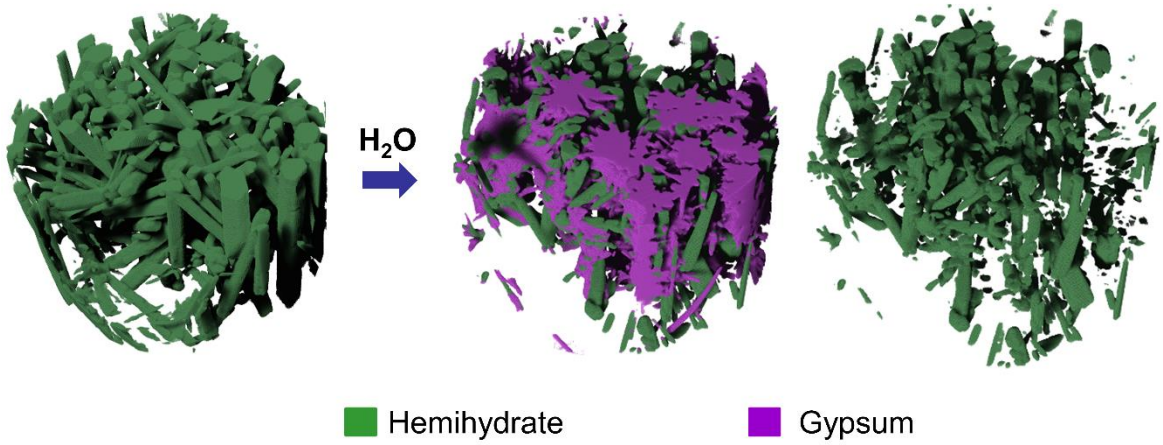

Figure 5. Exemple du résultat de l'application d'un CNN U-Net 2.5D pour récupérer les données volumétriques de l'hémihydrate en dissolution à partir de l'échantillon complet. La première reconstruction 3D à partir de la gauche est une portion du capillaire remplie de cristaux d'hémihydrate secs, la seconde est la même portion du capillaire après hydratation montrant la présence d'hémihydrate (en vert) et de gypse (en violet), et la dernière est la fraction d'hémihydrate extraite.

L'exploitation de ce résultat a permis de calculer la surface réactive de l'échantillon massif d'hémihydrate pendant la dissolution. Les valeurs de surface ont ensuite été utilisées pour calculer la vitesse de dissolution en utilisant l'approche proposée par Daval et al. (2010) [21] et pour la comparer avec de précédents résultats [22].

Conclusions et perspectives

L'objectif principal qui a motivé le développement de ce travail de doctorat était de démontrer comment de nouvelles techniques expérimentales pouvaient représenter un outil prometteur pour caractériser des processus complexes tels que l'hydratation du plâtre. Le principal défi de ce projet était d'appliquer ces techniques non conventionnelles, la s3DXRD en particulier, à un système qui n'avait jamais été caractérisé de cette manière. Comprendre les étapes du processus d'hydratation du plâtre n'était cependant pas le seul objectif. Je voulais fournir une caractérisation plus complète et multi-échelle dans l'espoir de répondre à certaines des questions de longue date qui intéressent la communauté scientifique travaillant sur le plâtre de gypse depuis de nombreuses années.

Le premier point de cette caractérisation hiérarchique s'est focalisé sur les structures cristallographiques des α et β-hémihydrates. Les mesures effectuées par HR-XRPD sur la ligne de lumière ID22 de l'ESRF ont révélé pour la première fois des différences structurelles entre l'hémihydrate produit par voie humide (α) et l'hémihydrate produit par voie sèche (β). Auparavant, des études XRPD et SXRD avaient été réalisées afin de comprendre si les deux formes d'hémihydrate présentaient ou non des structures différentes [9] [10] [23]. Dans aucun de ces cas, la preuve de structures cristallographiques différentes n'avait été apportée. Seuls Follner et al. (2002) [23] ont abordé la présence de caractéristiques différentes dans le diagramme de diffraction des poudres

de l'α-hémihydrate par rapport au β, mais la preuve de ces caractéristiques n'a jamais été apportée. La raison pour laquelle les différences entre l'α et le β-hémihydrate n'ont jamais été pleinement comprises réside dans le manque de résolution angulaire des analyses qui ont été faites précédemment. Avec la HR-XRPD, il a été possible non seulement d'observer la division des pics qui caractérise les schémas de l'α-hémihydrate, mais aussi de les affiner avec la méthode de Rietveld. Il est maintenant évident que les différentes méthodes de synthèse, telles que la précipitation de l'hémihydrate à partir de la solution et la calcination du gypse, donnent des composés finaux avec des caractéristiques différentes. Dans le cas de l'α-hemihydrate, l'échantillon contient plus d'une phase I2 monoclinique avec des paramètres de maille légèrement différents et de l'eau désordonnée, alors que dans le cas du β-hemihydrate, une seule phase I2 monoclinique est présente avec de l'eau ordonnée. La pertinence de cette information est compréhensible car les α et β-hémihydrates sont connus pour se comporter différemment pendant l'hydratation. Le type α présente un temps d'induction plus court par rapport au type β, qui s'hydrate alors plus rapidement produisant un plâtre moins performant [2]. Les différences que nous avons trouvées entre l'α et le β-hémihydrate pourraient représenter une raison supplémentaire pour leur comportement d'hydratation différent : le type α contient une plus grande densité de « défauts structurels », ce qui entraîne une plus grande réactivité lorsqu'il est exposé à une solution sous-saturée. L'analyse détaillée de la diffraction des monocristaux a également permis de constater que de la mosaïcité est présente le long de la direction [001]. C'est la première fois que cela est directement quantifié à l'aide d'une technique structurelle (la précédente par Stawski et al. (2019) [24] provenait d'observations TEM de nanodomaines). L'occurrence de cette mosaïcité soutient le modèle de formation de la bassanite à partir de l'agrégation orientée de clusters de sulfate de calcium.

Pour la deuxième partie de cette étude hiérarchique, nous nous sommes intéressés à une plus grande échelle en étudiant comment la dissolution de l'α-hémihydrate et la précipitation du gypse sont liées d'un point de vue morphologique et cristallographique. Le principal résultat de cette étude est la démonstration que l'application combinée de deux techniques complémentaires, la s3DXRD et la PCT, représente un outil approprié pour étudier les processus de transformation de phase *in situ* tels que celui qui résulte de l'hydratation de l'hémihydrate en gypse. Notre approche a permis une caractérisation multi-échelle qui relie les caractéristiques cristallographiques et texturales du système d'hydratation. Les mécanismes couplés qui impliquent la dissolution de l'hémihydrate, la formation de zones locales sursaturées dans les pores entre les cristaux d'hémihydrate, et la précipitation du gypse ont été reconstruits à travers toutes leurs étapes grâce aux mesures de PCT. Les mesures de s3DXRD nous ont permis d'établir qu'aucune corrélation cristallographique n'était présente entre les cristaux d'hémihydrate de départ et les cristaux de gypse finaux, excluant la présence d'une croissance épitaxiale de gypse sur les surfaces d'hémihydrate dans notre système. À partir des informations complémentaires obtenues à la fois par s3DXRD et PCT, il a été possible d'observer la dynamique de dissolution préférentielle des plans (010) et (100) des cristaux d'α-hémihydrate confirmant les résultats des calculs théoriques [18]. La dissolution préférentielle que nous avons observée peut être liée à la présence de défauts structurels dans certaines directions spécifiques des cristaux d'hémihydrate qui conduisent au développement de textures en couches pendant la dissolution. Dans ce travail, le processus d'hydratation du plâtre a été caractérisé à méso-échelle, fournissant un lien entre les processus microscopiques et macroscopiques dans le même système, et ouvrant la voie à des investigations

innovantes. L'adéquation des techniques couplées de s3DXRD et de PCT pour étudier les processus de dissolution/précipitation ouvre de nouvelles possibilités à la fois à des fins industrielles, comme la maitrise des réactions de prise dans les liants hydrauliques, et dans le domaine de la géochimie, pour étudier l'altération des minéraux.

Dans la dernière partie de ce travail, nous nous sommes concentrés sur la dissolution de l'α-hemihydrate en suivant le processus à partir de deux échelles d'observations différentes. Un nombre considérable de travaux ont été réalisés précédemment sur la compréhension du comportement de dissolution du gypse et de l'anhydrite à l'échelle atomique [25] [26] [27] [28] alors que l'hémihydrate n'avait jamais été observé auparavant. Notre approche, qui comprenait la préparation de solutions avec des additifs utilisés dans les processus industriels, nous a permis d'observer la dissolution en surface de l'α-hemihydrate et de mesurer la surface de la fraction d'hémihydrate en dissolution à partir d'un échantillon complet. Dans un cas, l'utilisation de PAA, qui est considéré comme un polymère modèle pour les superplastifiants, nous a aidé à ajuster la cinétique de la dissolution des cristaux d'hémihydrate. Cela nous a permis d'acquérir un ensemble de données d'images AFM qui montre la dissolution préférentielle des bords des cristaux par rapport aux surfaces, fournissant ainsi la preuve d'un phénomène qui avait été précédemment proposé par Arvidson et al. (2003) [29]. Dans l'autre cas, l'ajout de BNS à la solution qui a été utilisée pour hydrater *in situ* un échantillon d'α-hémihydrate a conduit à la précipitation de cristaux de gypse avec une forme uniforme qui a contribué à les distinguer des cristaux d'hémihydrate dans les mesures PCT. L'application de méthodes de segmentation par apprentissage profond pour séparer les cristaux d'hémihydrate et de gypse s'est avérée être un outil fiable pour traiter les systèmes hétérogènes où les méthodes de segmentation simples ne parviennent pas à récupérer les informations nécessaires. Dans ce cas, le CNN U-Net 2.5 entraîné, disponible dans le logiciel Dragonfly, nous a permis à séparer la fraction d'hémihydrate de celle de gypse grâce au contraste de phase accru fourni par l'algorithme de Paganin et aux formes différentes des deux phases. Cette approche n'avait jamais été appliquée auparavant pour étudier le développement des réactions de dissolution. Jusqu'à présent, une seule étude a été réalisée sur la mesure de la vitesse de dissolution de l'hémihydrate à partir de l'analyse BET [22]. Notre étude fournit pour la première fois une estimation de la vitesse de dissolution en masse de l'α-hemihydrate et une mesure directe de la surface réactive.

Dans l'ensemble, le processus d'hydratation qui conduit à la formation du plâtre à partir de l'α-hemihydrate, a été caractérisé dans tous ses sous-processus en utilisant des techniques non conventionnelles, innovantes et complémentaires qui ouvrent de nouvelles perspectives pour les applications industrielles et la connaissance fondamentale des processus de dissolution et de précipitation. Les principales questions scientifiques que ce doctorat introduit et qui pourraient être étudiées dans de futurs travaux peuvent être résumées en ces points :

- La caractérisation cristallographique des structures α et β-hemihydrate, qui a démontré que différentes synthèses produisent des composés avec différents paramètres de réseau très probablement dus à différentes quantités d'eau incorporées, rouvre la question de savoir comment cela est lié aux propriétés du plâtre hydraté. En particulier, la preuve de mosaïcité et la présence de défauts le long de la direction [001] dans les cristaux d'α-hémihydrate, pourrait être liée à la dissolution préférentielle à partir du centre des cristaux qui a été observée à partir des mesures de

s3DXRD et de PCT. Une reproduction de la même approche expérimentale sur des échantillons de β-hémihydrate pourrait révéler un comportement différent de la dissolution. En particulier, si nous considérons que la présence de défauts le long de la direction [001] des cristaux d'α-hémihydrate sont des caractéristiques héritées de la voie de nucléation à plusieurs étapes, ils ne devraient pas être présents dans les cristaux de β-hémihydrate qui sont produits par la calcination du gypse. Si une mesure de la mosaïcité et un examen détaillé de la forme des réflexions des données SXRD des cristaux de β-hémihydrate révélaient une telle différence dans la mésostructure des deux formes d'hémihydrate, cela pourrait représenter un facteur qui influence le processus d'hydratation.

- Puisque nous avons établi l'adéquation de la technique s3DXRD pour l'étude des processus *in situ* dans le système du plâtre, cela ouvre la voie à de nouvelles études possibles. Par exemple, nous pouvons envisager de nous concentrer sur les propriétés de la pâte de gypse durcie. Des expériences in situ combinant la s3DXRD et la PCT pourraient être réalisées en appliquant des forces externes ou en augmentant la température de la pâte durcie. L'un des principaux avantages de la s3DXRD est qu'il est possible de reconstruire les gradients de déformation à travers l'échantillon. Sur la ligne de lumière ID11 de l'ESRF, il est possible d'assembler un environnement d'échantillon pour recréer les conditions que nous voulons étudier. Récemment, Thakur et al. (2023) [30] ont réalisé une expérience similaire sur du béton à la ligne de lumière ID11. Les auteurs ont mesuré et modélisé l'évolution de la microstructure du ciment lorsqu'il est exposé à de petites déformations et à des charges de compression. Pour ce faire, un appareil de compression uniaxiale a été monté sur la station 3DXRD de ID11 et des données 3DXRD et XRD-CT ont été collectées en augmentant de manière incrémentale la force appliquée sur l'échantillon [30]. Une approche expérimentale similaire pourrait également être utilisée pour étudier la réponse du plâtre à de telles stimulations externes, ce qui permettrait d'accroître les connaissances sur les propriétés et la durabilité du matériau.

- Une autre voie intéressante à explorer serait de comprendre comment le rôle des différents additifs influence la dissolution de l'hémihydrate et la précipitation du gypse à partir d'expériences de tomographie *in situ*. Dans le cas de ce travail de doctorat, seul le BNS a été utilisé pour préparer la solution pour hydrater les cristaux d'hémihydrate pendant l'expérience de tomographie, mais il pourrait être utile de répéter les mêmes expériences également avec du PAA et du polystyrène sulfonate (PSS). De plus, dans ce travail, seule la dissolution de l'hémihydrate a été étudiée. Dans de futurs travaux, il pourrait être intéressant de se concentrer également sur la précipitation du gypse. Grâce à la méthode innovante de récupération de la surface réactive de l'hémihydrate en dissolution et du gypse en précipitation que nous avons proposée, les taux de dissolution de l'hémihydrate et les temps d'induction des réactions d'hydratation pourraient être calculés et comparés. Cela fournirait des informations précieuses pour approfondir notre compréhension du rôle des additifs qui sont généralement utilisés dans l'industrie pour contrôler le processus d'hydratation du plâtre et peut-être aussi pour optimiser leur utilisation à l'avenir.

Table of contents

1. General Introduction

Calcium sulfate hemihydrate and gypsum are two mineral phases belonging to the calcium sulfate system. Calcium sulfate minerals and their synthetic equivalents are relevant for both the geological and industrial scientific communities. For this reason, they have been the subject of flourishing research activity for many years. The importance of calcium sulfate minerals from a geological point of view is mainly due to their widespread presence in the Earth's crust and the paleoenvironments in which they formed. From an industrial point of view, calcium sulfate compounds represent some of the most produced man-made materials. The large application of calcium sulfates, calcium sulfate hemihydrate and gypsum in particular, in several industrial compartments, benefits from the advantage of their low costs and high availability. The most important material that is produced from calcium sulfates is gypsum plaster [1] [2]. Even though the use of gypsum plaster in the construction industry, medicine, and pharmacology is an old and well-established practice, several fundamental questions would benefit from additional investigations. Nowadays, the scientific community has access to extremely powerful tools that provide the possibility to gain information with an unprecedented level of detail. The recent upgrade of the European Synchrotron Radiation Facility (ESRF) to the new Extremely Brilliant Source (EBS) has opened the way to new kinds of experiments in which we can characterize a process while it is happening (*in situ* conditions) with high temporal and spatial resolution. With this Ph.D. thesis, we have explored some of the new possibilities that a large-scale facility, such as a 4th generation synchrotron, can offer to perform multiscale, *in situ* characterizations on the system of the hydrating gypsum plaster. In the first part of the project, we focused on the crystallographic characterization of calcium sulfate hemihydrate, which is the starting material to produce gypsum plaster. The ID22 beamline of the ESRF, with its unique high-resolution powder diffraction instrument, represents a tool to unravel structural features that remain obscure to any conventional powder diffraction instrumentation. For this reason, it was used to investigate the possible presence of crystallographic differences between calcium sulfate hemihydrate samples synthesized in different ways. For the second part of the thesis, we performed *in situ* experiments at the ID11 beamline of the ESRF combining imaging and diffraction-based imaging techniques to observe the transformation from calcium sulfate hemihydrate to gypsum during hydration. ID11 is a versatile beamline that is specialized in materials science characterization. One of the main advantages of this beamline lies in the possibility to tune the X-ray beam down to sub-micron sizes allowing to probe a sample at different scales in a hierarchical way. This peculiar feature and the complementarity of imaging and diffraction-based imaging techniques resulted to be a promising approach to investigate the link between the crystallographic and textural properties of complex systems, such as the hydration of gypsum plaster. The last part of this Ph.D. project was dedicated to the observation of the calcium sulfate hemihydrate *in situ* dissolution at the surface and bulk level. The observation and interpretation of the dissolution of calcium sulfate hemihydrate crystals at any scale are complicated by both experimental and practical issues related to the properties and the morphology of the material. With the right experimental approach, which in our case was exploited using atomic force microscopy at the ISterre laboratories and tomography at ID11, and the use of sophisticated deep learning data processing tools these issues have been overcome.

In the first section of this thesis, the state of the art about knowledge on calcium sulfate natural phases and the use of gypsum plaster in the industry is addressed in detail. Successively, the scientific questions that motivated the development of this thesis are introduced. The second section of the thesis is dedicated to the methods that have been used to characterize the system. The theoretical basis of both the conventional and unconventional techniques that were applied are explained together with the data analysis procedures. In the last section, the results obtained from the multiscale characterization of the hydration process of gypsum plaster in all its sub-processes are presented and discussed.

2. State of the art

2.1. Calcium sulfate group minerals

Calcium sulfate minerals represent the most abundant type of minerals from the sulfate group in the Earth's crust [1]. Three are the main crystalline phases with different degrees of hydration: gypsum (or dihydrate $CaSO_4 \cdot 2H_2O$), bassanite (or hemihydrate $CaSO_4 \cdot 0.5H_2O$), and anhydrite ($CaSO_4$).

Evaporite deposits, composed mostly of gypsum and anhydrite, represent the most abundant natural source of calcium sulfate. Evaporites are rocks that form by precipitation of saturated brines as a result of evaporation [31]. Gypsum, together with Halite (NaCl), is one of the most common phases in the so-called primary evaporates [31].These are rocks made of salts, formed directly by the evaporation of hypersaline waters on the crust's surface. The evaporite salts can be found in brines and seaways. The minerals are present exhibiting different textures that are representative of the depth at which they precipitated and the stability of the phase. Gypsum can be found in monomineralic layers or beds containing interlayered mixtures. For example, laminae crystals generated by chemical settling dominate the typical subaqueous type of stratification.

Anhydrite minerals are often found in secondary evaporite deposits. Secondary evaporites are defined as rocks that have experienced diagenesis. In this case, anhydrite is not formed from precipitation as a primary phase. Instead, it replaces gypsum or forms as an intrasediment salt from the penetration of fluids. These kinds of intrasediment salts are typical of sabkha environments [31]. The first evaporitic deposits date back to the great oxidation event in the Paleoproterozoic [32] [1]. One of the oldest, two billion years old, known evaporitic deposit containing calcium sulfate, is located in Russian Karelia and has been described recently [33]. Several evaporitic deposits, mainly halite and calcium sulfates, that were found in the Mediterranean basin during drilling campaigns are geologically more recent. These massive evaporites formed during the Messinian salinity crisis around 6 million years ago and the mechanism of their deposition is still under debate [34] [1]. Figure 2.1 shows an example of Messinian gypsum deposit (Spain) associated with the Messinian salinity crisis [35] [1]. The Messinian salinity crisis is not the only event that led to the formation of giant salts, but it is generally considered the most important [36].

Figure 2.1. Modified after Van Driessche et al. (2019) [1]. Gypsum deposits associated with the Messinian salinity crisis found in Alicante, Spain [35] [1].

Even though the majority of the natural calcium sulfate minerals comes from evaporites, they were also found in other environments and conditions, such as deep marine sediments. One example is the tabular gypsum crystals that were found in a Pleistocene core. From the study of the stratigraphic distribution of the foraminifera associated with gypsum in the core, the formation of the crystals was associated with the mixing of Antarctic Bottom Water with the water of the Weddell Sea that caused the dissolution of foraminiferal ooze (rich in calcium) [37] [1]. Gypsum and anhydrite crystals can also form as the result of a diapiric phenomenon. These happened in the Gulf of Cadiz where the crystals formed as a result of high salinity near surface diapirism in the mud volcanoes [38] [39] [1]. Gypsum was also found in association with the giant cold-water mound in Ireland. In this case, it seems that gypsum formed as the result of diagenesis and oxidation of sulfide minerals triggered by the arrival of currents rich in oxidizing fluids [40] [1]. Gypsum euhedral crystals can also form as a result of brines seeping. An example is the case of the Menes caldera in Egypt where the precipitation of gypsum crystals was induced by ascending fluids saturated in gypsum from the dissolution of Messinian evaporite layers [41] [1]. Gypsum was also found to be formed as a consequence of the alteration of marine sediments rich in volcanogenic material, bringing to a high concentration of calcium in the porewaters [42]. Last but not least for marine sediments, for some salt deposits it was demonstrated that the serpentinization process, driven from the seawater, could bring conditions of increased salinity in the aqueous brines leading to gypsum precipitations [43].

When calcium sulfate (mostly gypsum) is not part of evaporitic deposits nor is located in deep marine or lacustrine environments, it can be found in caves. This event is rare and only a few examples have been discovered in the world up to now. The most famous and extraordinary one is probably the giant gypsum crystals formation in the Naica Mine in Mexico shown in Figure 2.2. The formation of the extremely large gypsum crystals, in this case, is due to hydrothermal activity [44] [45] [46] [1].

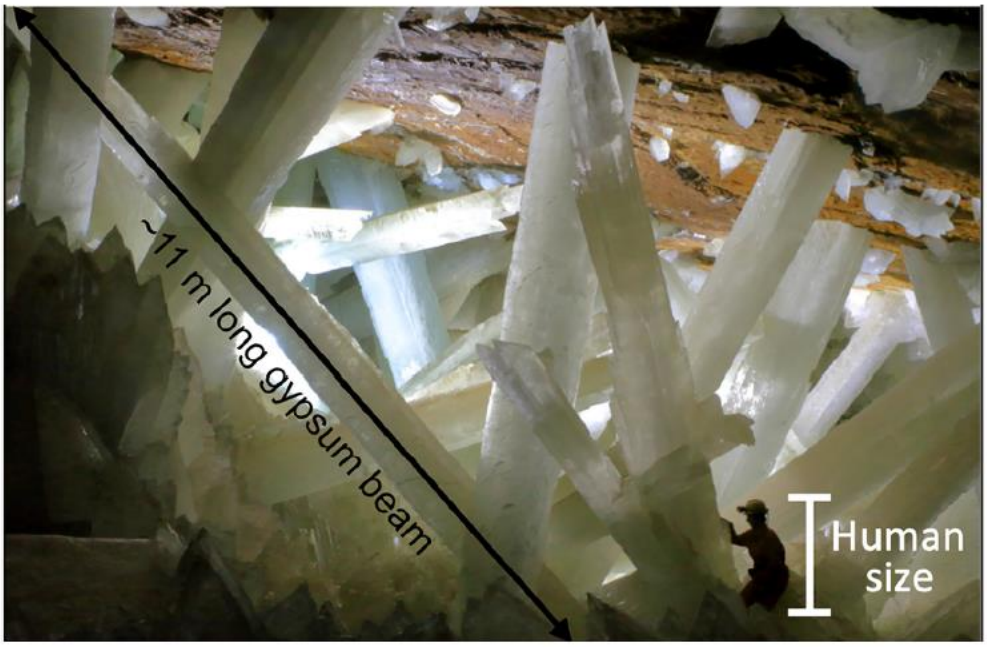

Figure 2.2 Huge crystals of gypsum found in the Naica mine in Mexico [1].

All the previous examples report the occurrence of gypsum and in smaller part anhydrite. When it comes to finding bassanite crystals in natural settings, the chances are low. Bassanite is a

metastable phase in natural environments. This means that, depending on the degree of hydration and temperature, bassanite is very likely to transform quickly into gypsum or anhydrite [1].

Calcium sulfates, in particular gypsum and bassanite, have been detected also on the surface of Mars. For example, from the data of the orbital instrument OMEGA, it was possible to understand that gypsum is present in some specific regions of Mars [47] [48] [1]. Bassanite veins, containing also gypsum and some anhydrite, have been identified recently in the Gale crater using instrumentations from the Curiosity rover [49] [50] [51] [1]. Many possible mechanisms of formation have been hypothesized for these Martian calcium sulfates. For the moment, as reported by Van Driessche et al. (2019)[1], the most plausible scenario for the formation of bassanite on Mars' surface seems to be the precipitation from surface waters rich in salts and underground post-depositional fluid [1].

Calcium sulfate phases are not only important from a geological point of view. Calcium sulfates play a considerable role also in different industrial compartments. Nowadays, gypsum is one of the most used materials for industry and in the first quarter of 2022 its extraction from mines all over the world counted 150 million tons of material (US Geological Survey, Mineral Industry Surveys, Gypsum in the first quarter of 2022). The dominant application of calcium sulfates is in the production of construction materials. Gypsum and anhydrite, are used as additives in cement pastes to tune the hydration reaction and therefore the setting of the cement [52] [53] [1]. Regarding bassanite, whereas its relevance in the geological world is limited, it is very important industrial material. Synthetic calcium sulfate hemihydrate is used to produce one of the most widespread materials in the world, namely gypsum plaster. Gypsum plaster, also known as plaster of Paris because of its first application in Paris in the 17th century to protect wooden houses from fire [54] [55] [1], is made by adding water to the hemihydrate, which, after dissolving in the solution, leads to the precipitation of entangled gypsum needles that form a porous material with important mechanical properties. Different applications of gypsum plaster and the industrial procedures used to tune its properties are discussed in detail in Section 2.3.

Since the availability of bassanite is imited on the Earth's crust, it has to be produced synthetically. The most common way to produce it is by dehydration of gypsum (at temperatures around 160 °C) [1].

The atomic structural details of gypsum, bassanite and anhydrite are very similar. Together with anhydrite, these three phases share the common feature of the Ca-SO_4 chains in which two calcium atoms are coordinated to SO_4 tetrahedra [56]. In the rest of the chapter, the state of the art about knowledge of the $CaSO_4$-H_2O system, from the crystallographic and morphological characteristics of the single phases to their uses in the industry, will be discussed in detail.

2.1.1. Anhydrite – $CaSO_4$

Three stable polymorphs of anhydrite exist. The stable phase at the Earth's surface (below 1200°C) is called β-$CaSO_4$ or insoluble anhydrite. It can be found naturally both in evaporitic and fumarolic deposits, as it has a broad range of paragenesis [31]. The crystal structure of the insoluble anhydrite can be described in the orthorhombic space group Cmcm (also reported with different settings in Amma and Bmmb) [57] [58] [59] [60]. When the temperature is higher than 1200°C, the stable anhydrite phase is the α-$CaSO_4$, which transforms rapidly into β-$CaSO_4$ when cooled. The third polymorph is the hexagonal γ- $CaSO_4$ (or soluble anhydrite), which is metastable in air and water. It forms when gypsum is heated in air over 100-130°C but it rehydrates quickly to hemihydrate or gypsum. A representation of the crystal structure of the orthorhombic (Amma space group) β-$CaSO_4$ [58] and the hexagonal ($P6_222$ space group) γ- $CaSO_4$ [61] is shown in Figure 2.3.

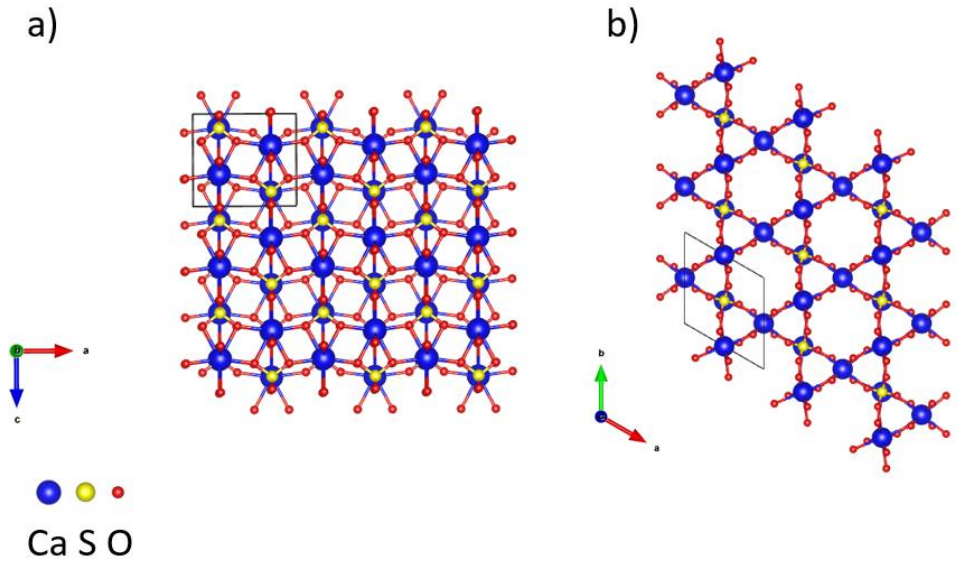

Figure 2.3. Crystal structure of β-$CaSO_4$ with Amma space group (a) [58] and γ- $CaSO_4$ with $P6_222$ space group (b) [61]. The diagrams of the crystal structure have been done with the software *VESTA* [62].

2.1.2. Bassanite or calcium sulfate hemihydrate – $CaSO_4 \cdot 0.5H_2O$

The structure of bassanite or calcium sulfate hemihydrate, when referred to a synthetic compound, differs from the anhydrite in the presence of structural water. The water molecules are placed inside water channels that run parallel to the [001] direction as shown in Figure 2.4c.

Synthetic calcium sulfate hemihydrate can be produced in different ways, resulting in the formation of two types of hemihydrate called α and β. For industrial applications, hemihydrate is usually produced via the dehydration of gypsum. When the dehydration is performed under dry air or vacuum (calcination), the β-hemihydrate is produced. When the gypsum is heated in solution or under high water pressure, the type of hemihydrate obtained is the α. The current state of the art is that these two types of hemihydrate differ mainly in the size and morphology of the crystals, which influence the available surface area and therefore their behavior when hydrated [2]. A more detailed investigation of the structural differences between these two types of calcium sulfate hemihydrate is one of the objectives of this thesis. Figure 2.4 shows two SEM pictures of (a) the α-hemihydrate and (b) the β-hemihydrate. The α-hemihydrate crystals are large, usually more than 100 µm, and show euhedral habits characterized by the typical "pencil" shape as shown in Figure 2.4a. The β-hemihydrate crystals are smaller than 50 µm, presenting anhedral crystal habits, as is shown in Figure 2.4b. For a long time, the scientific community has debated the existence of a structural difference between the α and β-hemihydrate. Some researchers supported the hypothesis that the α-hemihydrate crystallizes in the monoclinic I2 space group and the β-hemihydrate in the trigonal form with the $P3_221$ space group [63] [2]. Others sustained instead that the two hemihydrates only differ in the shape and morphology of the crystals [64]. The proof of a real difference in the α- and β-hemihydrate structure has been never established and nowadays there is a consensus on the fact that both hemihydrates which contain 0.5 molecules of water, whether it is α or β, and crystallize in the I2 setting [9] [10]. Sub-hydrates with a different amount of water resulting in the trigonal structure have been also reported [10].

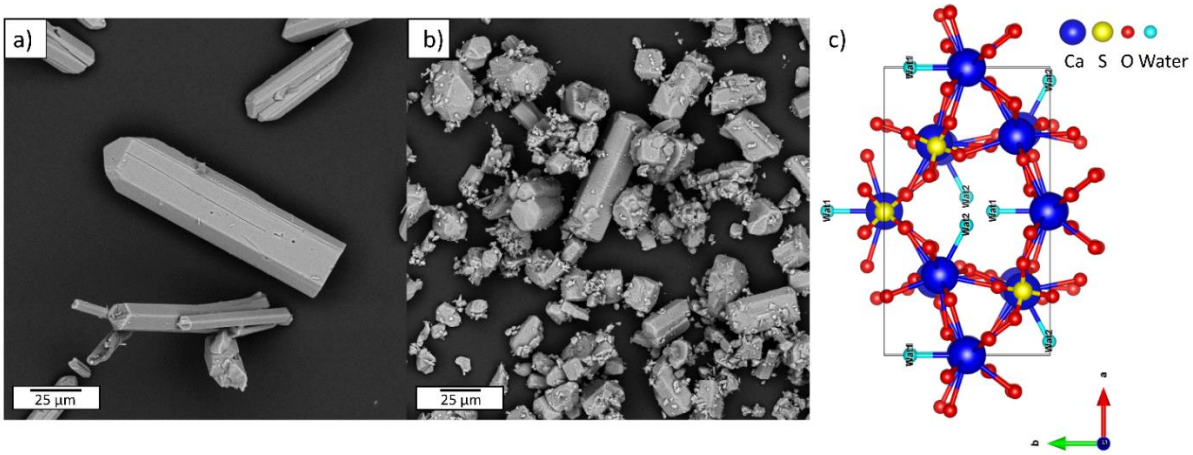

Figure 2.4. SEM pictures of the two different morphologies of α- and β-hemihydrates, were obtained with a TESCAN vega SEM. a) α-hemihydrate. b) β-hemihydrate. c) Water channels along the [001] direction in the hemihydrate I2 structure [8]. The structure of the hemihydrate was visualized with the software *VESTA* [62].

It is known that the two types of hemihydrate generate gypsum plasters with different properties, as reported by Sigh and Middendorf [2]. Lewry and Williamson [67] carried out experiments with different techniques to understand the hydration process of the two hemihydrate forms. In one experiment, the response of the two hemihydrates in terms of electrical and temperature resistance with time was probed. From these experiments, it was possible to see that α and β-hemihydrate were responding similarly but they were showing differences in the development of the hydration process. Figure 2.5a shows the difference between the temperature rises for the two hemihydrate forms during the hydration. The α type shows a shorter induction time than the β, but the β hydrates much faster than the α after the induction time. This can be explained by the larger surface area of the β-hemihydrate, with small crystals that tend to fragment into smaller ones. Figure 2.5b shows the electrical resistance per unit length as a function of the hydration time. From the trend of the two curves, it is clear that the hydration can be divided into three parts. The first part happens between 5 and 10 minutes and shows the lower values of electrical resistance from both the α- and β-hemihydrate. The electrical resistance is low in this part of the reaction because the solubility of calcium and sulfate ions is maximum. In the middle part of the reaction, the resistance increases due to the precipitation of gypsum. After 100 minutes, at the end of the hydration, the hemihydrates show the highest electrical resistance, due to the lower solubility of gypsum. During the hydration of the hemihydrate, two processes happen: the dissolution of the hemihydrate and the precipitation of gypsum. The differences in the curves reported in Figure 3 can be related to the different rates of dissolution of the two hemihydrate types. The dissolution rate is not only influenced by the particle size but also by the crystal habit and degree of lattice defects [2].

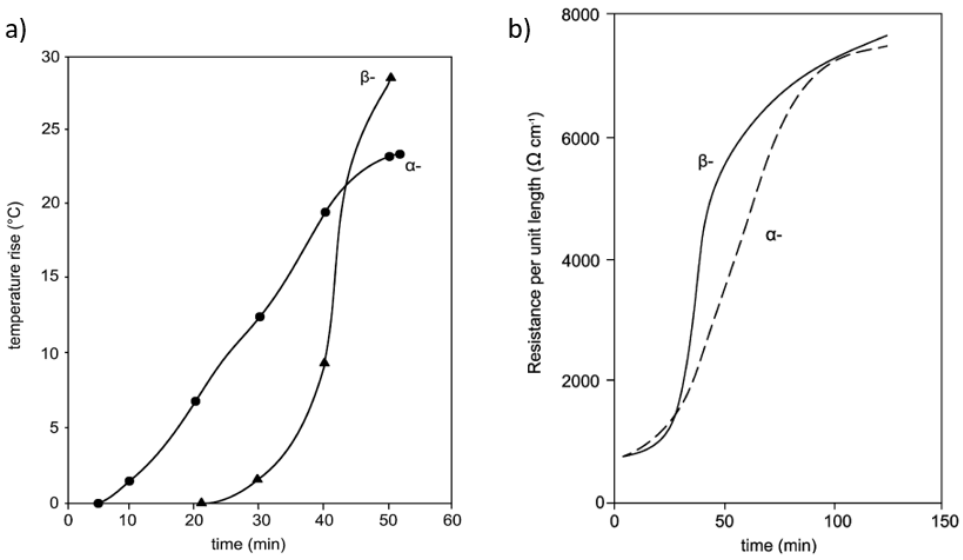

Figure 2.5. Modified after Singh & Middendord (2007) [2]. a) Amount of heat released from both α- and β-hemihydrates during hydration. b) Electrical resistance of both α- and β-hemihydrates during hydration [2].

2.1.3. Gypsum – $CaSO_4 \cdot 2H_2O$

Gypsum is the most abundant natural sulfate on the Earth's surface. Due to the geological, environmental and industrial importance of this mineral, its structure has been studied extensively in the literature. Gypsum crystallizes in the monoclinic system. The structure of gypsum is characterized by layers of Ca-SO_4 tetrahedra with water molecules that are placed between the layers [68]. The water molecules, arranged in the [010] direction, give gypsum its peculiar cleavage along the same direction. Figure 2.6 shows the structure of gypsum (C 2/c space group) described by Boeyens and Icharam [69] with the cleavage direction [010] indicated by the dashed line.

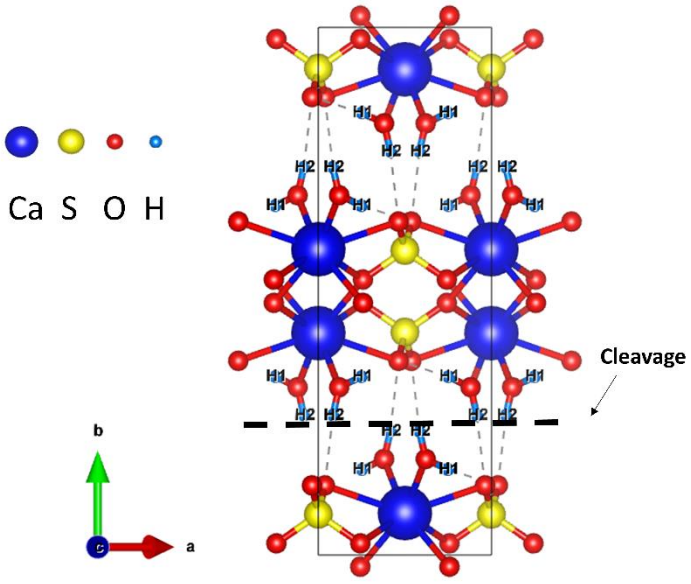

Figure 2.6. Structure of gypsum as seen along the c direction. The H atoms show the atomic sites of water and the place where the cleavage of gypsum occurs [69]. The diagrams of the crystal structure have been done with the software *VESTA* [62].

The typical crystal habit of gypsum is in the form of tabular crystals, with varying thickness, along the [010] direction. The conditions that lead to the growth of different morphologies in pure gypsum crystals are an active area of research. In particular, findings of unexpected morphologies in natural environments have triggered investigations on understanding the conditions that allowed such morphologies to occur, which could be the key to unraveling geological processes and also the starting point to reproduce those morphologies in the laboratory. An example of this are the large gypsum crystals that were found in Naica (Mexico) that renewed the interest in the topic of its stability and morphology [68]. Along these lines, one of the main scientific challenges nowadays regards how additives that act on the crystallization and morphology of the crystals [70] [68] influence the structure of gypsum.

A very important characteristic of gypsum is the presence of twinning. Five twinning laws have been described in the literature: (100, 001, $10\bar{1}$, 201, 101) [71] [72] [73] [68]. All five laws are represented in Figure 2.7. According to Aquilano et al. (2016) [68], the (100) twin law is the most common due to the smaller twin energy and the compatibility with the equilibrium crystal shape [68]. The presence of twinning in gypsum crystals is a very important feature regarding gypsum production. This is because, in the area where the components of the twinning touch each other, the crystal presents reentrant angles, which could be the cause of different steps for the crystal growth [68].

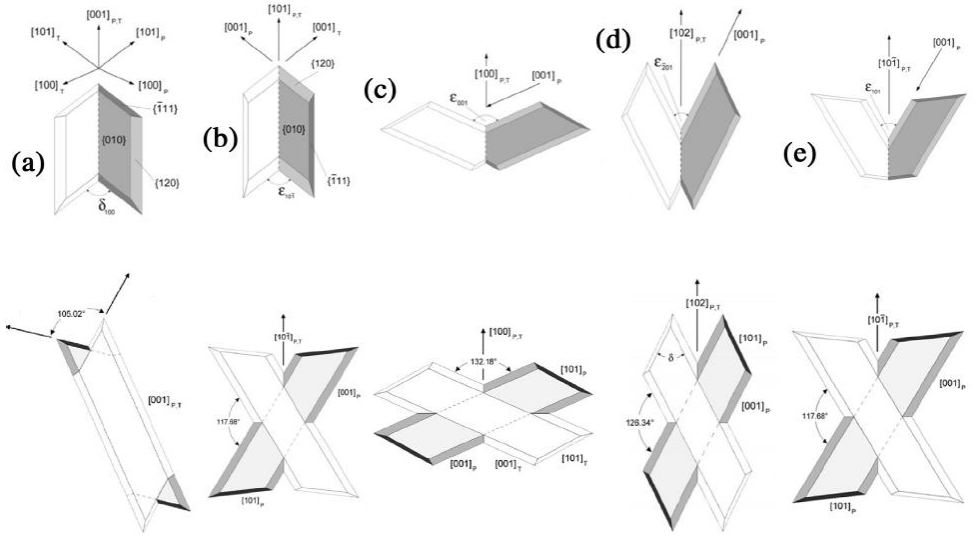

Figure 2.7. Picture was taken by Aquilano et al. (2016) [68]. On the top from (a) to (e), the five twin laws for gypsum are drawn, respectively (100, 001, 10-1, 201, 101). On the bottom, the penetration twins correspond to the twin laws.

2.2. The hydration reaction of the calcium sulfate group minerals

In this section, the $CaSO_4$-H_2O system will be discussed in detail with specific emphasis on the phase diagram, and the relative stabilities of the phases as a function of the pressure, temperature, and salinity. The current theories and evidences about the nucleation of calcium sulfate phases from the solution will be also described. Lastly, the hydration process that generates gypsum plaster from bassanite will be described.

2.2.1. Phase diagram of the calcium sulfate minerals

Understanding the transformation and crystallization of the calcium sulfate phases is a very important matter for both the reconstruction of geological records and the improvement of industrial processes. Many studies have been devoted to the comprehension of how the solubility of calcium sulfate phases is influenced by different temperatures, pressures, and the presence of ions and organic molecules in solution [75] [56].

At different temperatures, the calcium sulfate phase that precipitates (the stable phase) is the one with the lowest solubility. The graph in Figure 2.8 shows the stability regions of calcium sulfate phases in the temperature range of 0-200 °C. As it is clear from the intercepting regions between the curves of gypsum (green), β-anhydrite (blue), and bassanite (orange), a fixed value of transition temperatures has not yet been provided. The transition between gypsum-anhydrite and gypsum-bassanite in particular is associated with a range of temperatures between 42-60 °C in the first case, and 80-110 °C in the second [75] [56].

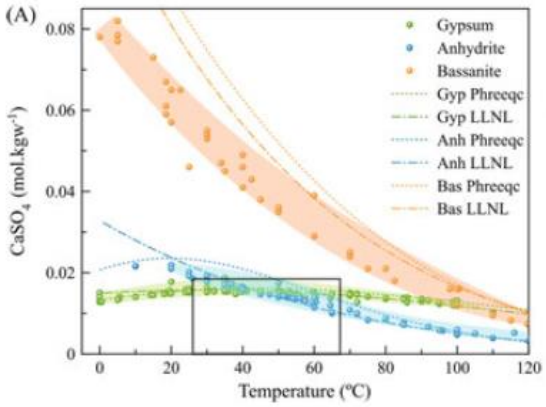

Figure 2.8. Modified after Van Driessche et al. (2016) [75]. Solubility curves of gypsum, bassanite, and β-anhydrite. The data plotted are relative to experimental data collected (dots in the plot) by Van Driessche et al. (2016) [75] from the literature, and solubility curves calculated based on the PHREEQC (dotted lines in the plot) and LLNL (dot and stripe lines) databases. The experimental data are extracted from the works of Poggiale (1843) [76], Marignac (1874) [77], Droeze (1877) [78], Tilden and Shenstone (1884) [79], Raupenstrauch (1885) [80], Boyer-Guillon (1900) [81], Cameron (1901) [82], Hulet and Allen (1902) [83], Melcher (1910) [84], Hall et al. (1926) [85], Hill (1937) [86], Hill and Wills (1938) [87], Patridge and White (1929) [88], Roller (1931) [89], D'Ans (1933, 1968) [90] [91], Booth and Bidwell (1950) [92], Madgin and Swayles (1956) [93], Bock (1961) [94], Dickson et al. (1963) [95], Marshall et al. (1964) [96], Zen (1965) [97], Marshall and Slusher (1966) [98], Power et al. (1964, 1966) [99] [100], Block and Waters (1968) [101], Blount and Dickson (1969, 1973) [102] [103], Culberson et al. (1978) [104], Innorta et al. (1980) [105], Kontrec et al. (2002) [106], and Azimi and Papangelakis (2010) [107].

The transition temperature between gypsum and anhydrite is complicated to measure because anhydrite crystallizes at a slow rate below 70 °C [56]. As reported by Freyer and Voigt (2003) [56] and Van Driessche et al. (2016) [75], the first value of the transition temperature between gypsum and anhydrite was proposed by Van't Hoff et al. (1903) [108]. He proposed a temperature of T= 63°C based on both thermodynamic considerations and dilatometric experiments [56]. After this

study, a number of other studies provided different values for this transition temperature. A table with all the values of the transition temperature between gypsum and anhydrite, listed by Van Driessche et al. (2016) [75], is reported in Table 2.1.

Authors	T °C	Method
Van't Hoff et al. (1903)	60-66	Experiments and thermodynamic calculations
Patridge and White's (1929)	38-39	Solubility measurements of anhydrite at high temperature and extrapolation
Hill (1937)	42 ± 1	Solubility measurements of anhydrite at lower temperatures (65, 45, and 35 °C) and interpolation
Posnjak (1938)	42 ± 2	Solubility measurements
Kelly et al. (1941)	40	Measurements of thermochemical properties of solid gypsum and anhydrite and calculation of the transition temperature
Bock (1961)	42	Solubility measurements of anhydrite and gypsum
Marshall et al. (1964)	42	Solubility measurements
Zen (1965)	46 ± 25	Calculations based on revised thermodynamic data of Kelly et al.
Power et al. (1966)	41 ± 1	Solubility measurements of gypsum and anhydrite
Hardie (1967)	58 ± 2	Water activity measurements
Blount and Dickson (1973)	56 ± 3	Solubility measurements of anhydrite at high temperature (>70 °C) and extrapolation
Knacke and Gans (1977)	55.5 ± 1.5	Equilibration experiments in solutions containing both gypsum and anhydrite
Innorta et al. (1980)	49.5 ± 2.5	Solubility measurements
Corti and Fernandez-Prini (1983)	42.6 ± 0.4	Thermodynamic calculations
Hamad (1985)	46	Solubility measurements at high pressure and extrapolations to 1 atm
Raju and Atkinson (1990)	59.9	Thermodynamic calculations
Kontrec et al. (2002)	40	Solubility measurements and phase transition experiments
Azimi et al. (2007)	40 ± 2	Modeling of CaSO4 solubility

Table 2.1. Modified after Van Driessche et al. (2016) [75]. All the transition temperatures that have been proposed for the gypsum-anhydrite transition.

The transition temperature between gypsum and bassanite has been investigated less in the literature, due to the metastability of bassanite in natural environments. Even though this transition is less relevant to geological studies, it remains fundamental for most of the industrial applications of calcium sulfate. Based on the data available, the range of temperatures for the gypsum/bassanite transition is between 80-110°C [75]. As for the case of the gypsum/anhydrite transition, the first experimental and theoretical study has been done by Van't Hoff et al. (1903) [108] providing a temperature value of T= 106°C. Posnjak (1938) [109], and Partridge and White (1929) [88] found similar values of temperatures between 97-100°C. Finally, Azimi et al. (2007) [110] calculated a transition temperature between gypsum and bassanite of 99°C. As also explained by Van Driessche et al. (2016) [75], in general, the transition temperatures provided in the years for the gypsum/bassanite transition are more coherent than those provided for the gypsum/ anhydrite transition [75].

Since bassanite is assumed to remain metastable for all the range of temperatures between 50-1200°C, no temperature for the phase transformation has been observed or calculated so far [106] [75].

The temperatures of phase transformation of the calcium sulfate system are influenced by the presence of salts and electrolytes in the solution. The most relevant example is how the presence of sodium chloride (NaCl) influences the solubility of gypsum and β-anhydrite, as shown in Figure

2.9. When NaCl is added to a solution between 0 to 1 M, there is an important increase in the solubility of gypsum and anhydrite. When the concentration is high enough, as highlighted in Figure 2.9 by the black arrow, the solubility curves of gypsum and anhydrite cross. This means that with high concentrations of NaCl, the gypsum/anhydrite transition temperature has lower values [75]. Bassanite is obtained, due to kinetic inhibition to the precipitation of anhydrite, at temperatures down to 70°C [111] [112] [75].

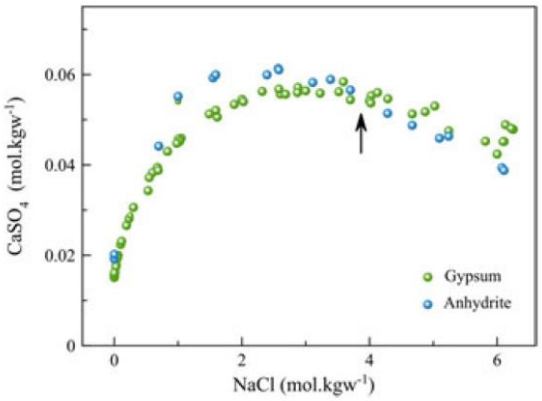

Figure 2.9. Modified after Van Driessche et al. (2016) [75]. Solubility curves for gypsum and β-anhydrite with increasing concentration of NaCl. The black arrow indicates the expected temperature of transition between gypsum and anhydrite at 25°C and 4 M NaCl [75]. The experimental data reported in the form of dots are extracted from the works cited in Figure 2.8.

The effect of pressure is also considerable. The solubility of gypsum and anhydrite is known to increase with increasing pressure [75].

2.2.2. Nucleation of calcium sulfate phases

Due to the abundance of calcium sulfate phases in nature and the vast range of applications that they have in the industrial and engineering world, the topic of $CaSO_4$-H_2O nucleation and crystallization from solution has been an active area of research. Unravelling the steps of the precipitation process of gypsum and bassanite contributes to understanding the geological and geochemical records of not only the Earth but also Mars's surface. Moreover, in the case of bassanite, this helps to improve the performances of gypsum plaster. Having a full picture of how calcium sulfate phases form in aqueous systems is also the starting point to design methods to prevent precipitation from happening in desalinization plants or water pipes.

There are several studies that aimed to understand how gypsum nucleates from a solution and successively how it grows. These works, can be divided into two categories. The first one includes all the studies in which the nucleation of gypsum has been described in the framework of the classical nucleation theory (CNT). The second category instead, includes all the studies in which the nucleation of gypsum has been described as a multi-step process differing from the CNT [75].

The CNT is the most commonly used theory to describe the nucleation of a new thermodynamic phase [113]. The theory describes the nucleation of either solids or liquids, but in this paragraph, only the case of the nucleation of solids from solution will be reported. When spherical nuclei, with radius *r*, are forming homogeneously, there is a change in the free energy of the system and this change can be expressed as [113]:

$$\Delta G = \frac{-4\pi r^3}{3\upsilon} KT \ln S + 4\pi r^2 \sigma \qquad \text{Eq.2.1}$$

The total free energy of the system in which the nucleation of a new phase occurs is composed of the sum of two terms. The first term in Eq.2.1 represents the bulk free energy and the second term represents the free energy of the interface (between the bulk and the surface that is going to nucleate). Figure 2.10 shows how the total free energy of the system changes when r increases. In the first part of the reaction, when r is smaller than the critical value r_c, the total free energy is dominated by the surface contribution. After the critical point, when the nuclei have reached a radius bigger than r_c, the total free energy is decreasing due to the increase of the bulk free energy, related to the change in chemical potential.

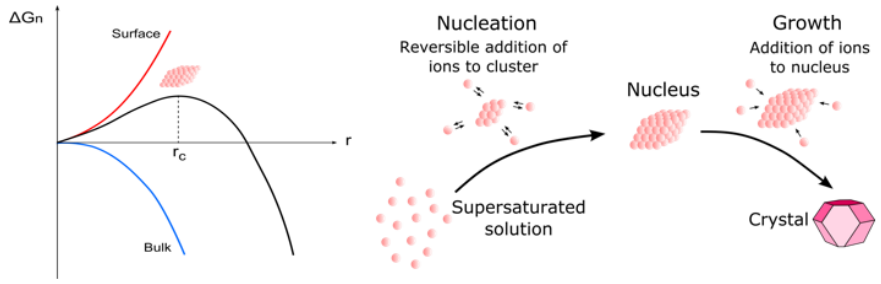

Figure 2.10. Explanation of the nucleation process of solids from liquids following the CNT.

Reaching the critical point means that the system is in a metastable equilibrium and any further increase in the size of the nuclei would start the growth of the crystals. The CNT thus proposes a nucleation and growth model in which the reaching of local supersaturation in a solution triggers the agglomeration of nuclei, that having a size coincident with the r_c, start to grow. Based on the CNT it is also possible to calculate the nucleation rate. The definition of the nucleation rate considers a fundamental assumption called capillary approximation. The capillary approximation states that the nuclei that start to grow are characterized from the very beginning by the structure of the final crystal. This means that in the framework of the CNT, a modification of the structure of the crystals during their growth it is not allowed [114] [113].

The first studies on the precipitation of gypsum from solution, performed by Conley and Boundy (1958), Schierholtz (1958), Smith and Sweett (1971) [75], agreed in describing this process within the CNT. In the same period, some studies were performed that measured the induction time of the precipitation of gypsum [115] [116]. Liu and Nancollas 1973 described the nucleation of gypsum as following the non-classical model described by [117]. A large number of studies focused on measuring the induction time associated with the precipitation of gypsum were also performed between 1980 and 2010 [118] [119] [120] [121] [122] [123] [124] [125] [126] [127] [128] [75]. All of the studies cited so far, which can be considered the earliest studies on the nucleation of gypsum, describe the process as more or less in line with the CNT, at least for the description of the kinetics of the process [75].

A big step forward in the understanding of this subject was done some years later. In 2012, four studies were published about the precipitation of gypsum suggesting a revolutionary way of describing its nucleation process [75]. The first work is attributable to Wang et al. [129]. They characterized the precipitates formed from mixing two equimolar solutions of $CaCl_2{\cdot}2H_2O$ and Na_2SO_4 with different final concentrations of $CaSO_4$ at different times. They prepared a series of solutions to obtain final concentrations of Ca^{2+} and SO_4^{2-} between 15 and 100 mM, and then they characterized the precipitates with TEM, XRD, Raman spectroscopy, and Thermogravimetric analysis (TGA). The results that they got were showing, for the first time, that the precipitation of gypsum is a process that involves the formation of intermediate phases. When the concentration

of $CaSO_4$ is slightly higher than the saturation limit (15 mM $CaSO_4$), at room temperature, it is possible to detect the formation of short-life nanometric amorphous domains containing calcium and sulfur. The TEM picture showing the amorphous calcium sulfate (ACS) is reported in Figure 2.11a. With higher concentrations of $CaSO_4$, such as 50 mM, the precipitate passes through a crystalline intermediate phase of calcium sulfate hemihydrate before the crystallization of gypsum takes place. The sub-nanometric crystals of hemihydrate found by Wang et al. are shown in the TEM picture in Figure 2.11b. With higher levels of concentration of $CaSO_4$, 100 mM, no intermediate phase was detected while the system was characterized by precipitation of gypsum [129]. The TEM picture of the gypsum needles precipitated by Wang et al. is reported in Figure 2.11c.

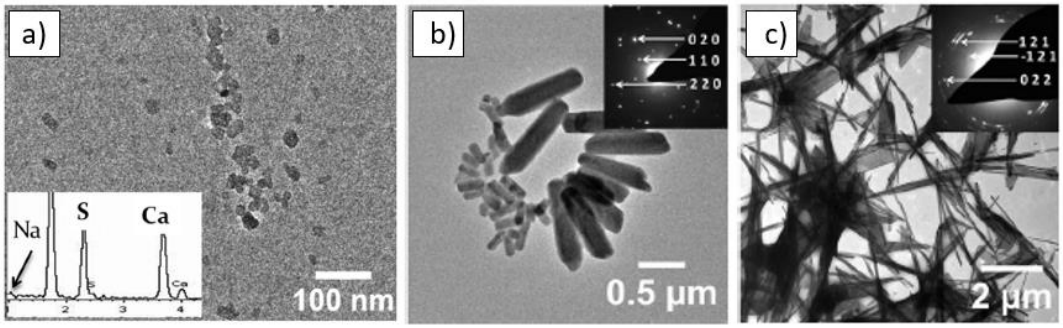

Figure 2.11. Modified after Wang et al. (2012) [129]. a) TEM picture of amorphous $CaSO_4$. b) TEM picture of the hemihydrate precursor phase to the crystallization of gypsum. c) TEM picture of gypsum crystals.

The second important work is the one of Van Driessche et al. [130]. In this case, the precipitation of gypsum was performed in gypsum supersaturated solutions, and the precipitate, after being filtered and quenched, was observed using high-resolution TEM (HR-TEM). The focus of the work was to understand the mechanism of gypsum precipitation during the early stages of the process. With this approach, they found out that the precipitation step is characterized by the formation of nanodomains of calcium sulfate hemihydrate with diameters of 10-15 nm. These domains, with rounded shapes, remained stable in the solution for a reduced time. Successively the domains started to grow along the c-axis in what they call nanorods that present the structure of calcium sulfate hemihydrate. The nanorods then formed oriented aggregates maintaining the hemihydrate structure until they finally transformed into bigger, micrometer-sized, gypsum crystals [130]. Even though in this case the amorphous intermediates were not observed, this study offered another proof that the precipitation of gypsum does not follow the classical pathway of the CNT but is instead characterized by the presence of multiple steps of precipitation. Figure 2.12 shows the TEM pictures of the observed nanodomains and nanorods of calcium sulfate hemihydrate formed at the beginning of the precipitation (a), and the final gypsum crystals (b) [130].

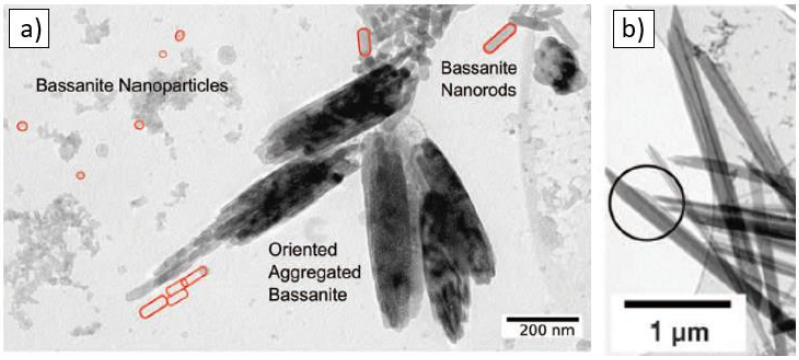

Figure 2.12. Modified after Van Driessche et al. (2012) [130]. a) TEM picture of the aggregates of bassanite nanoparticles and nanorods, precursors of the gypsum crystallization. b) TEM picture of the final large gypsum crystals.

The work of Saha et al. [131] also contributed to shedding light on the process of gypsum precipitation. Saha et al. performed time-resolved cryo-TEM experiments to investigate the precipitates formed from a supersaturated solution prepared by dissolving calcium sulfate hemihydrate. Their study observed that after only 1 s from the start of the precipitation process, amorphous nanoparticles with the size of 4-10 nm were already formed. After 15 s, the nanoparticles were grown and started to show some crystallinity coherent with the structure of gypsum indicating that the particles were starting to order internally. Finally, already after 30 s, the particles were showing the typical aspect of gypsum crystals. A diagram, showing also the timeframe of the precipitation process, of the findings of Saha et al. [131] is shown in Figure 2.13.

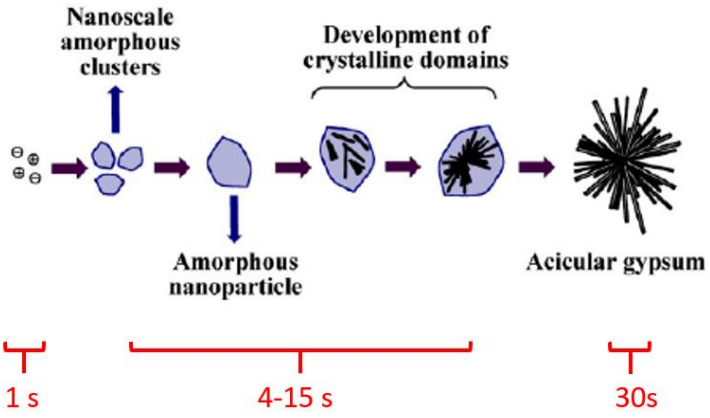

Figure 2.13. Modified after Saha et al. (2012) [131]. Model of the early stages of the crystallization of gypsum proposed by Saha et al. (2012) [131].

The last work published in 2012, is the study by Jones (2012) [132]. Here, the authors studied the precipitation of gypsum using Fourier transform IR spectroscopy in ATR mode. They monitored the crystallization of calcium sulfate from a solution with 41 mM concentration of Ca^{2+} and SO_4^{2-} during its evaporation [132]. As a result, the increasing intensity of the water bands with the development of the crystallization suggested the formation of a disordered precursor that was then transforming into the crystalline phase, either bassanite or gypsum. The fact that this disordered intermediate was quite persistent in the solution, suggested also that the ordering of water could represent a fundamental aspect of the multi-step precipitation pathway of gypsum. Figure 2.14 shows the FTIR spectra of gypsum crystallization stages from the early process (a), to the successive stages (b).

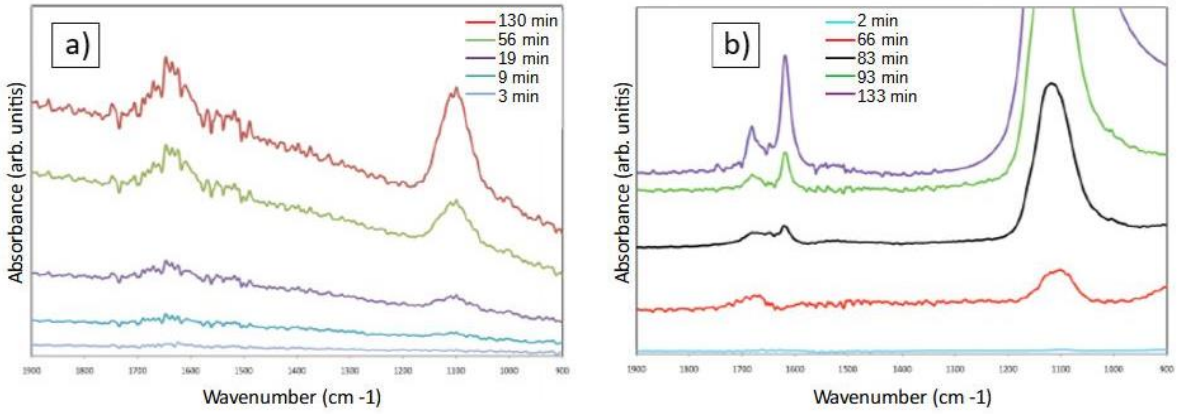

Figure 2.14. Modified after Jones (2012) [132]. a) FT-IR spectra of the early stages of the crystallization of gypsum. b) FT-IR spectra of the crystallization of gypsum in more advanced stages.

All these studies that were published in the year 2012 [129] [130] [131] [132] contributed to establishing a new crystallization pathway for gypsum from solution. However, even though the general conclusions are all agreeing in proposing a multi-step precipitation process involving the formation of intermediate phases with different atomic arrangements compared to the final gypsum, there is still a lot of confusion in describing in detail all the intermediate phases. As it is suggested by Van Driessche et al. (2016) [75], the origin of the discrepancies lies in the experimental approaches used. If is true that *in situ* experiments such as the one of Jones (2012) [132], provide insights into the precipitation while it is happening, it is also true that it does not allow for visualization of the particles that are precipitating. The opposite problem instead is associated with the TEM analyses of Van Driessche et al. (2012) [130], Wang et al. (2012) [129], and Saha et al. (2012) [131], in which the resolution of the technique permits to see the particles and characterize them but only after complex sample preparation processes [75].

After a few years, Stawski et al. (2016) [133] published a synchrotron-based in situ SAXS/WAXS (small angle and wide angle scattering) study in which they demonstrated that the precipitation of gypsum happens through a four-step process. This work is very important because it permitted us to overcome the experimental limitations that generated discrepancies in the previous studies [133] [75]. The precipitation of $CaSO_4$ was induced by mixing two equimolar solutions of $CaCl_2{\cdot}2H_2O$ and Na_2SO_4 to obtain a concentration of 50 mM $CaSO_4$. During the *in situ* experiment, the mixed solution was constantly pumped through a capillary that was placed in front of the X-ray beam to probe continuously the precipitation process. The four stages of the precipitation process of gypsum discovered by Stawski et al. (2016) [133], are summarized in the schematic representation by Van Driessche et al. (2016) [75] and reported in Figure 2.15.

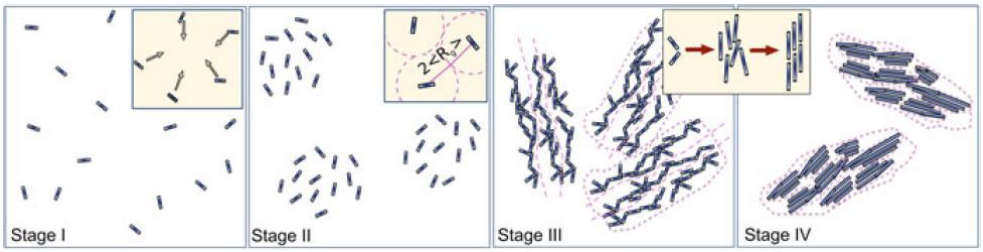

Figure 2.15. Modified after Stawski et al. (2016) [133] and Van Driessche et al. (2016) [75]. Four stages of gypsum precipitation and crystallization process unravel by SAXS/WAXS synchrotron experiments.

Stage I happens during the firsts 30-120 s, as soon as the system reaches the supersaturation level needed. Stage I corresponds to the formation of non-aggregated primary species of Ca-SO_4. These primary particles have a length of around 3 nm and a diameter of 0.5 nm. At this stage, the particles are not yet hydrated. In stage II, between 150-390 s, the particles start to agglomerate and assemble, maintaining a considerable distance between them. The third stage, which happens between 420-1500 s is characterized by the assembly of particles and the formation of denser and more ordered agglomerates. Stage IV, after 1500s, is the last one and corresponds to the formation of the prototypes of gypsum crystals, made by the aggregation and order of the primary units. The evidence of the intermediate phases found by Stawski et al. (2016) [133] however, does not solve the problem of identifying unambiguously what the nature of these phases is. In particular, the assembly of primary particles that Stawski et al. observed in stages II and III (Figure 2.15), could either represent the amorphous phase detected by Wang et al. (2012) [129], Saha et al. (2012) [131], and Jones (2012) [132], or the bassanite nano domains observed by Wang et al. (2012) [129] and Van Driessche et al. (2012) [130] [75]. The work of Tritschler et al. (2015a) [134] provides important insights into the formation of bassanite as a predecessor phase to the crystallization of gypsum. In particular, they observed the precipitation of stable and uniform bassanite nanorods

from supersaturated solutions of $CaSO_4$ and ethanol [134] [75]. Tritschler et al. (2015) [134] also observed that the stability of bassanite is favored by low water contents and changes based on the type of organic solvent. Figure 2.16a reports a TEM picture of the bassanite porous nanorods obtained by Thritschler et al. (2015) by quenching the precipitation process in excess of ethanol [134] [75]. Figure 2.16b-c shows SEM pictures of the same bassanite nanorods with different magnifications [134].

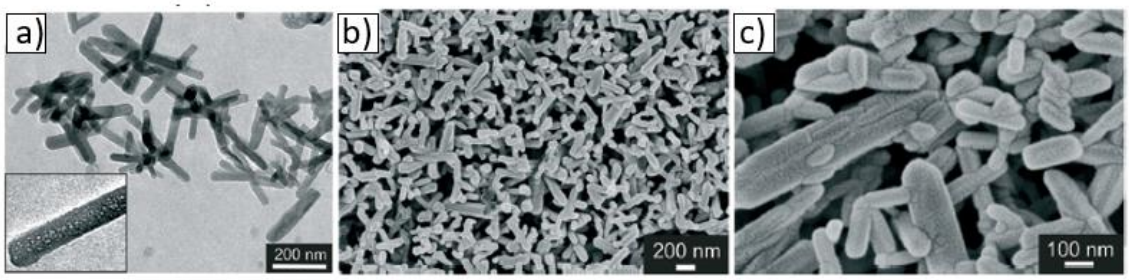

Figure 2.16. Modified after Tritschler et al. (2015) [134]. a-c) TEM pictures of precipitated bassanite nanorods observed with different magnifications.

He et al. (2018) [135] proposed a new precipitation pathway for gypsum crystals based on *in situ* liquid cell microscopy observations. With their approach, they found out that the nucleation of gypsum can occur in two ways depending on the particle size of the primary nucleating units, which influence the enthalpy and free energy of the phase. When the diameter of the primary particles is small enough (below a critical value) the precipitation of bassanite is possible and thus there is the presence of bassanite as a precursor phase to the crystallization of gypsum, induced successively by hydration. If the primary particles have a bigger diameter, gypsum is the phase that directly nucleates from the solution and grows by the addition of nanoparticles. The two distinct pathways, proposed by He et al. (2018) [135], of precipitation of gypsum, are shown in Figure 2.17.

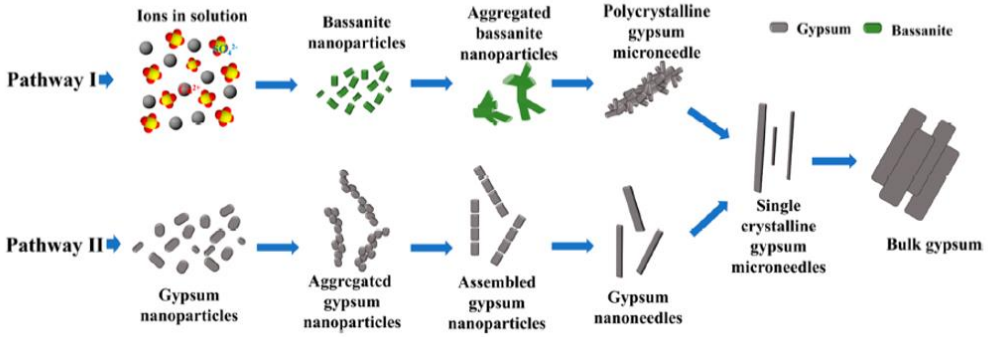

Figure 2.17. Two crystallization pathways of gypsum prosed by He et al. (2018) [135].

Whereas the number of studies addressing directly the nucleation and growth of gypsum has increased, studies dealing with the nucleation of bassanite and anhydrite are more scarce. Nevertheless, the physical-chemical conditions needed for bassanite precipitation in an aqueous solution have been constrained quite precisely.

The first studies that permitted an understanding of the conditions needed to trigger the precipitation of bassanite in aqueous solutions were done by Cruft and Chao (1970) [111], Jiang et al. (2013) [136] and Ossorio et al. (2014) [112]. In particular, Ossorio et al. (2014) designed a series of experiments to follow the gypsum-bassanite-anhydrite transition from precipitation of calcium

sulfate in solution. In these experiments, two equimolar solutions of $CaCl_2 \cdot 2H_2O$ and Na_2SO_4 were mixed with solutions at low, medium, and high salinity. The mixed solutions were then exposed to temperatures between 40 and 120°C for different periods. The results that they got from the X-ray powder diffraction analysis of the precipitates are shown in figure 2.18.

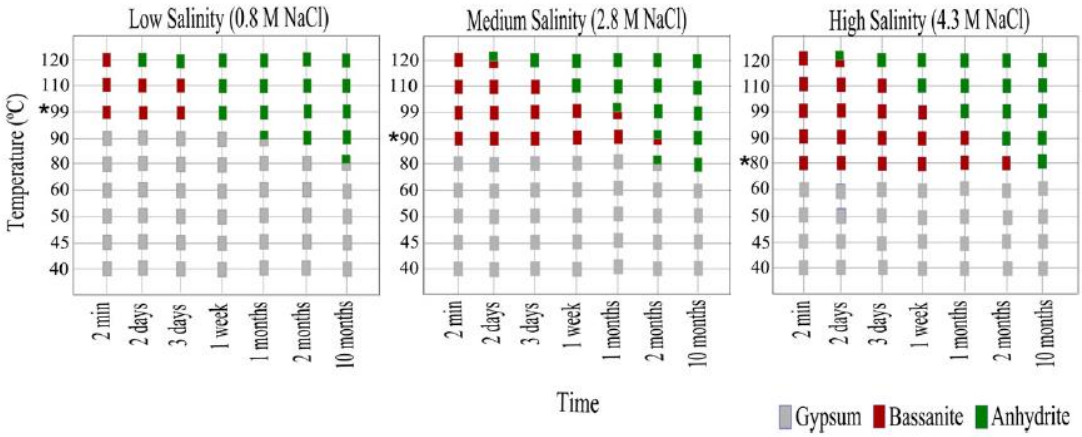

Figure 2.18. Diagrams showing the gypsum-bassanite-anhydrite transitions temperatures in solutions with different salinities [112].

Bassanite and anhydrite are the phases that precipitate at temperatures higher than 60°C. Moreover, they showed that the stability of bassanite increases with the salinity of the solution in which it precipitates.

A big step forward in understanding the precipitation of bassanite was taken in 2020 by Stawski et al. [137]. They demonstrated that the precipitation of bassanite follows the same pathway as the precipitation of gypsum (Figure 2.15). They conducted *in situ* SAXS/WAXS experiments coupled with Raman characterization and observed the early stages of nucleation of bassanite. With this approach, they found out that also in the case of bassanite, the nucleation starts with the formation of nanosized primary species. Moreover, a "brick-in-the-wall" model similar to the one proposed for gypsum, was used to explain the formation of aggregates of primary species. These aggregates present features comparable with those of the aggregates observed in the early stages of gypsum nucleation (Figure 2.15, stage II). The crystallization is finally driven by the reorganization of the aggregates, which potentially brings in the formation of mesostructured single bassanite crystals [137]. A schematic representation of the precipitation process of bassanite proposed by Stawski et al. (2020) [137] is shown in Figure 2.19.

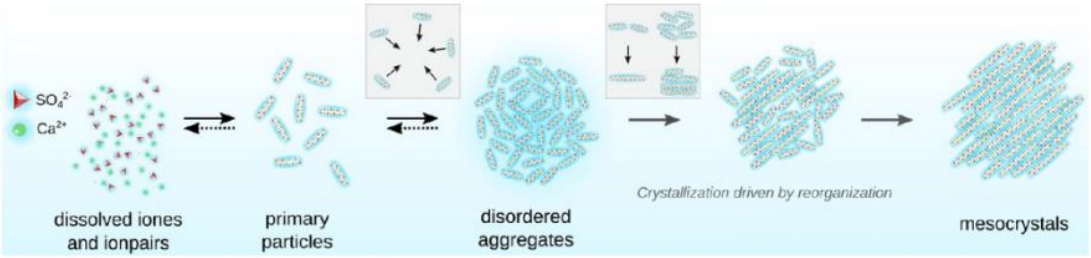

Figure 2.19. Model of the precipitation of bassanite (applicable also to all the other $CaSO_4$ phases) based on the results of Stawski et al. (2020) [137].

Another step forward in the understanding of the crystallization and growth of bassanite was taken by Jia et al. (2022) [16]. In this study, Jia et al. observed two distinct crystallization pathways of bassanite and they also gained insights into how gypsum grows from it. These authors used TEM and SAED to analyze samples of calcium sulfate precipitate from 1 min to 40 min. The first phase

that was observed at the beginning of the crystallization (around 1 min) was made of nanometric domains with bassanite structure. The finding of this work is that these nanoparticles were assembled to form either assembles of bassanite nanorods (elongated in the [001]) or bassanite rosettes. In the case of the rosettes, the growth of the single crystals was *via* elongation along the [001] direction. With TEM resolution, the components of the rosettes appeared well-faceted suggesting a growth by the addition of primary units of either ions or clusters. In the case of the agglomerated nanorods instead, their boundaries were observed from the TEM images, suggesting a growth by aggregation of nanometric particles co-oriented along the [001] direction [16]. Figure 2.20 reports the diagram reported by Jia et al. (2022) that explains the two different crystallization pathways they observed.

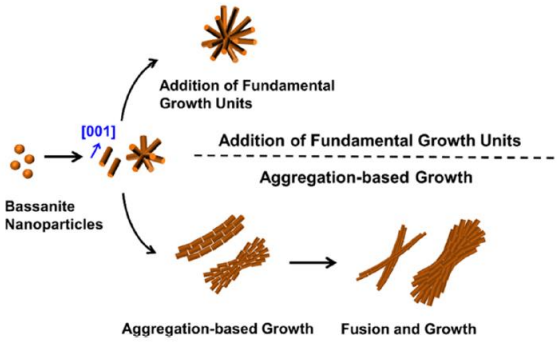

Figure 2.20. Diagram showing the two possible precipitation pathways of bassanite, modified after Jia et al. (2022) [16].

Regarding anhydrite, as described in Van Driessche et al. (2016) [75], only Fan et al. (2010) [138] have studied its precipitation kinetics [138] [75]. More recently instead, Tritschler et al. (2015) [139] observed for the first time the direct precipitation of anhydrite in alcoholic solutions with low water concentration [139]. Shortly after the mixing of the solutions, they isolated the particles relative to the first turbidity of the solution, and from electron diffraction (ED) demonstrated that the aggregates of primary units that were visible from the TEM displayed the structure of anhydrite. Figure 2.21 reports a TEM picture of the aggregates of anhydrite composed of nanocrystals of 10-20 nm size.

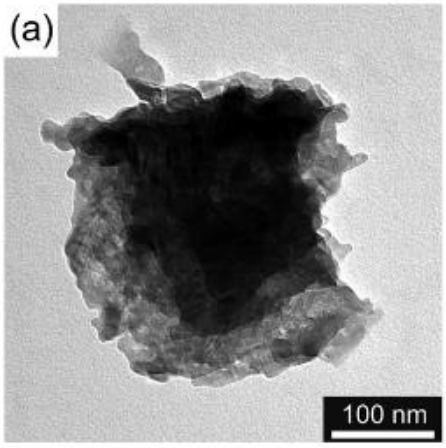

Figure 2.21. TEM picture of precipitated pure anhydrite [139].

In light of all the research that has been done on unrevealing the precipitation pathways of calcium sulfate phases, and despite the small discrepancies between some of the results, it is clear that all evidence point to a common scenario. The view of a multi-step pathway of precipitation applies not only to the nucleation and crystallization of gypsum but also to bassanite and anhydrite,

suggesting the existence of a common precipitation process for all the $CaSO_4$ phases. The diagram made by Van Driessche et al. (2016) [75] in Figure 2.22 summarizes perfectly all the steps that seem to happen during the precipitation of a calcium sulfate phase from solution.

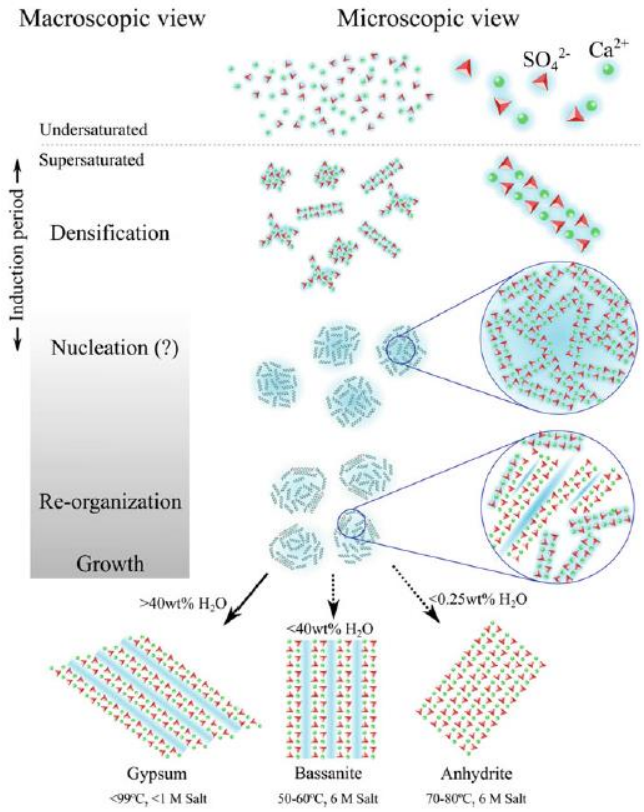

Figure 2.22. Steps of the precipitation of calcium sulfate phases from solution in the frame of a multi-step nucleation process. Taken from Van Driessche et al. (2016) [75].

2.2.3. Hydration of bassanite to form gypsum

Among all the transformations mentioned, that from bassanite to gypsum is the most important one from an industrial point of view. It is therefore a flourishing topic in terms of research. As already introduced, gypsum can be obtained from bassanite through a hydration reaction:

$$CaSO_4 * 0.5\ H_2O + 1.5\ H_2O = CaSO_4 * 2H_2O + Q \qquad \text{Eq. 2.2}$$

Where Q is the heat generated from the exothermic reaction. Understanding the kinetics of this reaction is crucial when producing gypsum plaster as it determines the development of the properties of the final material. The hydration reaction of cementitious materials is also called the "setting process" during which the material develops its strength. At the end of the setting process, when all the water has been incorporated into the hydrates, the material obtained is characterized by high porosity due to the entanglement of the crystals that create a network of needles or plates [2]. Several factors are responsible for the development of the mechanical and engineering properties of gypsum plaster. All of them are strictly related to the microstructure of the material. The term microstructure includes both the characteristics of the single gypsum crystals and the characteristics of the full matrix, i.e., the way the crystals are distributed and oriented. This means that the development of the strength of gypsum plaster is dependent on the size, morphology, and impurities that can be present in the crystals of gypsum, but also on the strength of the bonds between the crystals and the porosity of the entire matrix [67]. The evaluation of the properties of gypsum plaster does not depend only on the state of the final product. Another factor that has

proven to influence the microstructure and strength of gypsum plaster is the way the hemihydrate has been produced [67]. Various studies reported that the use of α or β-hemihydrate to obtain gypsum plaster brings different properties to the final material because of a different setting process [140] [67] [23] [2]. One of the reasons why gypsum plaster produced from α or β-hemihydrates presents different strength is the water/plaster (W/P) ratio needed for the setting process. The α-hemihydrate form requires less water compared to β-hemihydrate to hydrate. Having less water results in the formation of plaster with fewer porosity and therefore higher mechanical performance [67].

For example, Follner et al. (2002) [23] investigated the kinetics of gypsum formation from α and β-hemihydrate using electron imaging at different times. Jointly to calculations of the different structures that the hemihydrate can have when incorporating different amounts of water, they evaluated the setting process of gypsum plaster based on the pole figures of specific crystallographic planes of gypsum and the starting hemihydrate type. Comparing the orientation of the crystals resulting from the setting process of both α and β-hemihydrate, they discovered that traces of hemihydrate were still present, in both cases, at the end of the setting, but in different parts of the sample. Based on this evidence, they concluded that the setting process of the plaster is different depending on the type of hemihydrate used as a starting material and that α and β-hemihydrates probably do not differ only in the size and morphology of the crystals but also in the structure. A few years later, Singh and Middendorf (2007) [2] studied in detail the setting process of gypsum plaster from both α and β-hemihydrate in the presence of accelerating and retarding additives. They compared the modulus of elasticity, compressive strength, and porosity for gypsum produced from both α and β-hemihydrate in the presence and without the addition of organic acids to the system. From their results, they inferred that the hydration reactions generated from the two forms of hemihydrate are both exothermic but different in some aspects. They associated these differences with the production process of the hemihydrates, the morphology and specific area of the crystals, and the characteristics of the crystal's surface [2]. Song et al. (2009) [141] also supported the hypothesis of a different setting process of α and β-hemihydrate reporting evidence obtained with NMR and SEM analysis. They observed the evolution of the porosity of the microstructure measuring the relaxation times of the water populations of both the hemihydrates over the setting time. As a result, they could see the evolution of different pore structures, which was also confirmed by SEM pictures showing a more entangled plaster in the case of the α-hemihydrate (Figure 2.23).

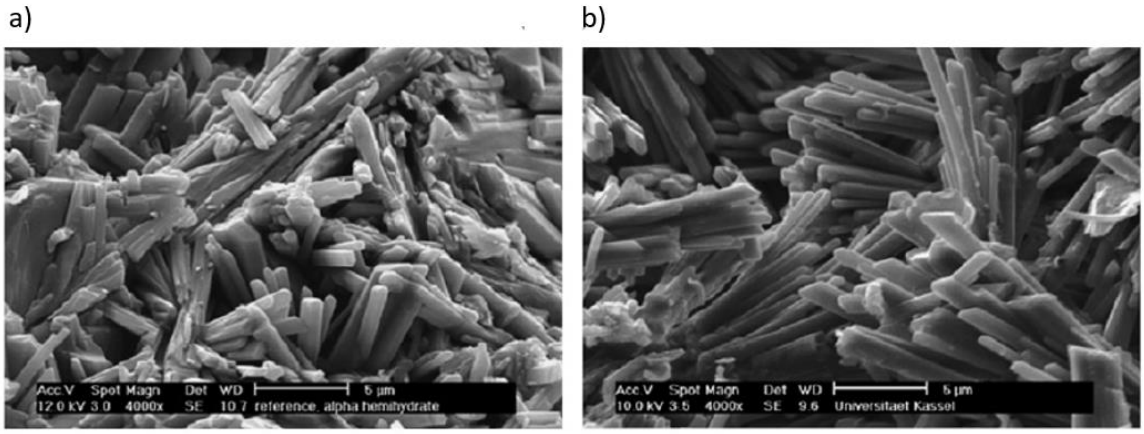

Figure 2.23. Modified after Singh and Middendorf (2007) [2]. a) Set of the α-plaster paste after 28 days of hydration. b) Set of the β-plaster paste after 28 days of hydration. The Two SEM pictures show the differences in the microstructure. The plaster obtained from the hydration of α-hemihydrate shows a higher degree of entanglement.

Another fundamental factor that influences the development of the properties of gypsum plaster is the presence of impurities in the gypsum crystals. This is related to the use of additives and how they are incorporated into the structure of gypsum. In 2002 Follner et al. [71] demonstrated by energy calculations that when external ions, or organic molecules or when a different ratio of water/plaster (which is the case of using α or β-hemihydrate) are involved in the formation of gypsum crystals, the occurrence of structural defects is favorable [71]. When additives are used, their incorporation in the crystallographic structure of gypsum is likely to modify it, giving rise to the growth of different morphologies of crystals, preferential orientations, and texture [71]. There is also another hypothesis on how the use of additives influences gypsum plaster. For example, nano and micro additives can influence the electro-conduction properties of gypsum crystals by changing the surface charge. Otherwise, the additives can act as crystallization centers, increasing the nucleation and therefore increasing the contact points and traction of the matrix. Moreover, additives can bring an excess of surface energy into the system that reflects in the morphology of gypsum crystals [142]. Kondratieva et al. (2017) [142] report an interesting example of how the use of additives modifies the structure of gypsum crystals and the degree of hydration of the setting process. These authors performed an X-ray powder diffraction study of the setting of gypsum β-plaster in the presence of silica and taurit. From the Rietveld refinements of the powder patterns, it resulted that the composition of the pastes remained the same since the concentration of the additives was not enough to create a new phase, but the intensities of the peaks of gypsum were varying from one sample to the other (Figure 2.24a). These differences in the structure of gypsum crystals were caused by different morphologies and thus the microstructure of the plaster as shown by SEM pictures (Figure 2.24 b-e). In the end, Kondratieva et al. (2017) [142] demonstrated that the use of additives (taurine and silica in this case) improved the intensity of the hydration, producing a more cohesive and therefore better performing microstructure.

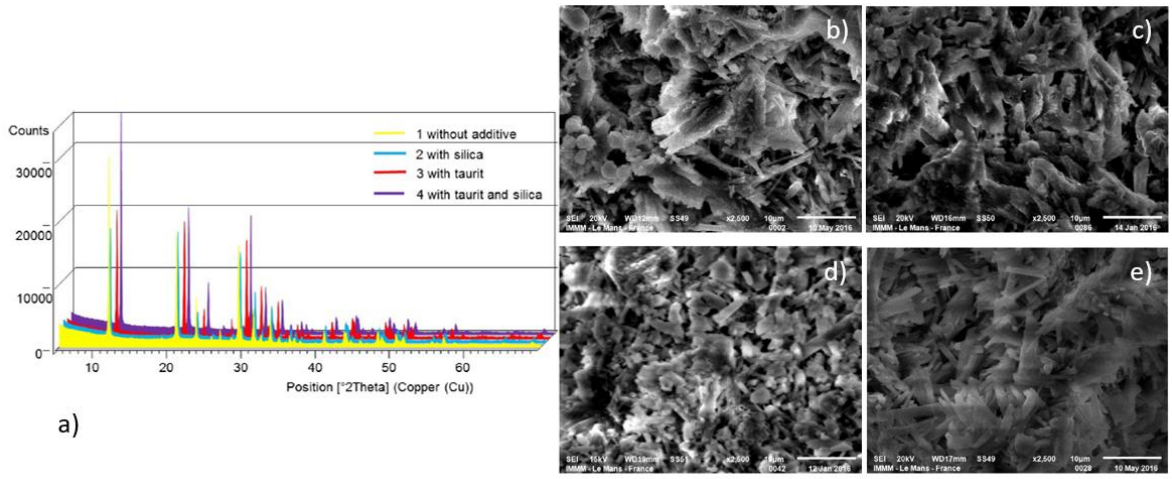

Figure 2.24. Figure modified from Kondratieva et al. 2017 [142]. a) Powder diffraction patterns of the hydrated β-plasters. The yellow pattern corresponds to the plaster without additives. The light blue pattern corresponds to the plaster with silica. The red pattern corresponds to the plaster with taurit. The purple pattern corresponds to the plaster with both silica and taurit. b) SEM picture showing the microstructure developed by the plaster with no additives. c) Microstructure of the plaster with the addition of silica. d) Microstructure of the plaster with the addition of taurit. e) Microstructure of the plaster with both silica and taurit.

2.3. Industrial uses of gypsum plaster

The use of gypsum plaster in construction is as old as the Neolithic period. In ancient times, gypsum plaster represented a convenient material for the realization of architectonic and artistic works. An example of an old application, as reported by de Brito and Flores-Colen (2015) [143], dates back to 6000 AC in Çatal Höyük, Turkey [144]. A few millennia later (4000-2000 AC), also the Egyptians made use of gypsum plaster for construction, in particular for the realization of pyramids [143]. Then, gypsum plaster appeared again during the Roman empire. Romans understood the advantages of using a versatile and cheap material and they used it to replace less available ones [143]. Successively, there is no record of large uses of gypsum plaster during the Middle Ages while instead during the Renaissance its application came back as decoration for architectonic constructions [143]. A certainly famous application of gypsum plaster is the one that coined the name “plaster of Paris”. The name derived from the application of gypsum plaster as a protective layer to cover the wooden houses of Paris from fire in the Seventeenth century. The large quantities of gypsum needed on that occasion were extracted by the quarries in Montmartre, Paris [54] [55] [1]. Gypsum plaster was largely used in the eighteenth century in Portugal where a school named “Class of Plaster and Design”, was founded to push the knowledge of gypsum plaster workability [143]. In the same period, gypsum plaster was also widely used in the production of ceilings. Later in the nineteenth century, a new type of decoration, based on gypsum plaster, spread under the influence of the Romantic Movement [143]. The nineteenth century saw also the use of gypsum plaster for the realization of ornaments and decoration during the Art Nouveau period. As modern times approached, the artistic applications of gypsum plaster decreased more and more, while its application in various industrial compartments increased.

Nowadays, gypsum plaster is one of the most produced materials in the world. In the year 2022, the totality of mined gypsum in the USA has been of 150 million tons, followed by 43 million tons of produced gypsum (US Geological Survey, Mineral Industry Surveys, Gypsum in the first quarter of 2022). An important part of the produced or mined gypsum is dehydrated to obtain calcium sulfate hemihydrate, which is then used to make gypsum plaster. Gypsum plaster obtained by the hydration of the hemihydrate, and some additives, is used to produce mainly stucco and wallboards. Van Driessche et al. (2019) [1] reported a schematic representation of the steps of the production of gypsum wallboard shown in Figure 2.25. As shown in the picture, the production of gypsum plaster is often treated by additives, represented in the picture with A and R containers, which can be either accelerators of the crystallization of gypsum or retarders. The hemihydrate is mixed with water and additives to form a paste that is placed in between layers of paper [1]. Once the setting process takes place, and the hemihydrate is transformed into gypsum, the system is bonded and ready to be used.

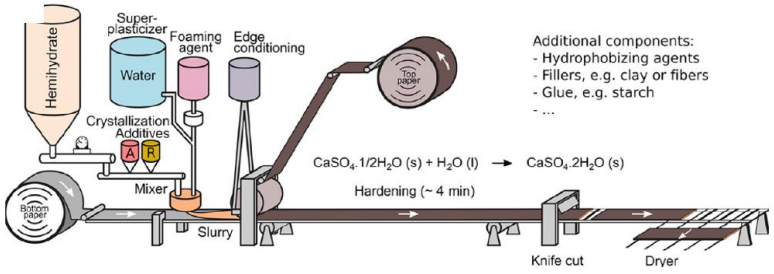

Figure 2.25. Modified after Van Driessche et al. (2019) [1]. Gypsum wallboard production.

Another application of gypsum related to the construction industry is its use as an additive for the setting of cement. As reported by Frigione (1983) [145], it seems that the first time in which gypsum

was added to a cement paste occurred by accident. This happened while mixing cement mortars in an environment where gypsum plaster had been mixed before, resulting in the contamination of the cement. From that, it was understood that gypsum, and in general calcium sulfate phases, influence significantly the rate of setting of cement by retarding it [145]. Nowadays gypsum is used in the production of Portland cement. The clinker, made by heating a mixture of limestone and clay, is mixed with a low percentage of gypsum. This helps to control the rate of setting of cement, enhancing the development of strength [146]. The clinker is then ground, producing heat that transforms part of the gypsum into hemihydrate. In some cases, the conversion of part of the gypsum to hemihydrate is relevant, since the water in gypsum crystals can cause problems during the storage of the cement. When no gypsum is added to the clinker, cement undergoes a setting process that is defined “flash set”, that results in poor strength development. A rapid setting of cement can happen also when too much hemihydrate is present in the system which, rehydrating to gypsum, gives rise to a premature setting of the cement, that is one of the causes of “false set”. In this case, however, the development of strength is not affected as in the case of gypsum absence [146].

2.4. Open scientific questions

In this section, all the scientific questions that motivated the development of this Ph.D. project will be explained in detail. In the first part of the section, the crystallographic studies and the current knowledge on the crystal structure of different forms of calcium sulfate hemihydrate and sub-hydrates are reviewed. The aim is to show that even though several works report the complex subject of the hemihydrate crystal structure, it is still not clear whether different production methods (for either the α or β) result in hemihydrates with different crystal structures and water content. Successively, the subject of hemihydrate-gypsum transition is explained. Only few studies that have been performed using powerful techniques (such as X-ray tomography) focusing on characterizing the hemihydrate-gypsum transition from different aspects. In none of these cases, the investigation of the morphological and spatial evolution of the process has ever been combined with a crystallographic characterization. In the last part, some of the theory of the dissolution of crystals is introduced together with the common experimental approach that is used by the scientific community to observe and quantify the rate of dissolution of crystals. The dissolution of calcium sulfate hemihydrate has never been investigated due to a series of obstacles arising from the shape and the solubility of the crystals. With the right sample preparation and the use of an innovative technical approach, a direct observation of the surface dissolution and even a measurement of the dissolution rate of calcium sulfate hemihydrate are possible.

2.4.1. Do α and β-hemihydrate have different crystal structure?

The crystal structure of calcium sulfate hemihydrate and all its possible sub-hydrates forms has been a subject of controversy. The origin lies in the complexity of the distribution of water molecules within the channels of the structure. The hemihydrate and various sub-hydrates ($CaSO_4 \cdot xH_2O$ $0.5 \leq x \leq 0.8$) have been extensively investigated in the literature using single crystal diffraction, powder diffraction and neutron diffraction. The stoichiometry of hemihydrate ($CaSO_4 \cdot 0.5H_2O$), when exposed to high air humidity, may also vary leading its structure to incorporate additional water.

Follner et al. (2002) [23] reported a detailed review of all the structural studies on the determination of hemihydrate crystal structure, from the first half of the twentieth century to the early 2000s. The first structural determination, obtained by the interpretation of Weissenberg photographs, is attributable to Gallitelli (1931) [3]. It is not reported whether Gallitelli measured crystals of hemihydrate obtained by dehydration of gypsum in dry conditions or in a saturated NaCl solution. The structure of the $CaSO_4 \cdot 0.5H_2O$ was described in the $P3_121$ space group, even though Gallitelli understood that the average structure was instead monoclinic [3] [23]. Figure 2.26 shows the crystal structure deriving from the study of Gallitelli. The O atoms of the water molecules are represented in ice blue.

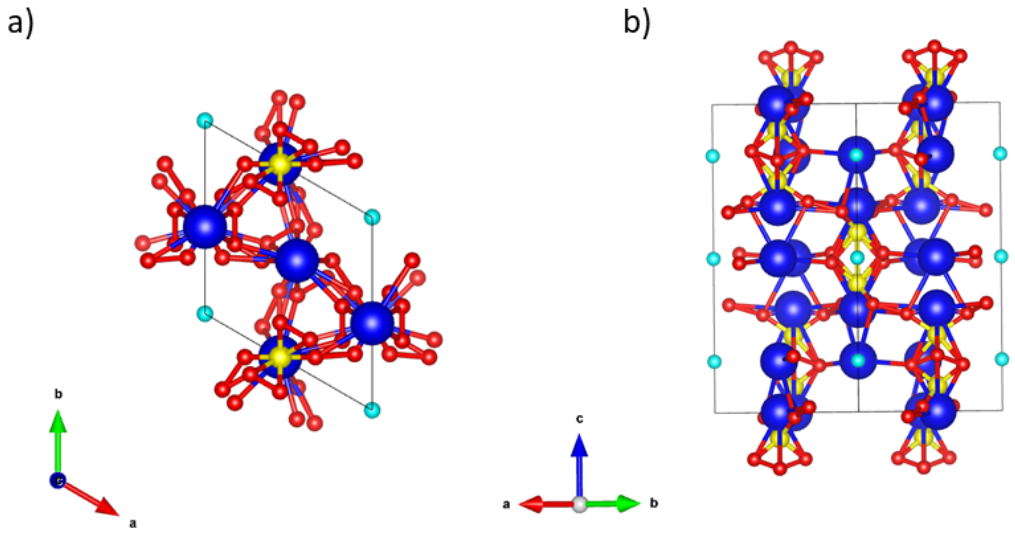

Figure 2.26. a-b) Crystal structure of calcium sulfate hemihydrate ($CaSO_4 \cdot 0.5H_2O$) described by Gallitelli [3]. The space group of the structure is $P3_121$. Legend: electric blue balls=Ca, red balls = O atoms (also H_2O molecules), ice blue balls= Water, yellow balls= S. The plots were created using the *VESTA* software [62].

Some decades later, Bushuev and Borisov (1982) [63] performed an X-ray diffraction study on both β-hemihydrate, obtained from the dehydration of gypsum, and α-hemihydrate obtained from heating gypsum in a water solution. Based on their results, the β-hemihydrate showed a trigonal structure with the $P3_121$ space group, while the α-hemihydrate ($CaSO_4 \cdot 0.67H_2O$) was refined in the monoclinic I2 space group. The structure of the monoclinic α-hemihydrate of Bushuev [4] is reported in Figure 2.27. In this case, the B2 space group was chosen for the refinement of the structure so that the water channels are running along the b-axis instead of the common representation along the c-axis. The water molecules' positions are highlighted in the diagram.

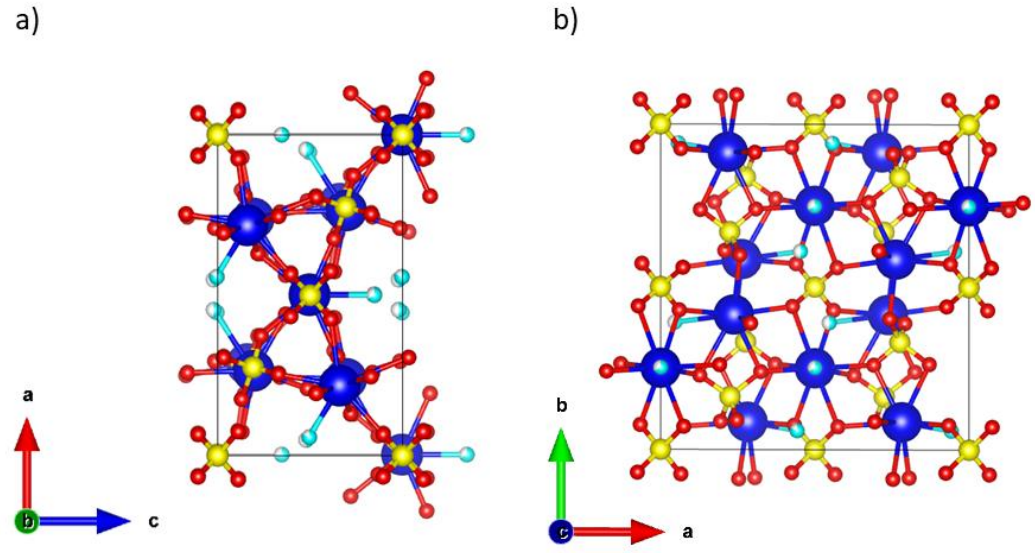

Figure 2.27. a-b) Crystal structure of calcium sulfate hemihydrate ($CaSO_4 \cdot 0.67\ H_2O$) described by Bushuev [4]. The space group of the structure is B2. Legend: electric blue balls=Ca, red balls = O atoms (also H_2O molecules), ice blue balls= Water, yellow balls= S. The plots were created using the *VESTA* software [62].

In the same period as Bushuev and Borisov, also Abriel [5] performed an X-ray diffraction measurement on a calcium sulfate sub-hydrate ($CaSO_4 \cdot 0.8H_2O$). The sample, prepared by wet methods and refined in the $P3_121$ space group, showed the highest value that has been found for

a calcium sulfate sub-hydrate with 0.8 molecules per unit cell. The crystal structure refined by Abriel [5] is reported in Figure 2.28.

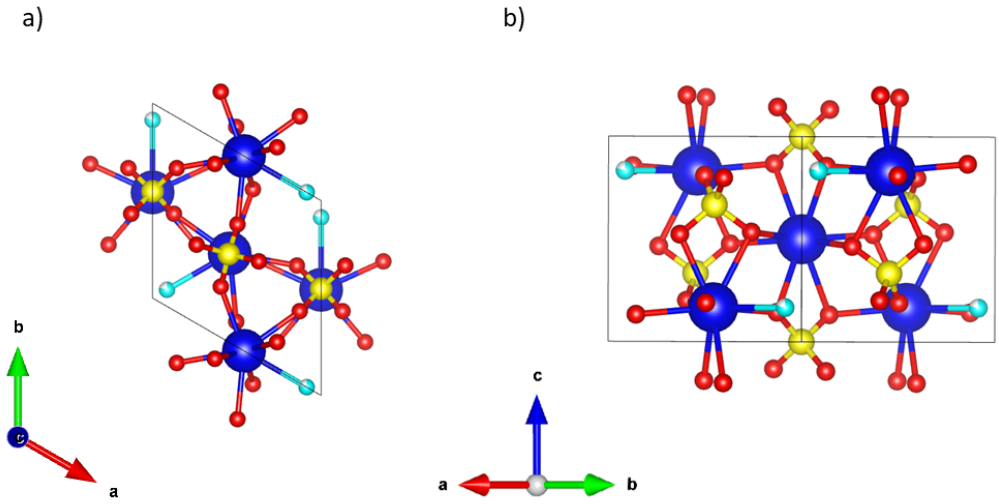

Figure 2.28. a-b) Crystal structure of calcium sulfate sub-hydrate ($CaSO_4 \cdot 0.80\ H_2O$) described by Abriel [5]. The space group of the structure is $P3_121$. Legend: electric blue balls=Ca, red balls = O atoms (also H_2O molecules), ice blue balls= Water, yellow balls= S. The plots were created using the *VESTA* software [62].

Some years later Abriel and Nesper re-determined the structure of $CaSO_4 \cdot 0.5H_2O$. They understood the pseudo-merohedric threefold twinning nature of the hemihydrate and they tried to refine the crystal structure in both the trigonal ($P3_121$) and monoclinic (I2) settings. From their results, the trigonal space group appeared to be the most suitable one. The structures solved by Abriel and Nesper [6] in the I2 (a) and $P3_121$ (b) space groups are shown in Figure 2.29.

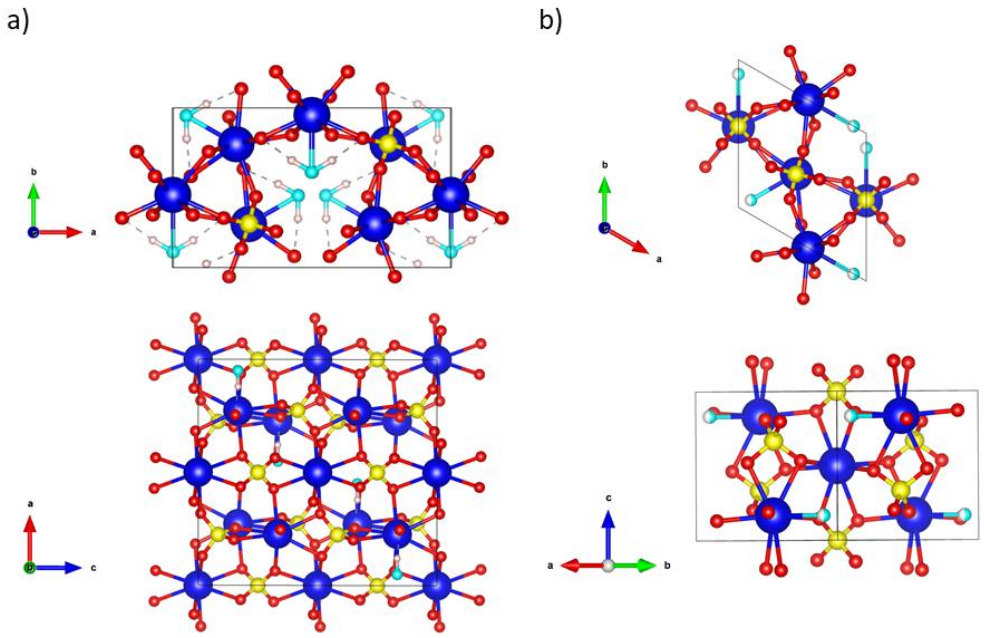

Figure 2.29. a) Crystal structure of calcium sulfate hemihydrate ($CaSO_4 \cdot 0.50\ H_2O$) refined by Abriel and Nesper (1993) [6] in the I2 space group. b) Crystal structure of calcium sulfate hemihydrate ($CaSO_4 \cdot 0.50\ H_2O$) refined by Abriel and Nesper (1993) in the $P3_121$ space group. Legend: electric blue balls=Ca, red balls = O atoms (also H_2O molecules), ice blue balls= Water, yellow balls= S, white balls = H. The plots were created using the *VESTA* software [62].

The crystal structure of calcium sulfate hemihydrate with formula $CaSO_4 \cdot 0.50H_2O$ and with formula $CaSO_4 \cdot 0.60H_2O$ have been also re-determined by powder diffraction methods, using both X-rays and neutrons, by Bezou et al. (1995) [7]. Both crystal structures were refined in the monoclinic I2 space group and are reported in Figure 2.30. The structure with less water corresponding to $CaSO_4 \cdot 0.50\ H_2O$ is shown in Figure 2.30a, while the structure with more water relative to $CaSO_4 \cdot 0.60\ H_2O$ is shown in Figure 2.30b. It is evident from the diagrams that only the crystallographic sites of water change from one crystal structure to the other.

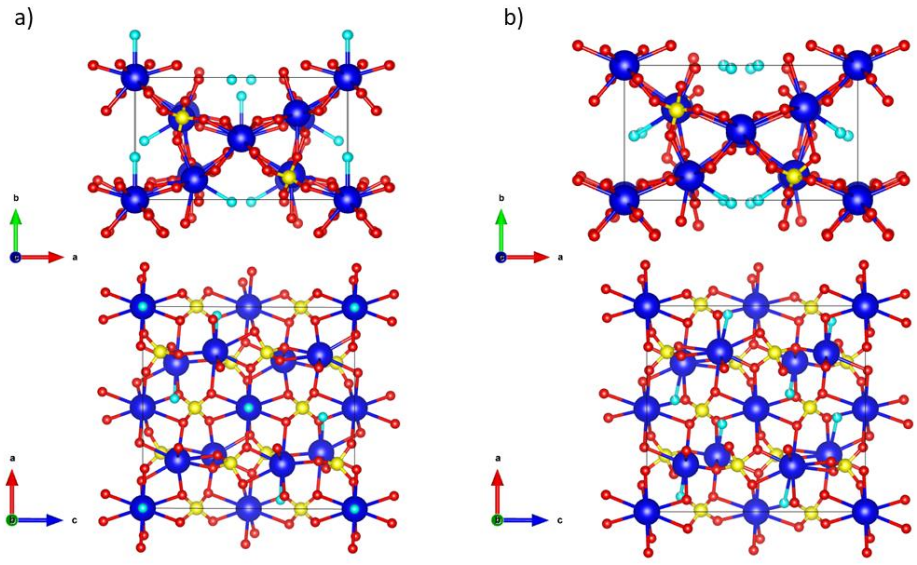

Figure 2.30. a) Crystal structure of calcium sulfate hemihydrate ($CaSO_4 \cdot 0.50\ H_2O$) refined by Bezou et al. (1995) [7] in the I2 space group. b) Crystal structure of calcium sulfate hemihydrate ($CaSO_4 \cdot 0.60\ H_2O$) refined by Bezou et al. (1995) [7] in the I2 space group. Legend: electric blue balls=Ca, red balls = O atoms (also H_2O molecules), ice blue balls= Water, yellow balls= S. The plots were created using the *VESTA* software [62].

The subject of the crystal structure of calcium sulfate hemihydrate was discussed again in 2001 by Ballirano et al. (2001) [8]. In this work, the authors obtained the hemihydrate starting from a γ-anhydrite sample. The sample, analyzed using X-ray powder diffraction, was prepared by heating gypsum in a furnace to obtain γ-anhydrite. Then the sample was placed in a borosilicate-glass capillary (to avoid as well texture issues during the Rietveld refinement) and left in contact with the air to rehydrate and form the hemihydrate. They refined the crystal structure in the I2 space group, that includes four Ca crystallographic sites, three S crystallographic sites, and 12 O. The crystal structure of $CaSO_4 \cdot 0.50H_2O$ refined in the I2 space group is reported in Figure 2.31 [8].

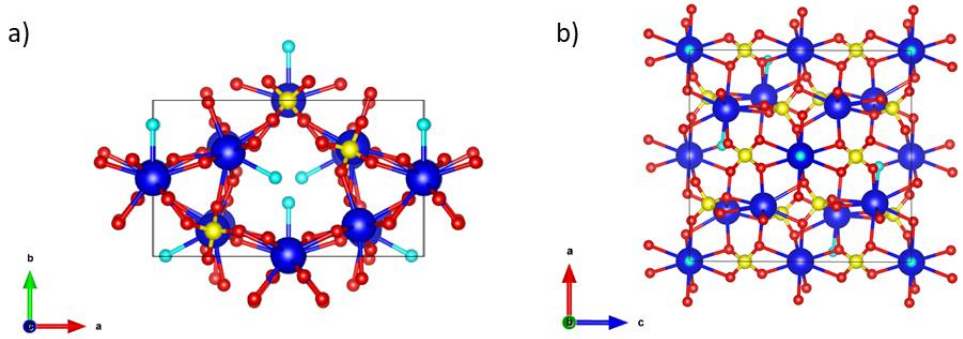

Figure 2.31. a-b) Crystal structure of calcium sulfate hemihydrate ($CaSO_4 \cdot 0.50\ H_2O$) refined by Ballirano et al. (2001) [8] in the I2 space group. Legend: electric blue balls=Ca, red balls = O atoms (also H_2O molecules), ice blue balls= Water, yellow balls= S. The plots were created using the *VESTA* software [62].

The motivation of Ballirano et al. (2001) [8] to re-investigate the structure of the hemihydrate by X-ray powder diffraction to overcome the problem of pseudosymmetry was demonstrated to be successful. A few years later, Christensen et al. (2008) proposed a structural study of β-hemihydrate based on synchrotron X-ray powder diffraction and described the structure as trigonal with space group P3(1) [228]. Subsequently, Weiss and Bräu (2009) [9] decided to investigate the crystal structure of β-hemihydrate (calcined gypsum) with X-ray single crystal diffraction with the aim to understand how much water can be incorporated in the hemihydrate or sub-hydrate structure. As already stated by Ballirano et al. (2001) [8], due to the pseudosymmetry, the single crystal refinements failed to describe the arrangement of the water molecules in the hemihydrate structure. In particular, Weiss and Bräu argued that the models always describe well the structure of the hemihydrate but the split positions of water are always refined with free occupancy parameters which may lead to a water content higher than 0.5 molecules per formula without providing experimental evidence of the excess water [9]. In their study, they coupled X-ray single crystal diffraction with DFT calculations to optimize the structure. They concluded that the structure of calcium sulfate hemihydrate is very unlikely to host more than 0.5 molecules of water per formula. To perform the refinement, they selected the C2 set which arises from the choice of three pseudo orthorhombic cells, highlighted in the reciprocal space cut (hk1) in Figure 2.32a. This cell choice was able to index all the reflections, while the other two hexagonal choices were not matching the systematic extinctions. To better understand the symmetry reductions that take place with the addition of water to the anhydrous calcium sulfate structure, Weiss and Bräu built the Bärnighausen tree from the $P6_422$ space group to the C2 space group. The Bärnighausen tree is reported in Figure 2.32b.

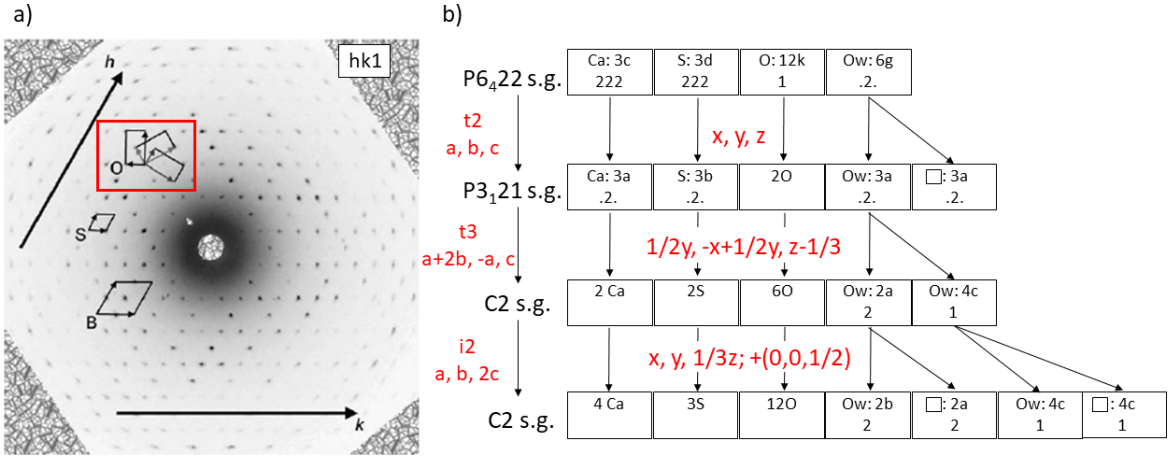

Figure 2.32. a) Reciprocal space cut of the hk1 showing all the possible choices of lattice for the calcium sulfate hemihydrate sample. The three orthorhombic cells highlighted by the red square were used by Weiss and Bräu to perform the refinement. b) Bärnighausen tree showing the decreasing of symmetry from the $P6_422$ space group ($CaSO_4$ in the absence of water) to the C2 (calcium sulfate hemihydrate). Modified after Weiss and Bräu (2009) [9].

Weiss and Bräu explained that the t2 and t3 translation transitions (Figure 2.32b) that take place when decreasing the symmetry from hexagonal to monoclinic indicate the presence of a twin of a three-fold twinning which results in a six-fold twinning. The suggestion of twinning based on the t3 translation of the Bärnighausen tree was consistent with the reflections observed, while the t2 translation which generates the additional three twins was revealed by the inversion of the three starting twins. The refinement of the structure, considering all six individuals of the six-fold twinning, leads to an ordered model with 0.5 molecules of water per formula. Weiss and Bräu argued that when the second twinning that brings to the formation of six individuals is ignored, the oxygen positions are split leading to compositions of $CaSO_4 \cdot xH_2O$ with $x>0.5$.

Following this last work, Schmidt et al. (2011) [10] also, reinvestigated the crystal structure from single crystal X-ray diffraction of α-hemihydrate at ambient conditions and high (75 %) relative humidity to demonstrate that calcium sulfate sub-hydrates can exist. To obtain the sub-hydrate, crystals of α-hemihydrate were stored in a dessicator with a relative humidity of roughly 75 %. Then, one of the crystals was placed in a capillary and measured under the same humidity conditions. The sub-hydrate, with formula $CaSO_4{\cdot}0.625H_2O$, was not stable and dehydrated back to $CaSO_4 \cdot 0.5H_2O$ at ambient conditions. For both the $CaSO_4{\cdot}0.5H_2O$ and $CaSO_4{\cdot}0.625H_2O$ forms they performed X-ray powder and single crystal diffraction. The powder patterns were used to perform Le Bail refinements of the lattice parameters. The crystal structures were then refined in the C2 space group with sixfold twinning for the $CaSO_4{\cdot}0.5H_2O$, and in the $P3_221$ space group for the $CaSO_4{\cdot}0.625H_2O$. Schmidt et al. gave a detailed explanation of the crystal structure of both calcium sulfate forms. In particular, they explained the ordering of water molecules when passing from 0.625 to 0.5 molecules and the associated modification of the lattice that generates the twinning. Both structures are characterized by Ca-SO_4 chains, which are the structural motif present in all calcium sulfates. The water molecules are contained inside the channels that form between the Ca-SO_4 chains. The $CaSO_4{\cdot}0.625H_2O$ form contains a water molecule more than $CaSO_4{\cdot}0.5H_2O$, and as a consequence, the water molecules are coordinated differently with the calcium polyhedrons. Figure 2.33a shows the view along the a-axis of the C2 lattice of the $CaSO_4{\cdot}0.5H_2O$ crystal structure. The O of the water molecules is represented in green. The water molecules inside the channels are shifted half of the translation vector of the lattice [10]. Figure 2.33b shows instead the view along the c-axis of the $P3_221$ structure of $CaSO_4{\cdot}0.625H_2O$. In this case, the distribution of the water channels is more complex compared with the C2 structure. Four different water channels are present.

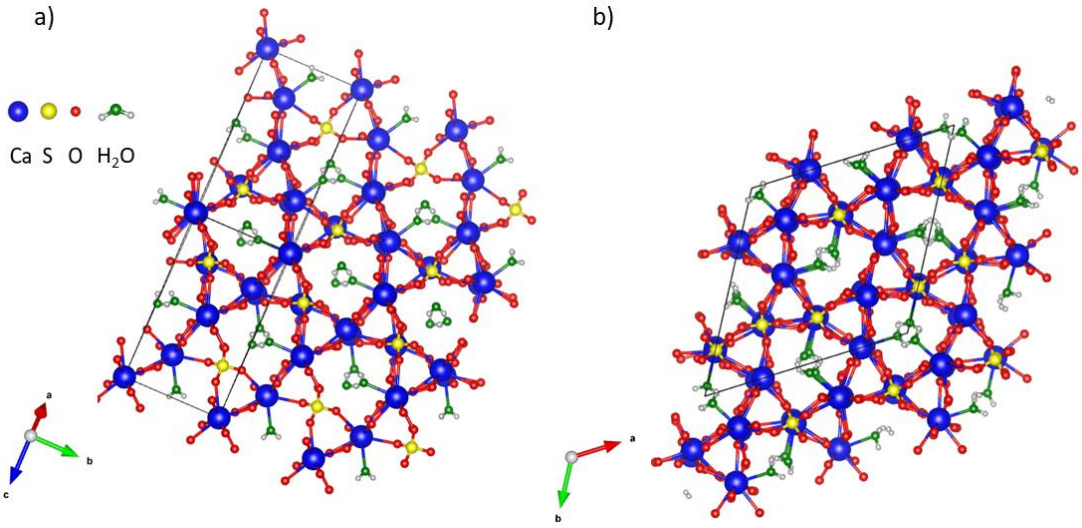

Figure 2.33. a) Crystal structure of the calcium sulfate hemihydrate ($CaSO_4{\cdot}0.5H_2O$) refined with the C2 space group by Schmidt et al. (2011) [10]. b) Crystal structure of the calcium sulfate sub-hydrate ($CaSO_4{\cdot}0.625H_2O$) refined with the $P3_221$ by Schmidt et al. (2011) [10]. The plots of the crystal structure have been done with the software *VESTA* [62].

Schmidt et al. explained in detail the differences between adjacent water channels of both the monoclinic and the trigonal structures. Figure 2.34 shows diagrams of the adjacent water channels that are present in the monoclinic $CaSO_4{\cdot}0.5H_2O$ (Figure 2.34a) and the trigonal $CaSO_4{\cdot}0.625H_2O$ (Figure 2.34b) [10]. In the case of $CaSO_4{\cdot}0.5H_2O$, the water molecules in two adjacent water channels can be at the same height or shifted of half of the translation vector of the lattice. In the $CaSO_4{\cdot}0.625H_2O$ structure, two adjacent water channels can be occupied by four water molecules each or by four and three water molecules (as shown in the bottom part of Figure 2.34b).

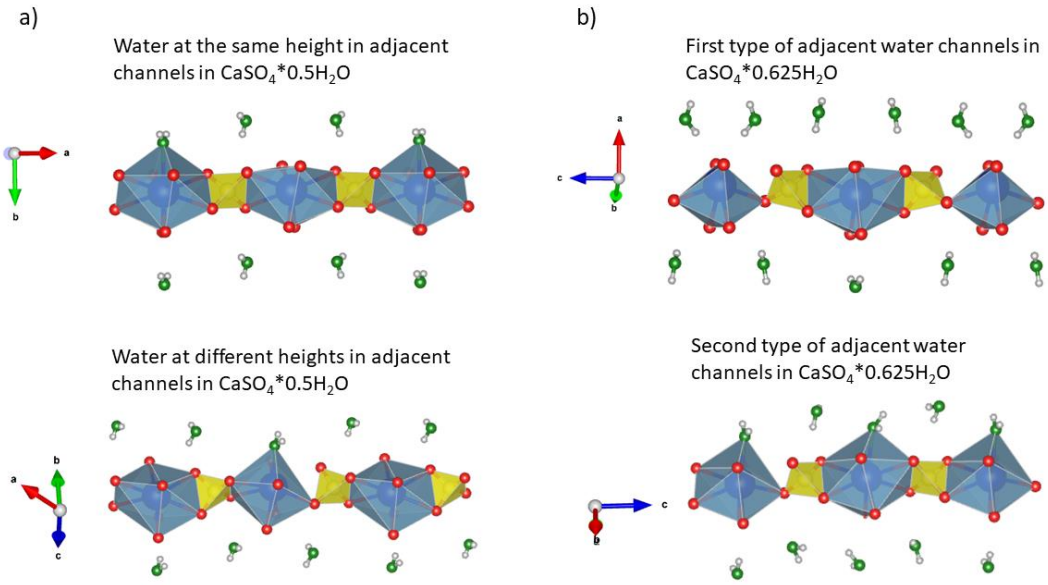

Figure 2.34. a) Representation of the two possible adjacent water molecules channels in the crystal structure of the calcium sulfate hemihydrate ($CaSO_4 \cdot 0.5H_2O$) refined in C2 by Schmidt et al. (2011). b) Representation of the two possible adjacent water molecules channels in the crystal structure of the calcium sulfate sub-hydrate ($CaSO_4 \cdot 0.5H_2O$) refined by Schmidt et al. (2011). Modified after Schmidt et al. (2011) [10]. The plots of the crystal structure have been done with the software *VESTA* [62].

Schmidt et al. [10] focused also on depicting the phase transition from the trigonal to the monoclinic phase. The steps of the phase transition described by Schmidt et al. [10] are reported in Figure 2.35. Starting from the $CaSO_4 \cdot 0.625H_2O$ structure, the lowering of the symmetry to the monoclinic $CaSO_4 \cdot 0.5H_2O$ structure is due to the ordering of part of the water molecules in adjacent channels with the same height (Figure 2.35a top). As a consequence, the structure adjusts with a stretching that generates internal strain that leads to the tilting of the structure that becomes monoclinic. The threefold twinning is associated to the translationengleiche transformation t3, that was already explained by Weiss and Bräu (2009) [9] (Figure 2.32b).

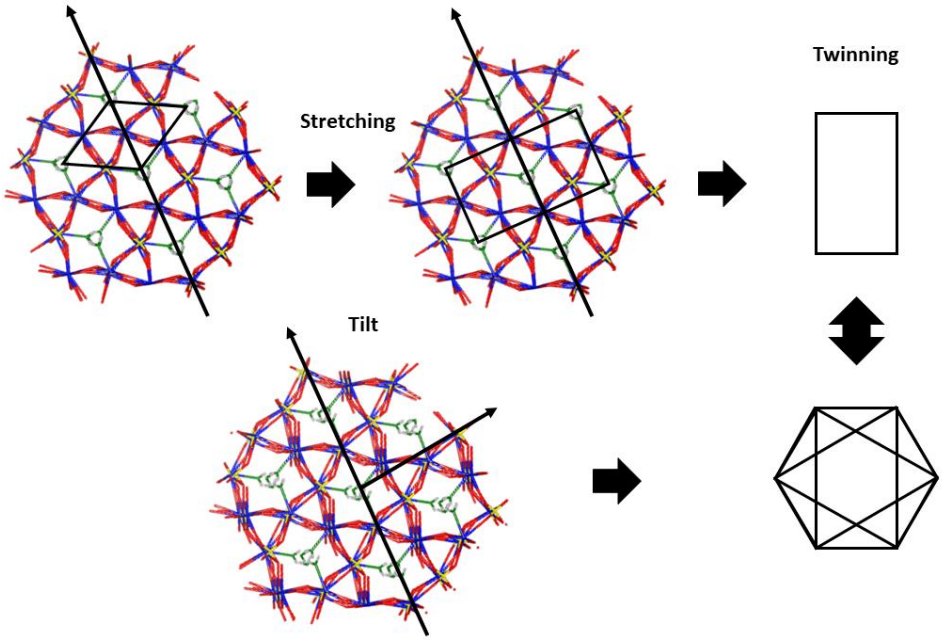

Figure 2.35. Phase transformation from the trigonal space group $P3_221$ to the monoclinic space group C2 explained by Schmidt et al. (2011) [10]. The adjustment of the water molecules due to their loss in the structure is the cause of the

stretching and tilting that transforms the lattice in monoclinic and generates the threefold twinning. Modified after Schmidt et al. (2011) [10]. The diagrams of the crystal structure have been done with the software VESTA [62].

Thanks to all the authors that worked on the crystallography of calcium sulfate hemihydrate, the problem of the twinning has been identified, and the modifications induced to the crystal structure due to the incorporation of additional water have been explained. Nevertheless, there is still a point that remains unclear. In particular, we still do not know for sure if and how different production methods such as direct precipitation of calcium sulfate from solution or calcination of gypsum influence the crystal structure and water incorporation of the hemihydrate.

2.4.2. The hemihydrate-gypsum transformation

The first studies that were performed to understand the development of the hydration process of gypsum plaster were supported by the hypothesis of the presence of two distinct processes, dissolution and precipitation. Desch, in (1919) published a study in which he investigated the setting process of cement and plaster. He demonstrated that the process of dissolution of the hemihydrate and crystallization of gypsum were first explained by Le Chatelier in (1887). According to this first explanation, when the hemihydrate enters in contact with water it dissolves very quickly due to its high solubility (higher than gypsum). This produces a solution supersaturated with respect to gypsum that triggers its nucleation and crystallization, leading to the formation of a series of interlocked needles [11] [147]. A different mechanism was proposed by Michaelis in 1892. According to his study, the hemihydrate dissolves in contact with water, but before gypsum crystallizes, it passes through a colloidal state [148] [147]. Hansen also studied the hydration of bassanite in 1963 [149] and proposed a mechanism in which during the hemihydrate dissolution, a membrane of gypsum is formed around the dissolving crystals inhibiting their dissolution resulting in the induction time [148] [147]. Other early studies that were done in the second half of the twentieth century agreed with the mechanism proposed by Le Chatelier [150] [151] [152] (Ludwig and Singh 1978). Due to the high kinetics of this reaction, to have a direct observation of the hydration, *in situ* studies are needed. The very first study in which gypsum growth was observed *in situ* from the hydration of hemihydrate, using microscopy imaging, is attributable to Ridge (1958) [17]. After this, it was only in 2016 that the hydration of gypsum plaster was investigated again with *in situ* imaging experiments, in particular X-ray tomography. In this case, Adrien et al. (2016) [13] applied an X-ray tomography approach to follow in situ the setting of β-hemihydrate in conditions close to industrial processes. With their results, it was possible to observe the dissolution of the hemihydrate and the precipitation of gypsum (Figure 2.36a), providing evidence of the development of the hydration process from 3D volumetric images (Figure 2.36b) [13].

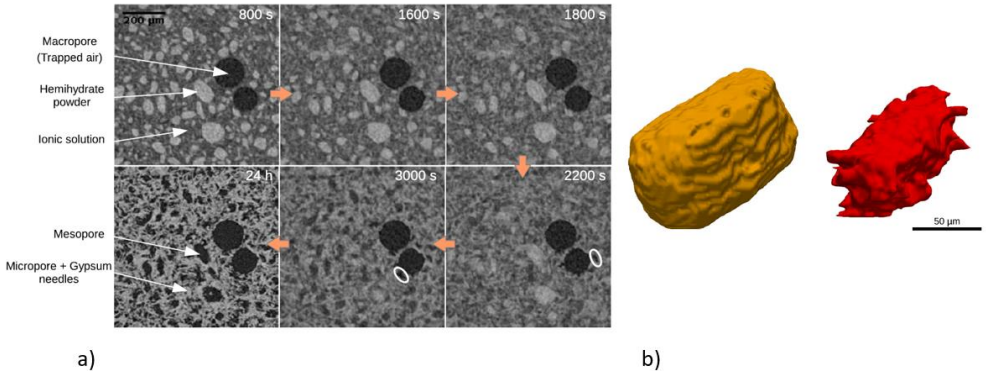

a) b)

Figure 2.36. Figure modified after Adrien et al. (2016) [13]. a) Evolution of the microstructure of gypsum plaster obtained from the hydration of β-hemihydrate from 800 s after the start of the hydration to 2200 s. The pictures show the dissolution of hemihydrate crystals followed by the precipitation of gypsum crystals and highlight the presence of mesopores generated from the vacancies left from the hemihydrate (with circles in the pictures at 2200 s and 3000 s of

hydration). b) 3D volume reconstruction of a hemihydrate particle, in yellow, and the mesopore left after its dissolution, in red.

More recently, Seiller et al. (2021) [14] performed another *in situ* X-ray tomography study of the evolution of gypsum plaster during hydration. This time the system was scanned using a synchrotron source using α-hemihydrate as a starting material. The advantage of the use of synchrotron sources compared to laboratories equipment was clear from his work, and thanks to the extraordinarily low voxel size (down to 0.163 µm) and high temporal resolution (~30 s) they were able to quantify the precipitation rate of gypsum crystals. Besides demonstrating the exceptional possibilities that a synchrotron source offers to study *in situ* processes, the observations of the work of Seiller et al. (2021) [14] also confirmed that the hydration of gypsum plaster proceeds by the first dissolution of bassanite and the second precipitation of gypsum induced by the first [14]. The sequence of tomography 2D slices that show the behavior of the hydration reaction are reported in Figure 2.37.

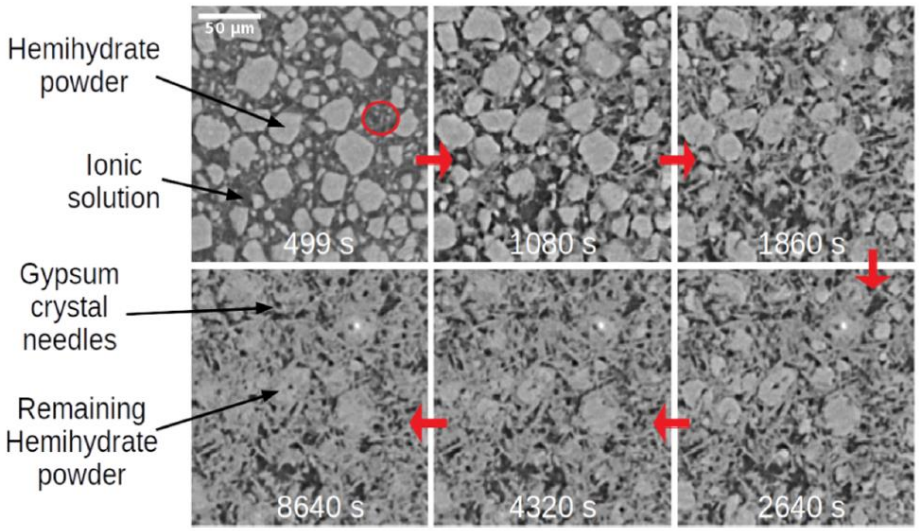

Figure 2.37. Figure modified after Seiller et al. (2021) [14]. A sequence of 2D synchrotron tomography slices shows the hydration of gypsum plaster obtained from α-hemihydrate. In the sequence, the formation of gypsum crystals from the ionic solution is highlighted in the red circle. In the time frame reported in this picture, the complete dissolution of the starting hemihydrate is not observed, but it can be seen in other tomography slices available in Seiller et al. (2021) [14] original work.

All these works provided detailed evidence of the nature of the hydration reaction of gypsum plaster based on chemical analysis and imaging studies. However, none of these authors investigated the crystallographic relationships that may be present between the dissolving phase and precipitating phase. A step forward in this direction has been done very recently with the two works of Ilett et al. (2022) and Jia et al. (2022) [15] [16]. Ilett et al. (2022) [15] performed correlative *in situ* liquid cell transmission electron microscopy (LCTEM), cryo-TEM, and Raman spectroscopy to observe the phase transformation from hemihydrate to gypsum. This work is the example of how a complementary technique approach could provide multiple evidence of a single process, to make some considerations about the crystallographic relationship between gypsum and the hemihydrate. Hemihydrate nanorods (around 300 nm) were mixed with a solution of water and ethanol so that the transformation occurred in an undersaturated solution of calcium sulfate. The pictures that they acquired show that gypsum is forming through a homogeneous nucleation process due to the dissolution of hemihydrate (Figure 2.38).

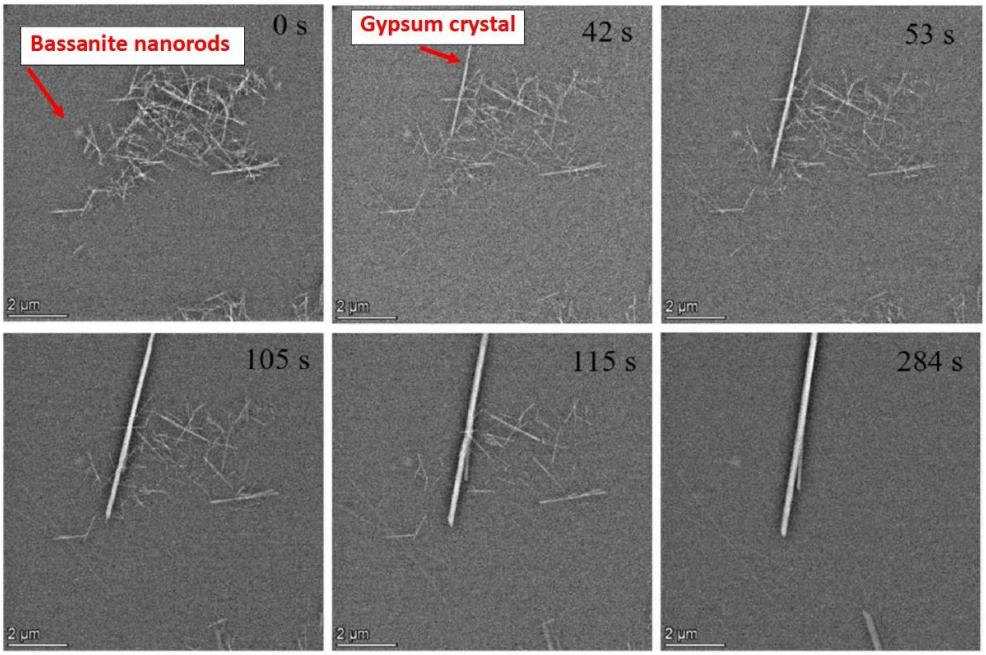

Figure 2.38. Figure modified from Ilett et al. (2022) [15]. LCTEM pictures show the dissolution of bassanite nanorods and the homogeneous growth of gypsum from the solution.

However, from a crystallographic point of view, and based on both the structures of the hemihydrate and gypsum and from calculations of surface free energies, the heterogeneous nucleation of gypsum from the hemihydrate crystals could also be possible. This would proceed from the [001] direction of the hemihydrate to the [001] direction of gypsum, even though not observed in this particular case [15]. In another recent work, Jia et al. (2022) [16] studied the early-stage nucleation of calcium sulfate from solution and the phase transformation from hemihydrate to gypsum by quenching the sample at different times of the reaction and observing it with the TEM. They found out that in their system, gypsum was nucleating heterogeneously from the tip of hemihydrate crystals with a coalignment of the [001] directions (Fig. 2.39).

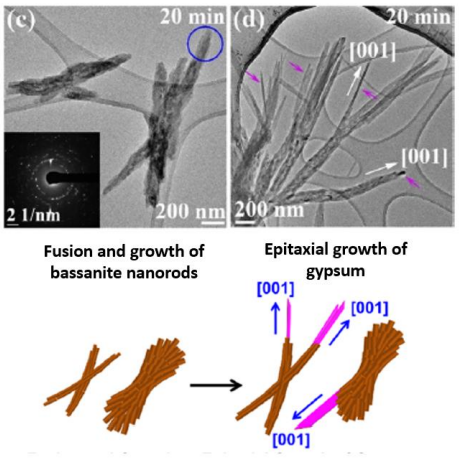

Figure 2.39. Figure modified after Jia et al. (2022) [16]. The TEM pictures and associated drawings, show first the fusion of bassanite nanorods to form co-aligned bigger crystals and second the growth of gypsum crystals from the tip of the bassanite crystals.

This result did not provide a measurement of the orientation of the crystallographic faces of the crystals. Though, it clearly shows the possibilities of both homogeneous and heterogeneous nucleation of gypsum from the hemihydrate to be equally possible depending on the conditions of

the system. A detailed crystallographic study based on X-ray diffraction to provide evidence of the crystallographic relationships between the two phases was not performed in any of these works. A combined approach of both morphological and crystallographic information could provide for the first time a link between the evolution of the microstructure of gypsum plaster and the crystallographic relationships between the dissolving and precipitating crystals.

2.4.3. The dissolution of crystals. What do we know about calcium sulfate hemihydrate?

Mineral dissolution is a fundamental process in nature and industrial settings, associated to natural weathering, corrosion and alteration processes at large. Mineral dissolution is usually associated to interfacial re-precipitation, due to the high concentrations of solutes at mineral-water interfaces, which often control the transfer of matter across these interfaces [19]. Due to the high interest that these dissolution-precipitation processes represent, they have been often studied at different length scales (from kilometers of length to the angstrom level as reported by Luttge et al. (2019) [20]). The study of crystal dissolution and growth has seen a great increase in the last decades due to the availability of techniques allowing the observation of these processes at the proper scale [20]. Techniques that are often used to observe these processes include: AFM, SEM, TEM, FIB and VSI. Nevertheless, accessing the dissolution and precipitation of crystals from an experimental point of view it is not always possible or does not always allow the detail of observation that is needed. For these reasons, it is necessary to couple the observations with theoretical calculations [20]. Focusing on the theories on crystal dissolution, one of the biggest issues is how to link the behaviour of the dissolution at the atomic scale with the dissolution of the bulk crystal. As reported by Luttge et al. (2019) [20] in a recent and detailed review about the theories behind fluid-solid interactions, the stepwave model [154] is still nowadays the link between all the key points of the dissolution of crystals from the microscopic level (nucleation of etch pits) to the macroscopic one (dissolution of the crystal surfaces) [20], and it is generally used to define the dissolution kinetics in material science and geochemistry. The subject of crystal dissolution has developed less when compared with crystal growth [154]. This depends mostly on the fact that crystal growth usually happens in systems close to equilibrium (Gibbs free energy ΔG close to ΔG_{crit}), therefore the size and shape of the crystal, the level of impurities and structural defects are all result from the growth rate law and can be monitored quite easily with an AFM. In the case of the dissolution of a crystal instead, the system is often far from equilibrium (Gibbs free energy $\Delta G < \Delta G_{crit}$) and the dependence of the dissolution rate from the ΔG conditions is inevitable. The fundamental concept of the stepwave model is that the bulk dissolution rate (dissolution of the entire crystal) is governed by phenomena that occur at the surfaces of the crystal [154]. In particular, in situations of high undersaturation, the formation of etch pits in the surface of a crystal is the “spark” that initiate a series of steps generating dissolution stepwaves that control the rate of dissolution of the crystal [154]. Lasaga and Luttge developed the stepwave model performing Monte Carlo simulations of the dissolution of crystals starting from dislocation defects (e.g. etch pits). Figure 2.40a shows a simulation made by Lasaga and Luttge [154]. The etch pit in the middle of the image is the defect that initiates and enhances the dissolution stepwaves, indicated in the image as the big steps of material that is removed from the surface of the crystal. Figure 2.40b shows the expansion of step waves from the etch pit with a contouring program. Figure 2.40c shows what happens in the case of a natural crystal where several etch pit open in a surface. Each etch pit generates a step wave that combines with the other to dissolve the surface of the crystal [154].

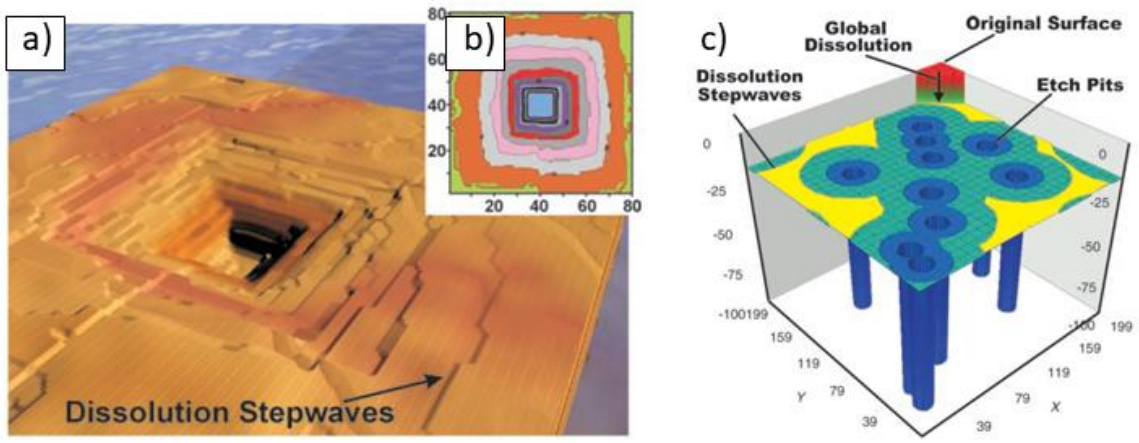

Figure 2.40. Modified after Lasaga and Luttge (2001) [154]. a) Monte Carlo simulation made by Lasaga and Luttge (2001) to explain the stepwaves propagation from an etch pit. b) Model of the dissolution stepwaves propagation from an etch pit made with contouring programs [154]. c) Complete stepwave model [154].

The result of the generation of these stepwaves that cross the crystal surfaces is the removal of layers of atoms that overall give what can be called global dissolution rate [20]. The rate of dissolution of a crystal (*r*), described in the frame of the stepwave model, can be calculated in this way [154] [20]:

$$r = A\left(1 - e^{\frac{\Delta G}{kT}}\right) \tan h\left[\frac{B}{f(\Delta G)}\right] f(\Delta G) \qquad \text{Eq. 2.3}$$

where $f(\Delta G) \equiv 1 - \frac{1-e^{\Delta G/kT}}{1-e^{\Delta G_{crit}/kT}}$ and A and B are constants that can be calculated from the dissolution experiment.

Another way of writing the equation to calculate the dissolution rate of crystals is this one [155] [156] [21]:

$$r' = k_0 \exp\left(-\frac{E_a}{RT}\right) A_{min} g(I) \Pi a_i^{ni} f(\Delta G_r) \qquad \text{Eq. 2.4}$$

with k_o (mol s^{-2} s^{-1}) being a constant, E_a (J mol^{-1}) being the activation energy, R (J mol^{-1} K^{-1}) and T (K) being the ideal gas constants, A_{min} (m^2) being the reactive surface area, g(I) accounts for the dependence that could be in place between the *r'* and the ionic strength of the solution and Πa_i^{ni} considers the presence of aqueous species such as OH^- or H^+. F(ΔGr) is the same term found in Eq. 2.3. Since there is a linear dependence of the rate of dissolution *r'* with A_{min}, it is common to express the rate of dissolution as "normalized dissolution rate" in mol m^{-2} s^{-1} [21].

The most recent studies aiming to observe the behavior of the dissolution of crystals, and calculating the rate of dissolution when possible, have been performed using the AFM [157] [158] [159] [27], SFM (scanning force microscopy) [160] [28] [161] [27], SECM (scanning electrochemical microscopy) [162] [27], VSI (vertical scanning interferometry) [29] [163] [164] [154] [27] and DHM (digital holographic microscopy) [165] [166] [27]. All these techniques represent perfect tools to observe the dissolution at the surface of crystals. Before the spread of these techniques, the dissolution behavior of crystals was often investigated from the bulk using techniques that control the mass transport of a system [21] or with experiments on particulate suspensions [27]. In the literature there is only one study in which the normalized dissolution rate of calcium sulfate hemihydrate was calculated from the dissolution of the bulk. This is the case of the work of Brandt and Bosbach (2001) [22], where the dissolution of the hemihydrate to form gypsum in the presence

of cellulose ethers was monitored from BET measurements. There is no record instead about existing studies on the surface dissolution of the hemihydrate. The dissolution of gypsum, instead, have been thoroughly investigated. One of the most important reasons lies in the fact that gypsum can grow big crystal surfaces that facilitates its handling and observation with microscopic techniques. Calcium sulfate hemihydrate instead, does not grow big crystal surfaces and its peculiar elongated shape complicates the sample preparation and the surface recognition. The high solubility of the hemihydrate also adds another lever of complexity to the observation of the dissolution. The possibility to have access to the kinetics of the surface dissolution of a crystal is a useful tool that permits to gain experimental insights on the reactivity of the crystallographic faces. The different reactivity of the crystallographic surfaces of calcium sulfate hemihydrate can be observed optimizing the sample preparation and slowing down the dissolution kinetics. Moreover, the dissolution rate of a bulk hemihydrate sample can be calculated based on a direct measurement of the reactive surface area. This multi scale approach would provide an overall insight on the dissolution behavior of the hemihydrate from different scales of observations.

2.5. Aim of the thesis

This PhD project is divided into three parts with the aim of investigate all the aspects of the dissolution-precipitation process that occur when calcium sulfate hemihydrate is hydrated to form gypsum. The common thread of this project is to show how the combination of several synchrotron techniques, such as scanning three-dimensional X-ray diffraction (s3DXRD), X-ray phase contrast tomography (PCT) and high-resolution X-ray powder diffraction (HR-XRPD), may be a promising tool and useful resource to shed light into the relevant topic of the hydration of calcium sulfate hemihydrate to form gypsum. This work provides a multi-technique and multiscale investigation from the atomic structure of the starting material to the microstructure of the final gypsum plaster matrix.

2.5.1. Calcium sulfate hemihydrate (α and β) crystal structures

Weiss and Bräu (2009) [9] analyzed with X-ray single crystal diffraction the crystal structure of β-hemihydrate with formula $CaSO_4 \cdot 0.5H_2O$ refining it in the monoclinic C2 space group. Successively, Schmidt et al. (2011) [10] replicated the analysis with an α-hemihydrate sample with the same amount of water resulting in the same monoclinic C2 crystal structure. With their works both the groups of authors demonstrated that from X-ray single crystal diffraction, the presence of differences in the crystal structure of the two forms of α and β-hemihydrate could not be detected. However, it is interesting how Follner et al. (2002) [23] claim that, by comparing the X-ray powder diffraction patterns of α- and β-hemihydrate, the two forms of hemihydrate present different features which suggest different crystal structures. Based on the patterns that they acquired, they affirm that α- and β-hemihydrate present different intensities and, for α-hemihydrate, additional reflections and peak splitting not observed in the β-hemihydrate. The patterns of the α- and β-hemihydrate acquired with a laboratory equipment by Follner et al. (2002) [23] are reported in Figure 2.41. The patterns a) and c) in Figure 2.41a and b respectively are relative to the α-hemihydrate, while the other two are relative to the β-hemihydrate. From the quality of these patterns it is difficult to observe the differences that Follner et al. (2002) [23] addressed. Follner et al. (2002) [23] also attempted a Le Bail refinement of the patterns but did not show the results. Coupling the X-ray powder diffraction with Raman and NMR spectroscopy, they suggested that it is possible that monocrystalline aggregates of hemihydrate present domains with a different content of water [23]. The presence of domains with different quantity of water would indeed modify the cell parameters of the hemihydrate resulting in the splitting of reflections that Follner et al. (2002) [23] mentioned for the α-hemihydrate.

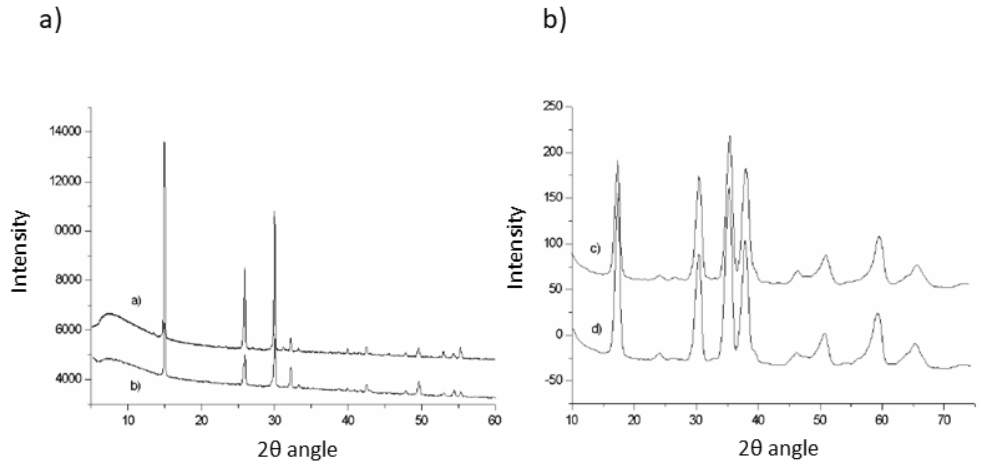

Figure 2.41. a) Bragg powder diffraction patterns acquired by Follner et al. (2002) [23] of a sample of α-hemihydrate (a) and β-hemihydrate (b). b) integrated area detectors images acquired by Follner et al. (2002) [23] of the same α-hemihydrate sample (c) and β-hemihydrate sample (d). Modified after Follner et al. (2002) [23].

We performed a detailed crystallographic study of the two forms of calcium sulfate hemihydrate (α and β) to unravel the possible presence of differences in their crystal structure. Samples of α-hemihydrate were synthesized in aqueous solutions with two different methodologies. The sample of β-hemihydrate was obtained from the BASF industry. The three types of sample were firstly pre-characterized with SEM, FTIR and TGA-DSC. Successively they were measured with HR-XRPD at the ID22 beamline of the ESRF. The two types of α-hemihydrate were also measured with single crystal XRD at the ID11 beamline to detect the presence of the typical pseudo-merohedral twinning of the hemihydrate structure and mosaicity of the samples. The HR-XRPD approach resulted to be the perfect tool to reveal the structural differences between the α- and β-hemihydrate samples shedding light on the different water incorporation of the crystal structures. Synchrotron powder diffraction beamlines have many advantages when compared to a common laboratory instrumentation. Some of the main benefits for example are: narrow peak widths, rapid data collections (essential for *in situ* experiments), highly monochromatic X-rays, narrow instrumental peak shape and tunability. When using HR-XRPD at the unique ID22 beamline, these advantages become even stronger. The presence of analyzer crystals in the beamline set-up, permits to obtain extremely narrow peaks with accurate positions insensitive to misalignment or other sample related problems. Thanks to the acquisition of high-resolution powder patterns of α- and β-hemihydrate, it was not only possible to observe clearly the peak splitting of the α-hemihydrate, but also to perform Rietveld refinements of all the three types of sample.

2.5.2. A combined diffraction and tomography approach to investigate the hemihydrate-gypsum transformation

A combination of synchrotron tomography and diffraction techniques is needed to establish precise relationships between the reactivity of the hemihydrate and the development of the microstructure of gypsum plaster. Diffraction-tomography techniques comprise all the techniques in which a sample is imaged based on the diffraction signal (coming from single crystals, powders or nanocrystals). A few examples from the literature show the use of diffraction-tomography techniques, in particular X-ray computed tomography (XRD-CT), to the study of construction materials. This is the case of the works of Artioli et al. (2010) [167], Artioli et al. (2015) [168] and Claret et al. (2018) [169]. With the XRD-CT approach, the diffraction spots coming from the single crystals in the sample are filtered out or simply ignored and the reconstruction of tomographic images is based on the patterns coming from the powder part of the sample. To explain what has been done in the past and what is the innovation that the use of s3DXRD has brought to this PhD work, a review of the previous examples is needed. In the work of Artioli et al. (2010) [167], XRD-CT was combined with X-ray micro-tomography (X-μCT) to monitor the spatial distribution of ettringite in the hydrating paste of Portland cement [167]. This was the first time in which XRD-CT was applied to such a complex system. One of the main motivations behind the realization of this work was to demonstrate the suitability of the diffraction-tomography approach to study the hydration products of cementitious materials. In Figure 2.42 is reported the diagram made by Artioli et al. (2010) [167] that explains the acquisition and treatment of XRD-CT data. They performed the experiment at the ID22 beamline of the ESRF using a micrometer beam and a CCD camera (FReLoN) as a detector. The samples were a glass capillary containing cement paste (cement and deionized water), and a mortar with cement paste and sand. During the XRD-CT measurement, the sample was scanned horizontally with a step size determined by the size of the beam. For each horizontal step, the sample was rotated to collect the diffraction signal from all the crystals and nanocrystal phases in the sample. In Figure 2.42, starting from the upper left side, is reported a stack of images acquired by the camera. As it can be seen from the camera images, both powder rings and Bragg spots were present. Artioli et al. (2010) [167] ignored the Bragg spots and from the azimuthal integration of the 2D diffraction patterns they extrapolated a series of 1 D diffraction profiles, as

shown in the upper right part of Figure 2.42. Then the patterns were dived into specifics ROIs as shown in the bottom right part of the figure. Finally, the sinograms of the different components of the sample, the glass capillary, and ettringite in this case, were reconstructed to visualize the distribution of the components in the sample (bottom left part of Figure 2.42) [167]. The strategy adopted from Artioli et al. (2010) [167] is not far from the one that has been used in this P.hD. project. The big difference between our approach and the one of Artioli et al. (2010) [167] lies in the treatment of the diffraction signal. Artioli et al. (2010) [167] in their work showed also a comparison between an XRD-CT slice showing the distribution of ettringite in one layer of the sample and the X-µCT reconstruction of the same portion of the sample. The comparison between the XRD-CT (a) and X-µCT (b) slices is reported in Figure 2.43. Ettringite was chosen for the reconstruction of XRD-CT maps because this was the phase characterized by crystallites that were small enough to be probed as a powder under the beam. The rest of the phases, such as the big quartz crystals, which are represented by black voids in the XRD-CT map (Figure 2.43a), were not considered for the reconstruction because they behaved as single crystals during the acquisition.

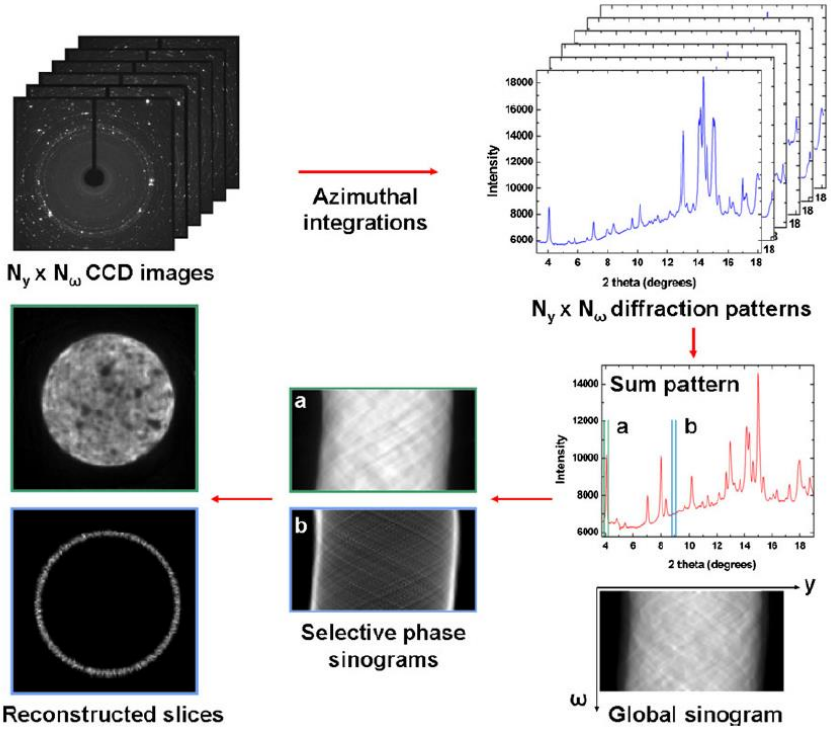

Figure 2.42. Diagram made by Artioli et al. (2010) [167] to explain the steps of the data treatment of XRD-CT data.

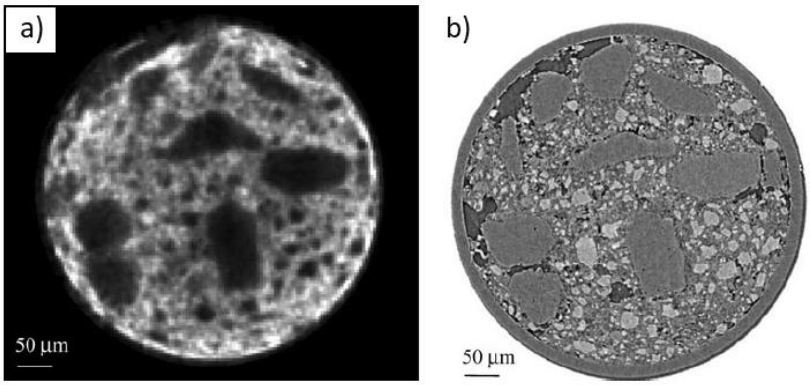

Figure 2.43. Modified after Artioli et al. (2010) [167]. a) layer of the sample probed with XRD-CT and reconstructed based on the ettringite diffraction pattern. b) same layer of the sample probed with X-µCT.

Artioli et al. (2015) [168] applied again XRD-CT to the system of the hydrating cement paste. In this case, the hydration of ordinary Portland cement (OPC) was followed *in situ* in the presence of PCE superplasticizer to observe how the additive influenced the dissolution-precipitation processes of the main phases of OPC (tricalcium silicate, dicalcium silicate, tricalcium silicate, C-S-H) from a spatial point of view [168]. This second example from Artioli et al. (2015) [168] showed again how the use of diffraction-tomography techniques is a promising tool to gain insights into the key questions of the field of cementitious materials. In particular, in this case, the main scientific motivation was to localize where the hydrated phase (C-S-H) precipitated compared with the cement before the hydration. As can be seen from Figure 2.44, the diffraction imaging approach led to unprecedented results [168].

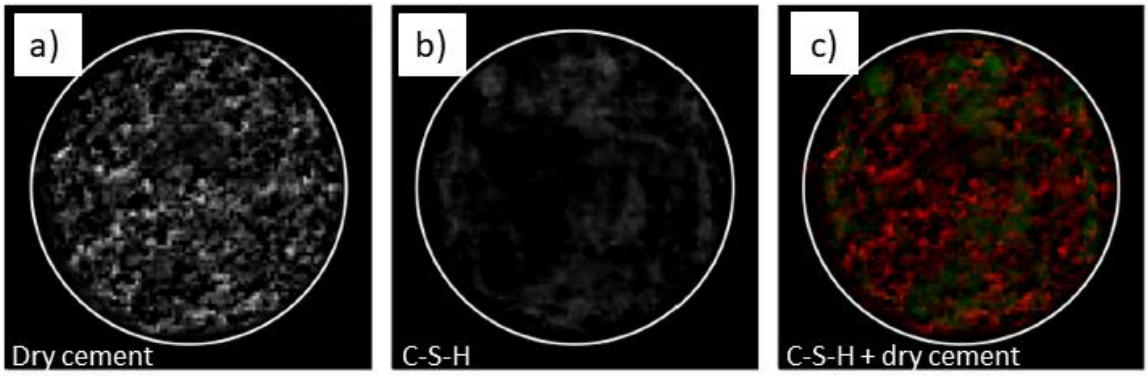

Figure 2.44. Modified after Artioli et al. (2015) [168]. a) XRD-CT map of the starting dry cement sample. The slice is reconstructed based on the diffraction patterns of all the phases. b) XRD-CT map of the spatial distribution of the C-S-H after the hydration of the cement. c) XRD-CT map of both the sample before being hydrated and the C-S-H.

The last example of the use of XRD-CT on cementitious materials is the one provided by Claret et al. (2018) [169]. Claret et al. (2018) [169] performed *in situ* XRD-CT experiments at the ID11 beamline to determine the distribution and reactivity kinetics of the main mineralogical phases in a cement paste. Thanks to this approach, Claret et al. (2018) could reconstruct XRD-CT maps of many mineralogical phases (calcite, C-S-H, ettringite, mullite, portlandite, quartz, and an amorphous phase) at different times of the hydration process of cement. All these three examples of previous applications of XRD-CT alone and combined with X-µCT prove the suitability of diffraction-tomography techniques to investigate the different aspects of cement hydration. Moreover, in contrast with EDS chemical analysis, or chemical mapping in general, which is often used to deal with cementitious materials characterization, they provide a way to perform non-invasive and non-destructive experiments independent from sample preparation artifacts. XRD-CT is used when we are interested in the spatial distribution of powder, nanocrystalline and amorphous phases. However, the crystallographic relationships between the phases cannot be accessed, as the information about the orientation of the various crystallites is only statistical. In the case of the hydration of gypsum plaster, not only the spatial distribution of gypsum compared to the starting hemihydrate is important, but also how the orientation of crystals that are spatially close are related. Once the orientation of each crystal in the space of the sample is known, we can understand the process that leads to the formation of gypsum, as well as the reactivity of each of the crystallographic faces of the dissolving hemihydrate crystal. From a technical point of view, this aim is achieved with the application of a combined approach of *in situ* s3DXRD and PCT to the hydrating system of gypsum plaster. With the s3DXRD, the Bragg spots are used to index the bigger crystals. The size, morphology and orientation of the individual crystals are reconstructed in the space based on the X-ray diffraction pattern. The s3DXRD method was introduced originally by Hayashi et al. [170] [171] [172] applied to metallurgical materials. It is evident how metals represent

an easy case study for s3DXRD, being cubic and presenting big packed grains. For metallurgical research, s3DXRD is useful to identify grain and twin boundaries, discriminate between the surface and the bulk of crystals, and also to follow the evolution of the strain due to external forces. Interesting examples of previous applications of s3DXRD to metallic matrices are the works of Hektor et al. (2019) [173], Henningsson et al. (2020) [174], and Hayashi et al. (2019) [175]. In these examples the growth of a whisker under annealing [173] [174] and the intragranular stress tensor development in a bulk steel sample [175] were monitored by indexing individual grains.

The previous applications of s3DXRD to metallic grains prove the potential of this technique to investigate the spatial and crystallographic relationships between hemihydrate and gypsum. In this PhD project, we have applied, for the first time in the topic of construction materials, semi-simultaneous s3DXRD and PCT measurements to follow *in situ* the development of the hydration of gypsum plaster. From the s3DXRD measurements we obtained the phase identification, lattice parameters, and orientations of the grains of hemihydrate and gypsum that were present in the sample during the hydration. From the PCT measurements we could reconstruct the full shape and morphology of the grains and follow the evolution of the microstructure of the gypsum paste.

2.5.3. Multiscale investigation of calcium sulfate hemihydrate dissolution

Neither a direct observation of calcium sulfate hemihydrate dissolution nor a direct quantification of the reactive surface area of the bulk while dissolving has been provided in the literature. This is due to several experimental and analytical issues. If we consider microscopy techniques, such as the AFM, to observe the surface dissolution of calcium sulfate hemihydrate, the main issues are the shape of the crystals and the high solubility of the phase in aqueous solutions (enhanced by ΔG conditions very far from equilibrium). Unfortunately, not much can be done to change the shape of the hemihydrate crystals to have bigger surfaces, but solutions are possible to slow down the rate of dissolution allowing to observe and collect images of the surface. A possible way to overcome this issue is to prepare solutions for the dissolution using additives that retard the crystallization of gypsum and/or delaying the dissolution of the hemihydrate. The use of additives for the production of gypsum plaster is a common practice in industry. Additives are used mainly to tune the setting process of gypsum plaster, retarding gypsum crystallization, and to facilitate the workability of the material. The strongest retardant additive of the crystallization of gypsum is polyacrylic acid (PAA). PAA is a base constituent of anti-scaling agents that mitigate the formation of mineral incrustations [176]. In this case, PAA was used to prepare aqueous solutions (10 mM PAA concentration) to hydrate crystals of hemihydrate to observe their dissolution with the AFM. The use of PAA coupled with a strategic sample preparation that permitted to hold the crystals of hemihydrate in place while exposing crystallographic surfaces to the AFM scan, allowed to obtain images of the *in situ* dissolution of the crystals.

Additives are also used in industrial applications to tune the morphology of gypsum crystals. It is demonstrated that the introduction of organic molecules to the gypsum plaster hydration system influences the crystallization process, which is linked to the development of macroscopic properties of gypsum crystals [177]. Here beta naphthalene sulfonate (BNS) was used to tune the crystallization process of gypsum to form crystals with a uniform shape that could be separated more easily from the dissolving bulk hemihydrate in PCT reconstructions. To measure directly the bulk normalized dissolution rate of hemihydrate, a direct quantification of the reactive surface area *in situ* is required. Tomography techniques, such as PCT in this case, provide a way to do it. The biggest problem in this approach is represented by the precipitation of gypsum which is coupled with the dissolution of the hemihydrate. Since hemihydrate and gypsum differ only by 1.5 molecules of water they have almost the same electron density. This reflects in very similar

intensities in the greyscale PCT images. Discriminating between hemihydrate and gypsum crystals in the same sample from PCT reconstructions is therefore quite hard if not impossible with basic segmentation tools. Artificial intelligence (AI) segmentation and deep learning segmentation with convolutional neural networks (CNNs) have proven to be useful tools in dealing with common segmentation problems of complex systems. Two interesting examples of the application of neural networks to solve segmentation problems in particle systems are those of Furat et al. (2018) [178] and Furat et al. (2019) [179]. In the first example, Furat et al. (2018) [178] did a complementary study on greisen-type ore using SEM-EDS for chemical 2D analysis and X-ray microtomography (which they call XMT) for 3D reconstruction of the sample [178]. The aim of the study was to be able to separate each particle in the 3D XMT volume to analyze their properties individually. Figure 2.45a-e shows all the major steps involved in the image processing strategy used by Furat et al. [178]. In Figure 2.45a, a portion of a slice of the volume after being binarized based on a local thresholding is reported, and Figure 2.45b shows the result of the application of the watershed algorithm to the same portion of the slice. As it is evident, the application of the watershed brings to a situation of over-segmentation which prevents from identifying all the different particles correctly. To overcome this problem of over-segmentation, Furat et al. (2018) [178] postprocessed the segmented slices using a neural network. Figure 2.45c and d show a slice of the sample before (c) and after (d) the application of the neural network. The task of the neural network was to decide if adjacent individual grains belonged to the same particle or not, and if yes to unify them. The result of the application of the neural network to all the 3D volume is shown in figure 2.45e.

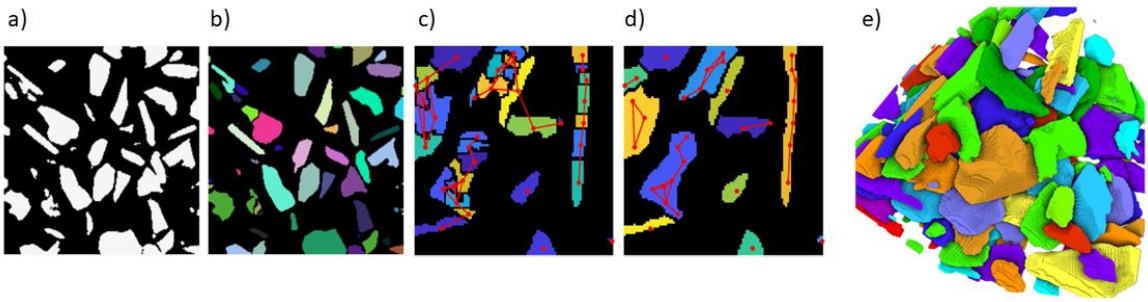

Figure 2.45. Modified after Furat et al. (2018) [178]. a) Portion of a slice of the sample measured with XMT after being binarized. b) Same portion of the sample after the application of the watershed algorithm showing over-segmentation issues. c) Another portion of the sample before the application of the neural network to separate the regions of over-segmentation. d) Result of the application of the neural network in the same portion of the sample. e) Result of the application of the neural to all the 3D volume of the sample [178].

In the second study, Furat et al. (2019) [179] give an overview of some studies where machine learning was used to solve issues with the processing of conventional imaging techniques data in the field of material science. In one particularly interesting example, these authors applied CNNs to an X-ray computed tomography (XCT) dataset of an Al-Cu alloy as a preprocessing tool to locate the grain boundaries between the crystals. Grain boundaries are not visible from tomography, for this reason Furat et al. (2019) [179] trained the CNN with input 3DXRD maps showing the location of the grain boundaries. The supervised training of a 3D U-Net on the 3DXRD “ground truth” grain maps permitted to enhance the contrast of the grain boundaries in the tomography reconstructions, paving the way to a possible grain-wise segmentation [179]. Figure 2.46 reports a sequence of slices relative to a particular layer of the sample [179]. Figure 2.46a is the 3DXRD ground truth information used to train the 3D U-Net to locate the grain boundaries in the XCT volume. Figure 2.46b shows the result of the neural network in enhancing the grain boundaries. Figure 2.46c shows the watershed grain-wise segmentation based on Figure 2.49b. Finally, figure 2.46d reports the grain boundaries extrapolated from the 3D U-Net application and postprocessing. Comparing Figure 2.46a and 2.46d we can see that the use of the neural network permitted to

extrapolate grain boundaries from XCT images which would have never been possible using basic segmentation tools.

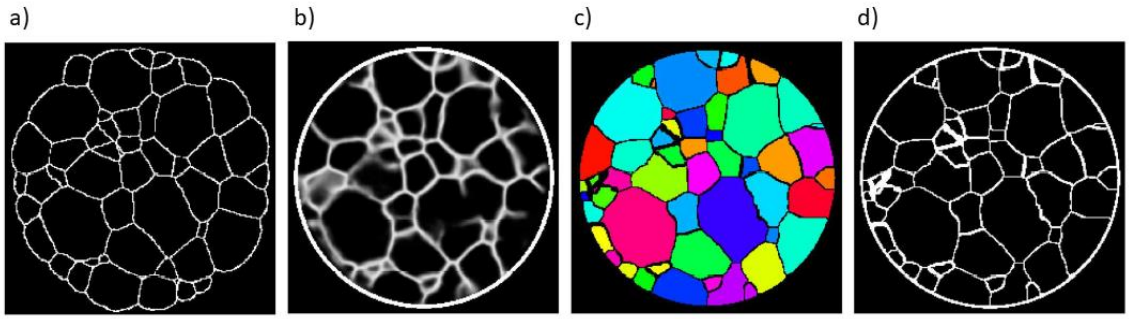

Figure 2.46. Modified after Furat et al. (2019) [179]. a) 3DXRD map of the grain boundaries used as ground truth for the training of the 3D U-Net on the XCT volume. b) Grain boundaries enhanced by the 3D U-Net in the XCT volume. c) Watershed segmentation of the grains based on the grain boundaries determined by the 3D U-Net of the XCT volume. d) Grain boundaries extrapolated by the 3D U-Net plus postprocessing of the XCT volume.

In our case, thanks to the application of the Paganin algorithm [180] for phase retrieval and the training of a 2.5D U-Net on the 3D PCT volumes of dissolving hemihydrate and growing gypsum, it was possible to separate the two different phases. The reactive surface area of the bulk hemihydrate was quantified during dissolution from the PCT using the ORS *Dragonfly* software (version 2021.1, Object Research System (ORS) Inc., Montreal, Canada). This approach allowed the calculation of the normalized dissolution rate of the bulk hemihydrate from an *in situ* experiment and direct quantification of the surface area. The dissolution process of calcium sulfate hemihydrate was studied from two different point of views, gaining complementary insights on the reactivity of the crystallographic surfaces of the crystals and the dissolution behavior of the bulk.

3. Methods

3.1. Laboratory methods

3.1.1. TGA-DSC

Thermal analysis is defined as the group of techniques that allows the measurement of the properties of a substance as a function of temperature. During a thermal analysis, a sample undergoes a thermal treatment while the effect of the energy exchange between the sample and the environment is measured. TGA-DSC technique belongs to the group of thermal analysis. TGA-DSC merges the TGA and DSC principles based on a particular geometry of the instrument. The term TGA stands for thermogravimetric analysis. It means that the technique is devoted to measuring the variation of weight of a sample under increasing temperature. DSC means instead differential scanning calorimetry and it is used to measure the heat flow into (or from) a sample when it is heated, cooled, or held isothermally at a constant temperature. The TGA-DSC instrumentation provides a versatile way to characterize the physical and chemical properties of a material under controlled atmospheric conditions. Thermogravimetric analysis needs only a small mass of sample. A microbalance detects the weight changes, due to the release or absorption of gas, while the sample is placed in a furnace that controls the temperature. The result is data about the evolution of the weight as a function of the temperature. The DSC analysis yields the heat flow produced by a certain reaction. Figure 3.1 shows an example of both a TGA (in blue) and a DSC (in red) curves obtained by heating hemihydrate crystals.

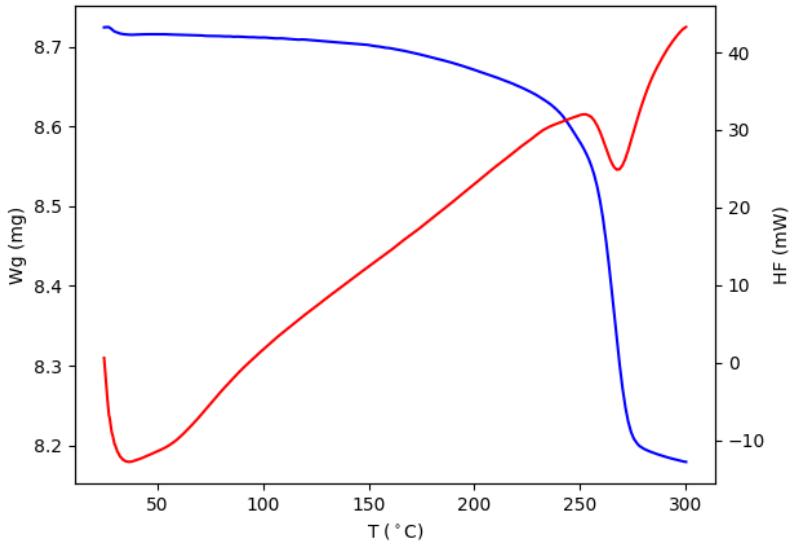

Figure 3.1. Example of a TGA (in blue) and a DSC (in red) curve obtained by heating hemihydrate crystals. The TGA curve shows the decrease in the weight of the sample with increasing temperature. The DSC curve shows the heat flow associated with the reactions that are taking place in the interval of temperatures between 25°C and 300 °C.

TGA-DSC analyses for this PhD thesis were done at ISTerre (UGA) using a MATTLER TOLEDO TGA/DSC 3+ instrument. A picture of the instrument used is shown in Figure 3.2.

Figure 3.2. MATTLER TOLEDO TGA/DSC 3+ instrument, installed at the ISTerre (UGA).

This instrument uses an micro-balance with a detection limit around 0.01 µg and a quantification limit of 0.1 µg.

Four samples were measured. Three α-hemihydrate samples and one β-hemihydrate sample. The TGA-DSC analyses were performed in the temperature range between 25°C and 500°C, increasing the temperature by 20°C per minute.

3.1.2. SEM

Scanning electron microscopy (SEM) is part of the broader range of electron microscopy techniques. Electron microscopy techniques offer unique possibilities to investigate many properties of a material such as its structure, topology, morphology, and composition. The SEM is not that different from a conventional optical microscope, but it offers many advantages. The biggest advantage is the level of magnification reached, which can be up to 1,000,000x. Moreover, the SEM benefits from a large depth of field, which results in much of the sample surface being in focus simultaneously. The SEM technique is based on the interaction between an electron beam and the surface of the sample. The electrons are typically generated from an electron gun and have energies in the range of 2-40 keV. The most common electron gun is the tungsten hairpin filament. The filament is heated to 2500°C and the electrons are generated by thermal emission. Another possible source of electrons is the lanthanum hexaboride (LaB_6). The LaB_6 filament generates a brighter electron beam but it is more expensive. Finally, the brightest electron beam is achieved with field emission guns. Electromagnetic lenses focus the electron beam into a fine probe that scans the surface of the sample. When the electrons interact with the sample, the production of secondary electrons, backscattered electrons, Auger electrons, and X-rays occurs. All these signals are collected by various detectors inside the chamber where the sample is placed. The signal chosen is then sent to the monitor creating a picture while the electron beam is scanning the surface. Figure 3.3 shows all the signals that result from the interaction between the electron beam and the surface

of the sample. The bubble represents the region of the sample that is involved in the interaction with the electron beam.

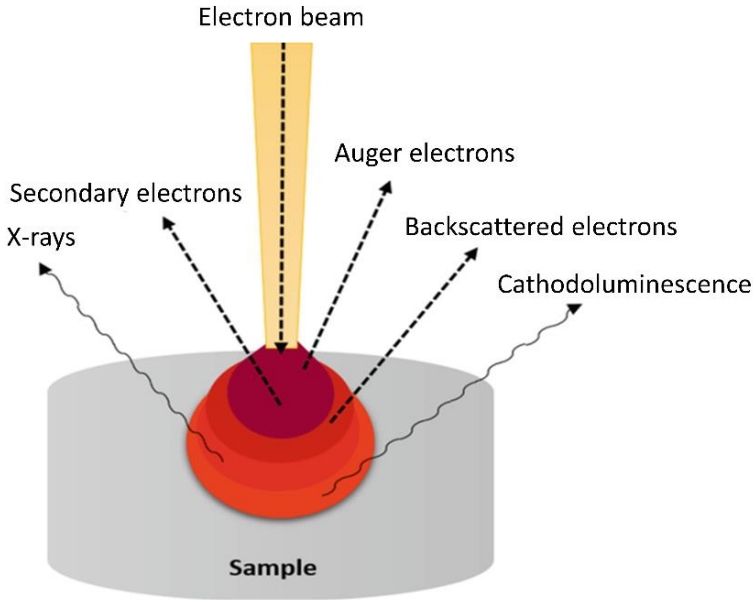

Figure 3.3. Interaction between the electron beam and the surface of the sample at the basis of the SEM functioning. Modified after Akhtar et al. (2018) [181].

When working with non-conductive materials, as in our case, the sample's surface has to be treated to become conducting so there is no charge accumulation. One way to do this is to cover the surface with a thin layer of gold. Once the sample is conductive, images of the surface can be acquired. The secondary electrons escape from the sample at low energies. They provide the highest spatial resolution images because they escape from a shallow, near-surface area of the sample. Secondary electrons give especially topographic information. The backscattered electrons are those that penetrate deeper into the sample surface and are scattered by the nuclei of atoms and ejected back through the surface. Backscattered electrons that reach the surface are less than the secondary electrons but much more energetic. They give rise to images with less resolution but they can be used to achieve compositional information [182]. For this work, two SEM machines have been used. One is an LEO 1530 (Gemini) placed in the chemistry laboratories of the ESRF. This was used to acquire pictures of the α-hemihydrate crystals that were used to perform combined scanning 3DXRD (s3DXRD) and Phase Contrast Tomography (PCT) experiments at the ID11 beamline. The crystals were coated with 50 nm of gold and the images were acquired with a voltage of 10 kV at 9 mm of working distance. The second one is a TESCAN VEGA placed at ISTerre (UGA). This one was used for the pre-characterization of both α and β-hemihydrate crystals that were used for the single crystal micro-X-ray diffraction experiments (μ-SXRD) at ID11, the high-resolution powder diffraction experiments (HR-XRPD) at ID22, and the AFM experiments at ISTerre. The crystals were coated with 50 nm of gold also in this case, and the images were acquired at a voltage of 16 kV.

3.1.3. FT-IR

Infrared spectroscopy (IR) is based on the phenomenon of the absorption of infrared radiation by matter. Infrared radiation is then converted into the molecular vibrations. The absorption is the fingerprint of the chemical bonds present in a specimen. When the absorption is measured as a function of the wavelength, an IR spectrum is emitted showing the type of molecular bonds present. Fourier-transformed infrared spectroscopy (FT-IR) is a particular type of IR in which the data is collected from an interference pattern to a spectrum. In the past, before the introduction of FT-IR,

samples were irradiated step by step with different wavelengths. With the FT-IR technique instead, the spectra of all wavelengths are collected simultaneously. The infrared radiation passes through an interferometer and is then directed to the sample. The result is an interferogram that represents the light intensity as a function of a mirror inside the interferometer. The signal is Fourier-transformed to produce the spectrum in which the intensity is a function of the wavenumber. The FT-IR is much faster than the normal infrared spectroscopy techniques and provides a better signal-to-noise ratio. Figure 3.4 shows how an FT-IR instrument is assembled.

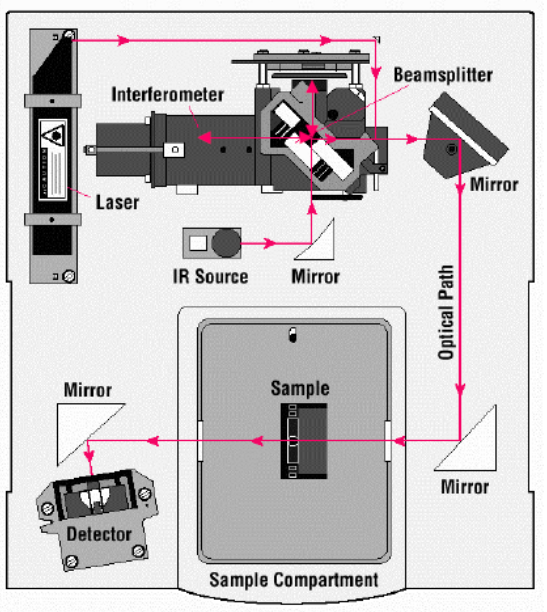

Figure 3.4. FT-IR instrumentation.

One of the ways of measuring FT-IR spectra is attenuated total reflection (ATR). In this case, the sample is pressed on a crystal (usually a diamond, ZnSe, or germanium). The infrared comes to the sample from the interior of the crystal, where an evanescent light is produced at the point where the main beam is reflected. Part of the radiation in the evanescent wave is then absorbed by the sample. This technique is therefore very sensitive to the surface of the material. Figure 3.5 shows the geometry of an ATR acquisition.

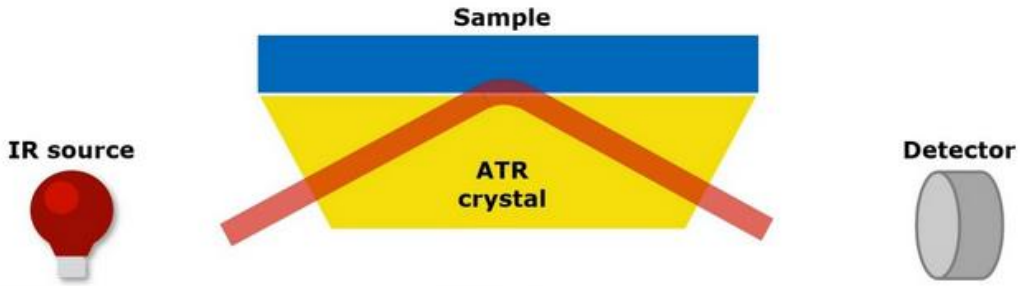

Figure 3.5. FT-IR ATR instrumentation set-up.

When the interaction happens, the molecules stretch and bend modifying the length between the bonds and the angles between the atoms. The stretching of a molecule can be either symmetric or asymmetric (see Figure 3.6). The bending vibrations that can occur are multiple and based on how the atoms move, we can have rocking, scissoring, wagging, and twisting of the molecule.

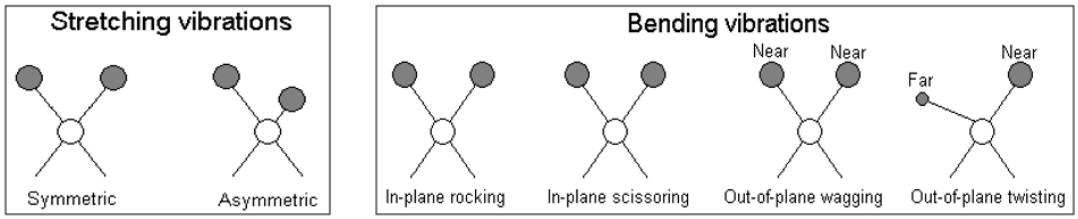

Figure 3.6. Different types of possible vibrations of a molecule that induced by the interaction with infrared radiation.

FT-IR spectra were measured at the laboratory of ISTerre using a Nicolet iS50 FTIR spectrometer in the ATR geometry. A picture of the instrument used is shown in Figure 3.7. A total of four samples were measured, three α-hemihydrate and one β-hemihydrate.

Figure 3.7. Nicolet iS50 FTIR spectrometer, installed at the ISTerre (UGA).

3.1.4. AFM

The atomic force microscope (AFM) was invented in 1985 [183]. The AFM is a high-resolution type of scanning probe microscopy that was developed as an evolution of the scanning tunneling microscope (STM) to provide a method to measure almost any kind of sample (covering many fields from materials science to biology). The potentiality of the AFM technique lies in the possibility to produce images of individual atoms on a surface. The basic concept of the method is to have a tip mounted on a scanning device. During the scan, the tip is almost in contact (0.2-10 nm distance) with the surface of the sample, and the atomic forces between the tip and the surface are used to monitor their interactions. The surface is imaged using a feedback system from the cantilever; this gives the information at the nanometric or Angstrom level depending on the resolution of the microscope. AFMs can be used for topographic imaging, measuring the forces between the sample and the tip and nano-manipulation. Usually, atomic force microscopes are equipped with beam deflection and present this generic set-up: a tip mounted on a cantilever, a laser beam used to sense the cantilever deflection, a feedback loop that detects deflection and position of the tip, a

piezo that moves the sample during the measurement and a way to convert the data into an image. The laser beam points on the top of the cantilever and it is reflected on the position-sensitive detector. Since the AFM method is based on the forces between the tip and the surface of the sample, these forces are also reflected in the images that can be produced. The forces in place between the tip of the cantilever and the sample cannot be calculated directly but they are calculated knowing the stiffness of the cantilever and measuring the deflection thanks to Hooke's law:

$$F = -kz \qquad \text{Eq. 3.1}$$

with F as the force in place, k as the Spring constant, and z as the deflection. When the tip is close to the surface the forces between the two components are repulsive, while when they are further away, there is attraction. When the tip is too far from the surface there is no interaction and therefore no deflection. When the forces are in place, the position of the tip and the deflection are measured by the photo-detector based on the position of the reflected laser beam. Van der Waals interactions are the dominant forces in the range of distances between the tip and sample in which the AFM operates. How these interactions are generated depends on the type of measurement. If the tip is tapping (100-200 nm oscillation amplitude) on the surface or is in contact with it (less than 0.5 nm distance), repulsive forces will be predominant while in non-contact mode (0.5-10 nm distances) there will be the most attractive interaction. The position and the movement of the tip define therefore also the type of imaging. A schematic drawing of the basic set-up of the atomic force microscope is shown in Figure 3.8.

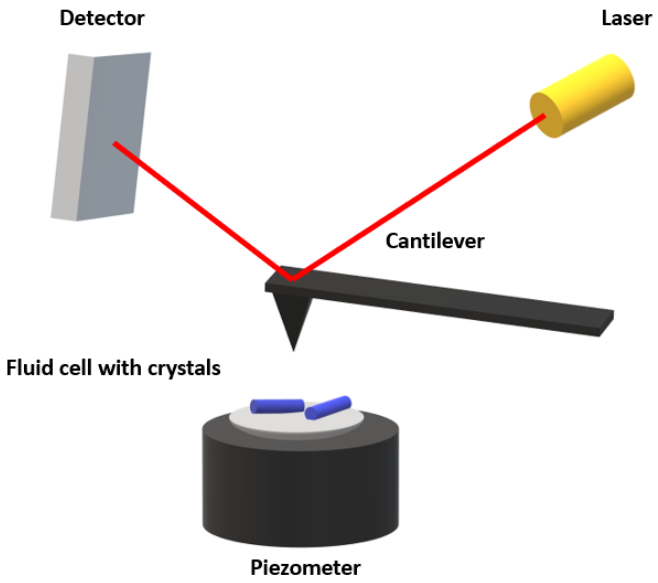

Figure 3.8. Schematic representation of the AFM set-up. A piezometer holds the sample that is attached to the substrate of a fluid cell. On top of the piezometer, the cantilever with the tip is used to scan the surface of the sample. A laser beam pointed on the top part of the cantilever, at the level of the tip, is reflected on a photo-detector that based on the position of the reflected beam produces the image of the surface of the sample.

The resolution that an AFM can achieve depends mostly on the type of piezometer and tip. The shape and size of the probe compared with the features of the surface is also a fundamental parameter to consider, to avoid as much as possible the presence of artifacts. In all cases, since the shape of the probe is never ideal, the AFM pictures will not reflect the exact sample topography.

AFM measurements have been done using an OXFORD MFP-3D Origin+, situated in the ISTerre laboratories. A picture of the AFM used is shown in Figure 3.9.

Figure 3.9. OXFORD MFP-3D Origin+ instrument, installed at the ISTerre institute.

Crystals of α-hemihydrate precipitated in solution were stacked at the bottom of a fluid cell using either mica disks or carbon tape as adhesive substrate. At first, images of the surface of the crystals were acquired in ethanol. This was done to have a reference for the pristine surface of different crystal faces of hemihydrate. The dissolution of the hemihydrate was observed in situ. A 10 mM solution of polyacrylic acid (PAA) and pure water was used to hydrate the hemihydrate crystals and promote their dissolution. The concentration of the solution was chosen by careful adjustment until the most suitable kinetic of dissolution was found. Technical difficulties due to the instability of the crystals on the tape and the fast dissolution rates limited the time of observation of the dissolution dynamics. One dataset of 10 images acquired with a time resolution of 1 minute was recorded. The images were treated with the WSxM software [184].

3.2. Synchrotron-based techniques

3.2.1. ESRF-EBS a fourth-generation synchrotron

The European Synchrotron Radiation Facility (ESRF-EBS) is currently the most brilliant Synchrotron Radiation Source (SRS) in the world. SRSs science is built on the phenomenon of the emission of X-rays from accelerated electrons. The ESRF, and usually each SRS, has four fundamental components: the linac, the booster synchrotron, the storage ring, and the beamlines. The electrons are generated with an electron gun at the start of the linac (linear accelerator). These electrons enter the booster synchrotron which is also an accelerator. Here the electrons are accelerated to an energy of 6 GeV and then passed to the storage ring. In the storage ring, the electrons are maintained at the 6 GeV kinetic energy where they run around the ring at almost the speed of light. The storage ring hosts a series of magnets, undulators, and bending magnets, which deviate the path of the electrons generating the synchrotron radiation. The X-rays generated are then directed to the optics of the beamlines where they are tuned (for example with a monochromator) to be ready for any kind of application. Beamlines are “laboratories” characterized by optics cabins (optic hutches), experimental cabins (experimental hutches), and control rooms.

The X-ray radiation is made of highly energetic electromagnetic waves and the X-rays produced by the ESRF are called “hard” X-rays with a wavelength between 0.10-0.01 nanometres. The high energy associated with X-ray synchrotron radiation is the reason why it is so useful for a wide range of scientific applications. Recently the ESRF went through a big upgrade and in the summer of 2020, it re-started operations as a 4th generation synchrotron under the name of ESRF-Extremely Brilliance Source (ESRF-EBS). The EBS machine upgrade was based on upgrading the storage ring, the HMBA lattice, which is now the leading design for fourth-generation synchrotrons. The new lattice has improved the brilliance of the X-rays of factor 100 compared to before, opening the way to a whole new set of scientific opportunities. The brilliance is defined as photons/sec/ (source area mm2)/ (source angular divergence mrad2). The brilliance, together with coherence and polarization, is one of the fundamental properties of X-rays. The brilliance measures the power of penetrating matter and returning information. Figure 3.10 shows a comparison between the values of brilliance that different X-ray sources can achieve.

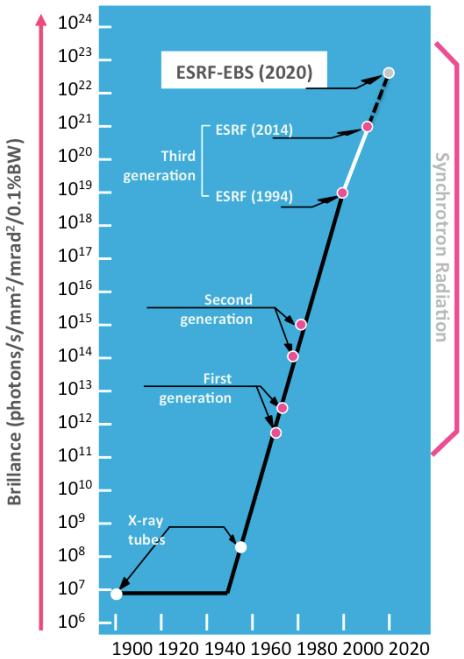

Figure 3.10. Diagram showing how the brilliance of different kinds of X-ray sources varied in time.

Many are the advantages in scientific outcomes related to the EBS upgrade. The new performances of the machine pave the way for a new kind of science starting from biology and soft matter to matter at extreme conditions. A full characterization of man-made materials is the primary aim of materials science. The possibility to perform *in situ* and *in operando* experiments gives us the chance to improve tremendously our understanding of many chemical and physical processes that govern any technical application in society.

The beamlines ID11 and ID22 of the ESRF are part of the Structure of Materials group. Most of the experiments of this thesis have been performed in these two beamlines. The performances of both beamlines were improved by the upgrade, but ID11 was particularly impacted by it. In particular, the flux of the beam incremented 20 times increasing also the speed of the experiments up to 50 times. It was due to these high performances that we could run *in situ* experiments such as scanning 3DXRD and phase contrast tomography with time resolutions of up to a few minutes. This allowed the realization of the core of this Ph.D. project.

3.2.1.1. ID11 beamline of the ESRF

The ID11 beamline of the ESRF is the Materials Science beamline. The beamline is dedicated to both diffraction and imaging studies permitting the investigation of a broad range of systems with many different techniques. Beyond the conventional crystallographic techniques used to characterize the structure of materials such as powder diffraction and single crystal diffraction, many other less common techniques are available at the beamline. For example, at ID11 it is possible to perform diffraction-tomography experiments using 3DXRD, s3DXRD, and diffraction-contrast tomography. But it is also possible to do imaging with conventional tomography. Then there is the possibility as well to perform pair distribution function, diffuse X-ray scattering, and X-ray fluorescence experiments. The possibility to get access to all of these techniques is an extremely useful resource to aim at a complete characterization of a system from different points of view.

The presence of a vast range of techniques requires also a lot of space for technical equipment. This is the reason why ID11 is organized into several hutches (Figure 3.11). When the beam enters the beamline the first thing that it finds is the optical hutch (OH1). OH1 contains the monochromator that is used for the energy/wavelength selection. In OH1 is also present a vacuum transfocator that is used to focus the beam. Once the beam is monochromatic it can enter the first experimental hutch (EH1).

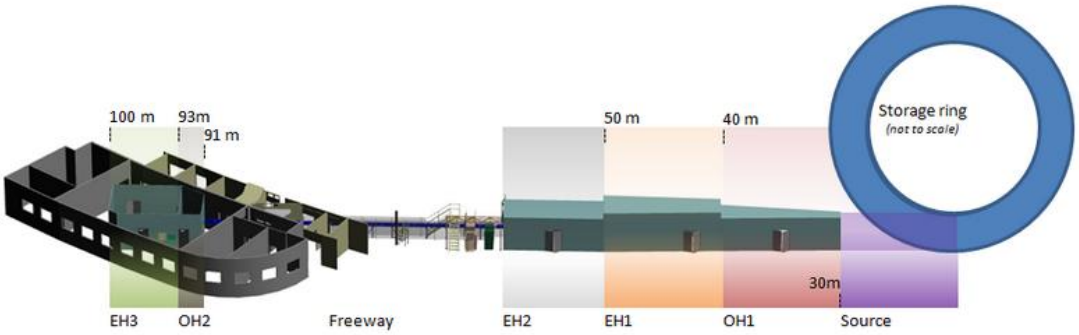

Figure 3.11. Rendering of the disposition of all the hutches that belong to the ID11 beamline.

EH1 contains a diffractometer that can hold heavy samples and sample environment equipment. The detector that is commonly used in this hutch is a 2D detector (a FReLoN camera) suitable for the acquisition of diffraction patterns. Before arriving at the last experimental hutch (EH3), which is where all the experiments of this thesis were performed, the beam crosses a long path through EH2, a piece of a freeway, and the second optical hutch (OH2). OH2 contains two optical systems:

a Kirkpatrick-Baez (KB) mirror and a transfocator (not in vacuum). Finally, the last component of the beamline is the third experimental hutch (EH3), see Figure 3.12.

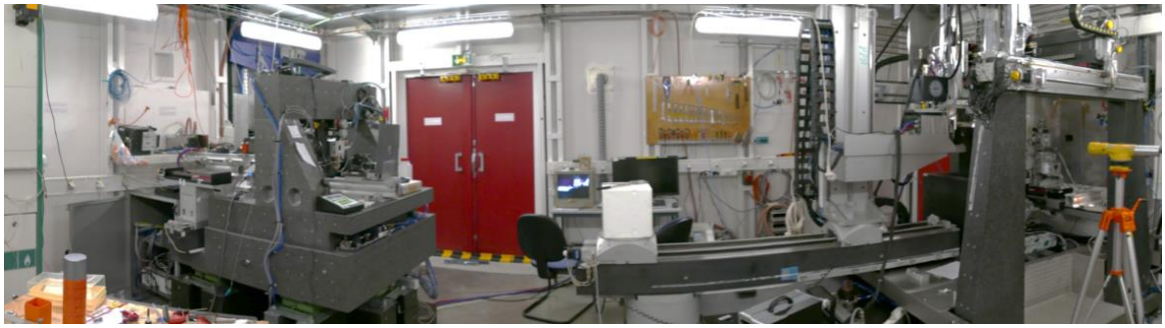

Figure 3.12. Panoramic of EH3 at the ID11 beamline. The beam enters the hutch from the right. The first end-station is the 3DXRD microscope. The second one on the left is the nanoscope.

EH3 is the last experimental hutch of ID11 and it is dedicated to micro-and nano-focusing applications in diffraction and microscopy experiments. EH3 contains two sample stations that permit the focus of the beam to different sizes depending on the type of experiment. Looking at Figure 3.12, the first station from the right is the 3DXRD station. This final installation of the 3DXRD microscope at the beamline was completed in 2009 as a result of more than 10 years of collaboration between the ESRF and the Risø laboratory in Denmark. The motivation for the realization of the 3DXRD microscope was to create a way of characterizing materials in three dimensions in a non-destructive way. In the beginning, the 3DXRD microscope was designed to perform mainly spatially resolved experiments on hard polycrystalline materials, but then it was also optimized for absorption and phase contrast tomography measurements [185] [186]. The sample stage, a motorized goniometer, is placed on top of a Huber diffractometer with a vertical rotation axis. A granite gantry holds a suite of ESRF FReLoN CCD detectors for both imaging and diffraction. A Marana sCMOS detector for imaging is also available.

The second station present in EH3 is the nanoscope station, shown in Figure 3.13. It is a very recently developed equipment for high-energy nano-focused beams. In this station, it is possible to focus the beam to a minimum of 150 nm in the range 40-75 keV. Such small beam sizes are produced using crossed compound refractive lenses (CRL) [187] [188]. When a pair of crossed CRL is used, the beam can be focused in two directions, both vertical and horizontal, resulting in a point-like beam [188]. When the CRL is in place it only accepts 50x50 microns and so it cuts a big part of the incident beam (that is 1x2 mm^2). For this reason, a pre-focusing of the beam can be done with the lenses in OH1. The diffractometer is a hexapod that is mounted on top of an XYZ piezo which is on a rotation stage. The sample stage that is placed over the diffractometer moves with nanometric precision (run out ~40 nm) to be accurate enough to maintain the sample in the center of the beam during the measurements. After focussing with the CRL, the beam passes through a pinhole before the sample. A beam stop is present to protect the detector from direct radiation. The detector is a Dectris Eiger2 4M CdTe. This detector is photon counting and is extremely high performance, reaching count rates higher than 1 million ph/s/pixel. It provides very high sensitivity with almost zero intensity levels for the background and can read out up to 500 images per second. A fluorescence detector is also mounted in the nanoscope station. The fluorescence detector can be used for alignment purposes or the detection of heavy elements [188].

Figure 3.13. Nanoscope station at ID11.

3.2.1.2. ID22 beamline of the ESRF

ID22 is the high-resolution powder diffraction beamline of the ESRF. The leading technique of the beamline is high-resolution powder diffraction (HR-XRPD). The possibility to generate high-resolution data represents a great alternative to single-crystal diffraction when it is not possible to isolate a single crystal from a material. Beyond HR-XRPD, at the beamline, it is also possible to study poorly crystalline materials with pair distribution function (PDF).

The X-rays are generated by an undulator and monochromatized with a channel-cut Si 111 monochromator. Since the beamline is devoted to the powder diffraction technique, the beam size must remain relatively big to illuminate completely the sample. For this reason, usually, the beam arrives at the sample without being focussed. In the experimental hutch of ID22 is placed a diffractometer that spins the sample, which is usually a capillary filled with powders. Figure 3.14 shows a picture of the experimental hutch of ID22. On the left, there is the robotic arm used to change the sample automatically during experiments, and on the right is the diffractometer with the complex system of detection that moves in the 2θ circle.

Figure 3.14. Picture of the experimental hutch of the ID22 beamline.

At the ID22 beamline, the undulator source permits the tune of a wide range of energies (6-80keV) [189]. When the X-ray diffracted radiation is emitted from the sample it hits nine analyzer crystals (Si 111). The X-rays diffracted from the analyzer crystals are then collected by a 2D HCP-detector (Dectris Eiger2 2M). Each high-resolution powder diffraction pattern that is collected from the detector is then summed with the others to generate one diffraction pattern with the software id31sum [190]. A representation of the multi-analyzer stage of the ID22 beamline is shown in Figure 3.15.

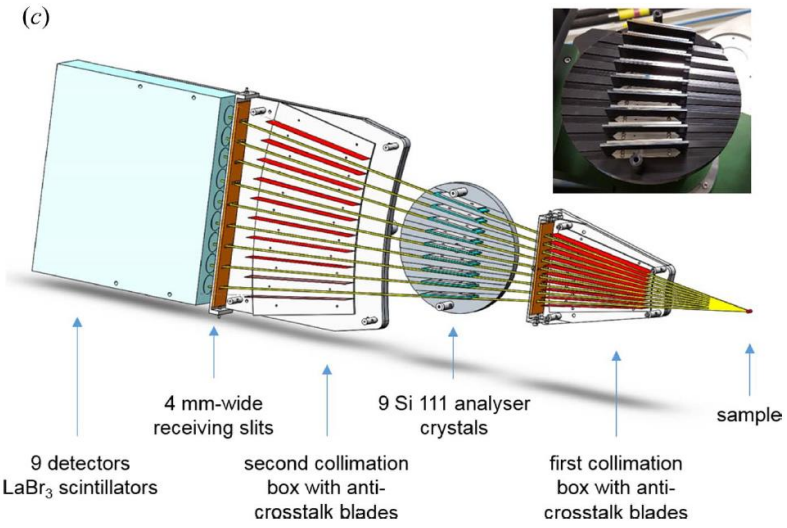

Figure 3.15. Multi-analyzer stage of the ID22 beamline.

3.2.2. X-ray diffraction from crystals

Before digging into the theory of X-ray diffraction (XRD) from crystals, it is useful to understand what defines a crystal and how the atoms are distributed in crystal structures. Crystals are by definition objects that give a sharp diffraction pattern. They can be considered arrays of atoms ordered by translation. The translation of atoms could be in three dimensions, in two dimensions, and even in just one dimension. The smallest element of the arrays of atoms that are repeating by translation is called a unit cell. The unit cell is described with three crystallographic axes (a, b, and c) and the three angles between them (α, β, and γ). The unit cell is expressed using a mathematical concept named Bravais lattice. There are 14 lattices that explain the possible symmetric arrangements of points in 3D space and these are named after Bravais who first enumerated them. Seven crystal systems are used to classify the different Bravais lattices based on the length of the axes and the angles between them [191]. The repetition of the unit cell in the space is described by translations. This is why the structure of a crystal is symmetrical. All the symmetries known can be classified into groups. The groups of symmetry operations without translation are called point groups. The symmetry groups that include translation are called space groups. The Bravais lattice or direct lattice is used to describe the symmetric arrangement of points in real space. The phenomenon of diffraction from a crystal can be instead interpreted using a mathematical transform, the Fourier transform, which results in a reciprocal lattice. The reciprocal lattice permits the observation of the symmetrical properties of the direct lattice. Each node of the reciprocal lattice corresponds to a set of parallel planes in the direct lattice.

The direct lattice is defined with the vector:

$$r_{uvw} = ua_1 + va_2 + wa_3 \qquad \text{Eq 3.2}$$

Where u, v, and w are integers and a_1, a_2 and a_3 are the direct lattice basis vector. The reciprocal lattice vector is given as:

$$G_{hkl} = hb_1 + kb_2 + lb_3 \quad \text{Eq. 3.3}$$

The h, k and l terms are the Miller indices of the plane that is perpendicular to the G_{hkl} vector. The terms b_1, b_2 and b_3 are determined from the direct lattice knowing the volume (V) of the unit-cell in this way:

$$b_1 = \frac{a_2 \times a_3}{V} \quad b_2 = \frac{a_3 \times a_1}{V} \quad b_3 = \frac{a_1 \times a_2}{V} \quad \text{Eq. 3.4}$$

The lattice planes are indicated with the Miller indices. The Miller index of a plane defines where the plane is intercepting the crystallographic axis in the lattice. Miller indices are useful to determine the orientation of the lattice planes in space. A set of planes that have the same hkl values will be characterized by parallel planes of atoms separated by the same d-spacing value. The vector perpendicular to the set of planes hkl will be the G_{hkl} vector.

If we now consider the X-rays that are scattered from a crystal, we consider that many photons will be scattered by the electrons of the atoms situated in different positions. X-ray photons will be scattered in all directions and will therefore undergo either destructive or constructive interferences. To understand how the diffraction from a crystal works, let us consider r_{uvw} and its lattice function L(r). Let us also consider the electron density that the lattice of an infinite three-dimensional crystal would have as ρ(r). The electron density function of the entire crystal would be the convolution of L(r) and ρ(r) (for the whole derivation of the function consult the book "Fundamentals of crystallography" Giacovazzo et al. (2011) [192]). The amplitude of the wave scattered by the entire crystal is the Fourier transform $F_{crystal}(r^*)$. $F_{crystal}(r^*)$ contains the volume of the unit cell (V) and G_{hkl}. The G_{hkl} vectors are vectors such that the structure factor of $F_{crystal}(r^*)$ is non-zero. When these conditions are met, they are called Laue conditions. The $F_{crystal}(r^*)$ that has non-zero values gives rise to the reciprocal lattice. The diffraction intensity in each node of the reciprocal lattice is proportional to the square of the magnitude of the scattered vector [192]. In order to visualize when the Laue conditions are met and be able to measure the diffraction intensity of each node, the sphere or construction of Ewald becomes useful. If we consider placing a crystal in the center of a sphere, namely the Ewald sphere, of radius r=k/λ and irradiate it with an incident beam I, a specific family of planes (hkl) will be diffracted, as shown in Figure 3.16a. The incident beam, after going through the crystal will exit the sphere. The specific point at which the beam touches the Ewald sphere (O) is the origin of the reciprocal lattice that is indicated in light blue in Figure 3.16b. When the Laue conditions are encountered for an orientation of the crystal, which means for a given family of planes hkl (associated to a G_{hkl}), the segment between O and the node of the lattice that is tangent to the sphere (A) will give a vector OA equivalent to $1/d_{hkl}$. Considering CO = 1, we can say that:

$$AO = BO \sin\theta = 2 \sin\theta \quad \text{Eq. 3.5}$$

And since AO is also equal to λ / d_{hkl}:

$$2d_{hkl} \sin\theta = n\lambda \quad \text{Eq. 3.6}$$

This equation is called Bragg's Law. Since this condition will be true not only for G_{hkl} but also for $2G_{hkl}$, $3G_{hkl}$ and so on, the factor *n* indicates that any integer number is included.

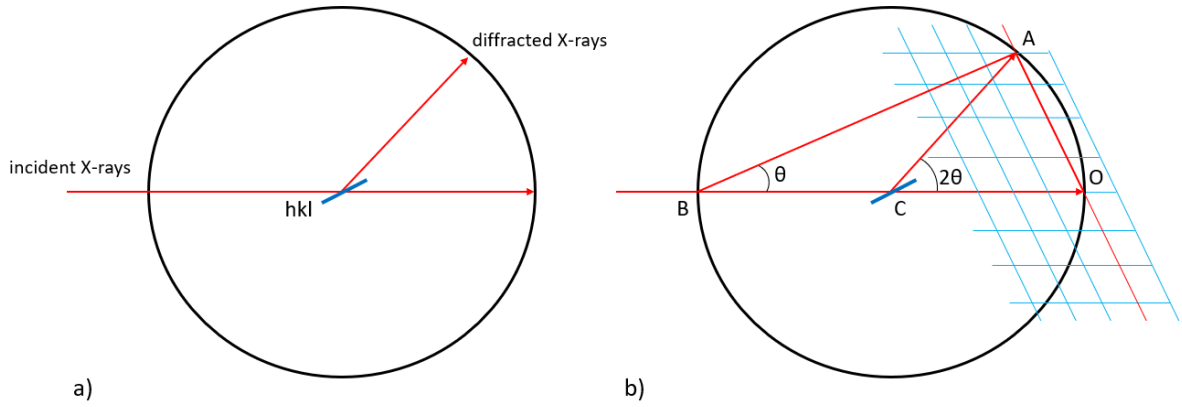

Figure 3.16. Ewald sphere or construction. When the Laue conditions are met, the Ewald sphere permits to construct the reciprocal lattice generated from a crystal.

The diffraction effects generated from a single crystal are easy to understand when picturing the Ewald construction in Figure 3.16. A bit more challenging is the diffraction generated from a collection of crystals, called crystallites, which are randomly oriented in space. If we consider the case of a polycrystalline material, made of many crystals of the same phase, the diffraction pattern will be the sum of many identical diffraction patterns. These X-ray patterns will have the same origin in space but they will be oriented randomly. Figure 3.17 shows how the diffraction pattern that is collected during an experiment changes based on the type of sample. Figure 3.17a shows the pattern that can be produced from a single crystal. Figure 3.17b shows the diffraction pattern that can be obtained by having two crystals with different orientations. Figure 3.17c shows the kind of diffraction pattern that an ideal powder made of infinite crystallite would look like. When many identical diffraction reciprocal lattices are generated from a powder sample, the nodes of the lattice are distributed evenly on concentric spheres. These spheres intercept the Ewald sphere by circumferences with different radii. If we imagine connecting all the points of the circumferences with the center of the reflection sphere, we obtain a series of concentric cones that are called Debye-Scherrer cones.

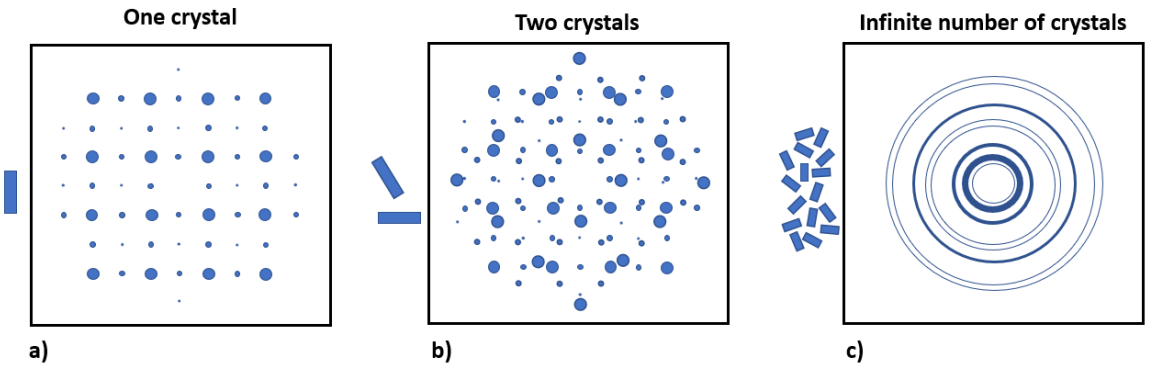

Figure 3.17. Example of the diffraction patterns generated by a) a single crystal, b) two crystals oriented differently in space, and c) an ideal powder made of infinite crystallites oriented randomly.

X-ray diffraction data have always been used to investigate many of the problems in materials science, from the most straightforward questions of phase identification and quantification to more intricate problems such as the determination of stress and strain during in situ experiments. Many of the materials used in our society are polycrystalline (cementitious materials, metals, ceramics,

etc.), which means that most of their properties are due to the nature and behavior of crystals. X-ray diffraction techniques permit unraveling the crystallographic relationships between crystals that are at the basis of the development of many mechanical and chemical properties. Each known crystal structure has a different distribution of atoms from either a chemical or symmetrical point of view. Each crystal structure is therefore associated with a space group and when it diffracts, it generates an X-ray pattern that is its fingerprint. The information that we can extract from an X-ray diffraction pattern is based on the position and intensity of the peaks. The position of the peaks allows us to understand the symmetry and the space group associated with a crystalline phase. The intensity of the peaks depends on many factors, among which is the square of the structure facture (F_{hkl}). Let us consider now selecting a node of the reciprocal lattice generated from the diffraction of a single crystal. The node that we would choose would be generated from the diffraction of a specific set of crystallographic planes hkl and the intensity of that node (I_{hkl}) would be:

$$I_{hkl} = I_0 pKTg(\theta)AF^2{}_{hkl} \qquad \text{Eq. 3.7}$$

The first term I_0 of the equation represents the incident radiation intensity. The term p represents the multiplicity of the reflection (in the case of a single crystal) and depends on the symmetry. K is a scale factor dependent on the experimental conditions and T is the time that the sample was exposed to the X-ray beam. The term g(θ) contains the Lorentz factor and the polarization factor, because the scattered X-rays are polarized. The Lorentz factor considers the time needed for each node to cross the Ewald sphere. The nodes of the reciprocal lattice have finite dimensions therefore the diffraction of a set of hkl planes happens under an interval of Δθ and a finite time. This term is important to understand if a set of planes is affected by defects. A is the absorption factor that considers the amount of radiation that is absorbed by the crystal that depends on the chemistry, shape, and size of the crystal and the energy of the radiation. The F^2_{hkl} is the square of the structure factor. The measurement of the F^2_{hkl} is the starting point for any kind of structural analysis. The value of F_{hkl} is proportional to the magnitude and phase of the (complex) scattered wave from the atoms in the unit cell. F_{hkl} is dependent on the chemical nature of the atoms, their position in the unit cell, and the direction of the diffracted beam. F_{hkl} is equal to:

$$F_{hkl} = \sum f_j \cos 2\pi\,(hx_j + ky_j + lz_j) + i\sum f_j \sin 2\pi(hx_j + ky_j + lz_j) \qquad \text{Eq. 3.8}$$

The term f_j is the atomic scattering factor. The f_j depends on the chemical nature of the atoms j and it is the Fourier transform of the scattering expected from an isolated atom. The scattering factor depends on the scattering angle of the photons and the volume of the electron cloud crossed by λ. The elements inside the round brackets indicate the positions of the atoms inside the unit cell. The fact that with a diffraction experiment we can measure only F^2_{hkl} means that only $|F_{hkl}|$ can be retrieved. This is known as the phase problem. The symmetry that can be observed between the nodes of the reciprocal lattice is called Laue symmetry (e.g. the symmetry of the diffraction pattern). The Laue symmetry is classified into 11 Laue classes. Away from an absorption edge, the atomic scattering factors are real numbers and so |F(hkl)| is equal to |F(-h,-k,-l)|, which is called Friedel's law. This adds an inversion symmetry to the diffraction pattern that might not be present in the crystal structure.

The applications of X-ray diffraction are multiple. For example, X-ray diffraction can be used to solve new crystal structures. When a new structure is solved, it is associated with a crystal group and the atoms in the unit cell are associated with specific crystallographic sites. Phase identification and quantification are probably the most common applications of X-ray diffraction. Phase identification is possible thanks to the databases in which all the patterns of the known structures are stored. The phase quantification can be done on polycrystalline samples using different kinds of methods, the most popular is Rietveld.

X-ray diffraction experiments had an important role in the investigations of this thesis. Different X-diffraction techniques have been coupled to achieve a better characterization of the system. Single crystal µdiffraction (µSXRD) was used to investigate the atomic structure of the hemihydrate synthesized from precipitation. High-resolution X-ray powder diffraction (HR-XRPD) was used to compare the crystal structure between α and β-hemihydrate samples. Scanning 3DXRD (s3DXRD) experiments were performed *in situ* to follow the spatial and crystallographic relationships between the dissolving hemihydrate and the growing gypsum crystals. All the X-ray diffraction experiments were performed at the European Synchrotron Radiation Facility (ESRF) between the beamlines ID11 and ID22.

3.2.2.1. HR-XRPD at ID22 beamline

High-resolution X-ray powder diffraction is a technique that relies on synchrotrons. The reason is the natural high collimation and intensity of the incident radiation and the wavelength tunability that can be achieved with a synchrotron source. At the ESRF, HR-PXRD is available at the ID22 beamline. High resolution is obtained at ID22 using analyzer crystals (Si 111). The analyzer crystals intercept the diffracted X-rays from the sample before they hit the detector. The X-rays are then diffracted a second time by the analyzer crystals at the precise Bragg angle necessary to send the X-rays to the detector [189]. The analyzer crystals select the 2θ angle for diffraction very strictly, resulting in a series of narrow peaks with accurate positions not afflicted by misalignments. The complete powder pattern is obtained by scanning the whole 2θ angle in which the arm containing the analyzer crystals and the detector are mounted (Figure 3.15). Figure 3.18 shows how an analyzer crystal works in detail. The green radiation is the diffracted X-rays that would be produced from a sample ideally placed on the diffractometer axis. The red radiation shows an example of possible displacement of the sample that results in a displacement also of the diffracted beam. The analyzer crystal, which is positioned at the precise Bragg angle needed in the specific case, thanks to an incredibly small tolerance (few arcseconds) ensures a strict definition of the 2θ angle.

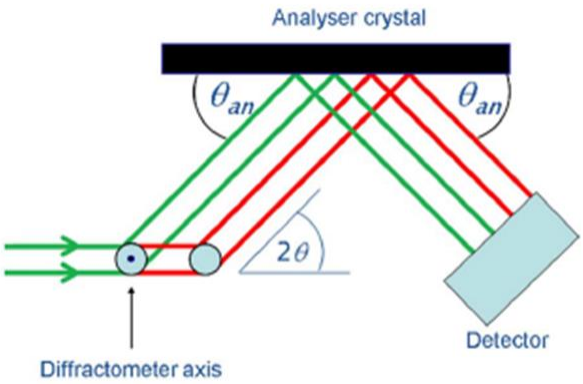

Figure 3.18. Explanation of how an analyzer crystal works. The incident diffracted radiation is diffracted again by the analyzer crystal, placed at a precise Bragg angle, resulting in a high-resolution pattern [189].

Three samples of hemihydrate, two α and one β were measured at the ID22 beamline. The measurements were performed at an energy of 31 keV. The samples were prepared by filling quartz capillaries with hemihydrate crystals. A standard sample made of Si powder was measured to perform instrumental calibration. The calibration and integration have been done using the in-house software developed at the ESRF pyFAI-calib and pyFAI-integrate [193]. The patterns of hemihydrate were analyzed using the software TOPAS5 [194]. Both Pawley fit and Rietveld refinements were performed.

The Pawley fit method, which was derived from the Rietveld method, is a whole powder pattern fitting (WPPF) procedure called cell-restrained. Pawley fitting allows fitting the peak positions of the observed pattern using the cell parameters of a calculated model. This results in a set of extracted intensities that are deduced from the experimental profile [195].

The Rietveld method [195] [196] was invented by Rietveld, Loopstra and Van Laar [197]. The Rietveld refinement aims to overcome the natural problem of the overlapping of reflections arising from a powder pattern. The Rietveld method is based on a mathematical expression that represents that calculates the intensities of the pattern from all of its components:

$$I_c = I_b + \sum I_h \qquad \text{Eq. 3.9}$$

The expression 3.9 considers the contribution from the background (I_b) and all the Bragg peaks of the powder pattern (I_h with h=hkl). Rietveld refinement is a very complex curve fitting problem and Eq. 3.9 depends both on the diffraction experiment (peak profile broadening, unit cell, and so on) and on the crystal structure of the sample (crystallographic sites, occupancies of the sites from the atoms and thermal factors). The least-squares method is used to minimize the refinement to match the calculated pattern with the observed intensities. The minimization is expressed by the formula:

$$M = \sum w\,(I_o - I_c)^2 \qquad \text{Eq. 3.10}$$

The w represents the weight of the variance of I_o which represents the observed intensities of the powder pattern. The quality of the refinements is evaluated by residual functions called factors R. The R factors express the convergence of a refinement scaled by the weighted (R_{wp}) and non-weighted (R_p) intensities. The "goodness of fit", χ^2, is evaluated from the residual functions:

$$\chi^2 = \frac{R_{wp}^2}{R_{exp}} \qquad \text{Eq. 3.11}$$

R_{exp} is the best ideal value of R_{wp} expected. The goodness of the Rietveld refinement will be much higher as χ^2 is close to unity.

3.2.2.2. µSXRD at ID11 beamline

The single-crystal XRD technique is as old as the discovery of the phenomenon of diffraction from a crystal, made by Max Von Laue in 1912 [192]. Since then, this technique has developed substantially, thanks also to the development of always more performing and innovative instrumentations. Considering the most common laboratory set-up for single crystal diffraction, the basic elements that are needed are three: an X-ray tube, a sample holder, and an X-ray detector. Usually, single-crystal diffractometers are equipped with 3 or 4 circle goniometers. In the case of a synchrotron source, the geometry and set-up of single-crystal diffraction experiments are different from the laboratory ones. The experiments for this thesis have been done in the nanoscope station of ID11. The beam was focused to a size of 5 x 7 µm using the CRL lenses. Two crystals of α-hemihydrate were measured. The crystals were glued on the Kapton micro-loop using a small amount of UV glue. The samples were then placed on top of the hexapod. The Eiger2 4M CdTe Dectris detector was used to collect the Bragg peaks. A total of 1440 frames were recorded with an exposure time of 0.25 s during a rotation of 360°. Figure 3.19 shows a diagram of the experimental set-up that was used to perform the experiments.

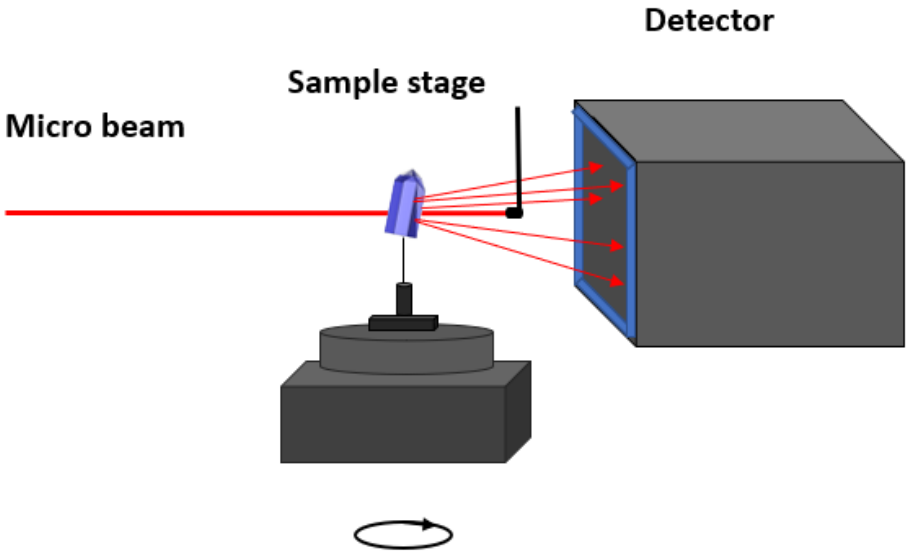

Figure 3.19. Experimental set-up used to perform the experiments of single-crystal X-ray microdiffraction at the ID11 beamline. The beam size used is 5 x 7 µm. The sample is a crystal of hemihydrate glued on a Kapton loop with UV glue. The sample was placed over the hexapod and rotated 360°. The diffraction intensities were recorded with an Eiger2 4M placed at 130 mm from the sample.

The datasets were reduced and interpreted using the software *CrysAlisPro*.

3.2.2.3. S3DXRD at ID11

Scanning 3DXRD is a recently developed X-ray diffraction-tomography technique. It is a variant of the 3DXRD technique that was first developed at the beginning of the 2000s [172]. A simple description of the 3DXRD method could be that it is a complementary technique between the two cornerstones of crystallography, namely single crystal diffraction and powder diffraction. 3DXRD was actually developed at the ID11 beamline of the ESRF together with the 3DXRD microscope. With the EBS upgrade instead, the flux of photons that probe the sample during the experiments is extraordinarily high, opening the possibility to perform also in situ experiments. To perform 3DXRD experiments indeed, a brilliant synchrotron source of X-rays (with energies between 20-100 keV) is required, aiming to provide a fast and non-destructive way of probing polycrystalline materials. The purpose of 3DXRD is to enable a simultaneous characterization of the position, morphology, crystallographic phase, and orientation of each grain of a polycrystalline specimen. Here only the set-ups of the 3DXRD microscope of the ID11 beamline will be discussed. In traditional (far-field) 3DXRD experiments, the monochromatic beam is focused (or constrained by slits) to a cross-section that probes the sample as a uniform field. During the acquisition, the sample needs to rotate around an axis (ω) perpendicular to the beam direction. If the purpose is to have a 3D reconstruction of the entire sample or a portion of it, then the measurement has to be repeated at different z-values. In the case of the ID11 3DXRD station, the far field detector is a FReLoN camera with a pixel size of around 50 µm that can be placed between 20-40 cm. The detector in this case collects the Bragg peaks coming from the polycrystalline sample in Debye-Scherrer pseudo-rings (see Figure 3.20) [198] [172].

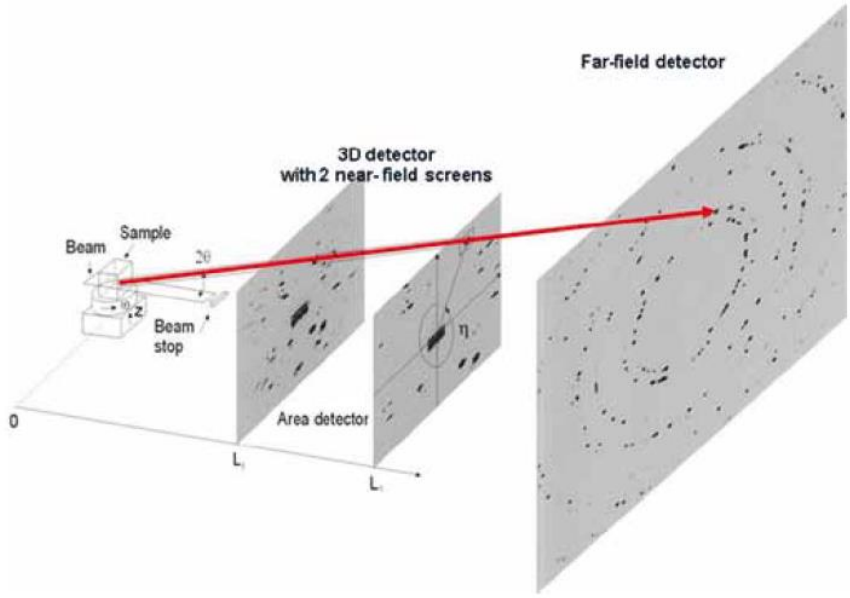

Figure 3.20. Possible set-ups to perform 3dxrd experiments at the ID11 beamline of the ESRF. The beam is focused on a cross-section that probes the sample during a rotation around the ω axis. The set-up with two near-field detectors is not discussed. The far-field approach permits collecting on the detector the Bragg spots coming from the polycrystals in the Debye-Scherrer pseudo-rings arrangement [198].

The most common problem arising from the 3DXRD approach is due to the peaks overlapping. The reconstruction of the single orientation matrices of each grain is indeed based on the position and shape of the diffraction spots in the pseudo-rings collected on the detector. When the specimen is made of a large number of grains, contains mosaicity, or other types of reticular defects, or texture, this can lead to the overlap of some of the reflections. A possible solution to the issue of the peaks overlapping is represented by the s3DXRD modification. In this case, the beam is focused in two directions resulting in a pencil beam (beam size smaller than the average size of the grains). An example of the set-up that would be used for a s3DXRD experiment is shown in Figure 3.21. The specimen is probed by translation of the sample in the x and z direction and rotation around ω. The Bragg spots are collected in the far-field detector [170].

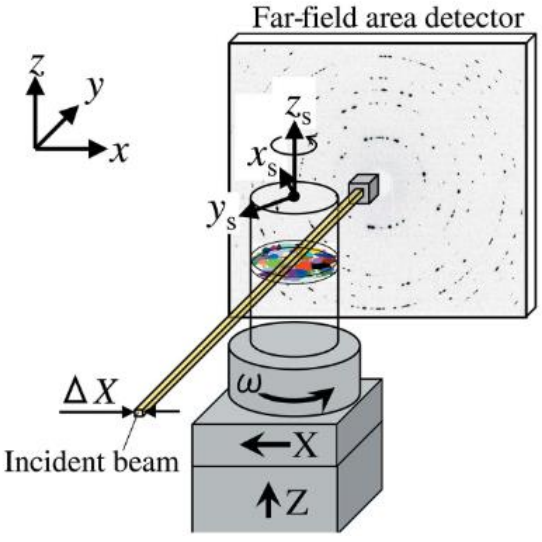

Figure 3.21. Schematic representation of the scanning 3dxrd approach. A pencil beam probes the polycrystalline sample that rotates and translates to collect all the Bragg spots in the far-field detector [170].

In our case, the in situ s3DXRD experiments were conducted in the 3DXRD microscope station of the ID11 beamline. The polycrystalline sample was made by an agglomeration of hemihydrate crystals inside a glass capillary that was hydrated in situ with a solution saturated in calcium sulfate. The α-hemihydrate crystals type obtained by precipitation in solution were chosen to perform the s3DXRD experiments because of the size of the crystals. The average length of the crystals was between 50 and 100 µm with a diameter of roughly 50 µm. The size of the crystals is an important parameter to consider because it influences the quality of the reconstructions from the s3DXRD data analysis. The solution for the hydration was prepared with pure water saturated in calcium sulfate to avoid the rapid dissolution of the hemihydrate crystals and allow the observation of much more detailed development of the dissolution-precipitation process. A monochromatic beam with an energy of 43.575 keV (Nd edge) was focused to a pencil beam size of 5x5 µm. The beam was focused using the CRL. A FReLoN camera, with 2048 x 2048 pixels of 47.2 x 47.2 µm pixel size, placed at a 15.4 cm distance from the capillary (far-field area) was used to detect the Bragg spots. Considering the schematic representation of the s3DXRD method in Figure 3.21, the parameters used are: beam size Δx = 5 µm, angular step for the rotation of the sample $\Delta\omega$ = 1 degree, rotation range $0<\omega<180$ degrees, exposure time s = 0.08 s. Only one layer of the capillary was probed and the scans were acquired by moving the capillary horizontally with a 5 µm translation after each 180 degrees rotation. In total, two complete datasets were acquired, one before hydrating the sample and one after 36 hours of hydration. The choice of acquiring only two datasets was based on the fact that we wanted to calculate the orientation of the hemihydrate crystals before the start of the dissolution, and the orientation of the gypsum crystals when they were grown enough to give good reconstructions.

The data analysis of s3DXRD data is a complex procedure. The fact that this technique is a diffraction-tomography technique, means that all the steps of the data analysis are aimed at retrieving both crystallographic and morphologic information from the same dataset. All the data analysis for the 3DXRD datasets has been done using Jupyter notebooks based on the *ImageD11* software that is part of the *FABLE-3DXRD* suite [199] [200] [201]. Once all the Bragg spots coming from the sample have been collected in the form of 2D images, the peaks need to be extracted and processed. The extraction of the peaks from the detector images is called the “segmentation” process. During the segmentation, the peaks are separated from the background, based on a given tolerance value, and compressed in a list of peaks file. To give a label to each peak, the peaks are determined as connected components in the detector space (a 2D space for each ω) and associated with their center-of-mass coordinates [200]. The center-of-mass coordinates are then transformed into the G vectors. In figure 3.22 the center-of-mass of a few of the G vectors calculated is plotted, namely the position of the peaks in the space. As we can see from the plot, the peaks are arranged into concentric spheres which is a result of projecting the Debye-Scherrer pseudo-rings in 3D.

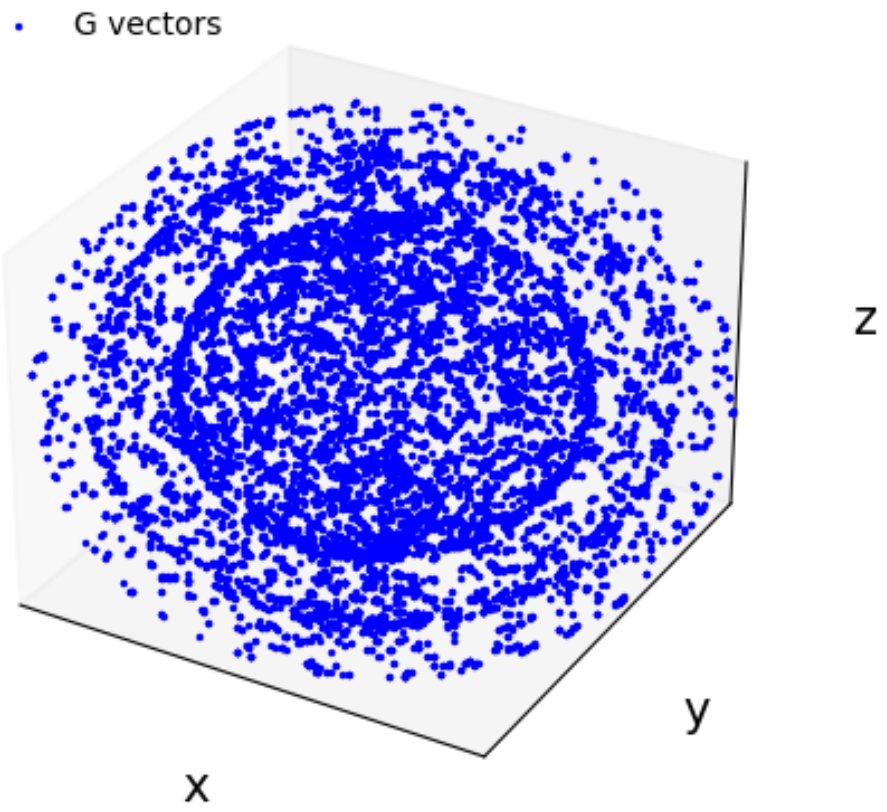

Figure 3.22. Projection in three dimensions of the G vectors calculated from the position of the peaks in the space

When all the peaks of dataset have been extracted they can be transformed in the 2θ-η diagram (azimuthal integration) to check the crystallographic phases present in the sample and choose which rings to use for the indexing of the grains. Figure 3.23 shows the entire segmentation process from the extraction of the peaks on the 2D images of a complete rotation around ω (a), to the sum of the peaks from a complete dataset (b) to eventually the azimuthal integration of the pseudo-powder rings in the 2θ-η diagram (c).

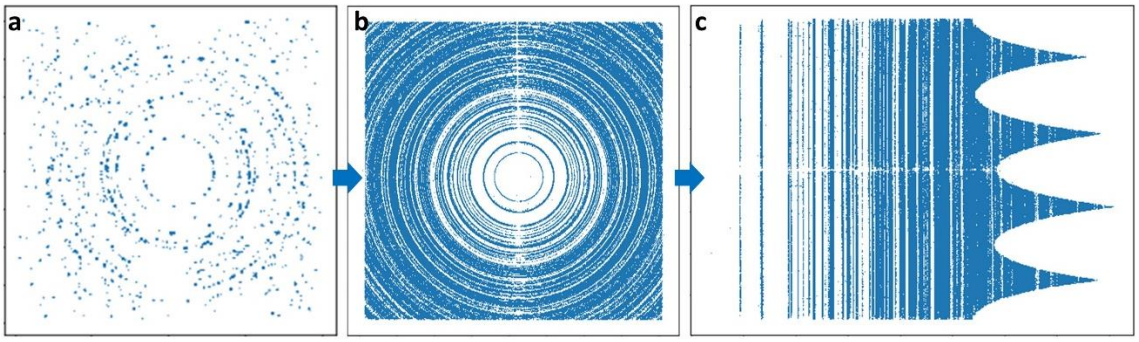

Figure 3.23. The segmentation of the peaks sequence. From the left: a) peaks extracted from one complete rotation ω, b) peaks extracted from a complete dataset, c) azimuthal integration of the pseudo-powder rings into the 2θ-η diagram.

If the crystallographic phase inside the specimen is known, as in the case of this work, then the observed pattern can be compared to a theoretical one. Figure 3.24 reports an example of the comparison between the dataset acquired before starting the hydration process (blue pattern) and the hemihydrate structure (orange lines).

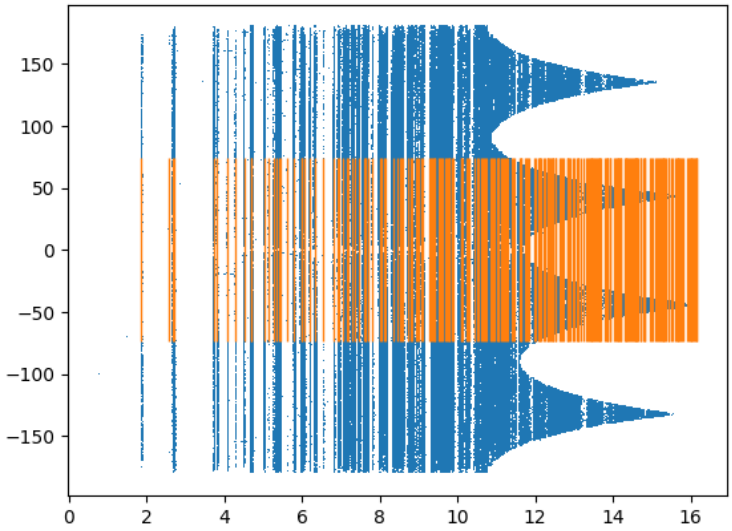

Figure 3.24. Example of the comparison between one of the datasets acquired during one of the scanning 3dxrd experiments in blue, and the calculated rings relative to the hemihydrate structure in orange.

It is often useful to reduce the dataset to a maximum of low 2θ values (around 6) to reduce the number of peaks that have to be associated with a grain. The geometric parameters, such as the sample-detector distance, the beam center, and the tilt of the detector, can be refined and saved in a parameters file that will be used later to refine the position and crystallographic orientation of each grain.

The next step in the data analysis workflow is the indexing process. To perform the indexing, two pseudo-rings can be chosen from the 2θ-η diagram. For each peak on the first ring, the indexing algorithm of *ImageD11* will calculate the angle that it generates with all the peaks in the second ring and checks these against expected values. The algorithm works by comparing the angles between the pairs of G-vectors (diffraction directions) and the angles between the crystallographic directions of the model. The pairs of geometrical correspondent peaks identified are assigned to a specific grain based on a tolerance value which defines how close the (h,k,l) of the peaks are to be integers [200]. At this point, the indexed grains can be accepted or not to be reconstructed depending on the total number of peaks that they index. The two datasets that were processed, presenting two different average sizes of the grains. In the case of the hemihydrate, it was chosen to reconstruct only the bigger grains and to discard the fragments so the minimum number of peaks to assemble the grains was set to 1000. For the gypsum dataset instead, since the grains were smaller in size (between 5-10 µm) and the value of the minimum peaks was set to 200.

The output of the indexing process is a file containing the grains, the center of mass of the grains, the number of peaks, and the orientation matrix (UBI) of each grain. The orientation matrices are called UBI and are the inverse of the traditional UB [201]. The orientation matrices and the positions of the grains in the sample can be refined based on the geometry. The grain orientation has been fitted using the makemap.py script [199]. Subsequently, also the geometry of the system has been fitted based on the indexed grains using the refine_em.py script [199].

At this point, a .map file has been created which contains the refined information about the grains that can be used to reconstruct the morphological and crystallographic information about the sample. The UBIs are 3x3 matrices that link the hkl indices of the crystallographic planes of the grains to their scattering vectors. The rows of the UBIs give the a, b, and c axis vectors in the sample coordinate system. The crystallographic orientations of the indexed grains can therefore be plotted together with their position in the space of the sample. An example of the reconstruction of the

position and orientation of the grains is shown in Figure 3.25. The black spots are the position of the grains in the sample, the red arrows are the vectors relative to the directions of the c-axis in the grains, the blue vectors are the b-axis and the green vectors are the a-axis.

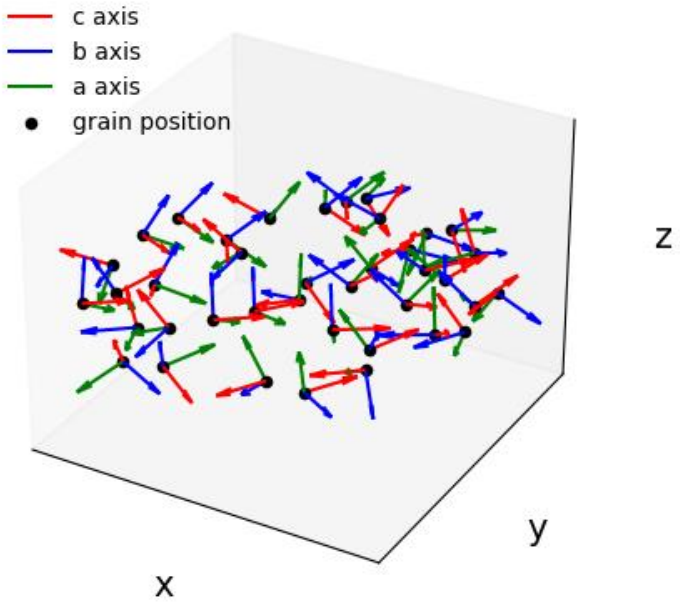

Figure 3.25. An example of the crystallographic information that is achieved from the indexing process of the grains. The blue points are the position of the grains, the red vectors are the c-axis directions, the blue vectors are the b-axis and the green vectors are the a-axis.

The shape of the grains can then be visualized by performing an *iradon* transformation on all the individual sinograms. Figure 3.26 shows the sinogram of one of the indexed grains (a) and its iradon transformation (b). Since many peaks with low intensity, which were not assigned to any grain, remained in the background of the sinogram, the *iradon* image was treated to remove the noise. The peaks in the background were removed by applying an intensity threshold in each pixel. The result of this treatment was a series of cleaned pictures, in which the position and the shape of the grains were reconstructed. In the end, the pictures of the individual grains were summed up to create the final grain maps.

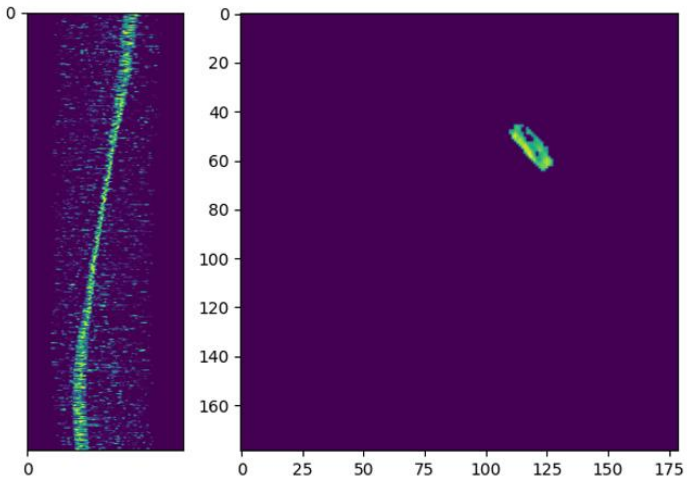

Figure 3.26. From the left: example of the sinogram of an indexed grain and iradon transformation to visualize its shape and position in the sample.

The orientation of the grains can be expressed in many different ways. A 3x3 UB matrix is the algebraic way to express it, but sometimes it can be useful to express the orientation in the form of three parameters. One of the possibilities is to convert the U matrices into Euler angles. In this case, the Euler angles (φ_1, ϕ, φ_2), which explain the rotations around the three axes, were calculated based on the Bunge convention [202]. The transformation from the U matrix to the Euler angles was done using the u_to_euler function of the tools.py [199]. Once the Euler angles were calculated they were used to generate pole figures of the orientations of the grains in the [100], [010], and [001] directions using the ATEX software [203].

3.2.3. X-ray phase-contrast tomography

For the realization of this work, in situ phase contrast tomography (PCT) experiments were also performed. PCT is a particular mode to acquire X-ray tomographic data using a synchrotron source. The principle of phase contrast tomography is to exploit coherent interference fringes that arise as well as the beam absorption. When a sample is placed in front of an X-ray beam, the transmitted beam is collected on a CCD camera. The absorption coefficient of a material (μ) is related to the ratio between transmitted and incident photons by the Lambert-Beer law [204]:

$$I = I_0 e^{-\int \mu(s) ds} \quad \text{Eq. 3.12}$$

where I is the intensity of the transmitted beam and I_0 is the intensity of the incident monochromatic X-ray beam. The result of radiography is the projection of the sample in which the volume probed is projected as a 2D image [205]. However, to acquire tomographic data, the information about the sample must become three-dimensional. To do this, the classic way is to acquire a series of radiographs during a rotation between 0 and 180 degrees or 0 and 360 degrees. The volume of the sample can then be reconstructed using algorithms from the 2D images. The most commonly used algorithm is the filtered back-projection (FBP) [206]. With the FBP algorithm, each projection is back-projected to its angle. Increasing the number of angles, the quality of the reconstructed slice also increases. Independently from the kind of X-ray source (here only the synchrotron set-ups will be discussed), X-ray tomography can be performed in three different ways. The absorption contrast tomography is used when we have strong absorption contrast and the sample is placed very close to the detector, to avoid the propagation of the transmitted beam that would result in the phase effect. With monochromatic beams, the absorption coefficient is related to the grey levels of the images so it is possible to perform quantitative evaluations based on that [205]. Another tomography acquisition method is holotomography. In this case, several acquisitions are done at different sample-detector distances. The treatment of all the projections permits to retrieve the mass density of the sample and permits also three-dimensional analysis of the density of the sample [205]. Finally, the last mode of acquisition is the phase contrast tomography method. The sample in this case is placed farther away from the detector compared with the absorption contrast tomography mode. The contrast due to the retardation in the propagation of the waves is added to the contrast coming from the adsorption leading to a better edge detection inside the sample [205].

3.2.3.1. Phase contrast tomography at ID11

The phase contrast tomography experiments of this thesis were performed at the ID11 beamline of the ESRF. Two *in situ* experiments have been done with small differences in the set-ups. The measurements were done on the 3DXRD microscope station of the beamline.

The first PCT measurements were done in combination with the scanning 3DXRD acquisitions. The two techniques were alternated semi-simultaneously by fast adjustments in the set-up of the beamline. Figure 3.27 shows a representation of the set-up used for the tomography experiments.

The monochromatic beam with energy 43.575 keV (Nd edge) was not focused and presented a size of 1 mm. The sample was mounted on the rotation stage ω and 500 images were collected from the detector at each angle during complete rotations of 360 degrees. The detector that was used to acquire the projections was a CCD camera (FReLoN) with a region of interest (ROI) of 500 x 550 pixels. The detector was placed at a 30 cm of distance from the sample to allow the phase contrast effect. A magnification lens of 7.5 X was used to magnify the projections providing a voxel size of 1.56 µm. The sample was the same one used for the s3DXRD measurement (see Section 3.3.2.3.)

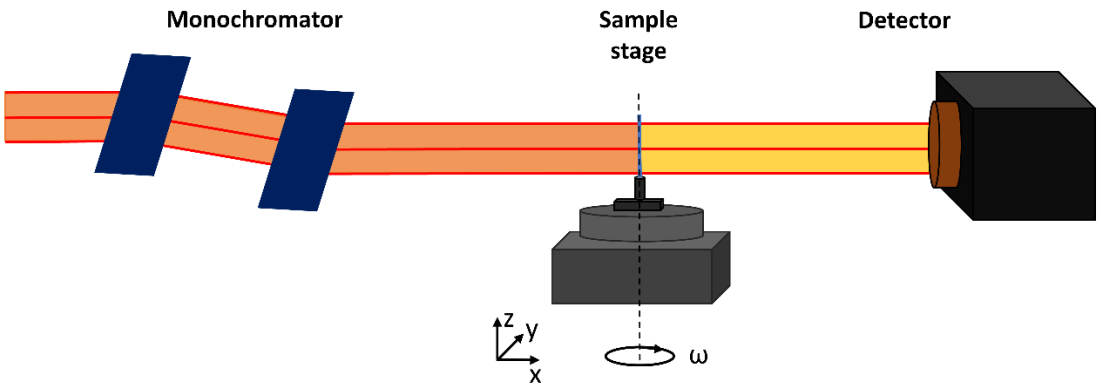

Figure 3.27. Representation of the beamline set-up used to perform the phase contrast experiments. The monochromatic beam enters the experimental hutch of the beamline without being focused by any optical device. The interesting region of the sample is probed entirely while it rotates around ω with a Δω of 1°. The transmitted beam is then collected from the detector.

The experiment was done in situ because we wanted to observe the hydration of the hemihydrate grains, therefore the capillary was hydrated after acquiring the first scan of the dry sample. The solution for the hydration was prepared by mixing pure water with gypsum crystals until supersaturation. Part of the solution was then filtered with a 0.45 µm filter to keep only the Ca^{2+} and $SO4^{2-}$ dissolved in the solution. The decision of using a saturated solution in calcium sulfate was made to decelerate the dissolution of the hemihydrate and enhance the precipitation of gypsum. This allowed us to acquire more scans and have a better idea of the development of the dissolution-precipitation process. The first scan was measured before hydrating the sample. After the hydration, scans were acquired every 30 minutes until 36 hours of hydration and almost complete depletion of the hemihydrate.

The reconstruction of the datasets was done using the ESRF in-house software *Tomwer* and *Nabu*. Figure 3.28 shows the complete pipeline that was followed for the reconstruction of the data from the first to the last steps. All the projections coming from an entire rotation of 360° were loaded into *Tomwer canvas*. First of all, a dark and flat field correction was applied to each dataset. The dark and flat field correction, assuming only transmission effect, is defined in this way [207]:

$$I = \frac{I_{rec} - I_{dark}}{I_{flat} - I_{dark}} \qquad \text{Eq. 3.13}$$

For I_{rec} it is meant the intensity of the full projection collected, with I_{dark} the background coming from the screen of the detector without any beam, and with I_{flat} the intensity of the beam on the detector without the sample in between. *I* is the intensity of the corrected projection. Subsequently, all the projections were aligned in the center of rotation. To find the perfect location of the center of rotation, the software permits superimposing the projections acquired at 0° and 180° and manually moving the images to be perfectly matching. Once the center of rotation is defined, it is possible to finally reconstruct a slice and subsequently all the transversal slices of the sample using the FBP algorithm. In one case the datasets were reconstructed by directly applying

the FBP, in the other, before back projecting the images, also the Paganin algorithm was used [180]. The Paganin algorithm is used to retrieve the phase, which results in an enhancement of the contrast in the images, permitting an easier segmentation of the different components in the sample. In the end, all the transversal slices, one for each voxel row, can be reconstructed allowing the subsequent visualization of the entire volume.

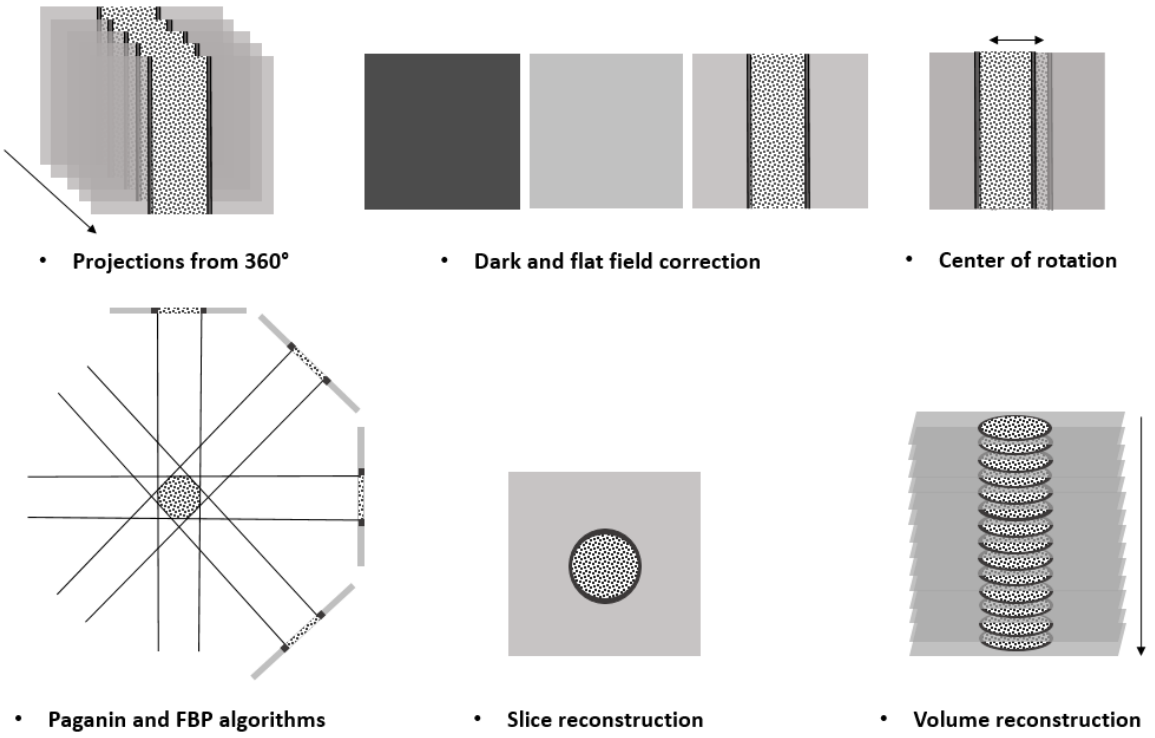

Figure 3.28. representation of the pipeline of the reconstruction of phase contrast tomography data using *Tomwer* and *Nabu*. At first, all the projections of a dataset are loaded, then a correction for the flat and dark field is applied, subsequently, the Paganin and FBP algorithms are used and the slices of the volume of the sample are reconstructed.

Once all the transversal slices of a dataset are ready, they can be loaded into visualization software to perform the segmentation. In this case, the software *Fiji-ImageJ* [208] and *Dragonfly* were used. The segmentation of the sample was done in two different ways to achieve different insights into the hydrating system. In the case of the datasets reconstructed with the Paganin algorithm, a δ/β ratio of 30 permitted to have enough contrast to discriminate between the grains (both hemihydrate and gypsum) and the rest of the system (mainly air and water). This allowed us to segment only the grains and reconstruct their volume over time to monitor the evolution of the microstructure. In the other case, the slices reconstructed without the Paganin algorithm were segmented manually with the ROI painter tool of the Dragonfly software. The purpose was to select a few grains of both hemihydrate and gypsum that were also measured with the scanning 3dxrd to couple the results from the two techniques.

The second series of phase contrast tomography experiments were acquired with almost the same set-up as shown in Figure 30. The detector used in this case was the Marana and an optic lens 20 X was used to magnify the projections. The resulting voxel size was 0.63 µm. The sample was prepared in the same way. Big crystals of α-hemihydrate precipitated in solution (more than 100 µm in length in this case) were used to fill a quartz capillary of 0.3 mm in diameter. The open part of the capillary was covered with quartz wool to prevent the grains from moving during the

hydration with the solution. The solution used for the hydration was prepared with 10 mM of beta naphthalene sulfonate and pure water. The additive was added to tune the hydration reaction. In particular, the goal was to precipitate gypsum crystals with similar shapes and sizes to facilitate the segmentation process. The hydration was performed in situ using a syringe to inject the liquid inside the capillary. A first scan was measured in the presence of dry hemihydrate crystals. After the injection of the solution a scan every 6 minutes was collected until 24 hours of hydration.

The data analysis of these datasets was treated differently in this case compared with the previous one. The reconstruction of the transversal slices of the capillary was done following the same procedure explained in Figure 3.28. The aim of this experiment was to be able to separate the hemihydrate from gypsum during the segmentation process so the datasets were reconstructed using the Paganin algorithm with a high δ/β ratio of 1000. The δ/β ratio was set to a very high value to provide at least a slight contrast between the hemihydrate and gypsum which have almost equal electron density. Once the slices of the sample were produced, the segmentation process was done using Dragonfly. In this case, the tomography data were acquired alone without the need to couple the information coming from tomography with the one extrapolated from the scanning 3DXRD. For this reason, there was no need to segment a specific part of the volume to match the diffraction analysis. After an accurate observation of all the volume in 3D, only a quarter of it was used to perform the segmentation study. This decision was made based mainly on two reasons. The first reason is that we needed a smaller volume to make the segmentation process faster for all the scans that were treated. The second reason instead is that the part of the volume that was chosen presented a smaller amount of quartz wool in the sample, resulting in a more reliable segmentation process. The aim of the segmentation was to be able to distinguish between the hemihydrate and the gypsum grains that were dissolving and growing respectively during the hydration process. Even if the application of the Paganin algorithm created a slight contrast between the two sulfates, it was not possible to achieve a good segmentation only by tuning the parameters of the mask. The Dragonfly software permits to apply supervised machine learning techniques to perform the segmentation task, helping to sort out more complex systems. Here, a convolutional neural network (CNN) [209] U-Net 2.5D was used to train the software in recognizing three different phases in the volume: hemihydrate, gypsum, and background (air plus water). The parameters used to train the CNN U-Net 2.5D in *Dragonfly* are a patch size of 32, a stride ratio of 0.25, 15 epochs, OrsDiceLoss as loss function, and Adadelta as optimization algorithm. Figure 3.29 shows the procedure used to train the neural network that successfully brought the separation of the three components of the sample.

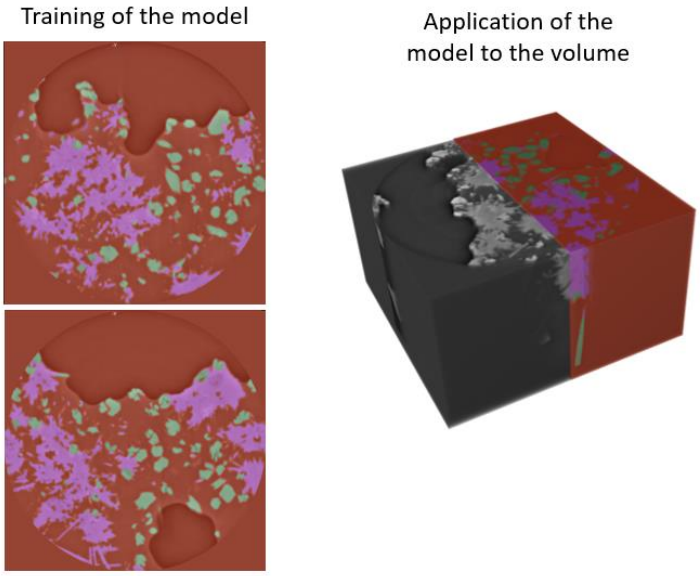

Figure 3.29. Workflow of the AI segmentation done with Dragonfly to discriminate between three phases: the hemihydrate crystals in green, the gypsum crystals in purple, and the background in red. The model has been trained by hand segmentation of a few frames.

4. Results and discussions

4.1. Pre-characterization of the samples

All samples used in the experiments of this thesis have been pre-characterized with SEM, TGA-DSC, and FTIR. Here, the methods used to synthesize the hemihydrate samples used and the results of their pre-characterization are reported.

4.1.1. Synthesis methods

Four samples of hemihydrate (three α-hemihydrate and one β-hemihydrate) were used to perform all the experiments reported in this manuscript. The procedures used to synthesize the α-hemihydrate samples and to produce the β-hemihydrate are described below.

- Precipitation of hemihydrate:

Calcium sulfate hemihydrate was produced from precipitation by a chemical reaction at 90°C. To obtain a final concentration of 60 mM of $CaSO_4$, a supersaturated solution of calcium sulfate was prepared by mixing two 1 M solutions of $CaCl_2{\cdot}2H_2O$ (Roth®, > 99 %) and Na_2SO_4 (Roth®, > 99 %) with a 5 M aqueous solution of NaCl. The procedure used is the same as described by Ossorio et al. (2014) [112]. All the solutions were heated at 90°C before proceeding with the mixing. The solutions were mixed in a glass bottle. After mixing, the final solution was placed in the oven at 90°C for a few hours. The precipitate was filtered using a vacuum pump system. A 0.44 µm filter of cellulose was used.

- Dehydration of gypsum in solution:

Calcium sulfate hemihydrate was obtained by heating gypsum in solution. Gypsum was precipitated at room temperature by mixing two 1 M solutions of $CaCl_2{\cdot}2H_2O$ (Roth®, > 99 %) and Na_2SO_4 (Roth®, > 99 %), to obtain a final concentration of 200 mM $CaSO_4$. After the precipitation of $CaSO_4{\cdot}2H_2O$ crystals, the solution was placed in the oven at 90°C while stirring for one night. The precipitate, which was transformed into calcium sulfate hemihydrate, was filtered with the same vacuum pump system described for the previous production method.

- Calcination of gypsum:

Calcium sulfate hemihydrate was produced by heating gypsum in a kiln at roughly 150°C. The procedure was done in dry conditions.

The details of the four samples are listed in Table 4.1. The name associated with each sample will be used throughout the chapter.

Sample name	Production method	Origin	Hemihydrate type
Sample 1	Precipitation of hemihydrate (wet)	Own synthesis	α
Sample 2	Precipitation of hemihydrate (wet)	Own synthesis	α
Sample 3	Dehydration of gypsum in solution (wet)	Own synthesis	α
Sample 4	Calcination of gypsum (dry)	BASF	β

Table 4.1. Classification of all the samples for the experimental part of this PhD project.

4.1.2. SEM results

The samples obtained with the syntheses and from the BASF industry were observed with the SEM for pre-characterization. The SEM pictures of Figure 4.1a-b are relative to Sample 1 which was used to perform the combined *in situ* s3DXRD and PCT experiment (section 4.3). The crystals were ground for experimental purposes. For this reason, several crystals appear fragmented. Nevertheless, for the majority of the crystals, it is possible to see the classic α-hemihydrate shape characterized by euhedral crystal habit and pencil shape. Figure 4.1b shows the detail of one large crystal with a size larger than 100 µm. The SEM pictures of Figure 4.1c-d are relative to Sample 2 which was used to perform the *in situ* PCT and AFM experiments (section 4.4) and the HR-XRPD experiment discussed below in this section (section 4.2). The crystals present the α-hemihydrate shape. Several crystals form agglomerates and their length and size are variable.

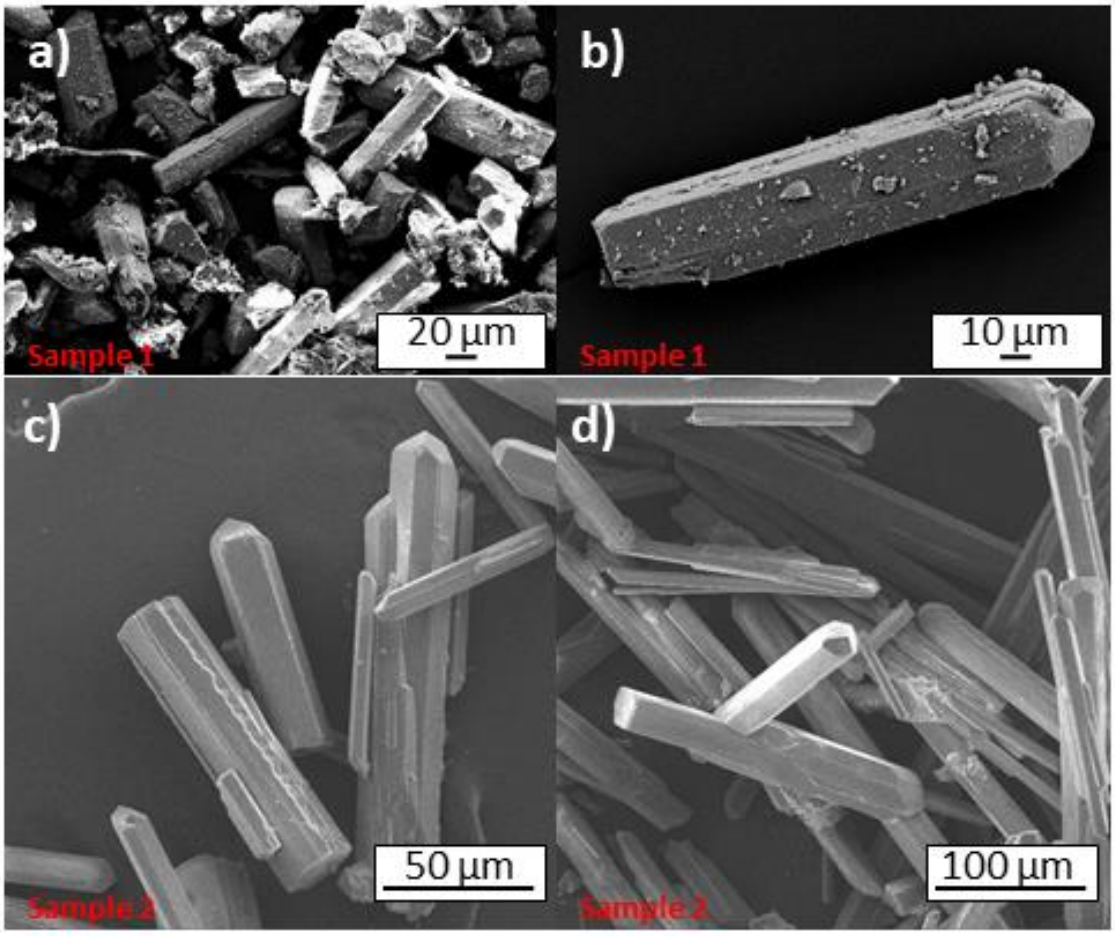

Figure 4.1. a) and b) SEM pictures of Sample 1. c) and d) SEM pictures of Sample 2.

The pictures in Figure 4.2 are relative to Sample 3 which was used for the HR-XRPD experiment. The first detail that is evident from Figure 4.2a is the presence of different sizes of crystals. The crystals present the typical α-hemihydrate shape. Figure 4.2 b shows the detail of one large crystal. In this picture, it is possible to observe very clearly one side of the tip of the crystal, showing also three of the crystallographic facets that compose the hexagonal habit.

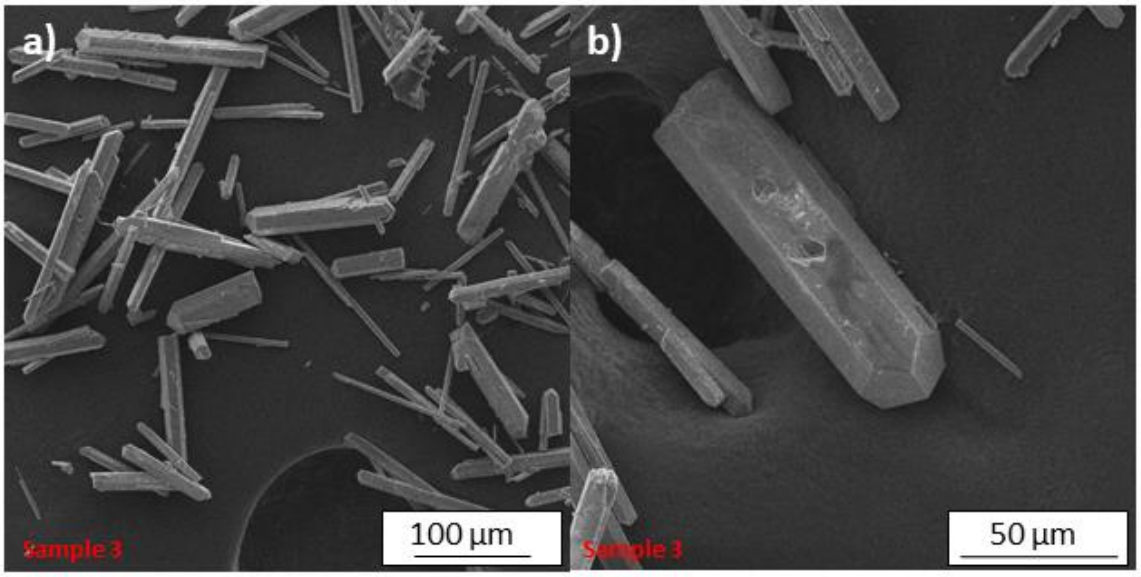

Figure 4.2. a) and b) SEM pictures of Sample 3.

The crystals shown in Figure 4.3 belong to Sample 4, which was used to perform the HR-XRPD experiment. The crystal habit is mostly anhedral as the crystallographic facets are not well distinguishable. The presence of fragments is also peculiar to the β-hemihydrate form as the fragility of the crystals brings to their fragmentation. The result of the fragmentation is the presence of crystals with several different sizes as shown in Figure 4.3b. All the crystals are surrounded by smaller fragments that seem different from the larger β-hemihydrate fragments. This could be due to the presence of impurities associated with the production process.

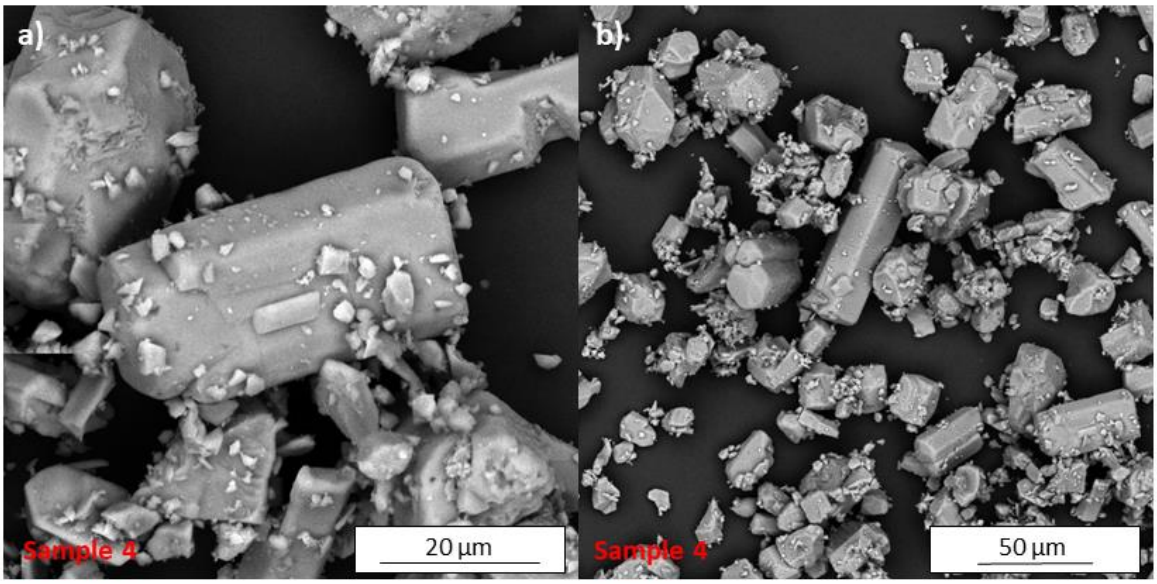

Figure 4.3. a) and b) SEM pictures of Sample 4.

4.1.3. TGA-DSC results

TGA-DSC analyses have been done on the four samples of hemihydrate to observe their behaviour during heating and to calculate the water content associated with weight loss. Figure 4.4 shows a plot of both the TGA (blue) and DSC curves (red) of all the samples. For all the samples the weight

loss associated with the dehydration of hemihydrate was calculated between 40°C and 400°C, which is the region of the main weight decrease. The region of the curves below 40°C was not considered because the weight loss that takes place there is likely to be due to the removal of adsorbed water. Sample 1, Sample 2, and Sample 3 show the same behaviour. The weight loss associated with the dehydration of hemihydrate occurs in the same temperature interval (between 40-400°C). The DSC curves of Sample 1, Sample 2, and Sample 3 show two downward peaks, the first at (92°C) and the second at (272°C). The downward peaks represent endothermic reactions, which in this case coincide with the dehydration reaction of the hemihydrate. The rest of the DSC curves represent exothermic heat change. This could be due to the phase transformation that takes place when the hemihydrate is transformed into anhydrite. The TGA curve of Sample 4 reflects faster dehydration compared with the other samples. The dehydration, in this case, occurs in a lower temperature range, between 40 and 300°C. The DSC curve presents one downward peak at 130°C and a shoulder at 90°C.

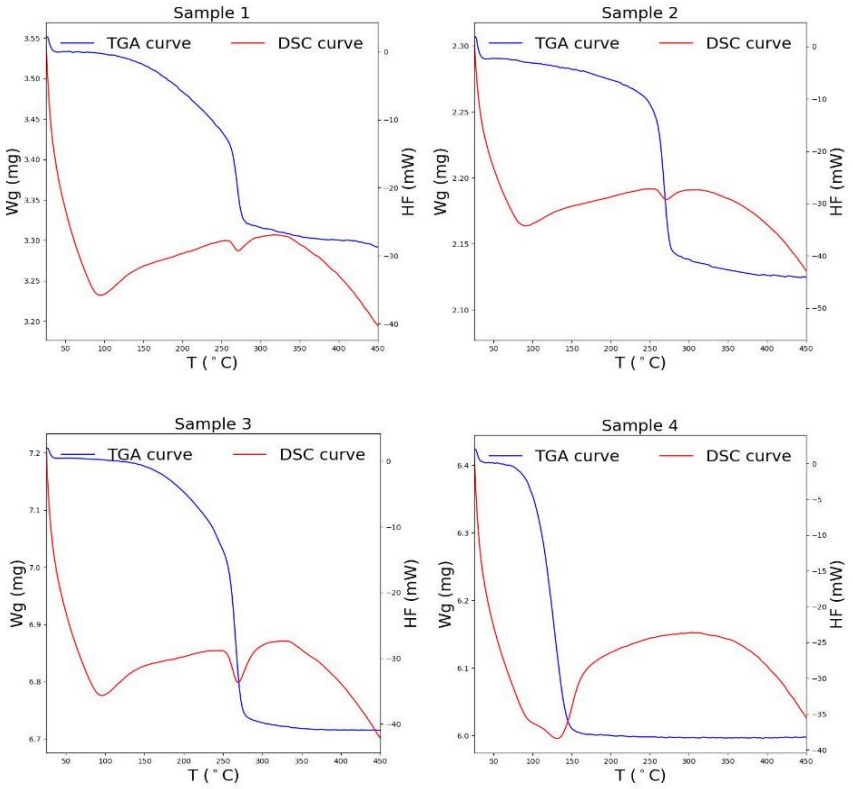

Figure 4.4. TGA-DSC curves of Sample 1, Sample 2, Sample 3, and Sample 4.

From the weight loss associated with the dehydration of the hemihydrate samples, it is possible to calculate the molecules of water contained in the four compounds. The percentage of water (Wat) contained in the hemihydrate with 0.5 molecules of water per formula ($CaSO_4 \cdot 0.5H_2O$) is equal to Wat=6.2 %. For each sample, we can calculate the weight loss ($WL_{0.5}$) that would be associated with the loss of 0.5 molecules of water with this equation:

$$WL_{0.5} = (6.2 \times W_{start})/100 \qquad \text{Eq. 4.1}$$

Knowing $WL_{0.5}$ and the real weight loss (WL_{obs}) observed between 40 and 400°C, we can calculate the molecules of water lost by each sample. The calculated values of water molecules X contained in the four samples are reported in Table 4.2.

Sample	W_{start} (40 °C)	$WL_{0.5}$ (40-400 °C)	WL_{obs} (40-400 °C)	X ($CaSO_4 \cdot XH_2O$)
Sample 1	3.533 mg	0.219 mg	0.233 mg	0.53
Sample 2	2.290 mg	0.142 mg	0.164 mg	0.58
Sample 3	7.190 mg	0.446 mg	0.475 mg	0.53
Sample 4	6.404 mg	0.397 mg	0.407 mg	0.51

Table 4.2. Values used to calculate the molecules of water contained in the four samples of hemihydrate. The values of W_{start} and X are taken from the TGA measurements.

4.1.4. FTIR results

FTIR spectra of the four hemihydrate samples have been collected and reported in Figure 4.5. Each spectrum shows absorption bands in the regions of scissoring of water (around 1596 cm^{-1}), OH-stretching of water (3652 and 3756 cm^{-1}), and in the region associated with the vibration of SO_4^{-2} (around 1000-1200 cm^{-1}). The regions marked as "ATR" in the plots indicate the noise due to the measurements in attenuated total reflection (ATR) mode. All the spectra are in agreement with previous FTIR spectra reported in the literature for both α and β-hemihydrate (Bensted and Varma, 1971) [211]. All the samples show the features associated with calcium sulfate hemihydrate without a visible contribution from gypsum, as the presence of gypsum would have generated an additional peak at 1690 $cm^{-1,}$ and the presence of three or four peaks in the region of the OH-stretching of water [132]. Sample 1, Sample 2, and Sample 3, which are relative to the α-hemihydrate, do not show clear absorption bands in the region of the OH-stretching of water. This suggests that in the case of the α-hemihydrate samples, the water is not fully ordered in the crystallographic sites. Sample 4, which is identified as β-hemihydrate, shows two distinct peaks in the region of the OH-stretching of water, suggesting a more ordered structure compared with the other samples.

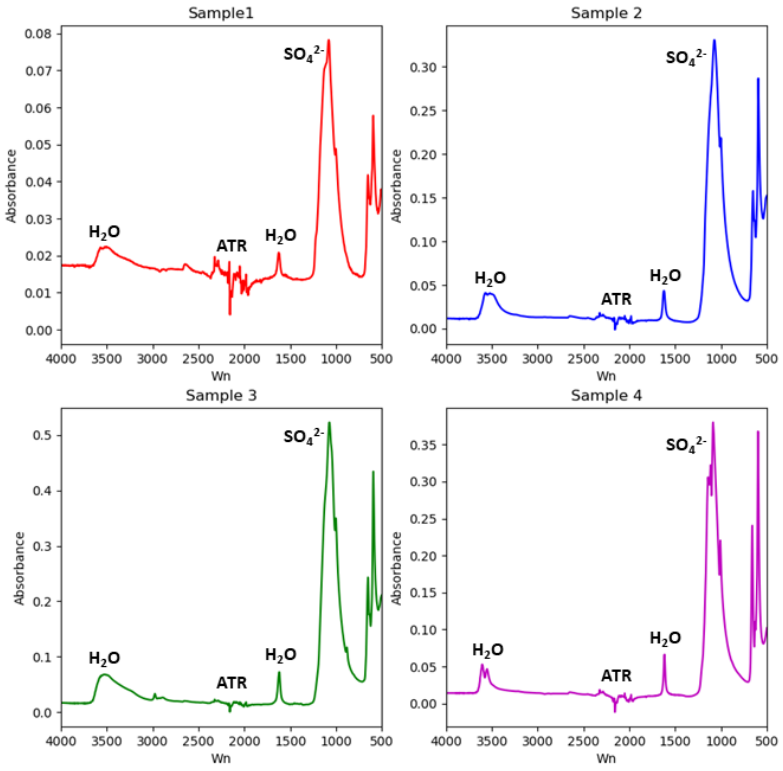

Figure 4.5. ATR FTIR spectra of Sample 1, Sample 2, Sample 3, and Sample 4.

4.2. Crystallographic structure of α and β-hemihydrate

In this section are reported the results and discussions about the investigations on the crystallographic differences between α and β-hemihydrate. The samples that were used to perform the experiments are Sample 2, Sample 3, and Sample 4. The results and discussions are relative to the HR-XRPD and µSXRD measurements.

4.2.1. HR-XRPD results

Samples 2, 3, and 4 have been measured with HR-XRPD in order to investigate the possible presence of structural differences between hemihydrates produced in different ways. Figure 4.6 shows a plot of the three patterns, with Sample 2 (α-hemihydrate) in red, Sample 3 (α-hemihydrate) in blue, and Sample 4 (β-hemihydrate) in green. Figure 4.6b shows the three patterns in the interval 2.2-15 2θ°. The first thing that is visible from this plot is the difference in intensity between Sample 4 and the other two samples. The zooms of the patterns in Figure 4.6a and c are relative to the regions between 3.75-3.86 2θ°, and 7.45-7.7 2θ° respectively. In these two selected areas, it is possible to see in detail the strong differences between the two α-hemihydrate samples (Sample 2 and 3) and the β-hemihydrate (Sample 4). In the case of the α-hemihydrates, the reflections are split and show a "triplet" of peaks. In the case of Sample 3 the three peaks are slightly more symmetric and intense compared with Sample 2, which appears less crystalline and probably more disordered. Sample 4 presents only one intense peak whereas the other two samples present three.

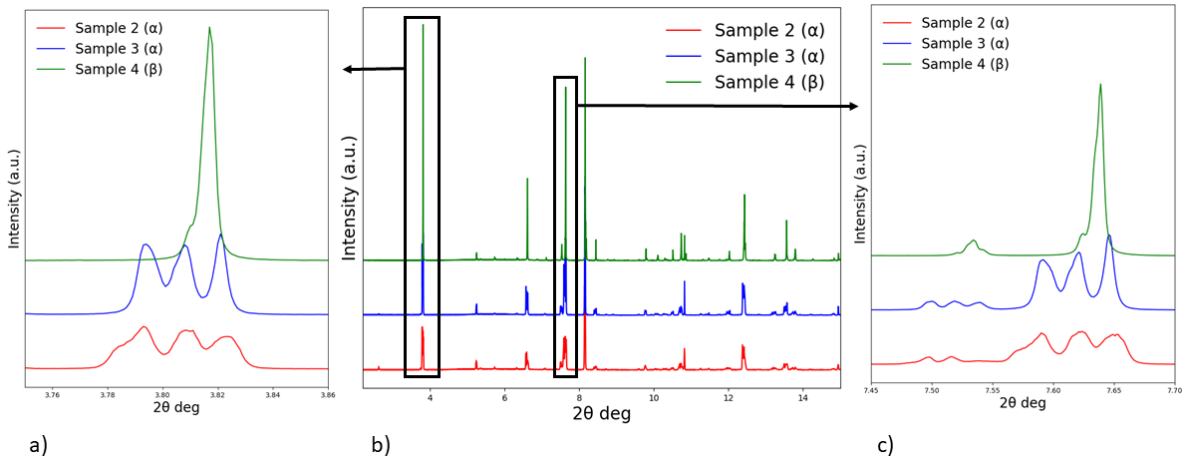

Figure 4.6. HR-XRPD patterns of Sample 2 (red), Sample 3 (blue), and Sample 4 (green).

To first evaluate them, the three patterns were plotted together with the patterns of Ballirano et al. (2001) [8] (I2 space group with $CaSO_4 \cdot 0.5H_2O$ formula) and Schmidt et al. (2011) [10] ($P3_221$ space group with $CaSO_4 \cdot 0.625H_2O$ formula) in Figure 4.7. In order to make all the patterns comparable they were transformed into q space and the intensities of Sample 2, Sample 3, and Sample 4 were divided by 100. The pattern relative to the monoclinic hemihydrate (I2) from Ballirano et al. (2001) [8] is represented in black and the pattern relative to the trigonal hemihydrate ($P3_221$) from Schmidt et al. (2011) [10] is in yellow. From Figure 4.7a, Sample 2 (red) and Sample 3 (blue) show no similarities with the literature patterns. In the case of Sample 4 (green), the position of the peak in the region 1.04-1.05 2θ° could be similar to the black pattern, suggesting a possible I2 setting of the unit cell of the sample.

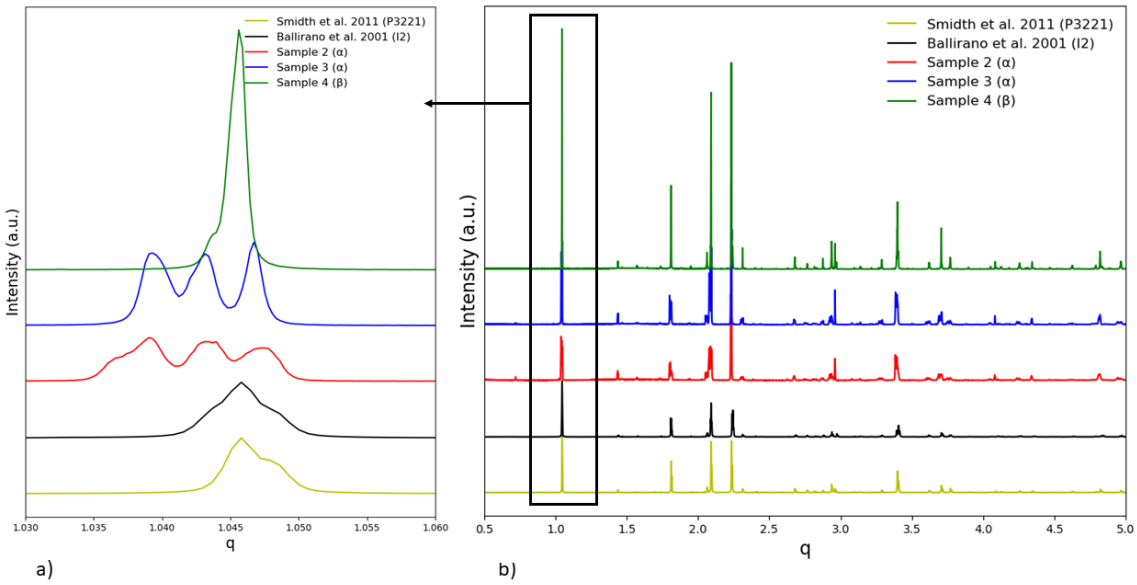

Figure 4.7. Comparison between the HR-XRPD patterns of Sample 2 (red), Sample 3 (blue), ans Sample 4 (green) with the pattern of the I2 hemihydrate from Ballirano et al. (2001) [8] (black), and the $P3_221$ hemihydrate from Schmidt et al. (2011) [10] (yellow).

Rietveld refinements were performed on the patterns of Sample 2, Sample 3, and Sample 4. Preliminary Pawley refinements were performed to check if the samples were presenting monoclinic or trigonal cell settings. All three samples resulted to be monoclinic.

The result of the Rietveld refinement of Sample 2 is reported in Figure 4.8. The refinement was performed using three I2 structures [8]. The three structures were added to the refinement step by step. The cell parameters were refined for each structure, and equal isotropic displacement parameters for equal atoms were also refined. The atomic positions and occupancies of the atoms were not refined except for the atomic positions and occupancy of water. The refinement, after adding the third I2 structure converged to R_{wp}=11.8. The refinement was performed in the range 2.2-37 2θ°. Figures 4.8a and b report the results of the refinement of Sample 2 in the range 3-9 2θ° and 10-20 2θ° respectively. The red curve is the calculated pattern, the blue curve is the observed pattern and the difference between them is reported in grey. The three I2 hemihydrate phases' contributions are reported in Figures 4.8c and d. The contribution from Hemihydrate 1 (25.01 %) is reported in blue, the contribution from Hemihydrate 2 (39.83 %) is reported in black, and the contribution from Hemihydrate 3 (35.16 %) is reported in green. The cell parameters, the occupancies of water, and the R factors, for each of the three contributions of Sample 2 are reported in Table 4.3.

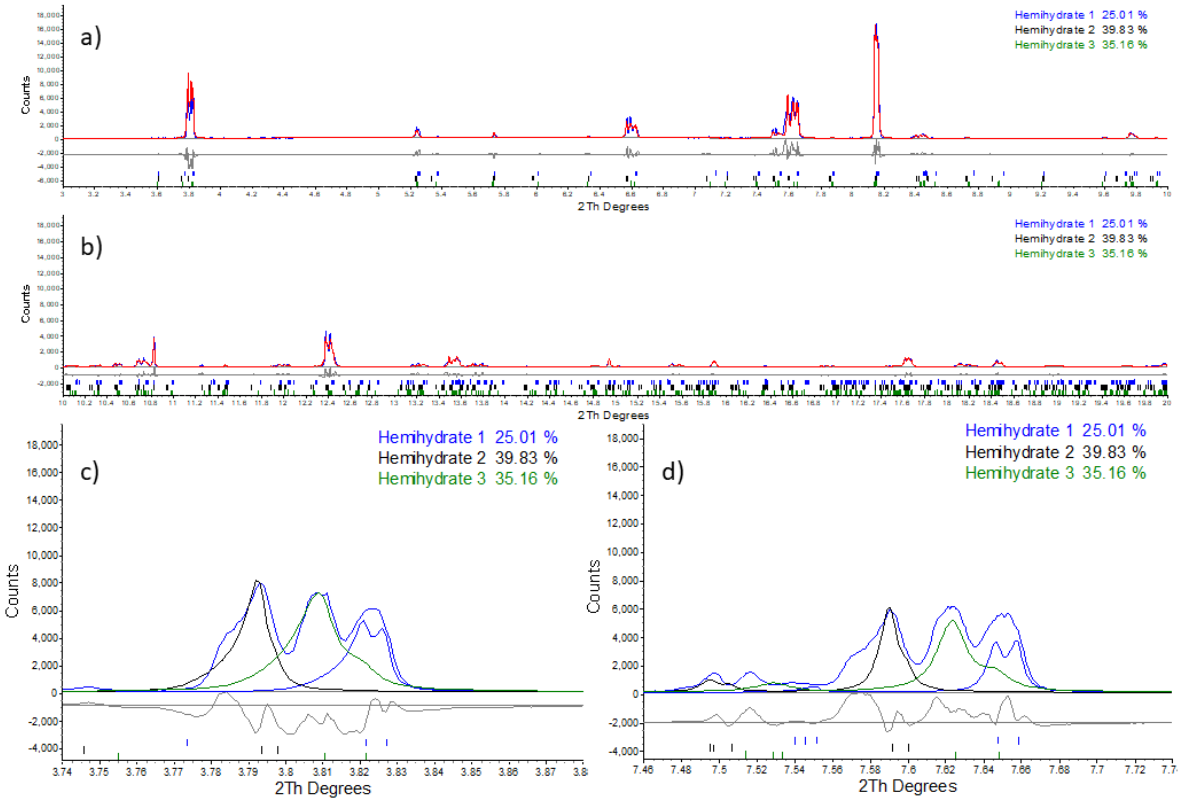

Figure 4.8. Rietveld refinement result of Sample 2. The observed pattern is plotted in blue, the total calculated pattern is reported in red, and the single contributions to the calculated pattern are reported in black, green, and blue. The difference between the calculated and the observed patterns is reported in grey. a) Refinement results in the interval 3-9 2θ°. b) Refinement results in the interval 10-20 2θ°. c) Refinement results in the interval 3.75-3.88 2θ°. D) Refinement results in the interval 7.46-7.7 2θ°. R_{wp}=11.8, R_{exp}=1.9, gof=6.2.

Sample 3 was refined using the same strategy that was used for Sample 2. In this case, after adding the third I2 component to the refinement, the R_{wp} decreased to 13.5. The results of the Rietveld refinement of Sample 3 are shown in Figure 4.9. The low-angle refinement (range 3-9 2θ°) and the high-angle refinement (range 10-20 2θ°) results are reported in Figures 4.9a and b with the calculated pattern in red, the observed pattern in blue, and the difference in grey. The three hemihydrates I2 contributions were called Hemihydrate 1, Hemihydrate 2, and Hemihydrate 3. The three contributions are shown in Figure 4.9c and d. Hemihydrate 1 (32.76 %) is shown in blue, Hemihydrate 2 (34.96 %) is shown in black, and Hemihydrate 3 (32.37 %) is shown in blue. The cell parameters, the occupancies of water, and the R factors, for each of the three contributions of Sample 3 are reported in Table 4.3.

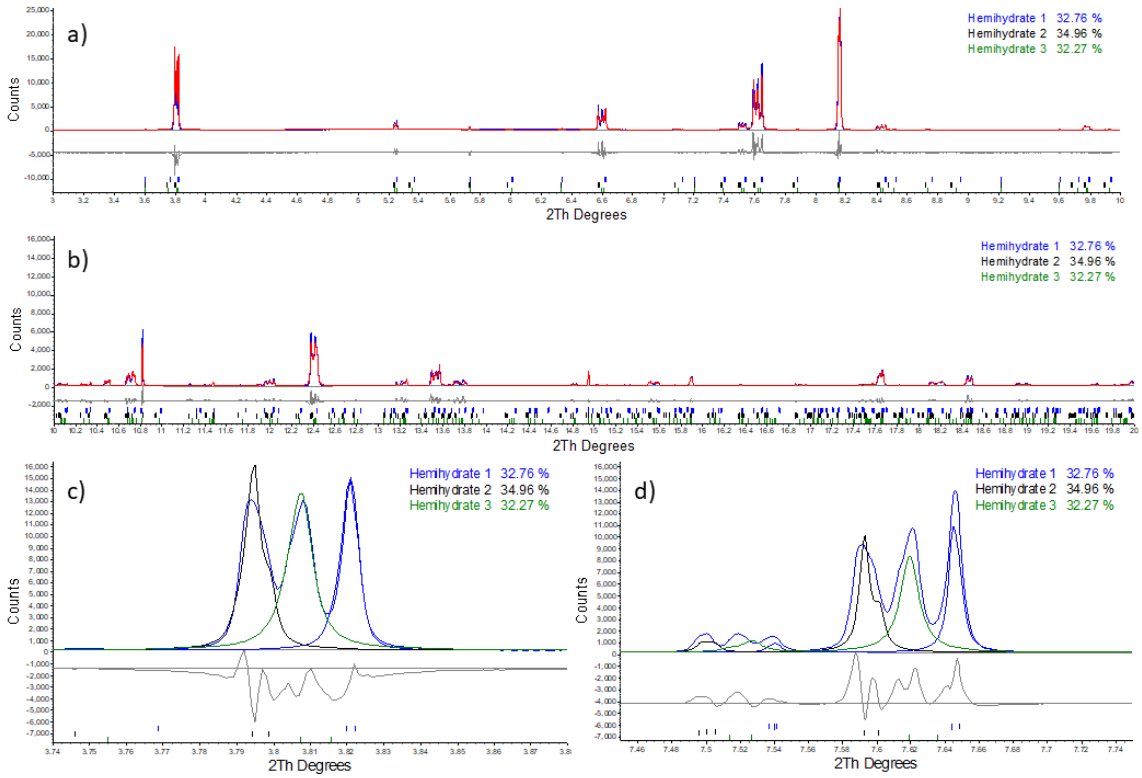

Figure 4.9. Rietveld refinement result of Sample 3. The observed pattern is plotted in blue, the total calculated pattern is reported in red, and the single contributions to the calculated pattern are reported in black, green, and blue. The difference between the calculated and the observed patterns is reported in grey. a) Refinement results in the interval 3-9 2θ°. b) Refinement results in the interval 10-20 2θ°. c) Refinement results in the interval 3.75-3.88 2θ°. d) Refinement results in the interval 7.46-7.7 2θ°. R_{wp}=13.5, R_{exp}=1.8, gof=7.3.

Sample 4 was refined using only one I2 structure [8]. The cell parameters, equal isotropic displacement parameters for equal atoms, and the positions and occupancies of water were refined. The atomic positions and occupancies of all the rest of the atoms were not refined. The observed pattern presented several small peaks that were associated with the presence of impurities in the sample. The peaks of the impurities were added manually to the refinement. The refinement of Sample 4 with one I2 structure and the impurities gave a R_{wp} = 13.8 value. Figure 4.10a and b show the results of the refinement in the low-angle region (range 3-9 2θ°) and in the high-angle region (range 10-20 2θ°). Figure 4.10c and d report the details of the refinement in the regions 3.75-3.88 2θ° and 7.46-7.7 2θ° respectively. The calculated pattern is plotted in red, the observed pattern is plotted in blue and the difference in grey. The peaks associated with the impurities are highlighted by a blue line throughout the pattern.

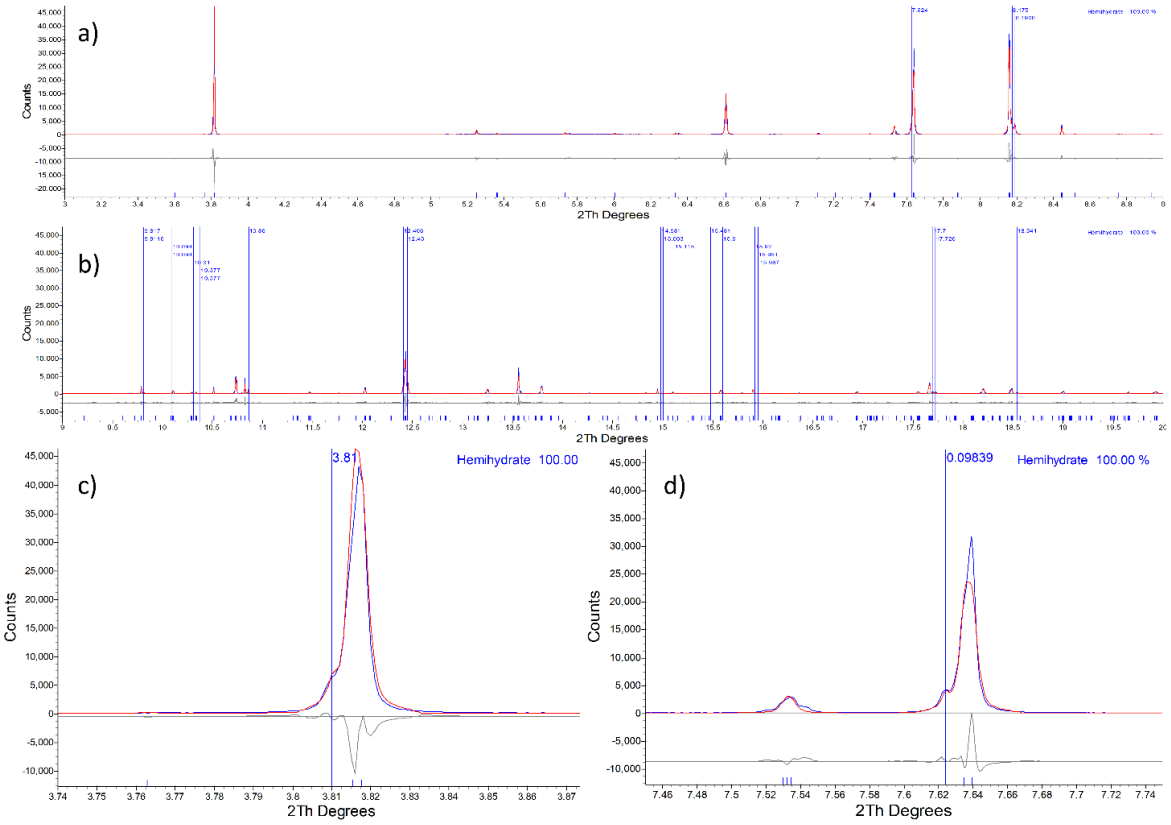

Figure 4.10. Rietveld refinement result of Sample 4. The observed pattern is plotted in blue and the calculated pattern is reported in red. The difference between the calculated and the observed patterns is reported in grey. a) Refinement results in the interval 3-9 2θ°. b) Refinement results in the interval 10-20 2θ°. c) Refinement results in the interval 3.75-3.88 2θ°. d) Refinement results in the interval 7.46-7.7 2θ°. R_{wp}=13.4, R_{exp}=2.0, gof=6.7.

The cell parameters, the occupancies of water, and the R factors, for each of the three contributions of Sample 4 are reported in Table 4.3.

Sample 2										
Phases	**s.g.**	**a**	**b**	**c**	**β**	**occ Ow1**	**occ Ow2**	**Rwp**	**Rexp**	**Gof**
Hemihydrate 1	I2	11.9974(2)	6.9134(1)	12.7284(2)	89.938(1)	1.00(9)	1.00(5)	11.8	1.9	6.2
Hemihydrate 2	I2	12.0727(2)	6.98063(9)	12.7280(1)	90.105(1)	0.86(6)	1.00(3)			
Hemihydrate 3	I2	11.9974(3)	6.9541(1)	12.7552(5)	90.041(2)	1.00(5)	1.00(3)			
Sample 3										
Phases	**s.g.**	**a**	**b**	**c**	**β**	**occ Ow1**	**occ Ow2**	**Rwp**	**Rexp**	**Gof**
Hemihydrate 1	I2	12.0019(1)	6.92440(9)	12.73021(8)	90.042(9)	0.93(7)	0.97(4)	13.5	1.8	7.3
Hemihydrate 2	I2	12.0706(2)	6.97959(6)	12.72586(9)	90.0505(8)	0.91(4)	0.95(3)			
Hemihydrate 3	I2	12.0098(2)	6.95832(9)	12.7295(2)	90.009(2)	1.00(5)	1.00(3)			
Sample 4										
Phases	**s.g.**	**a**	**b**	**c**	**β**	**occ Ow1**	**occ Ow2**	**Rwp**	**Rexp**	**Gof**
Hemihydrate	I2	12.01003(5)	6.93953(5)	12.72497(4)	89.972(4)	1.00(3)	1.00(1)	13.4	2	6.6

Table 4.3. Results of the Rietveld refinement of Sample 2, Sample 3, and Sample 4.

4.2.2. µSXRD results

µSXRD analyses were done on selected crystals of hemihydrate from Sample 2 and Sample 3. The crystal that was measured for Sample 2 is shown in the optical microscopy pictures in Figure 4.11. The crystal was particularly thin (20 µm diameter) and elongated. In order to have a focussed picture of all the parts of the crystal, three pictures were taken from the bottom to the top part. The crystal was isolated from the sample and mounted on a Kapton loop (50 µm diameter) using UV glue as shown in Figure 4.11a. The crystal appears transparent throughout its length and presents a fracture that is visible in Figure 4.11b. The fracture could be due to the twinning of the crystal. The top part of the crystal is shown in Figure 4.11c. The tip is characterized by the pointy shape of α-hemihydrate. The measurements with the 5µ beam were taken at the top part of the crystal as indicated by the red arrow in Figure 4.11c.

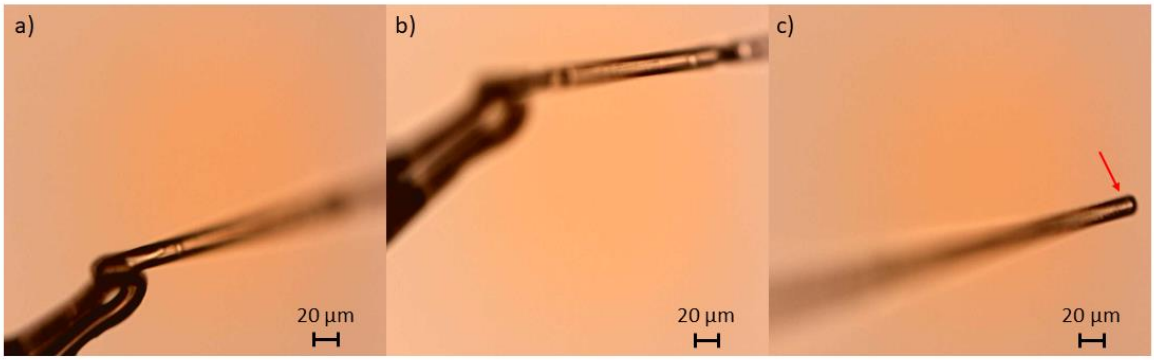

Figure 4.11. Optical microscope pictures of the crystal of Sample 2 used to perform µSXRD. a) Bottom part of the crystal mounted on a Kapton loop with UV glue. b) middle part of the crystal. c) Top part of the crystal. The red arrow indicates the region where the crystal was probed.

The 1440 frames acquired with the µSXRD scan of the crystal (Sample 2) were then loaded into *CrysAlisPro*. The Bragg reflections were extracted from the frames and visualized in the reciprocal space. The reflections were indexed with three monoclinic (pseudo-orthorhombic) cells, each one rotated 60° compared to the others. The twins were easily found by *CrysAlisPro*. The three monoclinic I cells indexed 92 % of the reflections. The indexing results for the crystal of Sample 2 are reported in Figure 4.12. The view is perpendicular to the c-axis which is shared between the twins. The first component (67.9 %) indexed the set of green reflections, the second component (13.3 %) indexed the blue reflections, and the third component (11.4 %) indexed the red reflections. When the reflections associated with all the monoclinic components are plotted together, they generate pseudo-trigonal symmetry.

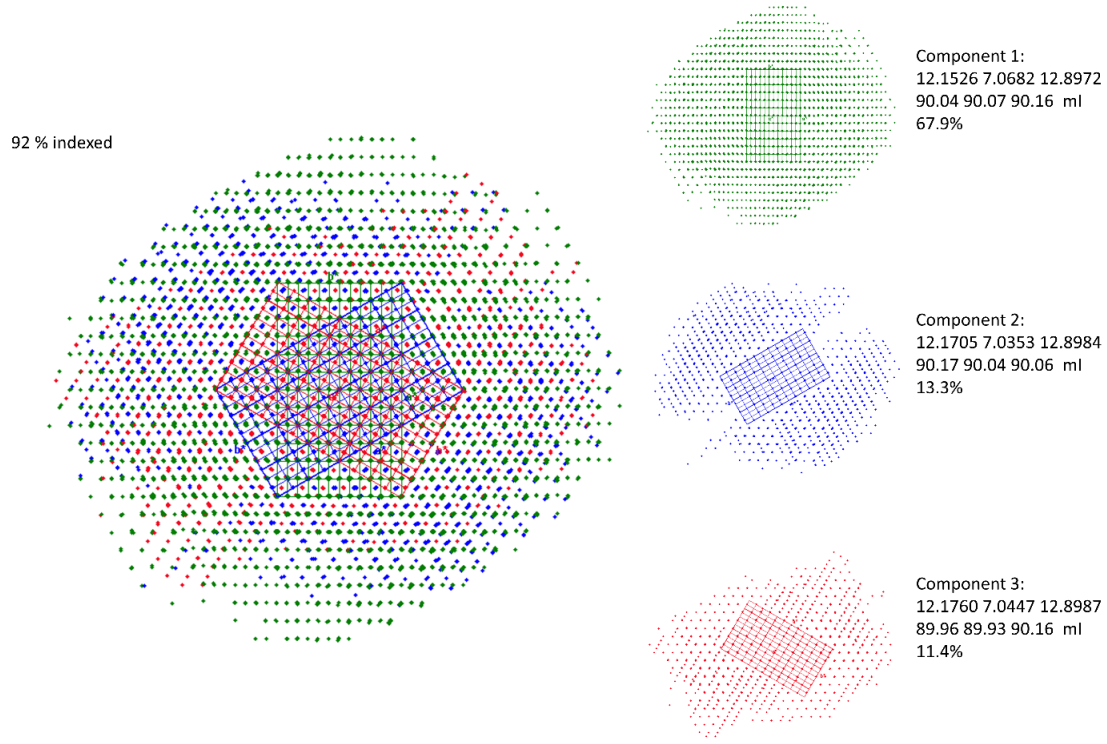

Figure 4.12. Plot of the reflections in the reciprocal space of Sample 2. The reflections were indexed with three monoclinic I cells. The three twin components are reported in green, blue and red. The indexing of the crystal was done with *CrysAlisPro*.

An optical microscopy picture of the crystal from Sample 3 that was measured with µSXRD is shown in Figure 4.13. In this case, the crystal was shorter and larger (around 40 µm diameter) compared with the one of Sample 2. The crystal was mounted in a Kapton loop (50 µm diameter) with UV glue. Here, the orientation of the crystal in the picture permits observing the full shape of the crystal. The detail of the tip of the crystal clearly shows the shape of the α-hemihydrate. The measurement was performed in the top part of the crystal corresponding to the region indicated by the red arrow.

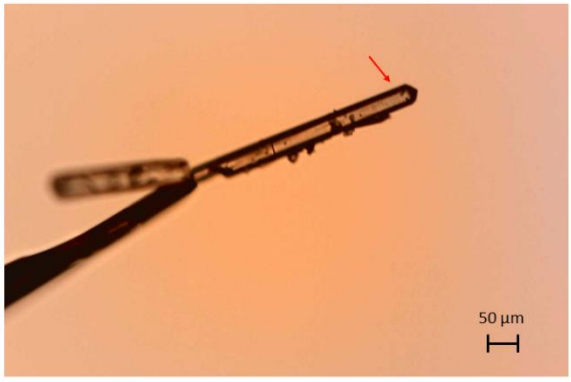

Figure 4.13. Optical microscopy picture of the crystal from Sample 3 measured with µ-XRD. The red arrow indicates the region where the crystal was measured.

The same procedure used to extract and index the reflections used for the crystal from Sample 2 was also used for the crystal of Sample 3. The three twin components of the crystal from Sample 3 are reported in Figure 4.14.

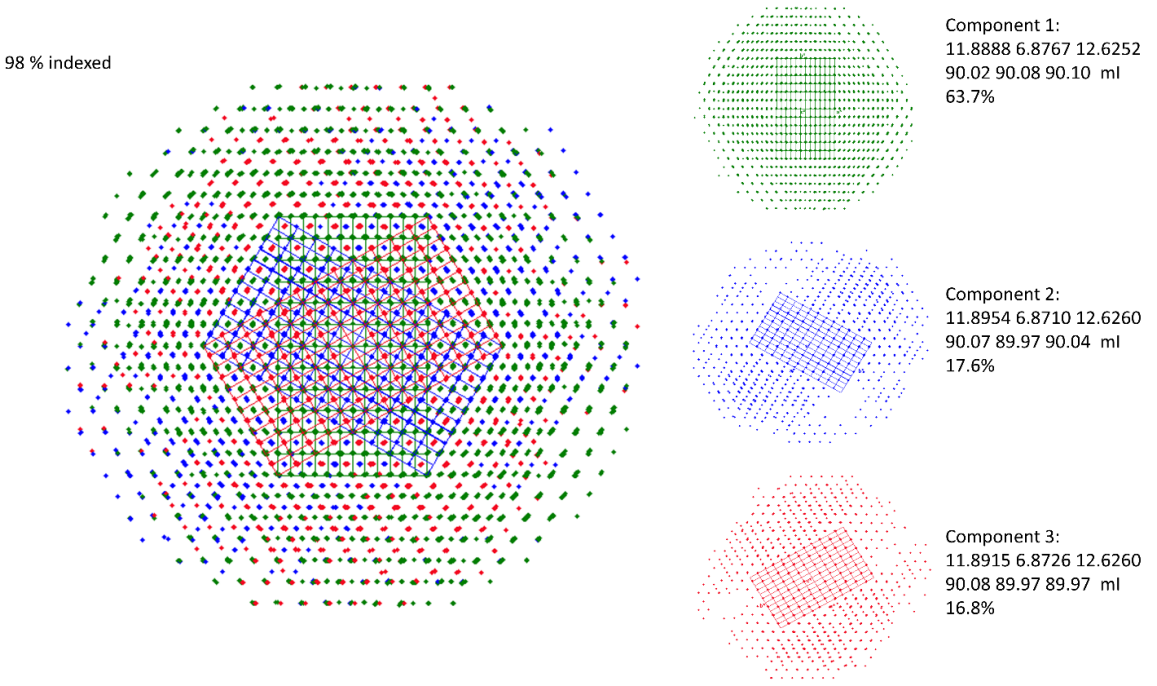

Figure 4.14. Plot of the reflections in the reciprocal space of Sample 3. The reflections were indexed with three monoclinic I cells. The three twin components are reported in green, blue and red. The indexing of the crystal was done with CrysalisPro.

4.2.3. Discussion

4.2.3.1. α and β-hemihydrate

Differences between α and β-hemihydrate samples resulted from SEM, TGA, FTIR and HR-XRPD analyses. The fact that crystals of α and β-hemihydrate show different crystal habits and sizes is not surprising and in agreement with the several evidences already provided in the literature [2]. The TGA-DSC curves of Sample 2 (α), Sample 3 (α) and Sample 4 (β) suggested different behavior during thermal decomposition. Follner et al. (2002) [23] had already reported these differences saying that β-hemihydrate dehydrates to anhydrite in two steps through the interval of 100 °C and 300 C°, while α-hemihydrate dehydrates in a unique step around 200 C°. In the case of Sample 2, Sample 3, and Sample 4, the dehydration occurs differently from what Follner et al. (2002) [23] described but shows that β-hemihydrate dehydrates in a shorter interval of temperatures compared to the α-hemihydrate (see Figure 4.4). The water amount calculated from the weight loss of the samples (Table 4.2) indicated that α-hemihydrate contains more water than β-hemihydrate. The FTIR curves of the samples (Figure 4.5) suggested the presence of some disorder in the distribution of water in the crystallographic sites of α-hemihydrate. The pre-characterization of the samples provided the first indications of the differences between α and β-hemihydrate that were confirmed and explained with the HR-XRPD analyses. From the Rietveld refinement of Sample 2 and Sample 3 (α form) three phases of I2 hemihydrate with slightly different cell parameters were found (Table 4.3). For both samples, the atomic positions of Ca, S, and O were not refined while the positions of water in the two crystallographic sites present in the structure of Ballirano et al. (2001) [8] were refined. Sample 2 resulted to have the highest amount of water from the TGA analyses (0.58 molecules per formula). This is in agreement with the HR-XRPD results. During the Rietveld refinement of Sample 2, the occupancy of water in the three hemihydrate phases was constrained in order to vary

between 0 and 1 as these values always tended to exceed 1. This suggests that the water contained in the three hemihydrate components of Sample 2 is too high to be allocated perfectly in the two crystallographic sites of the I2 structures [23][9], but yet too low to modify the structures into the trigonal $P3_221$ one observed for $CaSO_4 \cdot 0.625H_2O$ [10]. The high disorder of water molecules could also explain the shape of the pattern of Sample 2. Sample 3 resulted to have less water than Sample 2 which is in agreement with the TGA calculations (0.53 molecules per formula). In the first and second components of Sample 3, the crystallographic sites of water resulted to be not fully occupied while in the third component, they were constrained as they tended to exceed 1. From the results of the Rietveld refinements of Sample 3, the disorder of water seems to be present but in a reduced way compared to Sample 2. A more ordered structure could also explain the shape of the pattern of Sample 3, which presents peaks more narrow and symmetric than Sample 2. Sample 4 (β-hemihydrate) was refined with only one phase of I2 hemihydrate (Table 4.3). In this case, the occupancy of water refined to 1 in both the crystallographic sites in agreement with the ordered structure suggested by the FTIR spectrum and the amount of water (0.51 molecules per formula) calculated for the sample. Sample 4 presented several impurities peaks that were not identified in any inorganic compound. The SEM pictures of the sample shown in Figure 4.3 also suggest the presence of impurities. The smallest class of fragments that surrounds the hemihydrate crystals could be a residue of the production method.

From the application of HR-XRPD coupled with preliminary characterization tools, it was possible to demonstrate for the first time the differences between α and β-hemihydrate. These results are in agreement with what was already noticed but never shown by Follner et al. (2002) [23]. The HR-XRPD technique, thanks to the high resolution given by the analyzer crystals, permitted the observation of the splitting of several reflections in the patterns of α-hemihydrate. These features were never been observed before because the resolution of a laboratory X-ray diffraction instrument or a synchrotron diffraction beamline without analyzer crystals is not high enough to reveal them. Based on these results, it is possible to assert that different production methods such as those that are used to produce either α or β-hemihydrate influence the final product. In the case of wet methods, that are used to prepare α-hemihydrate, the sample that precipitates is characterized by a mixture of hemihydrates with variable cell parameters and water amount. When the hemihydrate is prepared by dry methods instead, the sample that is obtained does not present variability neither in the cell parameters nor in the amount of water present in the structure.

4.2.3.2. The complexity of the α-hemihydrate structure

The hemihydrate I2 structure is characterized by pseudo-merohedral three-fold twinning generated by three monoclinic (pseudo-orthorhombic) cells that simulate a trigonal pattern [10] [9]. The three monoclinic twins were identified and indexed for both Sample 2 and Sample 3 as shown in Figures 4.12 and 4.14 respectively. Twinning by pseudo-merohedry is common in monoclinic crystals with β angles close to 90 degrees [212]. In a pseudo-merohedral crystal only parts of the reflections of the twins are overlapped while the others are separated. Schmidt et al. (2011) [10] reported cut through the reciprocal space of the hk0 and hk1 layers of both a sample of C2 hemihydrate, which is the conventional setting for the I2 space group, and a sample of $P3_221$ hemihydrate. Figure 4.15 reports a comparison between the hk0 layers of Sample 2 and Sample 3 with the hk0 layer of the C2 hemihydrate reported by Schmidt et al. (2011) [10]. The patterns of the two samples and the reference from Schmidt et al. (2011) [10] are in agreement showing the pseudo-trigonal symmetry

and the absence of the additional reflections that should be present in the $P3_221$ pattern [10]. Even if it is not always straightforward to establish whether a pattern that shows trigonal symmetry is really trigonal or monoclinic and three-fold twinned [10], in the case of Sample 2 and Sample 3 there are some details that suggest the presence of twinning even before going to index the patterns. From both Figures 4.15a and b it can be seen that the reflections are gradually streaking with increased distance from the center. This feature is typical of twinned structures. In this case, the behavior of the reflections highlighted by the green arrows reflects precisely pseudo-merohedral twinning where part of the reflections perfectly overlaps and part of them splits.

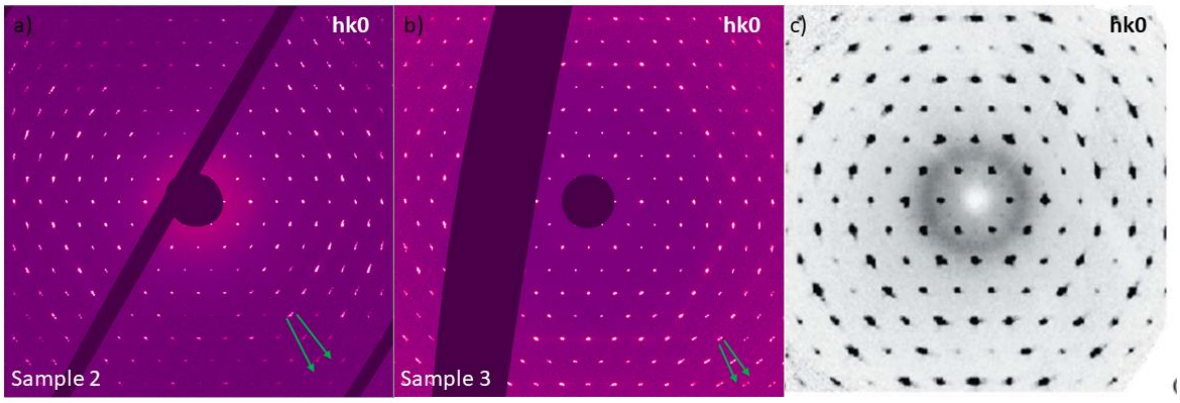

Figure 4.15. a) Cut through the layer hk0 of the reciprocal space of Sample 2. b) hk0 layer of Sample 3. c) hk0 layer of C2 hemihydrate from Schmidt et al. (2011) [10].

It has been demonstrated that calcium sulfate phases, including hemihydrate, maintain traces of their particle-mediated nucleation pathways in the grown crystals [24]. Hemihydrate single crystals were found to be built by anisotropic nanosized (10-20 nm) scattering domains by TEM analyses. Overall hemihydrate single crystals present mosaicity which classifies them as mesocrystals characterized by the coalignment of nanometric domains parallel to the [001] direction [24]. If we consider a crystal as an assembly of perfectly ordered unit cells, mosaicity is the measurement of the misalignment between volumes of unit cells. The presence of domains with slightly different orientations inside a single crystal is often the result of the presence of defects in the crystal lattice. In the case of calcium sulfate phases, the mosaicity can be associated with the presence of the nanosized domains [24]. A direct observation of mosaicity in single crystal diffraction patterns can be done by looking at the shape of the reflections. When a crystal presents mosaicity, the reflections are broadened, suggesting not only misalignment between domains but also possible variations in the domains' volumes and the lattice parameters between the domains [213]. *CrysAlisPro* permits to have an estimation of the mosaicity of a crystal. The mosaicity in *CrysAlisPro* is expressed with three parameters e1, e2, and e3. These parameters represent the mosaicity in different directions calculated considering a coordinate system for each reflection of the pattern. The mosaicity calculated with e1 is relative to a direction perpendicular to e2 and both these parameters are relative to directions tangent to the Ewald sphere. The mosaicity calculated in e3 is relative to the scanning direction [214]. e1, e2, and e3, and the average mosaicity (η) were calculated for both Sample 2 and Sample 3 resulting in higher values for Sample 3 (see table 4.4).

Samples	**e1**	**e2**	**e2**	**η**
Sample 2	0.16	0.18	0.64	0.33
Sample 3	0.2	0.2	0.84	0.41

Table 4.4. Mosaicity values calculated with the *CrysAlisPro* software.

Since the mosaicity in hemihydrate crystals is expected to be due to the assembling of nanosized domains in the [001] direction and consequent misalignment, cuts through the reciprocal space of Sample 3 have been done to evaluate the shape of the reflections. Figure 4.16 shows the h1l and 1kl layers of Sample 3. Both the layers of reflections show a particular behavior. Some of the reflections present broadening and in particular preferential streaking in specific directions. Figure 4.16c and d shows zooms of Figure 4.16a and b respectively. Here, it is very clear that specific sets of reflections are elongated along the h direction as highlighted by the green lines and arrows. It is curious how, in both the h1l and 1kl layers, only one repeating column of reflections presents the streaking. As a first interpretation, the evidence of the streaking of the reflections parallel to the [001] direction is in agreement with the findings of Stawski et al. (2019) [24]. In the case of Stawski et al. (2019) study, it was not specified if the streaking parallel to the [001] direction was observed in all the reflections or only in a specific one. However, comparing the electron diffraction pattern of the crystal of hemihydrate analyzed by Stawski et al. (2019) [24] (Figure 4.17) and Sample 3 (Figure 4.16), it is possible to say that the directions of the streaking are the same in both cases. This evidence could represent additional proof of how the process of coalescence of nanometric sub-units during the nucleation and growth of calcium sulfate phases remains imprinted in the crystals. According to this scenario, the grown crystal appears as a mesocrystal in which the local disorder is the result of the imperfect coalescence of nanosized domains that tend to reach higher levels of ordering by slow atomic diffusion [24]. In order to have a deeper understanding of the meaning of the distribution of the streaking in specific reflections, it is necessary to understand which atoms are contributing to those reflections. A possible way would be to calculate the contribution of each atom, in the hemihydrate structure, to the structure factor of the reflections. This could not only strengthen the theory of Stawski et al. (2019) [24] about the nucleation pathway of calcium sulfate hemihydrate but it could also give us insights into the dynamic of the coalescence of the nanosized domains.

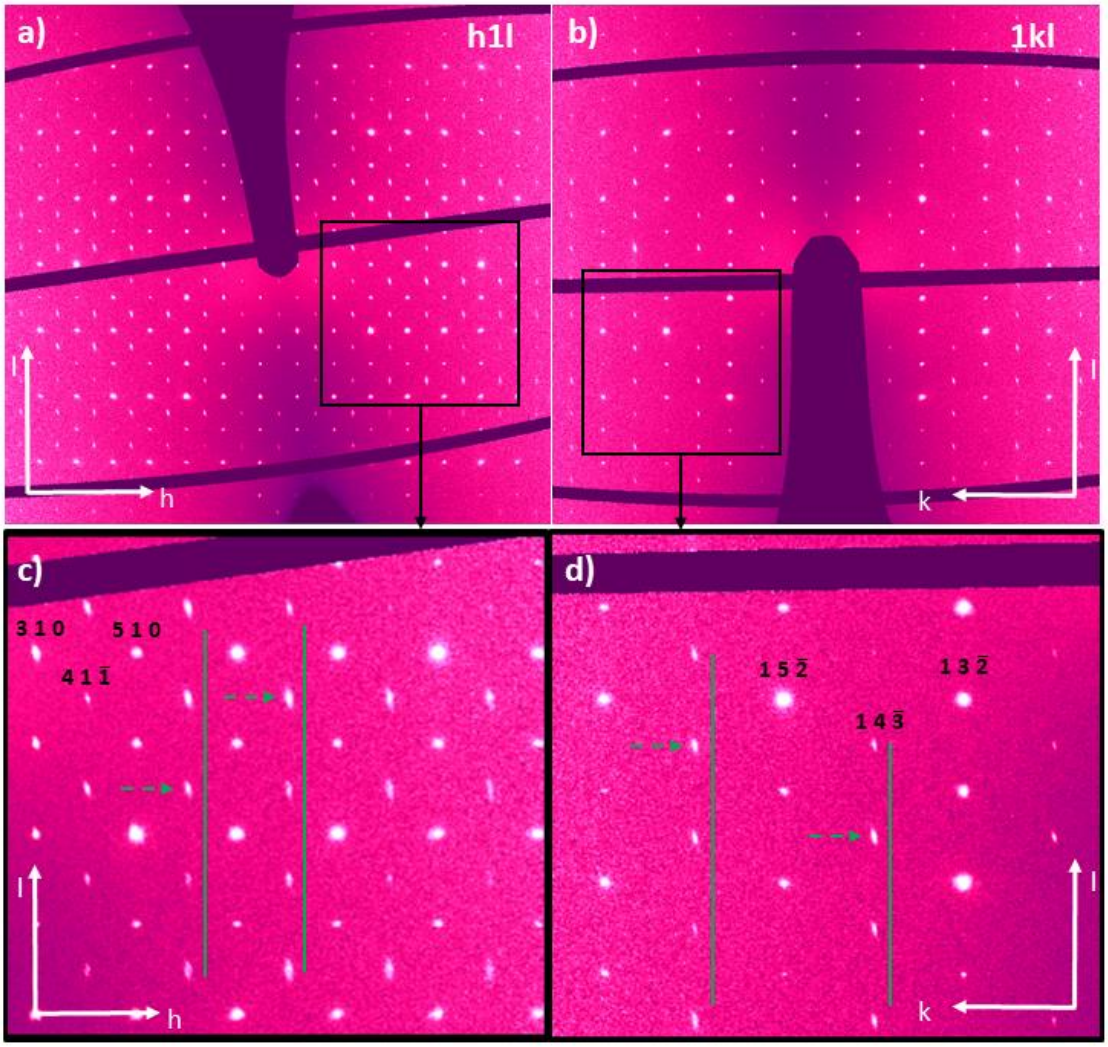

Figure 4.16. a) Cut through the h1l layer of the reciprocal space of Sample 3. b) Cut through the 1kl layer of the reciprocal space of Sample 3. c) Zoom of the h1l layer of Sample 3. The green lines and arrows indicate some of the columns of reflections that present streaking. d) Zoom of the 1kl layer of Sample 3. The green lines and arrows indicate some of the columns of reflections that present streaking.

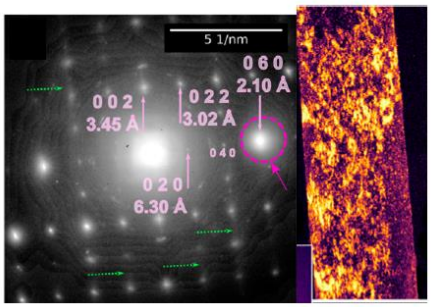

Figure 4.17. TEM diffraction pattern and DF-TEM image of the nanosized domains present in the hemihydrate crystal analyzed by Stawski et al. 2019. The direction of the streaking of the reflections in the diffraction pattern is [001] and is perpendicular to the green arrows. Modified after Stawski et al. (2019) [24].

4.3. The hemihydrate-gypsum transformation

In this section are presented the results and the discussions relative to the investigations on hemihydrate-gypsum transformation. In this study, s3DXRD was coupled with PCT and powder diffraction to monitor the hydration reaction that brings to the formation of gypsum plaster starting from the hemihydrate. Sample 1 was used as the starting material that was placed in a glass capillary (0.3 mm) and hydrated *in situ* with a solution saturated in calcium sulfate. The S3DXRD and PCT measurements were taken semi-simultaneously alternating parts of the set-ups.

4.3.1. Powder diffraction results

Two powder diffraction patterns were collected before performing the s3DXRD measurements in order to assess the purity of Sample 1 and the completeness of the hydration reaction. Le Bail refinements of the two patterns have been performed and they are shown in Figure 4.18. The powder patterns were collected in the 2θ region 1-10° with λ = 0.2817834. The Le Bail refinement in the 2θ region 1.8 - 8° of the starting dry hemihydrate sample (Figure 4.18a) confirmed the monoclinic setting I2 described by Ballirano et al. (2001) [8]. The final hydrated gypsum sample (Figure 4.18b) was refined in the C 2/c setting described by Boeyens and Ichharam (2002) [69]. The small peak labeled with the letter B indicates that a small amount of hemihydrate was still present in the sample after 36 hours of hydration. The experimental conditions (small beam size, crystallite size, and 2θ range) did not allow to perform a successful and reliable Rietveld refinement so it was not possible to retrieve the exact percentage of hemihydrate still present in the sample from the second pattern.

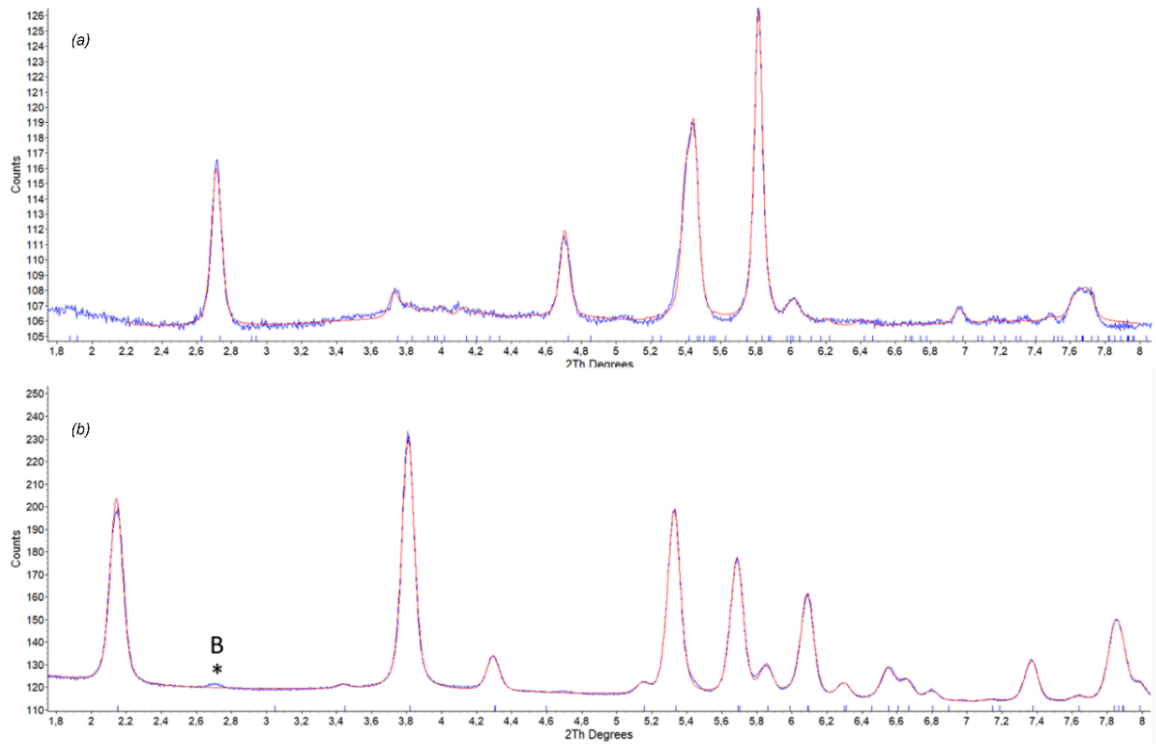

Figure 4.18. a) Le Bail refinement of the starting Sample 1 before being hydrated. b) Le Bail refinement of the final gypsum after 36 hours of hydration. A low quantity of hemihydrate, represented by the peak B in the pattern, was still present at the end of the hydration process.

4.3.2. Phase contrast tomography results

The first PCT scan was acquired before hydrating the sample in order to characterize its starting status. Successively, right after injecting the calcium sulfate solution into the capillary with a syringe, scans were acquired every 30 minutes up to 36 hours of hydration. Each PCT scan consisted of the acquisition of 800 projections plus dark, flat, and reference projections. The reconstructions made with *Tomwer* and *Nabu* software permitted obtaining the transversal slices of the sample that were used to visualize and analyze the 3D volumes. Figure 4.19 shows an example of the input files needed for the PCT reconstruction and one of the resulting reconstructed slices. This example is relative to the first PCT scan with dry hemihydrate grains. The first image from the left is one of the 800 projections showing the portion of the capillary (1 mm height) probed with the X-ray beam. The second and third images show both the dark and flat that were subtracted during the dark and flat field correction. The last image shows one of the 510 transversal slices reconstructed with the FBP algorithm.

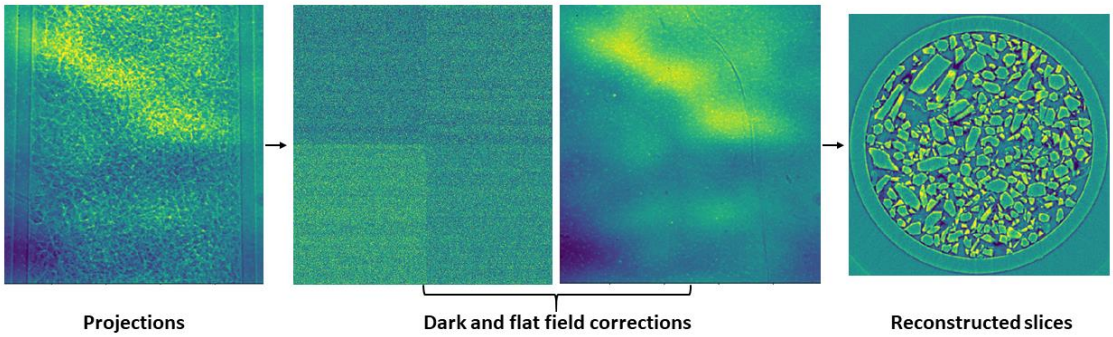

Figure 4.19. Example of the input files used for the reconstruction of PCT measurements and one of the transversal slices obtained as a result. The process of reconstruction of the PCT scans was done using the *Tomwer* and *Nabu* software.

Once the transversal slices of the capillary were reconstructed, the evolution of a specific set of particles was followed over time. Figure 4.20 from a-p reports the evolution of the same slice of the capillary that was probed also with s3DXRD. This permitted us to do a first evaluation of how the starting hemihydrate grains dissolved and to observe the formation and growth of gypsum particles in the free spaces. Each slice reported in Figure 4.20 is relative to a specific time of hydration. Figure 4.20a shows the first slice relative to the dry hemihydrate sample, Figure 4.20p shows the sample after 36 hours of hydration when almost all the hemihydrate was dissolved and replaced by the gypsum crystals network. The network of gypsum crystals appears to be well interlocked showing cohesive behavior due to the setting process. Figure 4.20 from q to t reports zooms of selected sections of Figure 4.20a-c-o-p. These sections have been selected to show the evolution of two hemihydrate particles throughout the hydration process. In Figure 4.20q the two hemihydrate particles show their pristine shape. One of the particles is cut perpendicular to its longitudinal axis exposing the hexagonal section typical of α-hemihydrate crystal habit. The other particle is cut parallel to its longitudinal axis showing the elongation of the crystal. The two hemihydrate grains remain recognisable in Figure 4.20r and s which correspond to 1 hour and 20 hours of hydration respectively. At the end of the hydration process, in Figure 4.20t the two hemihydrate grains are completely dissolved and replaced by a dense agglomerate of gypsum crystals.

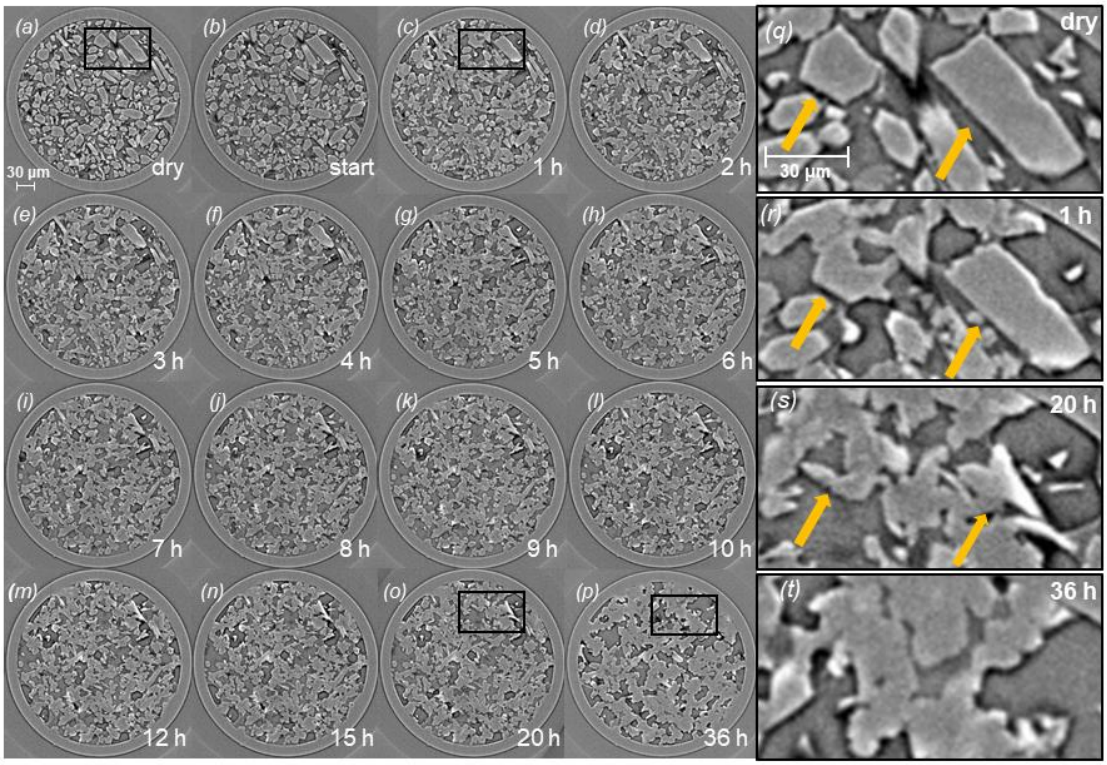

Figure 4.20. a-p) Sequence of PCT slices showing the evolution of the same set of particles from the dry state to 36 hours of hydration. q) Zoom of the area highlighted with a black square in a. The yellow arrows indicate two hemihydrate grains. r) Zoom of the area highlighted with a black square in c. The yellow arrows indicate the same two hemihydrate crystals that starts to dissolve. s) Zoom of the area highlighted with a black square in o. The two hemihydrate crystals are almost completely dissolved. t) Zoom of the area highlighted with a black square in p. The hemihydrate crystals are not present any more and they are replaced by gypsum crystals.

Before being able to visualize and analyze the 3D volumes of the sample, the 2D transversal slices of each dataset were segmented (binarized) in order to extract the grains of both hemihydrate and gypsum from the background. The background included quartz wool, air, water, and the glass capillary. The segmentation process was done using the *Dragonfly* software with two approaches. In one case, the 2D slices reconstructed without the application of Paganin algorithm [180] were segmented by hand using the *ROI painter* tool of *Dragonfly* to extrapolate selected particles of hemihydrate and gypsum from the full volume. Figure 4.21 shows an example of the workflow used to obtain the 3D volumes of single particles during the hydration process.

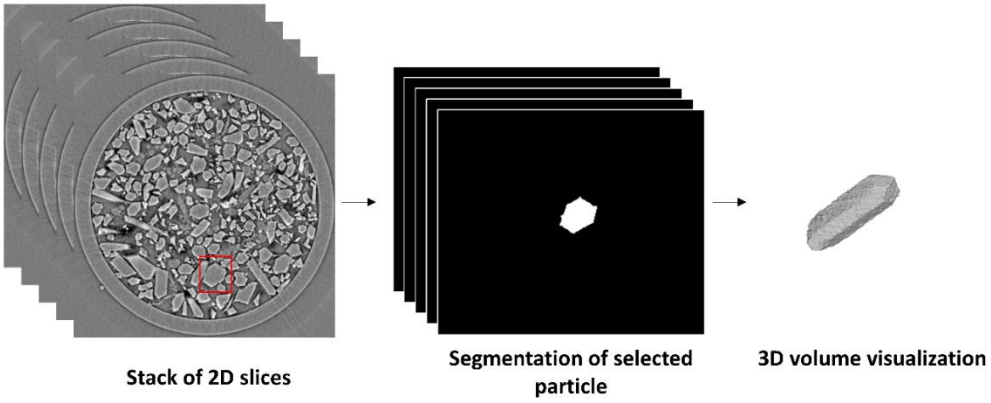

Figure 4.21. Workflow used to segment selected particles of hemihydrate and gypsum from the volumes of the sample. All the procedure was done with the *Dragonfly* software.

In the other case, the 2D slices reconstructed with the Paganing algorithm (δ/β=30) were segmented based on the histogram of grey levels with *Dragonfly* to extrapolate all the grains from the volumes. The workflow used for this segmentation procedure is shown in Figure 4.22.

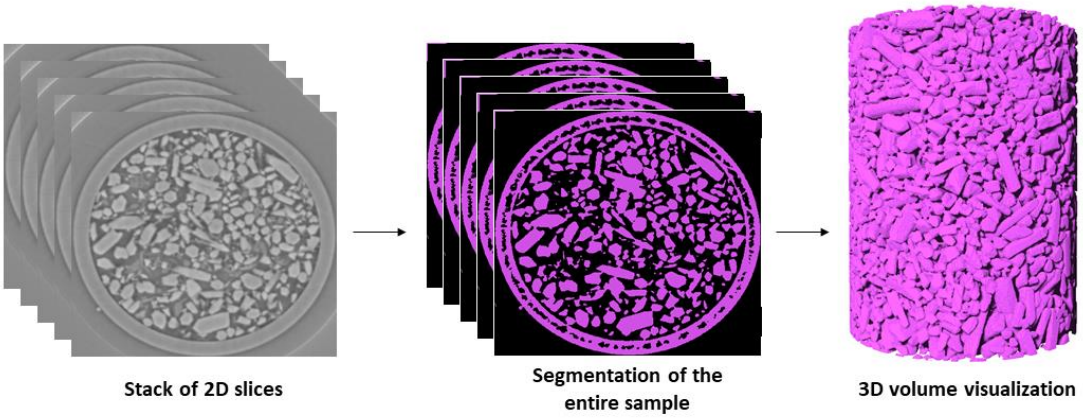

Figure 4.22. Workflow used to segment the full volumes of the sample. All the procedure was done with the *Dragonfly* software.

The segmentation procedure explained in Figure 4.21 was used to extract the 3D volumes of the two hemihydrate particles highlighted in Figure 4.20q-t. The two particles were reconstructed in dry conditions (a), after 2 hours of hydration (b), after 8 hours of hydration (c), and after 12 hours of hydration (d) and reported in Figure 4.23. The volumes of the hemihydrate particles show their dissolution behavior. The particles during the dissolution assumed a layered texture. This phenomenon suggests that the dissolution occurs preferentially in a specific direction, which coincides with the elongation direction of the particles.

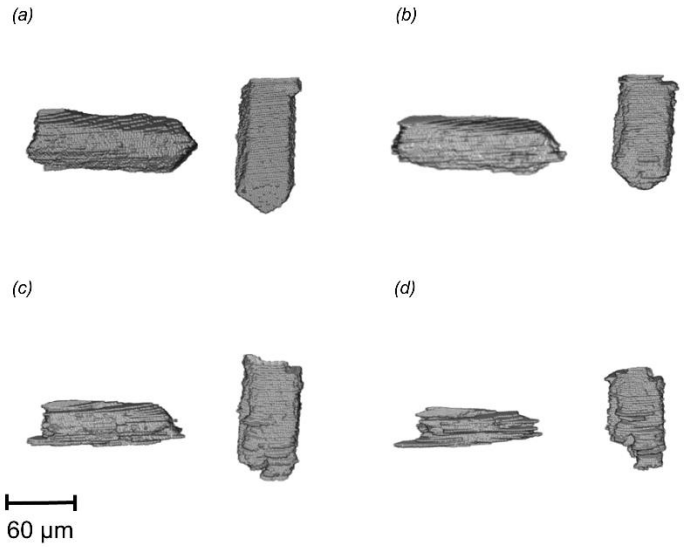

Figure 4.23. Volumetric reconstructions of the two hemihydrate particles highlighted in Figure 4.20q-t. a) Dry hemihydrate particles. b) Hemihydrate particles after 2 hours of hydration. c) Hemihydrate particles after 8 hours of hydration. d) Hemihydrate particles after 12 hours of hydration.

The segmentation procedure of Figure 4.22 was used to reconstruct the full 3D volumes of the capillary during the hydration reaction. Figure 4.24 reports a collection of half volumes of the sample from the dry condition to the last measurement taken at 36 hours of hydration. The volumes

were reconstructed in order to observe the development of the micro-texture. At the beginning of the process, when only hemihydrate grains were present in the capillary, most of the crystals were large and well distinguishable from each other. When the hemihydrate crystals started to dissolve and gypsum started to grow, the morphologies of the sample changed. Gypsum crystals precipitated in the pores between hemihydrate crystals and grew to form a dense network of interlocked grains that are the basis of the cohesive properties of gypsum plaster.

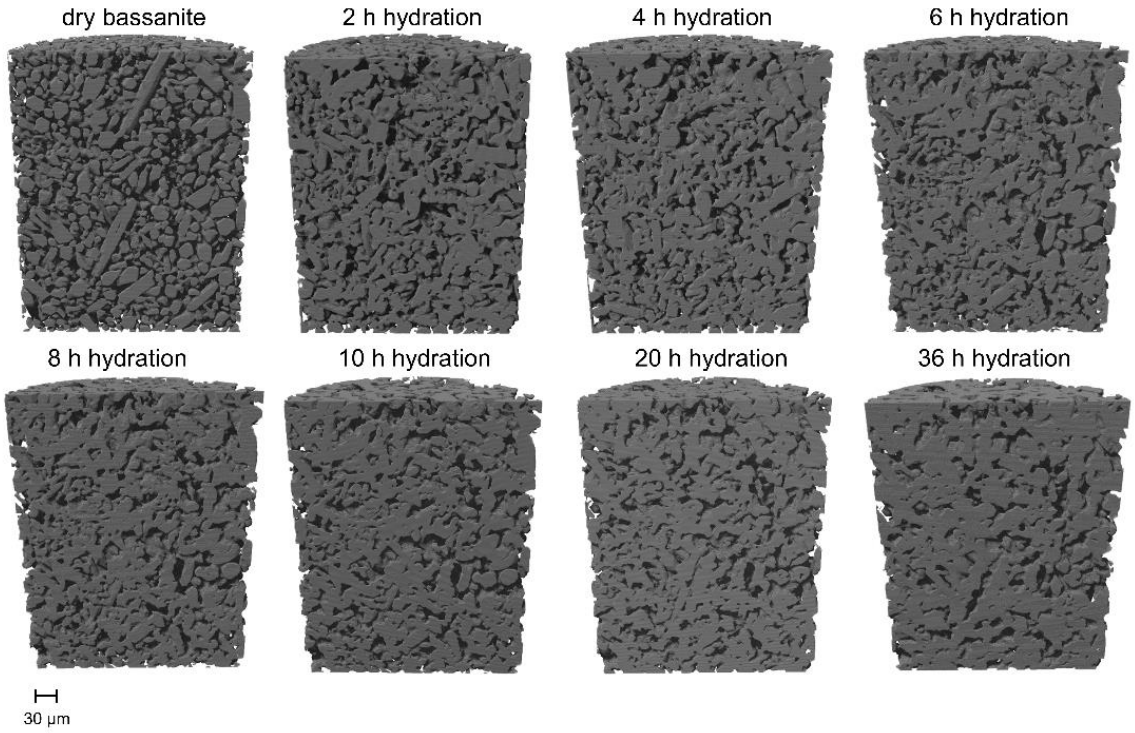

Figure 4.24. Collection of 3D volumes of the inside of the capillary during the hydration process. The reconstructions show the evolution of the microstructure of the sample from the presence of dry hemihydrate to the final dense network of gypsum crystals.

4.3.3. S3DXRD results

S3DXRD data were processed using Jupyter notebooks based on the *ImageD11* software following the pipeline described in Chapter 3. Two datasets of s3DXRD were acquired, one before starting the hydration process, to characterize the starting hemihydrate, and one after 36 hours of hydration. The first dataset contained only hemihydrate grains, therefore the diffraction spots extracted with the segmentation process were indexed with the monoclinic I2 cell parameters from Ballirano et al. (2001) [8]. To perform the indexing of the hemihydrate grains the rings ($\bar{1}01$) with 6670 peaks, and ($\bar{1}03$) with 11212 peaks were chosen. These rings were chosen because they contained a high concentration of peaks that resulted in the indexing of 107 grains of hemihydrate. During the indexing, peaks that belong to the same grain are assembled within a sinogram. The sinogram of one grain shows its position inside the sample within a rotation of 180°. Once the grains were indexed and the sinograms were built, the position and shape of the grains were reconstructed within grain maps. The indexing process is more successful for larger grains because they produce stronger and larger diffraction peaks that are easier to locate and therefore to be assigned to a specific grain. Sinograms that contain several strong peaks allow a more accurate reconstruction of the shapes of the grains in the grain map. For the dry hemihydrate s3DXRD

dataset, the grain map was done by summing only the larger crystals providing meaningful shape reconstructions. This helped with the correlation of the s3DXRD data with the PCT data. The position and shape of the grains in the grain map were reconstructed by iradon transformation of the individual sinograms. Figure 4.25a and b show two sinograms relative to two hemihydrate grains. The main features in white in the plots are the grain positions at each angle between 0° and 180° formed by the indexed diffraction peaks. Figure 4.25c and d show the result of the iradon transformation of Figure 4.25a and b respectively. In order to obtain a clean reconstruction of the grains, the background noise (the peaks that are not part of the sinograms but are dispersed in the background) was removed imposing an intensity threshold of 0.02 on each voxel. The final grain map, made by the sum of all 107 grains of hemihydrate, is reported in Figure 4.25e.

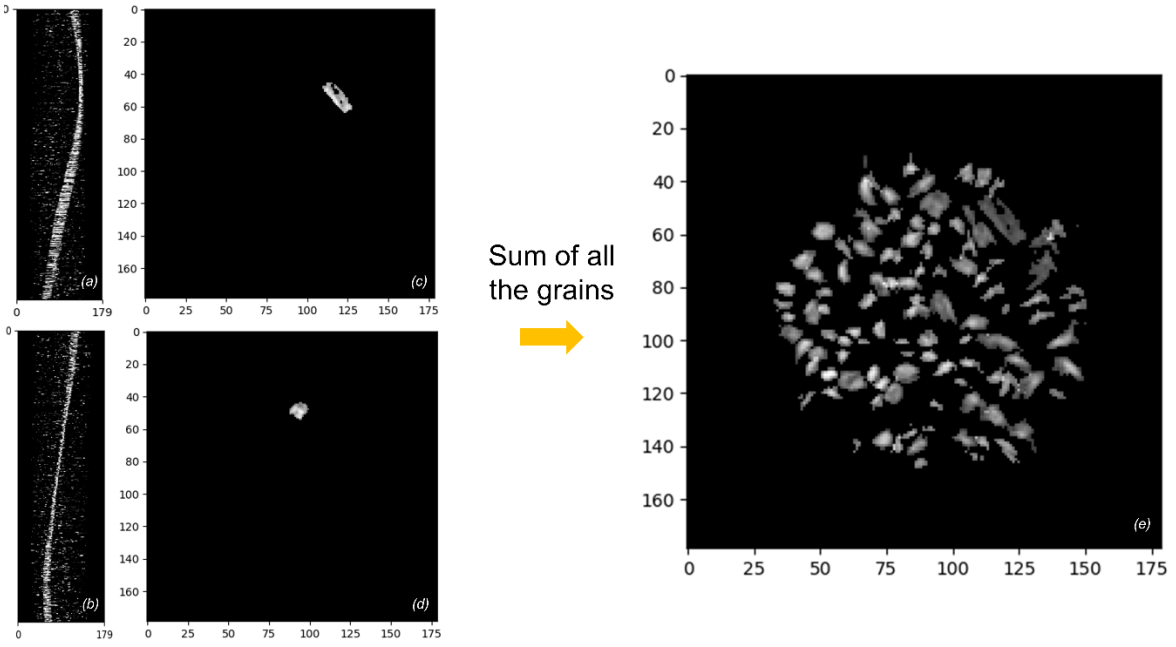

Figure 4.25. a) and b) Sinograms of two indexed hemihydrate grains showing their position at each angle of the rotation between 0° and 180°. c) and d) Iradon transformation of a) and b) respectively showing the shapes and positions of the two indexed grains of hemihydrate. e) Grain map made by the sum of the iradon transformations of the sinograms of all 107 indexed grains of hemihydrate.

For the second s3DXRD dataset, the indexing process was slightly more challenging. The reason was that the sample after 36 hours of hydration was composed of almost only gypsum crystals arranged in a complex and intricate matrix. In order to be able to select only the grains of gypsum with a larger size than the one of the beam (5 µm), simplifying the indexing process, we applied a higher intensity threshold during the segmentation. Figure 4.26 shows the difference between the 2D diffraction pattern with the same intensity threshold used for the hemihydrate grains (a) and the pattern resulting from the segmentation with a higher intensity threshold (b). It is evident that in Figure 4.26b large and more intense Bragg spots are present in the pattern facilitating the indexing of the peaks.

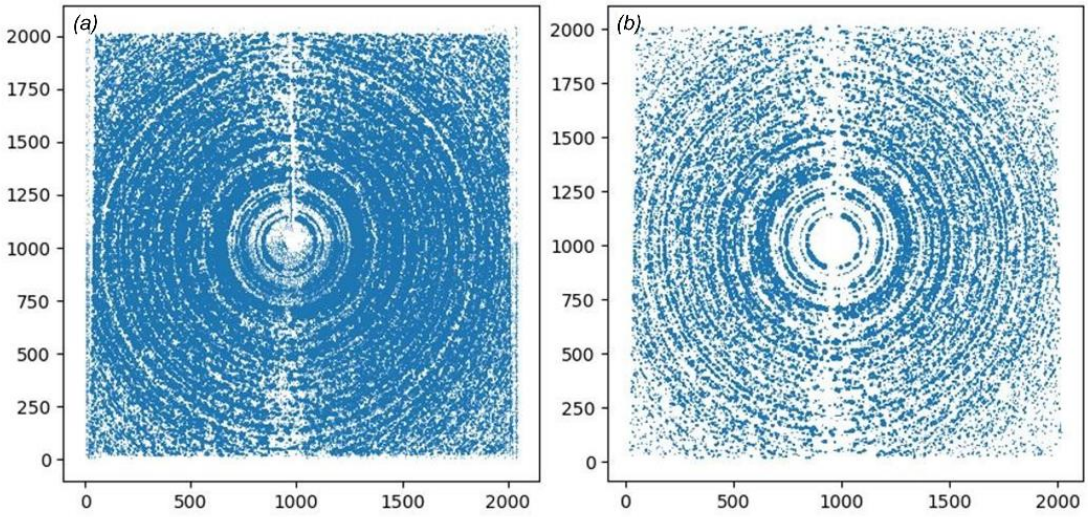

Figure 4.26. a) 2D diffraction pattern retrieved from the segmentation of the s3DXRD dataset after 36 hours of hydration with a lower intensity threshold. b) 2D diffraction pattern of the same dataset retrieved from the segmentation with a higher intensity threshold.

The grains of gypsum were indexed using the C 2/c lattice parameters refined by Boeyens and Ichharam (2002) [69]. The rings $(0\bar{2}0)$ with 51685 peaks and the ring $(\bar{1}\bar{1}0)$ with 8558 peaks were chosen. In total 102 grains of gypsum were indexed and the grain map showing their reconstruction is reported in Figure 4.27.

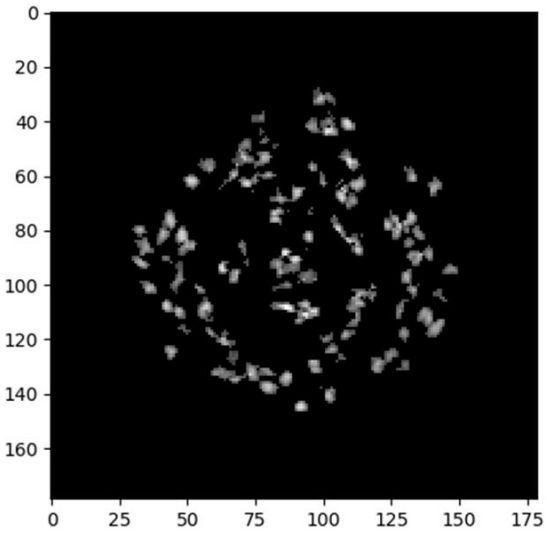

Figure 4.27. Grain map showing the 102 reconstructed gypsum grains.

A UBI is generated for each indexed grain. Since the rows of the UBIs (3x3 matrices) give the vectors of the a, b, and c-axis of the lattice of each crystal in the sample coordinate system, the vectors of the crystallographic lattice of each grain of hemihydrate (a) and gypsum (b) were plotted on top of the grain maps (see Figure 4.28). The red vectors represent the c-axis, the green vectors represent the a-axis, and the blue vectors represent the b-axis. From the distribution of the three vectors, it can be inferred that both the grains of hemihydrate at the beginning of the process and the grains of gypsum at the end of the hydration were oriented randomly.

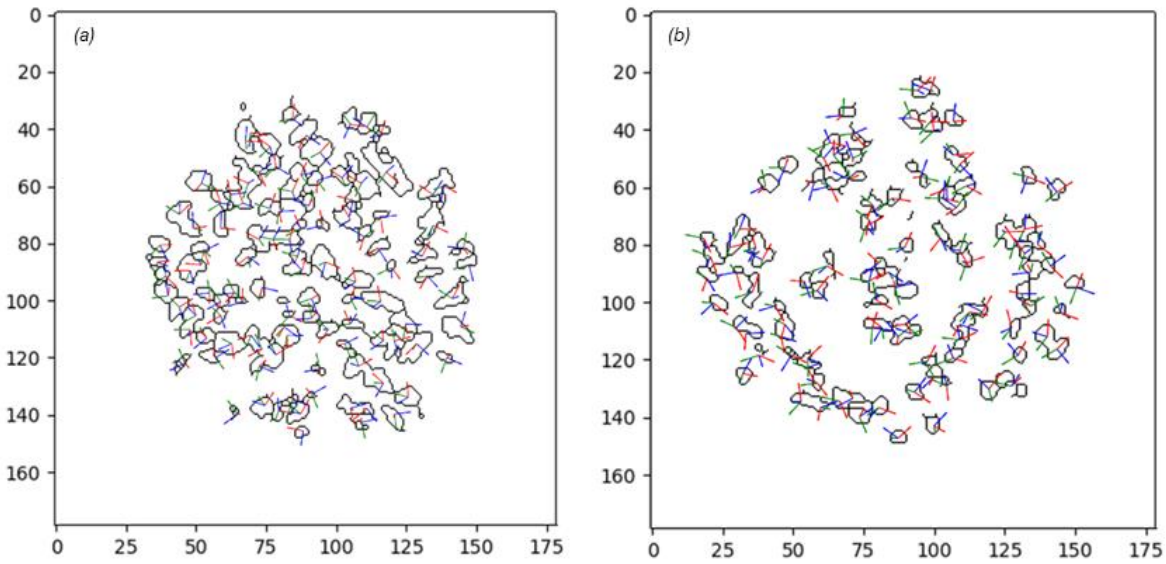

Figure 4.28. (a) Plot of the three lattice vectors of the hemihydrate indexed grains. The red vector is the c-axis, the green vector is the a-axis and the blue vector is the b-axis. (b) Plot of the three lattice vectors of the gypsum indexed grains. The color code for the crystallographic axis is the same one used for the hemihydrate grains.

4.3.4. Discussion

4.3.4.1. A promising tool for hierarchical characterizations

Precipitation and crystallization in porous materials or confined environments is a subject of great interest for geochemistry, environmental science, geology, and industrial applications. X-ray tomographic techniques alone and also coupled with diffraction imaging techniques, such as XRD-CT, have been used previously to monitor precipitation reactions. Some examples of these applications are the works of Godinho et al. (2019) [215], Godinho et al. (2016) [216], and Anduix-Canto et al. (2021) [217]. In the case of Anduix-Canto et al. (2021) [217], the combination of µ-CT and XRD-CT helped to demonstrate the *in situ* crystallization pathway of calcium sulfate phases in confined environments such as CPG rods. They reconstructed the 3D volumes of precipitated hemihydrate (Figure 4.29a-b-d-e) and gypsum particles and the 2D XRD-CT maps showing the spatial distribution of the calcium sulfate phases based on phase identification (Figure 4.29c-f). In this work, the advantage of coupling µ-CT with a diffraction imaging technique relies on the fact that XRD-CT confirms the nature of the crystallographic phases that are crystallizing within the porous media. However, even though this approach allowed observing *in situ* and in 3D the crystallization pathways of calcium sulfate that involve the formation of both bassanite and gypsum particles, it only permits to make considerations on the bulk sample behaviour.

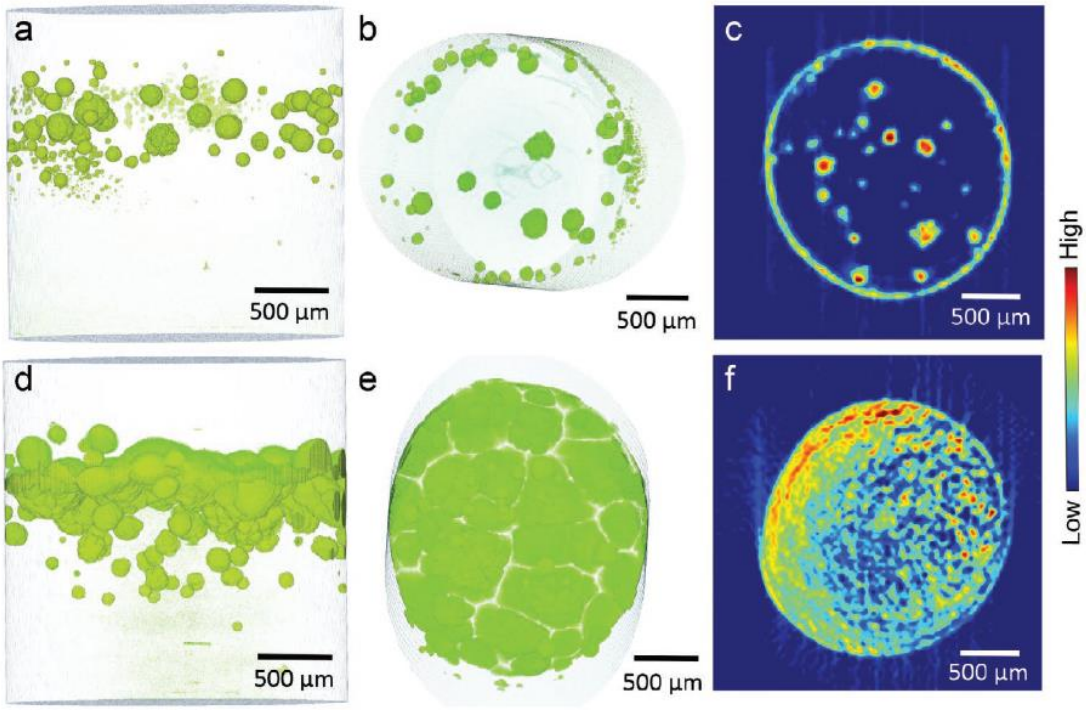

Figure 4.29. a), b), d), and e) 3D reconstruction of hemihydrate and gypsum particles precipitated into CPG rods. c) and f) XRD-CT maps showing the distribution of hemihydrate particles after 7h and 24h from the beginning of the precipitation. Taken from Anduix-Canto et al. (2021) [217].

Here, the combination of s3DXRD and PCT offers a way to overcome the scale barriers due to the fundamental properties of powder diffraction that do not permit probing crystals individually. The use of s3DXRD introduces the possibility to calculate the crystallographic orientation of each grain measured with a micrometric resolution. The combination of these techniques offers a potential hierarchical characterization of a system. One of the main advantages of the semi-simultaneous use of PCT and s3DXRD is reported in Figure 4.30. The Figure shows all the possible correlations that can be done between the complementary results at different scales of observation. Starting from the scale of the sample, we can compare the s3DXRD grain map (Figure 4.30a) with the PCT reconstruction (Figure 4.30c) of the dry hemihydrate grains that were measured. In order to compare the two reconstructions, the PCT map was made by adding three slices resulting in a thickness of 4.7 µm, which is close to the 5 µm thickness of the s3DXRD map. The comparison of the two maps shows that the distribution of the hemihydrate grains is coherent. The largest grains that were indexed and reconstructed with s3DXRD are clearly recognizable in the PCT reconstruction. The smaller grains and fragments that are present in the PCT map were not included in the s3DXRD grain map because they were discarded during the indexing process. Successively, we can move to another scale of observation comparing the results from s3DXRD and PCT at the single particles level. Figure 4.30b and d report a zoom of the s3DXRD map and PCT reconstruction respectively, showing the same hemihydrate grains reported also in Figures 4.20, and 4.23. The association of the 3D shape and morphological orientation of the single particles to their crystallographic orientation is a useful source of information permitting us to confirm, in the case of hemihydrate, that the crystals elongate in the [001] direction [23].

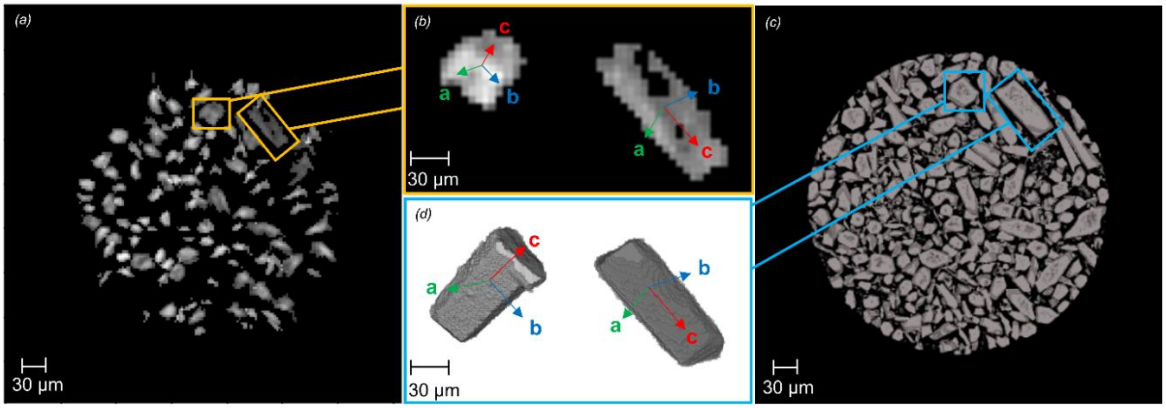

Figure 4.30. a) s3DXRD grain map showing all the grains that grains of hemihydrate that were indexed. b) Zoom on two hemihydrate particles highlighted in a) showing the orientation of a-axis (green vector), b-axis (blue vector), and c-axis (red vector). c) PCT 3D reconstruction of the region of the sample corresponding to the s3DXRD map shown in a). d) 3D reconstruction of the two hemihydrate particles reported in b) showing also the orientation of the crystallographic axis.

4.3.4.2. Link between dissolution and precipitation processes

The hydration reaction of gypsum plaster consists of dissolution and precipitation reactions as sub-processes. The result of the hydration is the phase transformation from hemihydrate to gypsum. The most common scenarios that explain how a phase transformation can occur during a hydration reaction are three. One possibility is the complete dissolution of the starting hemihydrate and subsequent precipitation of gypsum, another possibility is a coupled dissolution-precipitation process where gypsum starts to precipitate in local supersaturated areas due to hemihydrate slow dissolution, and in other cases, the presence of an epitaxial relationship between hemihydrate and gypsum [218]. The only reliable way of understanding whether or not the two phases are linked by the epitaxial growth of gypsum on hemihydrate surfaces is to calculate the crystallographic relationships between the starting hemihydrate crystals and the final gypsum crystals. S3DXRD providing the crystallographic orientation of the grains provides also the possibility of calculating their relationships. The crystallographic relationship between close grains in a microstructure is usually expressed with disorientation angles [219]. Disorientation angles can be identified for grains of the same type or for different crystallographic phases by calculating the smallest rotation angle needed to put two adjacent lattices in parallel conditions [220]. The calculation of the disorientation angles between close grains in a microstructure is a common practice in metallurgy. The properties of grain boundaries are strictly related to the nature of the misorientation between two adjacent grains. Since metallurgy deals with metals, disorientation angles are usually calculated for cubic crystals in metal matrices. Mackenzie (1958) [221], Mackenzie (1964) [222], and Handscomb (1958) [223] evaluated the maximum disorientation angles possible between two cubic grains with different methods [219]. Since the disorientation is calculated by rotating the crystal coordinate system to be coincident with the crystal coordinate system of another crystal, the two coordinate systems must be Cartesian [219]. Cubic crystals represent the perfect samples as the coordinate system of their lattices can be considered Cartesian but for all the other crystalline systems the situation is a bit more complicated. Few authors have calculated the maximum disorientation angle possible between two monoclinic crystals [220] [219]. In particular, Grimmer (1979) [220], calculated the density of distribution of the disorientation angles between monoclinic crystals in the case of no crystallographic correlation (random distribution of angles). Based on Grimmer's

calculation, the density of disorientation angles p(d), considering pairs of monoclinic solids with no correlation is found in this way [220]:

$$\text{For } 0° \leq d \leq 90°, \quad p(d) = (2/180)(1 - \cos d) \qquad \text{Eq. 4.2}$$

$$\text{For } 90° \leq d \leq 180°, \quad p(d) = (2/180)\tan(90°/2)\ \sin d \qquad \text{Eq. 4.3}$$

The curve showing the probability of distribution of disorientation angles, together with its mean (μ) and standard deviation (σ) resulting from the calculations of Grimmer (1979) [220] are the reported in the curve shown in Figure 4.31.

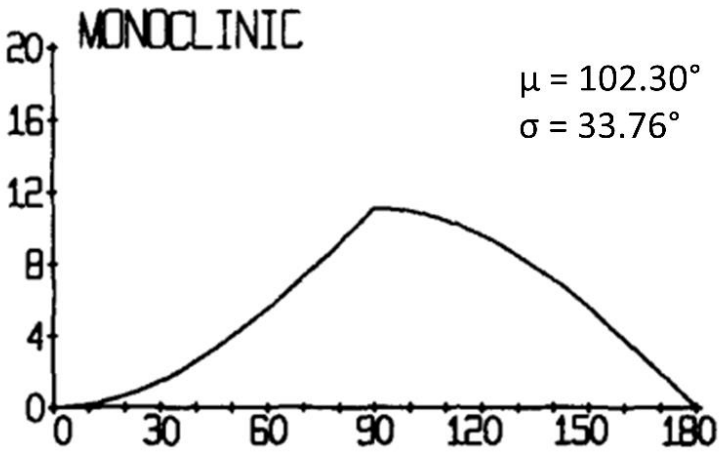

Figure 4.31. Curve of the p(d) calculated by Grimmer (1979) for a random distribution of disorientation angles between monoclinic grains [220].

In our case, the calculation of the disorientation angle between adjacent grains of hemihydrate and gypsum is complicated by their monoclinic structure. In particular, the hemihydrate grains were indexed with the I2 cell of Ballirano et al. (2001) [8], and the gypsum grains with the C2/c cell of Boeyens and Ichharam (2002) [69]. In order to overcome the difficulties arising from the non-Cartesian coordinates of the unit cell, the symmetry equivalents, and possible different choices of unique-axis, a different approach has been used to investigate the possible presence of correlation between the starting hemihydrate grains and the final gypsum grains. If we examine in detail the crystallographic structure of both hemihydrate and gypsum, we can see that there is a common crystallographic feature present in both of them. Figure 4.32 reports the crystallographic structures of hemihydrate [8] (a) and gypsum [69] (b). The common feature of both structures is highlighted by the black squares and extrapolated from the two unit cells. The fractional coordinates contained in the .cif files of both structures can be used to calculate the orientation in real space of a specific crystallographic element that is present in the structures. In this case, the fractional coordinates of Ca1 and Ca2 atoms (Figure 4.32) which are part of the common structural element between hemihydrate and gypsum structures were transformed into real space coordinates (laboratory space) via dot product with each UBI. Subsequently vectors were calculated to represent the direction of the distance between Ca1 and Ca2 atoms in the grains of both hemihydrate and gypsum.

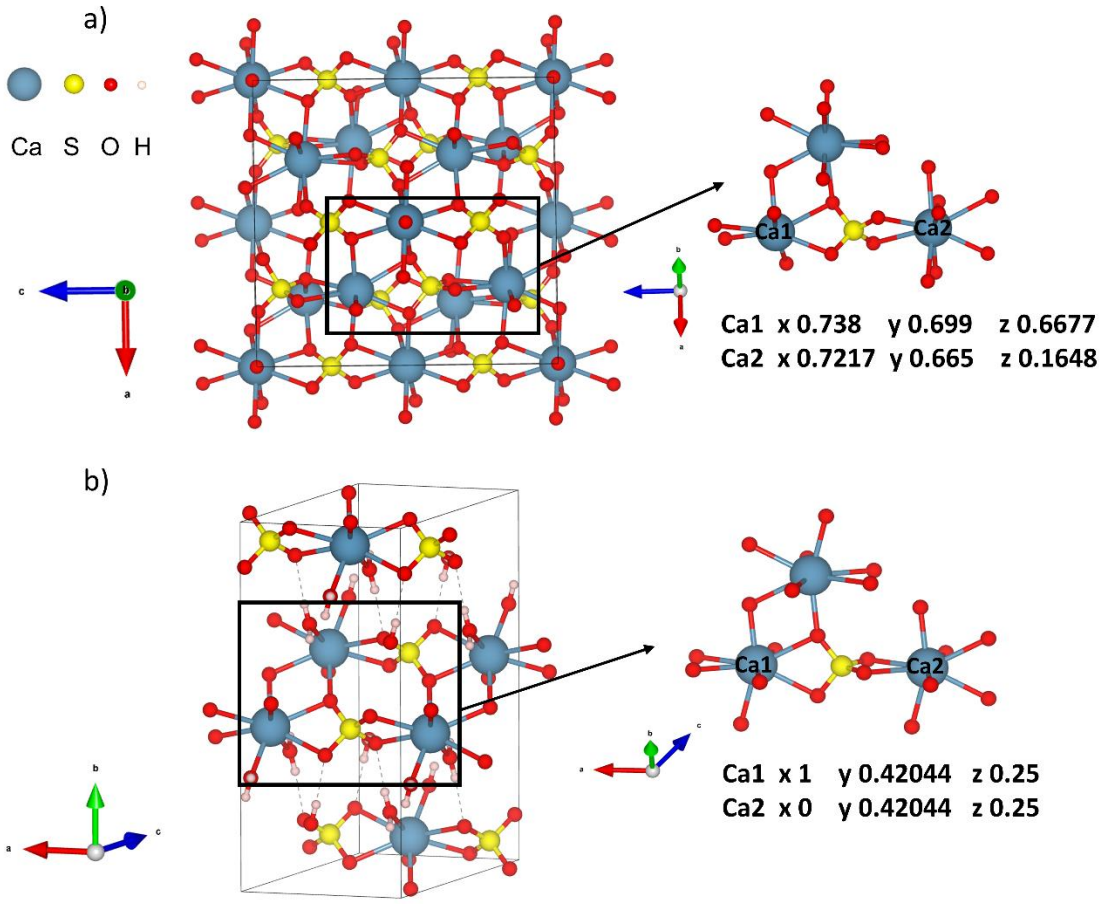

Figure 4.32. a) Hemihydrate I2 structure from Ballirano et al. 2001 [8]. b) Gypsum C2/c structure from Boeyens & Ichharam 2002 [69]. The common element between the two structures is highlighted.

A 3D visualization of the orientation in real space of the Ca1-Ca2 distance vectors for each grain of hemihydrate and each grain of gypsum is shown in Figure 4.33. The green arrows indicate where the Ca1-Ca2 distance vectors in each hemihydrate grain are pointing in the space and the purple arrows indicate the orientation of the same direction in the gypsum grains. The starting point of each vector is coincident with the position of each grain.

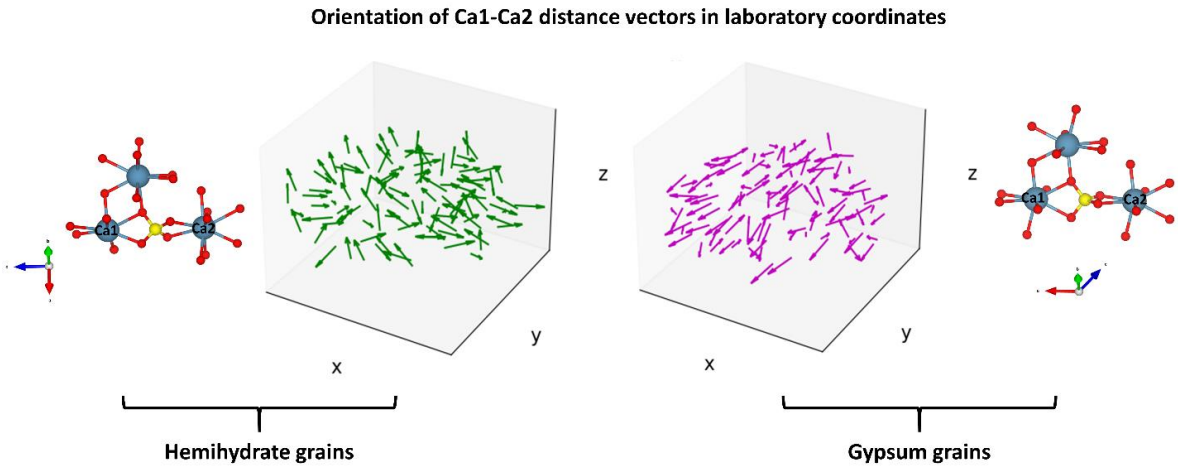

Figure 4.33. Plots of the orientation in real space of the Ca1-Ca2 distance vector for each hemihydrate grain (in green) and gypsum grain (in purple).

Once the vectors of the Ca1-Ca2 distance were calculated for all the grains, it was possible to calculate the disorientation angle between two nearest neighbour grains of hemihydrate and gypsum in order to check the possible presence of correlations. The histogram in Figure 4.34 shows the density of the distribution of the disorientation angles calculated for 102 pairs of nearest neighbour of hemihydrate and gypsum grains. The histogram shows a normal distribution with a mean of μ = 96.65°, and a standard deviation of σ = 30.82°.

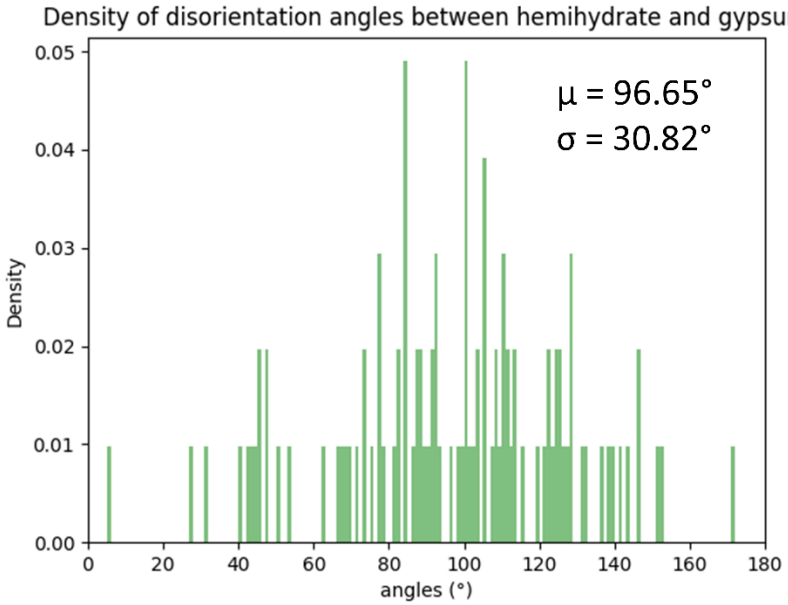

Figure 4.34. Histogram of the density of the disorientation angles calculated between the Ca1-Ca2 distance vector of two nearest neighbour grains of hemihydrate and gypsum.

The histogram and the values of the mean and standard deviation of the distribution of disorientation angles between pairs of hemihydrate and gypsum grains agree with the probability of distribution calculated by Grimmer (1979) [220] and shown in Figure 4.31. This means that there is no evidence of epitaxial relationships between dissolving hemihydrate and growing gypsum grains. In order to have additional proof of the non-correlation between the grains, pole figures representing the orientation of the [100], [010], and [001] directions were plotted (Figure 4.35). As it can be seen from the distribution of the orientations of both hemihydrate and gypsum grains, they are randomly distributed in the stereographic projections. Based on the calculation of the disorientation angles and the evaluation of the pole figures, we can say that in this system epitaxial nucleation if present is not a dominant process as it cannot be detected.

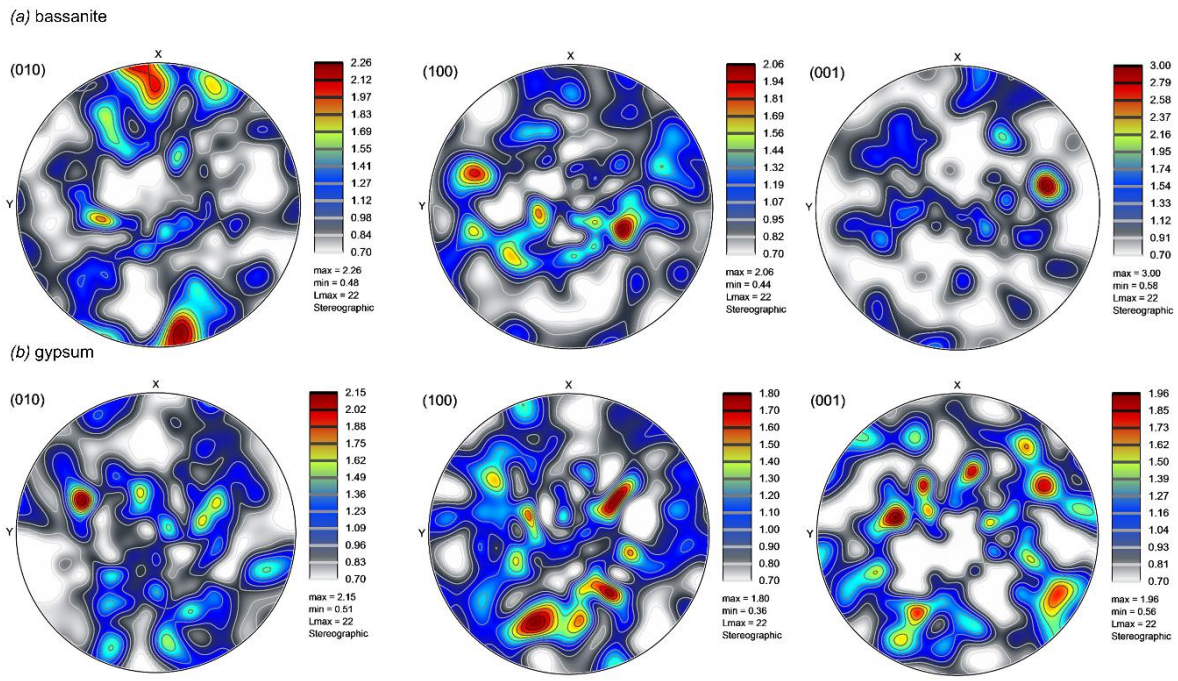

Figure 4.35. a) Pole figures showing the distribution of the orientations of hemihydrate grains in the [010], [100], and [001] directions. b) Pole figures showing the distribution of the orientations of gypsum grains in the [010], [100], and [001] directions. The pole figures were done using the software *ATEX* [203].

Since the hypothesis of epitaxial relationships between hemihydrate and gypsum has been ruled out, the hydration process must have occurred as a combination of dissolution and precipitation as was already proposed by Adrien et al. (2016) [13]. Since the capillary was not stirred during the hydration process in order to track the evolution of the same set of particles, the most plausible scenario is that the diffusion of ions from the dissolution of hemihydrate grains created local environments of supersaturation in the pores that drove the nucleation and precipitation of gypsum grains. This mechanism was already observed in other systems [19] [224]. The combination of s3DXRD and PCT permitted the reconstruction of the evolution of the coupled dissolution-precipitation process between hemihydrate and gypsum. Figure 4.36 shows the result of the 3D reconstruction of a pair of hemihydrate and gypsum grains measured with both techniques. The grain of hemihydrate is reconstructed from its dry conditions. During the development of the hydration process, the hemihydrate dissolves, showing preferential dissolution in specific crystallographic directions. After 1.5 hours of hydration, a particle of gypsum has grown enough to become visible from the PCT data. The particle of gypsum was growing spatially close to the hemihydrate, suggesting the formation of a local supersaturated environment in the pore between dissolving hemihydrate grains. The crystallographic orientation of the hemihydrate grain gave us the possibility to do considerations on the dynamic of its dissolution. In particular, from the 3D volumes, it is evident that the dissolution is preferentially driven from the center of the grain. This could be the result of the preferential dissolution of the more reactive (100) and (010) planes that are perpendicular to the elongation of the grain ([001] direction). In the first part of the dissolution (up to 3 hours), the hemihydrate particle maintains its elongation while in the last part it shrinks until complete dissolution. The gypsum grain, in this case, grew with a tabular morphology, showing its largest crystallographic surface corresponding to the {010} face. The dissolution behaviour shown by the hemihydrate grain in Figure 4.36 is the same that can be seen also in the

reconstruction of the two dissolving grains in Figure 4.23. This tells us that the "lamination" shown by the hemihydrate crystals is reproducible and occurs perpendicular to the [001] direction. The observation made in this study are in agreement with the theoretical calculations made by Mishra et al. (2021) [18] on the cleavage energy of specific crystallographic planes of calcium sulfate phases when exposed to hydration. From Mishra et al. (2021) [18] calculations resulted that the most reactive planes, and less stable when exposed to hydration, in the hemihydrate structure are indeed the (100) and (010). The preferential dissolution of (100) and (010) is also supported by the minimum number of bonds that have to be broken compared to the (001).

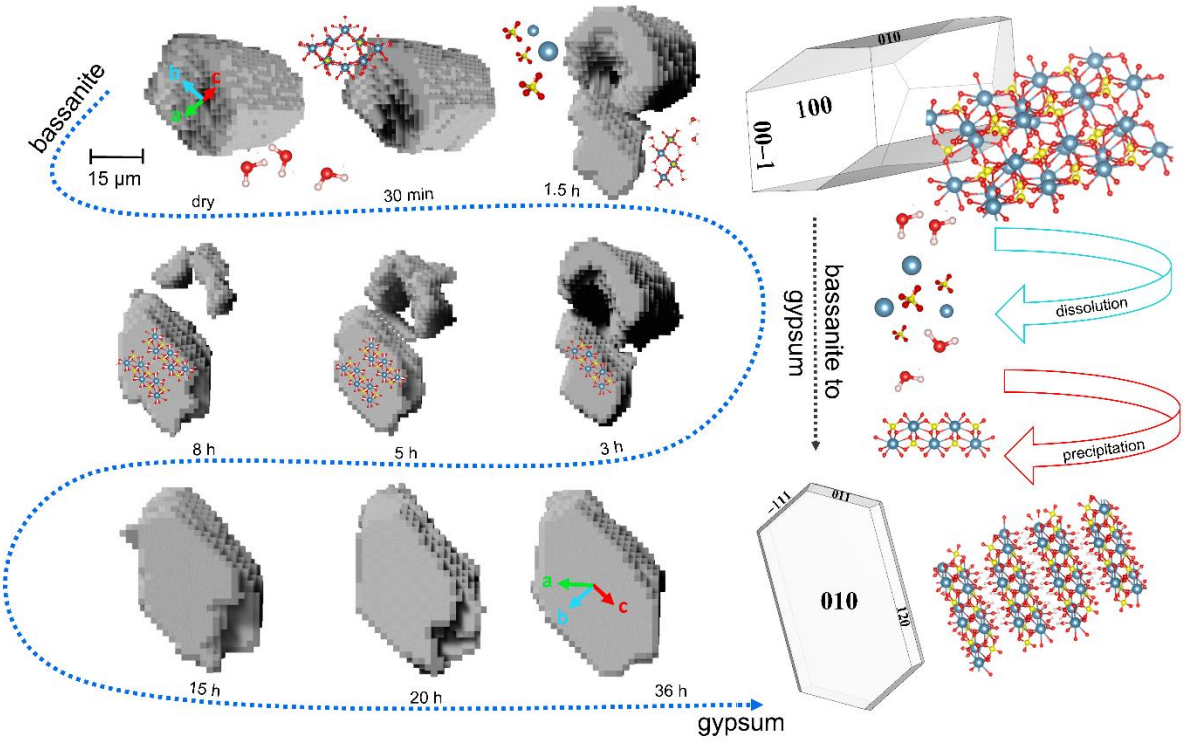

Figure 4.36. 3D reconstruction of one hemihydrate and one gypsum grain during their dissolution and precipitation. The grains are reconstructed following the hydration time from dry conditions to the last measurement taken at 36 hours of hydration. From the coupling of the PCT reconstructions and the s3DXRD orientation of the grains it is possible to understand the dynamic of the phase transformation process which is schematize in the right part of the Figure. Legend: grey balls = Ca atoms; yellow balls = S atoms; red balls = O; white balls = water molecules.

4.3.4.3. Accessing volumetric information during the hydration process

From the 3D reconstructions of the PCT data it is possible to calculate information such as the volume and the surface area of the particles during the hydration process. The reactive surface area in particular, is an important factor that influences the dissolution rate of crystals [225] [22]. Here, the surface area and the volume have been calculated for one dissolving grain of hemihydrate and one growing grain of gypsum. Figure 4.37 shows the two grains, hemihydrate in red and gypsum in blue, and the plots of their volume and normalized surface area. The segmentation of the two particles was done by hand using the ROI painter tool of the *Dragonfly* software, for this reason a segmentation range was considered for the values of volume and surface area. The segmentation ranges were calculated by eroding and dilating the segmented particles to establish a lower limit and an upper limit of voxels. The possibility of measuring the dissolution rate at the scale of an entire particle represents a great advantage for all the fields in which the dissolution of crystals is

studied. In particular, with this approach it is possible to calculate a mean dissolution rate of crystals independent from all the local defects that accelerate the dissolution providing different rates depending on the scale of the measurement [226] [227] [154] [26].

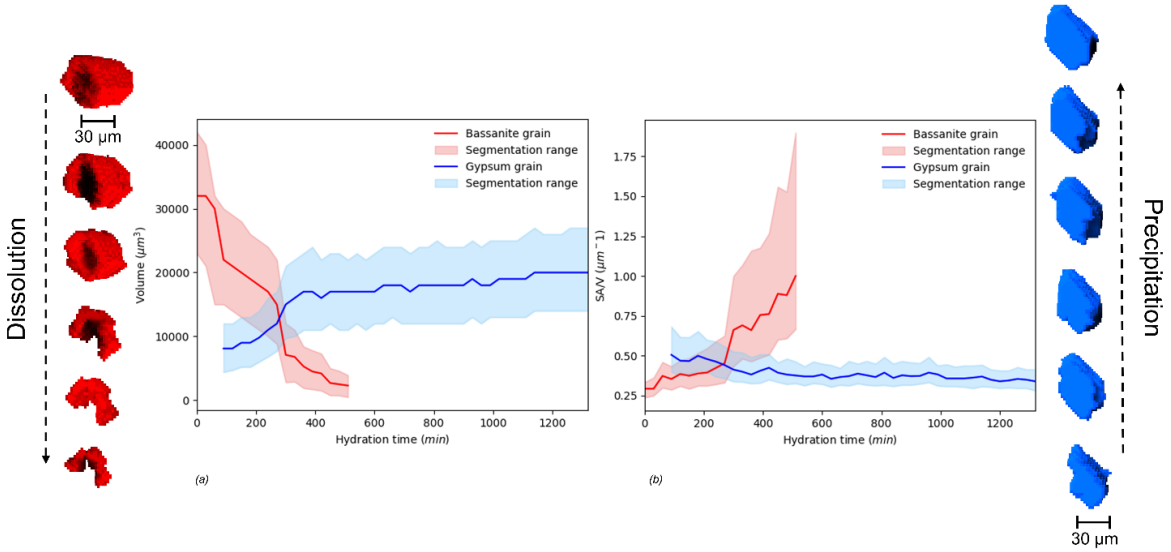

Figure 4.37. a) Plot of the variation of the volume of the hemihydrate grain reconstructed from PCT (red) and the gypsum grain reconstructed from PCT (blue) during the hydration process. b) Plot of the variation of the surface area normalized for the volume of the same hemihydrate grain (red) and gypsum grain (blue).

4.4. Hemihydrate dissolution

This section is dedicated to the results and discussions about the investigation of hemihydrate dissolution from different scales of observation. The study is divided into two parts. In the first part, the dissolution of crystals of Sample 2 in an aqueous solution with 10 mM polyacrylic acid (PAA), was observed *in situ* with AFM. In the second part, the dissolution of a bulk sample made of several crystals of Sample 2 with an aqueous solution prepared with 10 mM beta naphthalene sulfonate (BNS) was monitored *in situ* with PCT.

4.4.1. AFM results

Before performing the *in situ* dissolution experiment, AFM images of the surface of hemihydrate crystals submerged in ethanol were acquired to characterize the initial state of the surface. The images were acquired in contact mode, scanning the surfaces of the crystals that were attached to the bottom of a fluid cell with either mica disks or carbon tape. Figure 4.38 shows a picture of one of the crystals that was used to characterize the surface of hemihydrate in ethanol. The cantilever that was used to scan the crystal is the largest one of the picture, which reflects the laser. The crystal in this example was well attached to the mica disk while the tip located under the cantilever was scanning its surface.

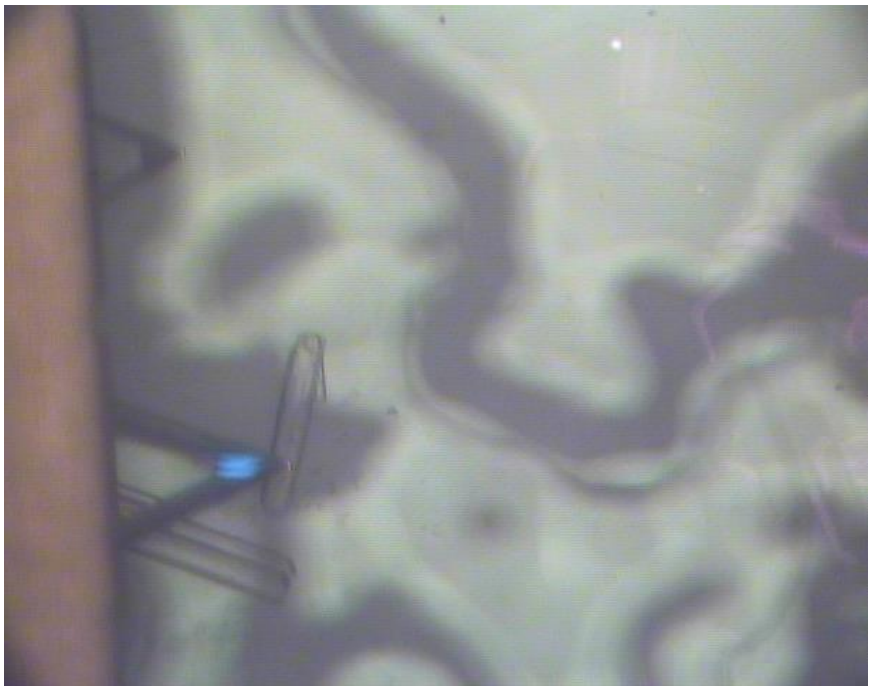

Figure 4.38. Example of the set-up of the AFM experiments. The largest cantilever that reflects the laser was used to scan the crystal that is attached to the mica disk.

Due to the hexagonal crystal habit of the α-hemihydrate crystals, it is not possible to determine which crystallographic surfaces were scanned. Two AFM images of the surface of a hemihydrate crystal in ethanol are presented in Figure 4.39. In both cases it is possible to see two distinct crystallographic surfaces separated by the edge between them. In Figure 4.39a the darkest surface presents some features which could be either imperfections from the growth process or etch pits due to the exposure to ethanol. The edge of the crystal presents a high concentration of defects providing a possible good spot to enhance the dissolution for the *in situ* measurements. The second surface presents a layered texture which is not present in the darker one.

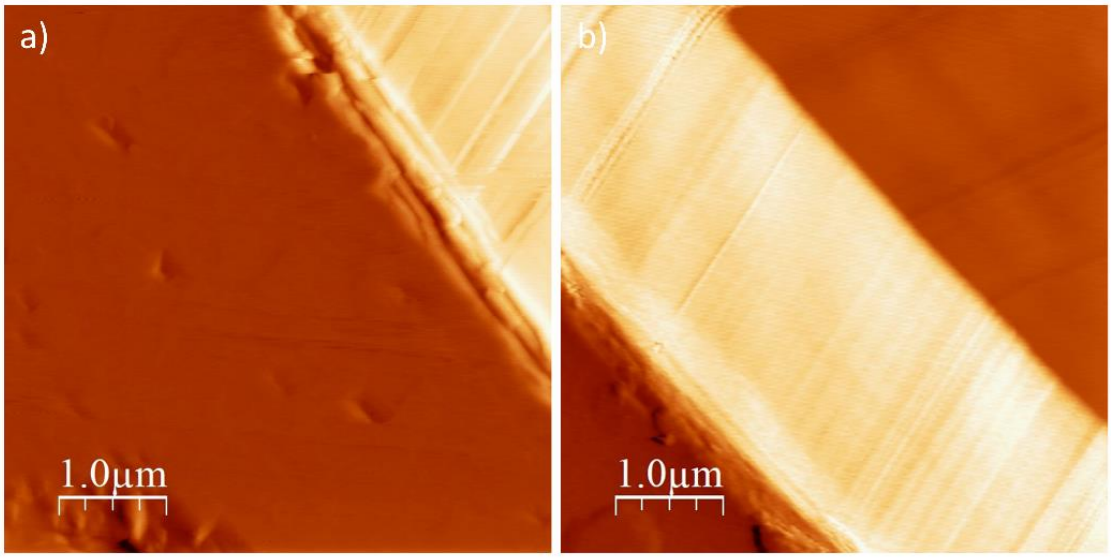

Figure 4.39. a) AFM image of a portion of a hemihydrate crystal submerged in ethanol. Two distint crystallographic surfaces separated by the edge between them are recognisible. The darker surface presents few defects. b) AFM image of a different portion of the same crystal of hemihydrate. In this case, also a portion of the mica disk that was used to keep the crystal in place is visible.

To observe the dissolution of the surfaces of hemihydrate crystals, solutions of PAA and pure water were prepared. The best conditions in terms of kinetics of dissolution were reached with a 10 mM PAA concentration. Crystals of hemihydrate were submerged in the solution while AFM images were acquired each minute to monitor their dissolution. The best dataset acquired is presented in Figure 4.40. A collection of 10 images were taken showing the behavior of different crystallographic surfaces of hemihydrate during dissolution. The first image (a) was taken right after submerging the crystal in the solution. It is difficult to find a reference that explains with enough precision which region of the crystal was scanned. The most plausible interpretation is that the region of the crystal that was scanned corresponds to an edge between two crystallographic surfaces. With the development of the dissolution, the surfaces in the central part of the image dissolve faster compared with the two external surfaces. After 7 minutes of hydration (h), the crystalographic surfaces present in the image were only three. In the last image (l) only the two external surfaces were left and the crystal shrinked considerably. After 9 minutes of hydration, it was not possible to scan the crystal anymore as it became to small and the tip of the cantilever lost the contact with it.

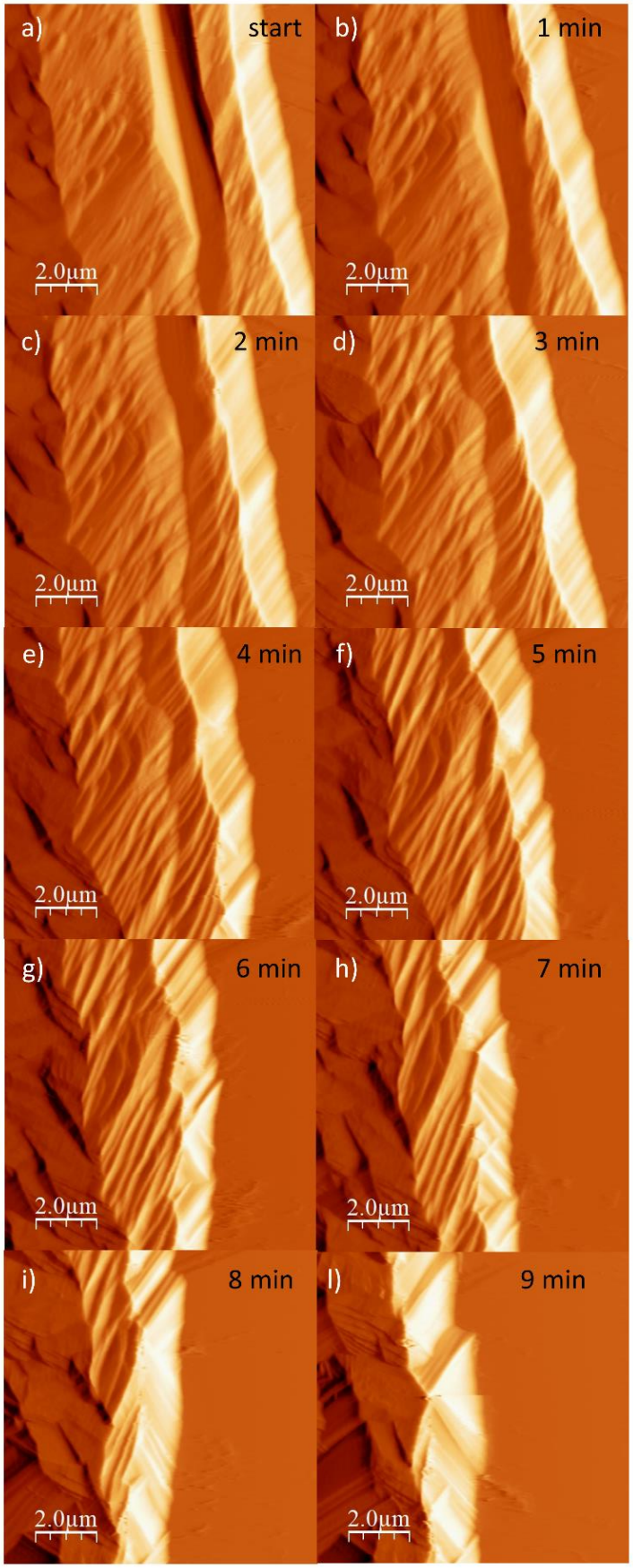

Figure 4.40. Collection of AFM images showing the dissolution of a portion of a hemihydrate crystal interpreted as the edge between two crystallographic surfaces.

In order to check the topography of the crystal, profiles were taken in the middle of the images including all the different surfaces. Figure 4.41a reports the first AFM image taken at the beginning of the dissolution. The profile shows six different surfaces identified based on their different slope. The crosses in the image correspond to the crosses in the profile indicating the borders between different surfaces. In Figure 4.41b, after 4 minutes of hydration, one of the surfaces that was present at the beginning of the process was disappeared. The surface that in (a) was delimited by the light blue and pink crosses, after 4 minutes of contact with the solution was not present anymore in the crystal. In the last images shown in Figure 4.41c, all the crystallographic surfaces that were present between the two external ones were disappeared. The topographic analysis of the AFM images confirms that the surfaces that the internal part of the crystal dissolved faster than the external ones.

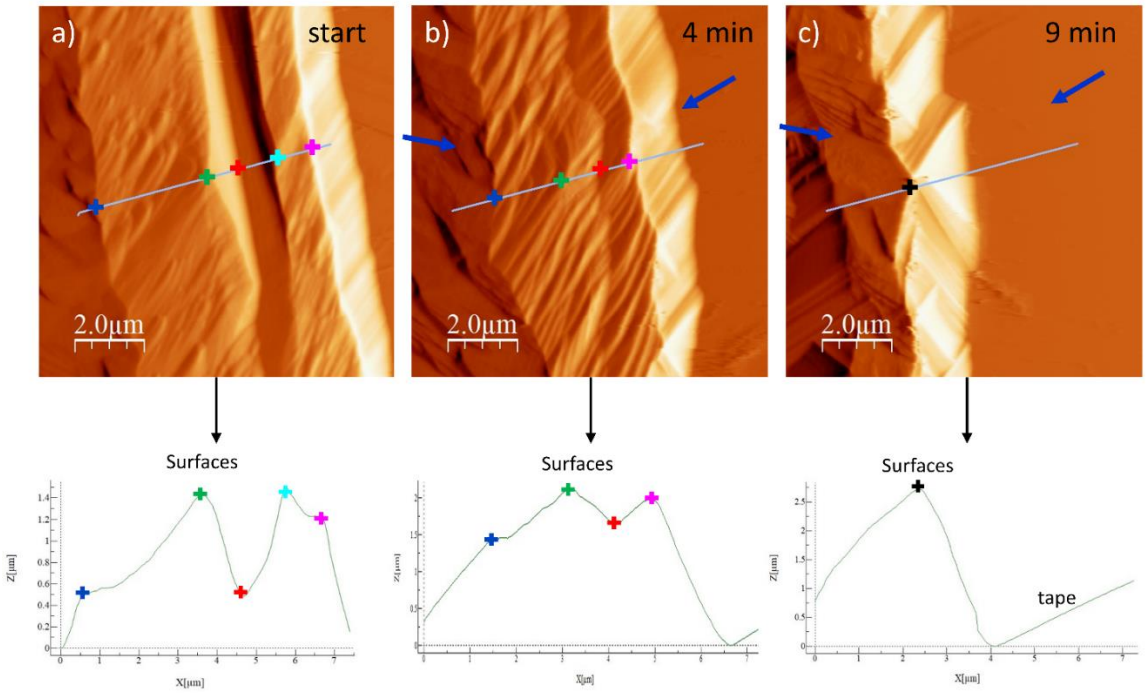

Figure 4.41. Topographic analysis of the AFM images taken during the *in situ* dissolution experiment of one crystal of hemihydrate.

4.4.2. PCT results

The sample that was scanned with PCT was prepared by filling a quartz capillary with crystals of Sample 2 and quartz wool on top to prevent the grains of hemihydrate from moving during the hydration. The projections of the capillary were reconstructed using *Tomwer* and *Nabu* in the same way explained in section 4.3.2. (see Figure 4.19). A first scan was acquired before hydrating the capillary in order to characterize the starting hemihydrate crystals. The first PCT scan and the one after 4 hours of hydration were reconstructed using the Paganin algorithm with δ/β ratio of 200 to do a first evaluation of the changes in the shape of the crystals. A 3D volumetric reconstruction of the dry sample is reported in Figure 4.42. The volume in green represents all the particles that were scanned. In the top part of the capillary were concentrated the quartz wool fibres, while the hemihydrate crystals were distributed in the rest of the capillary. The blue volume represents the

part of the capillary that was mostly filled by quartz wool and the orange volume represents the hemihydrate crystals. The large crystals of hemihydrate often exceeded 200 µm of length.

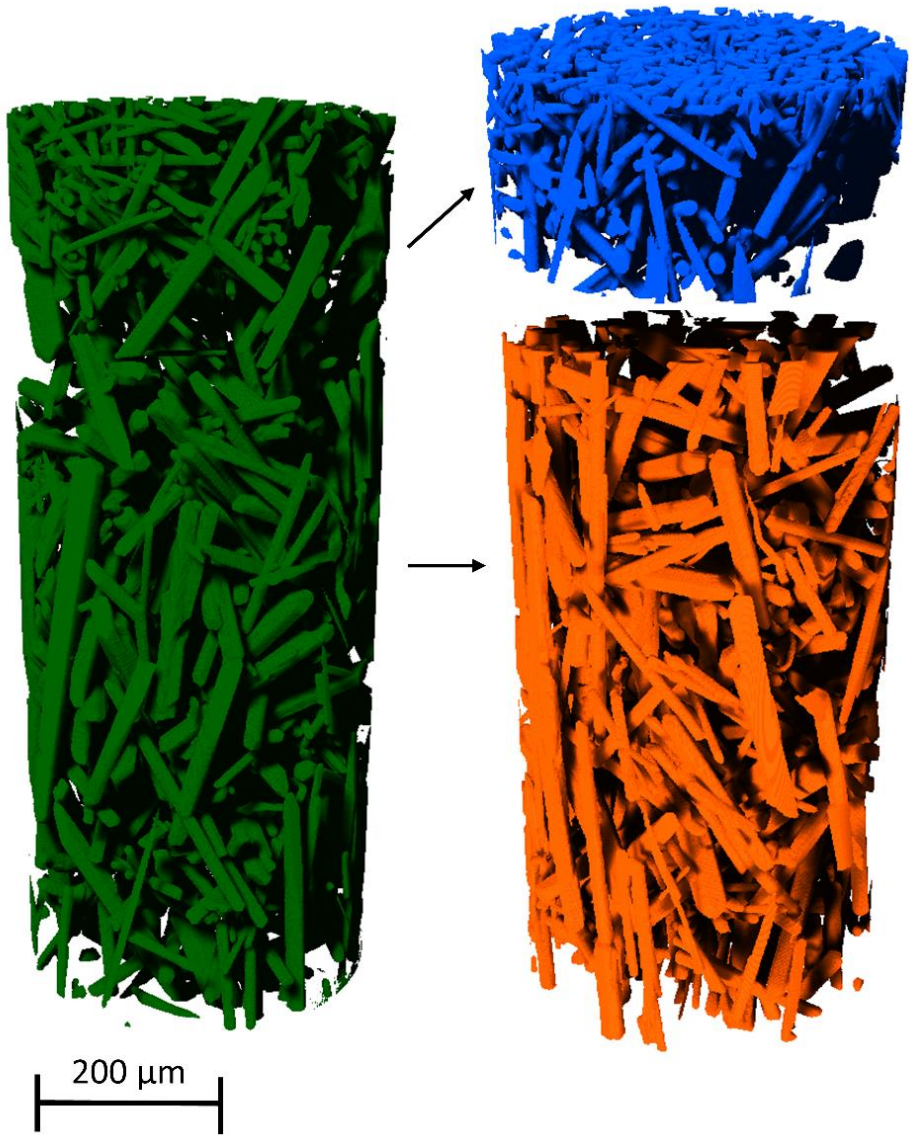

Figure 4.42. 3D reconstruction of the dry hemihydrate sample that was measure with PCT. The green volume represents the full sample scanned. The blue volume represents the portion of the sample that contained quartz wool fibres. The orange volume represents the portion of the sample that contained hemihydrate crystals.

The 3D reconstruction of the scan acquired after 4 hours of hydration, when gypsum crystals had replaced the hemihydrate in most of the sample, is reported in Figure 4.43. The top part of the sample is the region that was filled with quartz wool fibres and few hemihydrate crystals. From the whole volume it is clear how the top part of the sample did not change morphology. This is partly due to the fact that water did not stopped there and flow towards the bottom part of the capillary, and partly to the fact that in this region only few crystals of hemihydrate and many quartz wool fibres were present. The boundary that divides the part of the capillary that was in the water and the part that was not hydrated is recognisable in the volume as the curved line that separates the elongated but separated particles on top from the agglomerates of needles in the middle and bottom part of the capillary. In the hydrated part of the sample there are some empty regions that correspond to air bubbles that formed when the capillary was hydrated via a syringe.

Figure 4.43. 3D reconstruction of the sample after 4 hours of hydration. The volumes shows two distinct regions. The top part of the sample was not hydrated and shows a concentration of quartz wool fibres and few hemihydrate crystals. The middle and bottom part of the volume shows the region that was hydrated which at this point of the hydration is characterized by the presence of agglomerates of gypsum needles.

To be able to extract the dissolving hemihydrate crystals from the sample, the PCT datasets were segmented using a CNN U-Net 2.5 neural network implemented in the *Dragonfly* software. The bottom part of the capillary was selected for the application of the deep learning segmentation. This permitted to limit as much as possible the presence of quartz wool fibres and to speed up the training of the neural network compared to the treatment of the whole capillary. The slides were downsampled of a factor 2 in order to decrease the voxel size from 0.63 µm to 1.26 µm. This helped to improve the speed of the calculations during the training of the neural network. For a total of 500 slices, 3 frames were used to train the model. The frames were segmented by hand using the ROI painter tool of *Dragonfly* to attribute hemihydrate, gypsum and the background to different classes. The use of an additive, BNS in this case, to tune the shape of gypsum crystals to be uniform, together with the Paganin algorithm with δ/β ratio of 1000, helped to train the CNN to distinguish between hemihydrate and gypsum. Successively, when the model succeeded in replicate the

training frames, it was applied to all the rest of the volume. Twelve PCT scans, from the start of the hydration process to 4 hours of hydration, were analysed to investigate the dissolution of the bulk hemihydrate. Six of the twelve PCT scans were segmented using the deep learning tool. The first gypsum crystals became visible in the PCT slices after 1 hour of hydration. In total two models were trained. The first model was trained in the PCT scan relative to 1 hour of hydration in which only few crystals of gypsum were present. The second model was trained for the rest of the scans where the gypsum crystals concentration was increasing gradually. The last scan at 4 hours of hydration did not need any deep learning segmentation as all the hemihydrate crystals were dissolved. Figure 4.44 shows the results of the application of the deep learning segmentation in separating the hemihydrate from gypsum. The first volume in the series is relative to the dry portion of the capillary. The second volume is relative to the sample right after the injection of the solution. At 30 minutes of hydration, gypsum was not yet formed and the injection of the solution created an air bubble that forced some of the crystals of hemihydrate to move leaving an empty spot in the capillary. Gypsum started to be detectable after 1 hour of hydration and continued to grow until the last scan analysed after 4 hours of hydration. Gypsum crystals grew with uniform morphology creating agglomerates of needles which probably nucleated in the pores between dissolving hemihydrate crystals due to local enrichment in Ca^{2+} and SO_4^{4-} ions in the solution.

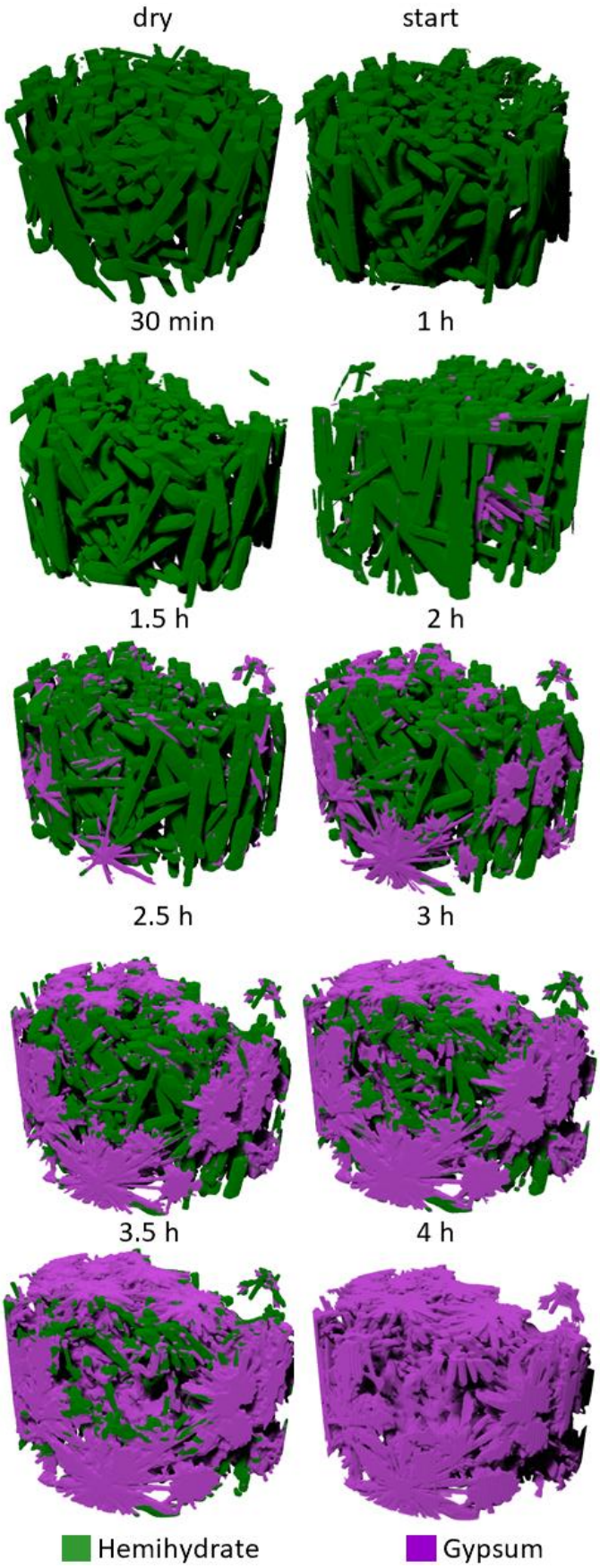

Figure 4.44. Results of the deep learning segmentation using the CNN U-Net 2.5 with the *Dragonfly* software. This approach permitted to separate the hemihydrate (green) from gypsum (purple). Gypsum started to be detected after 1 hour of hydration.

Once hemihydrate and gypsum were segmented as separated phases, it was possible to extract the hemihydrate component and to calculate the evolution of the volume and surface area during its dissolution. The 3D reconstructions of the bulk hemihydrate extracted with the deep learning segmentation are reported in Figure 4.45. The 3D volumetric reconstructions of the dissolving hemihydrate crystals suggest that the dissolution increased from 2 hours of hydration when the crystals appear visibly damaged. After 2.5 hours of hydration, the smallest crystals are almost completely dissolved while the largest maintain their elongated shape. After 3 hours of hydration, also the largest crystals appear shrunk and after 3.5 hours only small fragments of crystals are present. In the last reconstruction an agglomerate of thin fibres shaped particles is visible in the top part of the volume. This could represent a small amount of quartz wool that did not undergo dissolution.

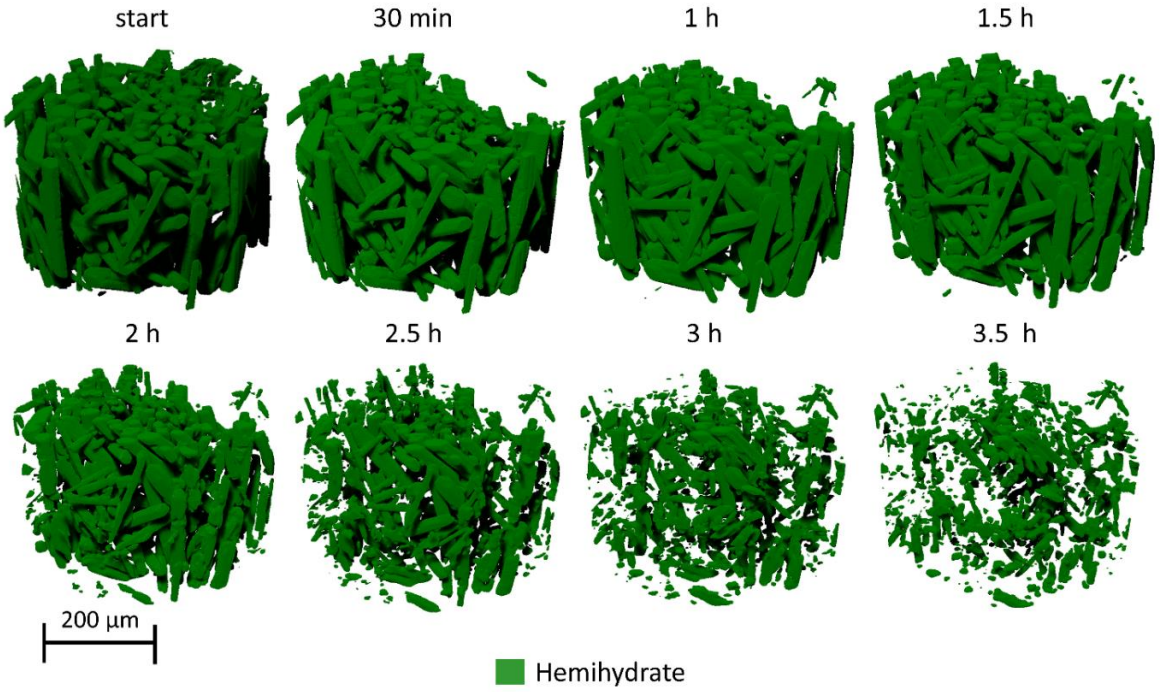

Figure 4.45. Volumes of hemihydrate bulk sample extracted from the full sample with the deep learning segmentation. The volumes show the evolution of the hemihydrate crystals during their dissolution.

The volume and specific surface area values of the dissolving bulk hemihydrate are plotted in Figure 4.46. The first data point is relative to the dry hemihydrate, the second is relative to the hemihydrate right after the injection of the solution, then three data points are taken every 12 minutes until 24 minutes after the hydration. From 30 minutes of hydration to 3.5 hours the data points are taken every 30 minutes. From the plots, it is evident that a first drop in the volume of hemihydrate occurs as soon as the solution is injected in the capillary. Then the system remains stable up to 1 hour of hydration. After 1 hour of hydration, the hemihydrate starts to dissolve fast until its complete dissolution at 3.5 hours from the start of the hydration. The reason of the first drop in hemihydrate volume could be due to the injection of the solution that moved part of the crystals towards the bottom of the capillary leaving an empty space (see Figure 4.45).

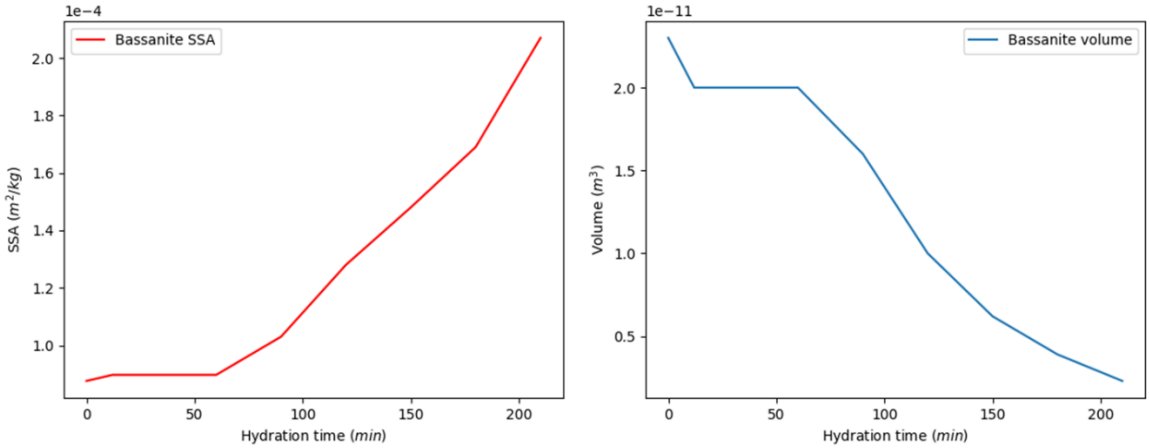

Figure 4.46. Plot of the surface area normalized by the volume (red curve) and the volume (blue curve) of the hemihydrate bulk during its dissolution.

4.4.3. Discussion

The shape and high solubility of calcium sulfate hemihydrate complicate the observation of its dissolution at the surface scale. The hexagonal crystal habit that is peculiar of α-hemihydrate for example, represents a limitation in the identification of the crystallographic surfaces that are scanned with the AFM. In particular, to perform the dissolution experiment at the AFM, the crystals were attached to the bottom of a fluid cell with carbon tape exposing the surfaces of the elongated part of the crystal to the tip of the cantilever. Figure 4.47 shows models of the crystal habit of α-hemihydrate crystals built on the hemihydrate structure of Ballirano et al. (2001) [8]. The models report some of the possible crystallographic surfaces that can be scanned with the AFM. Since most of the crystals were deposited in the tape by attaching the elongated part, anyone of the crystallographic surfaces shown in the first two models of Figure 4.47 could be scanned.

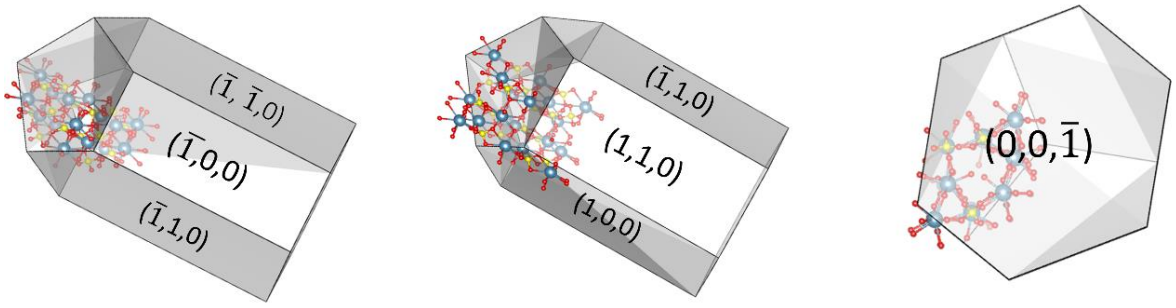

Figure 4.47. Models of the hemihydrate crystal habit made with VESTA on the structure of Ballirano et al. 2001.

PAA has been demonstrated to act as a retardant in the nucleation and growth of gypsum crystals. A recent study by Nicoleau et al. (2019) [176] suggested that the polymer molecules inhibit gypsum nucleation by decreasing the probability of collisions between the ions in the supersaturated solution. Figure 4.48 shows a diagram of the mechanism proposed by Nicoleau et al. (2019) [176]. In (a) is represented the nucleation process in the absence of the additive. The collisions between the ions in the supersaturated solution would bring to the formation of nuclei that, once they obtained the critical size, would form crystalline gypsum nuclei. In (b) is represented the same mechanism but in the presence of the retarding additive. PAA in this case, slows down via complexation the rate of the collisions between ions in the supersaturated solution causing a delay

in gypsum crystallization. The process described in Figure 4.48 is expressed in the framework of the CNT but Nicoleau et al. (2019) [176] specified that the same mechanism is applicable also to the precursors/primary phases that may be involved in the multi-step precipitation pathway of gypsum.

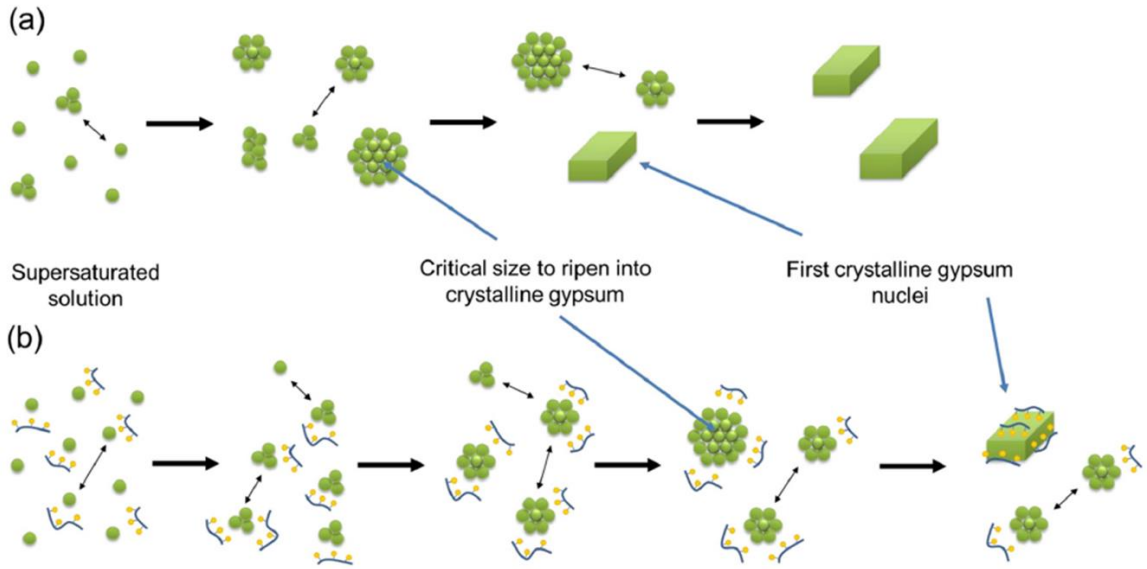

Figure 4.48. a) Nucleation of crystalline gypsum in the absence of additives. b) Nucleation of crystalline gypsum in the presence of retarding additives. Taken from Nicoleau et al. (2019) [176].

This mechanism is proposed to explain the interaction between retarding polymers and gypsum nuclei. Since no investigations have been done with the aim of understanding whether retarding additives also interact with hemihydrate, we do not know for sure what is reason for the decreased speed of dissolution observed. A possible explanation however, could be that the additive interacts with hemihydrate through surface adsorption inhibiting its dissolution. The most noteworthy observation that resulted from the AFM *in situ* dissolution experiment is that the region of the crystal associated with the edge between two crystallographic surfaces dissolved faster than the two external surfaces (Figure 4.41). This evidence is in agreement with what was previously observed by Arvidson et al. (2003) [29]. It has been proposed that the concentration of defects, such as kink sites and step densities, at the edges and borders between the crystallographic surfaces of crystals, could explain the discrepancy of few orders of magnitude in the dissolution rates measured at different scales. Arvidson et al. (2003) [29] found these discrepancies comparing the rate of dissolution of the surface of carbonate minerals with vertical scanning interferometry and the bulk dissolution of both single crystals and powders. The mechanism proposed by Arvidson et al. (2003) [29] (Figure 4.49) could also be the reason why in our hemihydrate crystal the region of the boundary between two crystallographic surfaces is dissolving faster than the rest of the crystal.

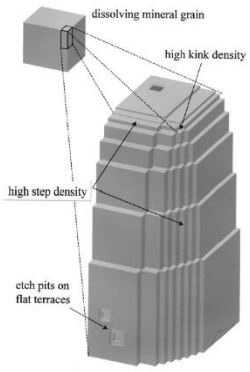

Figure 4.49. Drawing of the portion of an ideal crystal where the edge between two surfaces presents a dense concentration of steps and kink sites driving the dissolution, while the dissolution at the surface of driven by etch pits and stepwaves. Taken from Arvidson et al. (2003) [29].

Even though the use of the retarding additive permitted to slow down the dissolution kinetics enough to acquire few AFM images of the dissolving crystal, it was not possible to observe the formation of etch pits in the surfaces. It was therefore not possible to calculate the rate of dissolution at the atomic scale.

The presence of BNS in the solution for the hydration during the PCT *in situ* experiment, helped to tune the morphology of gypsum crystals. Figure 4.50 shows two agglomerates of particles of hemihydrate (a) and gypsum (b). The hemihydrate was segmented from the dry PCT scan and the gypsum was segmented from the PCT scan after 4 hours of hydration. The gypsum crystals presented needle shape and were agglomerated in flakes probably originated by local ion enrichment in the solution. The differences in the shape of the crystals of the two phases and the accentuated contrast between them that the application of the Paganin algorithm gave to the PCT reconstructions, made it possible to separate the two phases with the deep learning segmentation, introducing an innovative way to study the evolution of dissolution/precipitation reactions.

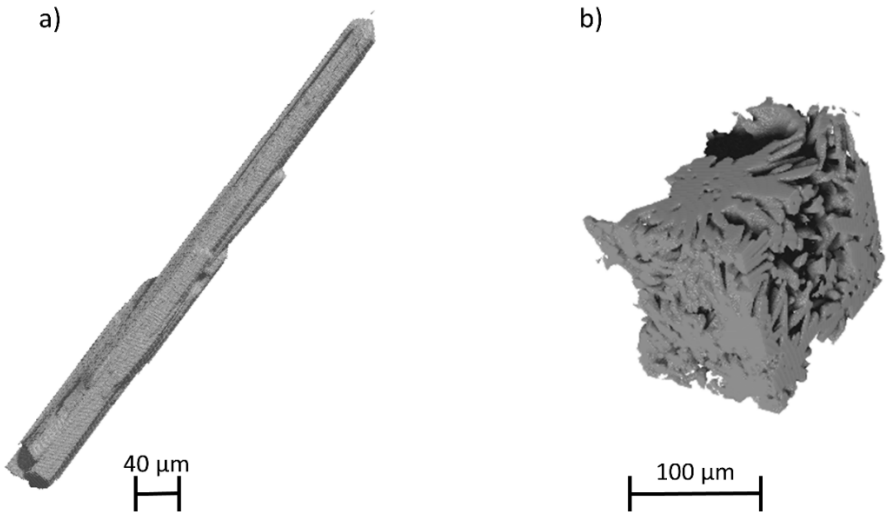

Figure 4.50. a) Agglomerate of hemihydrate particles segmented from the dry sample. b) Agglomerate of gypsum particles segmented from the sample after 4 hours of hydration.

The measurements of volume and specific surface area during the dissolution of hemihydrate reported in the plots of Figure 4.46 were used to calculate the surface area normalized dissolution

rate. The calculated value for the dissolution rate of hemihydrate in the presence of BNS (10 mM) is $r = 1.17 \times 10^{-3}$. The evolution of the reactive surface area has never been measured directly before during an *in situ* dissolution experiment. As reported in Chapter 2, Eq. 2.4, the reactive specific surface area is a direct factor in the definition of the dissolution rate, which makes its determination difficult. It is also a parameter that is difficult to access experimentally. There is only one example in the literature where the rate of dissolution of hemihydrate has been calculated from bulk powder as normalized BET surface rate [22]. There, the dissolution of different types of hemihydrates was measured in deionized water and in the presence of cellulose ethers (CE) in different concentrations. The rate of dissolution in deionized water of the most similar sample analysed by Brandt and Bosbach (2001) [22] to our Sample 2, is $r = 4.5 \times 10^{-4}$. Comparing the results of Brandt and Bosbach (2001) [22] with ours, it is evident that the use of BNS increases of one order of magnitude the velocity of the dissolution rate of bulk hemihydrate. This is not surprising considering that BNS has been demonstrated to act as a seeding material to promote the hydration of cement [229]. In the case of Portland cement, BNS can be used to precipitate nanocomposites of C-S-H-BNS that represent seeds for the early hydration of cement [229]. It is possible that a similar process of co-precipitation of gypsum and BNS occurs also in the system of gypsum plaster which enhances the precipitation of gypsum and therefore also the dissolution of hemihydrate. To investigate the possible occurrence of such process we would need to perform additional experiments.

5. Conclusions and perspectives

The main purpose that motivated the development of this Ph.D. work was to demonstrate how innovative and powerful techniques could represent a promising tool to fully characterize complex processes such as the hydration of gypsum plaster. The main challenge of this project was to apply unconventional techniques, s3DXRD in particular, to a system that was never been characterized this way. Understanding the steps of the hydration process of gypsum plaster, however, was not the only goal. I wanted to provide a deep multiscale characterization hoping to answer some of the long-standing questions that have interested the gypsum plaster scientific community for many years.

The first point of this hierarchical characterization was dedicated to shedding light on the topic of the α and β-hemihydrate crystallographic structures. The measurements made with HR-XRPD at the ID22 beamline of the ESRF revealed for the first time structural differences between the hemihydrate produced by wet methods (α) and the hemihydrate produced by dry methods (β). Previously, both XRPD and SXRD studies had been done to understand whether or not the two forms of hemihydrate presented different structures [9] [10] [23]. In none of these cases, proof of different crystallographic structures had ever been furnished. Only Follner et al. (2002) [23] addressed the presence of different features in the powder diffraction pattern of α-hemihydrate compared with the β but the proof of these features was never shown. The reason why the differences between α and β-hemihydrate were never fully understood lies in the lack of resolution of the analyses that were done previously. With HR-XRPD it was possible not only to observe the peak splitting that characterizes α-hemihydrate patterns but also to refine them with the Rietveld method. It is evident now that different synthesis methods such as the precipitation of hemihydrate from solution and calcination of gypsum, give final compounds with different characteristics. In the case of α-hemihydrate, the sample contains more than one monoclinic I2 phase with slightly different cell parameters and disordered water, while in the case of β-hemihydrate, only one monoclinic I2 phase is present with ordered water. The relevance of this information is understandable as α and β-hemihydrate are known to behave differently during hydration. The α type presents a shorter induction time compared to the β type, which then hydrates faster producing less performing plaster [2]. The differences that we found between α and β-hemihydrate could represent an additional reason for their different hydration behaviour: the α type contains a higher density of 'structural defects', which result in a higher reactivity when exposed to an undersaturated solution. The detailed single crystal diffraction analysis led also to the finding that mosaicity is present along the [001] direction. This is the first time that this is directly quantified using a structural technique (the previous one by Stawski et al. 2019 [24] was from TEM observations of nanodomains). The occurrence of this mosaicity supports the model of bassanite formation from the oriented aggregation of calcium sulfate clusters.

For the second part of this hierarchical study, we moved to a larger scale investigating how the dissolution of α-hemihydrate and precipitation of gypsum are linked from both a morphological and crystallographic point of view. The main result that we got from this study is the demonstration that the combined application of two powerful complementary techniques, s3DXRD and PCT, represents a suitable and useful tool to investigate *in situ* phase transformation processes such as the one that generates from the hydration of hemihydrate into gypsum. Our approach allowed a

multiscale characterization that linked the crystallographic and textural features of the hydrating system. The coupled mechanisms that involve the dissolution of hemihydrate, the formation of local supersaturated areas in the pores between hemihydrate crystals, and the following precipitation of gypsum have been reconstructed throughout all their steps thanks to the PCT measurements. The s3DXRD measurements permitted us to establish that no crystallographic correlation was present between the starting hemihydrate crystals and the final gypsum crystals, ruling out the presence of epitaxial growth of gypsum on the hemihydrate surfaces in our system. From the complementary information achieved from both s3DXRD and PCT, it was possible to observe the preferential dissolution dynamics of the (010) and (100) planes of α-hemihydrate crystals confirming the results of theoretical calculations [18]. The preferential dissolution that we observed may be related to the presence of structural defects in some specific directions of the hemihydrate crystals that lead to the development of layered textures during the dissolution. In this work, the hydration process of gypsum plaster was characterized at the mesoscale providing a link between microscopic and macroscopic processes in the same system, and paving the way for innovative types of investigations. Despite the complexities associated with the scale-up of experiments from the laboratory scale to the field, the suitability of coupled s3DXRD and PCT techniques to study dissolution/precipitation processes, opens new possibilities for both industrial purposes, such as tuning setting reactions in hydraulic binders, and in the geochemistry field, to study mineral weathering.

In the last part of this work, we focused on the dissolution of α-hemihydrate monitoring the process from two different scales of observations. A considerable amount of work has been done previously on understanding the dissolution behaviour of gypsum and anhydrite at the atomic scale [25] [26] [27] [28] while hemihydrate had never been observed before. Our approach, which included the preparation of solutions with relevant additives used in industrial processes, allowed us to observe the surface dissolution of α-hemihydrate and to measure the surface area of the dissolving hemihydrate fraction from a bulk sample. In one case the use of PAA, which is considered a model polymer for superplasticizers, helped us to tune the kinetics of the dissolution of the crystals of hemihydrate. This permitted us to acquire a dataset of AFM images that shows the preferential dissolution of the edges of the crystals compared with the surfaces providing evidence of a phenomenon that was previously proposed by Arvidson et al. (2003) [29]. In the other case, the addition of BNS to the solution that was used to hydrate *in situ* a sample of α-hemihydrate led to the precipitation of gypsum crystals with a uniform shape that helped to distinguish them from the hemihydrate crystals in the PCT measurements. The application of deep learning segmentation methods to separate hemihydrate and gypsum crystals proved to be a reliable and powerful tool to deal with heterogeneous systems where simple segmentation methods fail to retrieve the information needed. In this case, the trained CNN U-Net 2.5 available in the *Dragonfly* software separated successfully the hemihydrate fraction from the gypsum one thanks to the increased phase contrast provided by the Paganin algorithm and the different shapes of the two phases. This approach was never been applied before to study the development of dissolution reactions. Until now, only one study was done on measuring the dissolution rate of hemihydrate from BET analysis [22]. Our study provides for the first time an estimation of the bulk dissolution rate of α-hemihydrate and a direct measurement of the reactive surface area.

Overall the hydration process that brings to the formation of gypsum plaster from α-hemihydrate, has been characterized in all its sub-processes using unconventional, innovative, and complementary techniques that open new perspectives for both industrial applications and fundamental knowledge of dissolution and precipitation processes. The main scientific questions that this Ph.D. introduces and that could be investigated in future works can be summarized in these points:

- The crystallographic characterization of the α and β-hemihydrate structures, which demonstrated that different syntheses produce compounds with different lattice parameters most likely due to different amounts of water incorporated, reopens the question of how is this related to the properties of the hydrated gypsum plaster. In particular, the evidence of mosaicity and the presence of defects along the [001] direction in α-hemihydrate crystals, could be related to the preferential dissolution from the center of the crystals that was observed from the s3DXRD and PCT measurements. A reproduction of the same experimental approach on β-hemihydrate samples could reveal a different behaviour of dissolution. In particular, if we consider that the presence of defects along the [001] direction of α-hemihydrate crystals are inherited features from the multi-step nucleation pathway, they should not be present in β-hemihydrate crystals that are produced from the calcination of gypsum. If a measurement of the mosaicity and a detailed examination of the shape of the reflections from SXRD data of β-hemihydrate crystals would reveal such a difference in the mesostructure of the two forms of hemihydrate, this could represent a factor that influences the hydration process.

- Since we have established the suitability of the s3DXRD technique for the investigation of *in situ* processes in the gypsum plaster system, this opens the way to new possible studies. For example, we can think about focusing on the hardened gypsum paste properties. *In situ* experiments combining s3DXRD and PCT could be performed while applying external forces or increasing temperatures to the hardened paste. One of the main advantages of the s3DXRD is that it is possible to reconstruct strain gradients throughout the sample. At the ID11 beamline of the ESRF, there is the possibility to build sample environment setups to recreate the conditions that we want to investigate. Recently, Thakur et al. (2023) [30] performed a similar experiment on concrete at the ID11 beamline. They measured and modeled the evolution of the microstructure of cement when exposed to small strains and compressive loads. To do so, they mounted a custom uniaxial compression apparatus on the 3DXRD station of ID11 and acquired 3DXRD and XR-CT while the forces were incremented on the sample [30]. A similar experimental approach could be used also to investigate the response of gypsum plaster to such external stimulations increasing the knowledge of the properties and durability of the material.

- Another interesting route to explore is to understand how the role of different additives influences the dissolution of hemihydrate and the precipitation of gypsum from tomography *in situ* experiments. In the case of this Ph.D. work, only BNS was used to prepare the solution to hydrate the hemihydrate crystals during the *in situ* PCT experiment but it could be useful to repeat the same experiments also with PAA and polystyrene

sulfonate (PSS). Moreover, in this work, only the dissolution of hemihydrate was investigated. In future works, it could be interesting to focus also on the precipitation of gypsum. With the innovative way of retrieving the reactive surface area of dissolving hemihydrate and precipitating gypsum that we proposed, the dissolution rates of hemihydrate and also the induction times of the hydration reactions could be calculated and compared. This would provide valuable information to deepen our understanding of the role of the additives that are typically used in industry to tune the hydration process of gypsum plaster and perhaps also to optimize their use in the future.

List of acronyms

AFM	Atomic Force Microscope
CNNs	Convolutional Neural Networks
CNT	Classical Nucleation Theory
HR-TEM	High-resolution Transmission Electron Microscopy
HR-XRPD	High-resolution X-ray Powder Diffraction
ESRF-EBS	European Synchrotron Radiation Facility-Extremely Brilliant Source
PCT	Phase Contrast Tomography
PDF	Pair Distribution Function
SEM	Scanning Electron Microscopy
S3DXRD	Scanning Three-Dimensional X-ray Diffraction
XRPD	X-ray Powder Diffraction
TGA-DSC	Thermogravimetric Analysis-Differential Scanning Calorimetry
µSXRD	µ Single Crystal X-ray Diffraction

References

[1] A.E.S. Van Driessche, T.M. Stawski, M. Kellermeier, Calcium sulfate precipitation pathways in natural and engineered environments, Chemical Geology. 530 (2019) 119274.

[2] N.B. Singh, B. Middendorf, Calcium sulphate hemihydrate hydration leading to gypsum crystallization, Progress in Crystal Growth and Characterization of Materials. 53 (2007) 57–77.

[3] P. Gallitelli, Ricerche sul solfato di calcio semidrato e sull'anidrite solubile, Period. Mineral. 4 (1931) 132–171.

[4] N.N. Bushuev, On the structural features of CaSO4*0,5H2O and CaSO4*0,67H2O, Doklady Akademii Nauk SSSR. 255 (1980) 1104–1109.

[5] W. Abriel, Calcium sulfat subhydrat, CaSO4.0,8H2O, Acta Crystallographica C39. (1983) 956–958.

[6] W. Abriel, R. Nesper, Bestimmung der Kristallstruktur von CaSO4(H2O)0.5 mit Rontgenbeugungsmethoden und mit Potentialprofil-Rechnungen, Zeitschrift Für Kristallographie - Crystalline Materials. 205 (1993) 99–113.

[7] C. Bezou, A. Nonat, J.C. Mutin, A.N. Christensen, M.S. Lehmann, Of the crystal structure of gamma-CaSO4, CaSO4*0.5(H2O), and CaSO4*0.6(H2O) by powder diffraction methods, Journal of Solid State Chemistry. 117 (1995) 165–176.

[8] P. Ballirano, A. Maras, S. Meloni, R. Caminiti, The monoclinic I 2 structure of bassanite, calcium sulphate hemihydrate (CaSO4· 0.5 H2O), European Journal of Mineralogy. 13 (2001) 985–993.

[9] H. Weiss, M.F. Bräu, How Much Water Does Calcined Gypsum Contain?, Angew. Chem. Int. Ed. 48 (2009) 3520–3524.

[10] H. Schmidt, I. Paschke, D. Freyer, W. Voigt, Water channel structure of bassanite at high air humidity: crystal structure of $CaSO_4 \cdot 0.625H_2O$, Acta Crystallogr B Struct Sci. 67 (2011) 467–475.

[11] C.H. Desch, The setting of cements and plasters. A general discussion. The mechanism of the setting process in plaster and cement, Transactions of the Faraday Society. 14 (1919) 1–7.

[12] H. Le Chatelier, De l'action de la chaleur sur les argiles, bulmi. 10 (1887) 204–211.

[13] J. Adrien, S. Meille, S. Tadier, E. Maire, L. Sasaki, In-situ X-ray tomographic monitoring of gypsum plaster setting, Cement and Concrete Research. 82 (2016) 107–116.

[14] J. Seiller, T. Bonnal, J. Adrien, S. Meille, S. Tadier, E. Maire, A. Bonnin, 4D in situ monitoring of the setting of α plaster using synchrotron X-ray tomography with high spatial and temporal resolution, Construction and Building Materials. 304 (2021) 124632.

[15] M. Ilett, H.M. Freeman, Z. Aslam, J.M. Galloway, D.P. Klebl, S.P. Muench, I.J. McPherson, O. Cespedes, Y. Kim, F.C. Meldrum, S.R. Yeandel, C.L. Freeman, J.H. Harding, R.M.D. Brydson, Evaluation of correlated studies using liquid cell and cryo-transmission electron microscopy: Hydration of calcium sulphate and the phase transformation pathways of bassanite to gypsum, Journal of Microscopy. 288 (2022) 155–168.

[16] C. Jia, G. Zhu, B.A. Legg, B. Guan, J.J. De Yoreo, Bassanite Grows Along Distinct Coexisting Pathways and Provides a Low Energy Interface for Gypsum Nucleation, Crystal Growth & Design. 22 (2022) 6582–6587.

[17] M.J. Ridge, Effect of Temperature on the Structure of Set Gypsum Plaster, Nature. 182 (1958) 1224–1225.

[18] R.K. Mishra, K. Kanhaiya, J.J. Winetrout, R.J. Flatt, H. Heinz, Force field for calcium sulfate minerals to predict structural, hydration, and interfacial properties, Cement and Concrete Research. 139 (2021) 106262.

[19] R. Hellmann, R. Wirth, D. Daval, J.-P. Barnes, J.-M. Penisson, D. Tisserand, T. Epicier, B. Florin, R.L. Hervig, Unifying natural and laboratory chemical weathering with interfacial

dissolution–reprecipitation: A study based on the nanometer-scale chemistry of fluid–silicate interfaces, Chemical Geology. 294–295 (2012) 203–216.

[20] A. Luttge, R.S. Arvidson, C. Fischer, I. Kurganskaya, Kinetic concepts for quantitative prediction of fluid-solid interactions, Chemical Geology. 504 (2019) 216–235.

[21] D. Daval, R. Hellmann, J. Corvisier, D. Tisserand, I. Martinez, F. Guyot, Dissolution kinetics of diopside as a function of solution saturation state: Macroscopic measurements and implications for modeling of geological storage of CO2, Geochimica et Cosmochimica Acta. 74 (2010) 2615–2633.

[22] F. Brandt, D. Bosbach, Bassanite (CaSO4·0.5H2O) dissolution and gypsum (CaSO4·2H2O) precipitation in the presence of cellulose ethers, Journal of Crystal Growth. 233 (2001) 837–845.

[23] S. Follner, A. Wolter, A. Preusser, S. Indris, C. Silber, H. Follner, The Setting Behaviour of α- and β-CaSO4 · 0,5 H2O as a Function of Crystal Structure and Morphology, Cryst. Res. Technol. 37 (2002b) 1075–1087.

[24] T.M. Stawski, H.M. Freeman, A.E.S. Van Driessche, J. Hövelmann, R. Besselink, R. Wirth, L.G. Benning, Particle-Mediated Nucleation Pathways Are Imprinted in the Internal Structure of Calcium Sulfate Single Crystals, Crystal Growth & Design. 19 (2019) 3714–3721.

[25] M.M. Mbogoro, M.E. Snowden, M.A. Edwards, M. Peruffo, P.R. Unwin, Intrinsic Kinetics of Gypsum and Calcium Sulfate Anhydrite Dissolution: Surface Selective Studies under Hydrodynamic Control and the Effect of Additives, J. Phys. Chem. C. 115 (2011) 10147–10154.

[26] M. Peruffo, M.M. Mbogoro, M.A. Edwards, P.R. Unwin, Holistic approach to dissolution kinetics: linking direction-specific microscopic fluxes, local mass transport effects and global macroscopic rates from gypsum etch pit analysis, Phys. Chem. Chem. Phys. 15 (2013) 1956–1965.

[27] P. Feng, A.S. Brand, L. Chen, J.W. Bullard, In situ nanoscale observations of gypsum dissolution by digital holographic microscopy, Chemical Geology. 460 (2017) 25–36.

[28] D. Bosbach, W. Rammensee, In situ investigation of growth and dissolution on the (010) surface of gypsum by Scanning Force Microscopy, Geochimica et Cosmochimica Acta. 58 (1994) 843–849.

[29] R.S. Arvidson, I.E. Ertan, J.E. Amonette, A. Luttge, Variation in calcite dissolution rates:, Geochimica et Cosmochimica Acta. 67 (2003) 1623–1634.

[30] M.M. Thakur, N.A. Henningsson, J. Engqvist, P.-O. Autran, J.P. Wright, R.C. Hurley, On mesoscale modeling of concrete: Role of heterogeneities on local stresses, strains, and representative volume element, Cement and Concrete Research. 163 (2023) 107031.

[31] J.K. Warren, Evaporites: sediments, resources and hydrocarbons., Springer Science & Business Media, 2006.

[32] M. Babel, B.C. Schreiber, Geochemistry of evaporites and evolution of seawater. In book: Treatise on Geochemistry, 2nd ed., Elsevier, 2014.

[33] C.L. Blättler, M.W. Claire, A.R. Prave, K. Kirsimäe, J.A. Higgins, P.V. Medvedev, A.E. Romashkin, D.V. Rychanchik, A.L. Zerkle, K. Paiste, T. Kreitsmann, I.L. Millar, J.A. Hayles, H. Bao, A.V. Turchyn, M.R. Warke, A. Lepland, Two-billion-year-old evaporites capture Earth's great oxidation, Science. 360 (2018) 320–323.

[34] W.B.F. Ryan, Decoding the Mediterranean salinity crisis, Sedimentology. 56 (2009) 95–136.

[35] H. Corbí, J.M. Soria, C. Lancis, A. Giannetti, J.E. Tent-Manclús, J. Dinarès-Turell, Sedimentological and paleoenvironmental scenario before, during, and after the Messinian Salinity Crisis: The San Miguel de Salinas composite section (western Mediterranean), Marine Geology. 379 (2016) 246–266.

[36] J.M. Rouchy, A. Caruso, The Messinian salinity crisis in the Mediterranean basin: A reassessment of the data and an integrated scenario, Sedimentary Geology. 188–189 (2006) 35–67.

[37] M. Briskin, B.C. Schreiber, Authigenic gypsum in marine sediments, Marine Geology. 28 (1978) 37–49.

[38] L. Haffert, M. Haeckel, V. Liebetrau, C. Berndt, C. Hensen, M. Nuzzo, A. Reitz, F. Scholz, J. Schönfeld, C. Perez-Garcia, S.M. Weise, Fluid evolution and authigenic mineral paragenesis related to salt diapirism – The Mercator mud volcano in the Gulf of Cadiz, Geochimica et Cosmochimica Acta. 106 (2013) 261–286.

[39] L. Haffert, M. Haeckel, Quantification of non-ideal effects on diagenetic processes along extreme salinity gradients at the Mercator mud volcano in the Gulf of Cadiz, Geochimica et Cosmochimica Acta. 244 (2019) 366–382.

[40] H. Pirlet, L.M. Wehrmann, B. Brunner, N. Frank, J. Dewanckele, D. Van Rooij, A. Foubert, R. Swennen, L. Naudts, M. Boone, V. Cnudde, J.-P. Henriet, Diagenetic formation of gypsum and dolomite in a cold-water coral mound in the Porcupine Seabight, off Ireland: Diagenetic gypsum in a cold-water coral mound, Sedimentology. 57 (2010) 786–805.

[41] C. Huguen, J.P. Foucher, J. Mascle, H. Ondréas, M. Thouement, S. Gontharet, A. Stadnitskaia, C. Pierre, G. Bayon, L. Loncke, A. Boetius, I. Bouloubassi, G. de Lange, J.C. Caprais, Y. Fouquet, J. Woodside, S. Dupré, Menes caldera, a highly active site of brine seepage in the Eastern Mediterranean sea: “In situ” observations from the NAUTINIL expedition (2003), Marine Geology. 261 (2009) 138–152.

[42] G. Hoareau, C. Monnin, F. Odonne, The stability of gypsum in marine sediments using the entire ODP/IODP porewater composition database, Marine Geology. 279 (2011) 87–97.

[43] V. Scribano, S. Carbone, F.C. Manuella, M. Hovland, H. Rueslåtten, H.-K. Johnsen, Origin of salt giants in abyssal serpentinite systems, Int J Earth Sci (Geol Rundsch). 106 (2017) 2595–2608.

[44] J.M. García-Ruiz, R. Villasuso, C. Ayora, A. Canals, F. Otálora, Formation of natural gypsum megacrystals in Naica, Mexico, Geol. 35 (2007) 327.

[45] A.E.S. Van Driessche, J.M. García-Ruíz, K. Tsukamoto, L.D. Patiño-Lopez, H. Satoh, Ultraslow growth rates of giant gypsum crystals, Proc. Natl. Acad. Sci. U.S.A. 108 (2011) 15721–15726.

[46] A.E.S. Van Driessche, A. Canals, M. Ossorio, R.C. Reyes, J.M. García-Ruiz, Unraveling the Sulfate Sources of (Giant) Gypsum Crystals Using Gypsum Isotope Fractionation Factors, The Journal of Geology. 124 (2016) 235–245.

[47] Y. Langevin, F. Poulet, J.-P. Bibring, B. Gondet, Sulfates in the North Polar Region of Mars Detected by OMEGA/Mars Express, Science. 307 (2005) 1584–1586.

[48] A. Gendrin, N. Mangold, J.-P. Bibring, Y. Langevin, B. Gondet, F. Poulet, G. Bonello, C. Quantin, J. Mustard, R. Arvidson, S. LeMouélic, Sulfates in Martian Layered Terrains: The OMEGA/Mars Express View, Science. 307 (2005) 1587–1591.

[49] M. Nachon, S.M. Clegg, N. Mangold, S. Schröder, L.C. Kah, G. Dromart, A. Ollila, J.R. Johnson, D.Z. Oehler, J.C. Bridges, S. Le Mouélic, O. Forni, R.C. Wiens, R.B. Anderson, D.L. Blaney, J.F. Bell, B. Clark, A. Cousin, M.D. Dyar, B. Ehlmann, C. Fabre, O. Gasnault, J. Grotzinger, J. Lasue, E. Lewin, R. Léveillé, S. McLennan, S. Maurice, P.-Y. Meslin, W. Rapin, M. Rice, S.W. Squyres, K. Stack, D.Y. Sumner, D. Vaniman, D. Wellington, Calcium sulfate veins characterized by ChemCam/Curiosity at Gale crater, Mars: CALCIUM SULFATE VEINS AT GALE CRATER, J. Geophys. Res. Planets. 119 (2014) 1991–2016.

[50] D.T. Vaniman, D.L. Bish, D.W. Ming, T.F. Bristow, R.V. Morris, D.F. Blake, S.J. Chipera, S.M. Morrison, A.H. Treiman, E.B. Rampe, M. Rice, C.N. Achilles, J.P. Grotzinger, S.M. McLennan, J. Williams, J.F. Bell, H.E. Newsom, R.T. Downs, S. Maurice, P. Sarrazin, A.S. Yen, J.M. Morookian, J.D. Farmer, K. Stack, R.E. Milliken, B.L. Ehlmann, D.Y. Sumner, G. Berger, J.A. Crisp, J.A. Hurowitz, R. Anderson, D.J. Des Marais, E.M. Stolper, K.S. Edgett, S. Gupta, N. Spanovich, MSL Science Team, C. Agard, J.A. Alves Verdasca, R. Anderson, D. Archer, C. Armiens-Aparicio, R. Arvidson, E. Atlaskin, S. Atreya, A. Aubrey, B. Baker, M. Baker, T. Balic-Zunic, D. Baratoux, J. Baroukh, B. Barraclough, K. Bean, L. Beegle, A. Behar, S. Bender, M. Benna, J. Bentz, J. Berger, D. Berman, J.J. Blanco Avalos, D. Blaney, J. Blank, H. Blau, L.

Bleacher, E. Boehm, O. Botta, S. Böttcher, T. Boucher, H. Bower, N. Boyd, B. Boynton, E. Breves, J. Bridges, N. Bridges, W. Brinckerhoff, D. Brinza, C. Brunet, A. Brunner, W. Brunner, A. Buch, M. Bullock, S. Burmeister, M. Cabane, F. Calef, J. Cameron, J. “Iain” Campbell, B. Cantor, M. Caplinger, J. Caride Rodríguez, M. Carmosino, I. Carrasco Blázquez, A. Charpentier, D. Choi, B. Clark, S. Clegg, T. Cleghorn, E. Cloutis, G. Cody, P. Coll, P. Conrad, D. Coscia, A. Cousin, D. Cremers, A. Cros, F. Cucinotta, C. d’Uston, S. Davis, M. “Kenzie” Day, M. de la Torre Juarez, L. DeFlores, D. DeLapp, J. DeMarines, W. Dietrich, R. Dingler, C. Donny, D. Drake, G. Dromart, A. Dupont, B. Duston, J. Dworkin, M.D. Dyar, L. Edgar, C. Edwards, L. Edwards, B. Ehresmann, J. Eigenbrode, B. Elliott, H. Elliott, R. Ewing, C. Fabre, A. Fairén, K. Farley, C. Fassett, L. Favot, D. Fay, F. Fedosov, J. Feldman, S. Feldman, M. Fisk, M. Fitzgibbon, G. Flesch, M. Floyd, L. Flückiger, O. Forni, A. Fraeman, R. Francis, P. François, H. Franz, C. Freissinet, K.L. French, J. Frydenvang, A. Gaboriaud, M. Gailhanou, J. Garvin, O. Gasnault, C. Geffroy, R. Gellert, M. Genzer, D. Glavin, A. Godber, F. Goesmann, W. Goetz, D. Golovin, F. Gómez Gómez, J. Gómez-Elvira, B. Gondet, S. Gordon, S. Gorevan, J. Grant, J. Griffes, D. Grinspoon, P. Guillemot, J. Guo, S. Guzewich, R. Haberle, D. Halleaux, B. Hallet, V. Hamilton, C. Hardgrove, D. Harker, D. Harpold, A.-M. Harri, K. Harshman, D. Hassler, H. Haukka, A. Hayes, K. Herkenhoff, P. Herrera, S. Hettrich, E. Heydari, V. Hipkin, T. Hoehler, J. Hollingsworth, J. Hudgins, W. Huntress, S. Hviid, K. Iagnemma, S. Indyk, G. Israël, R. Jackson, S. Jacob, B. Jakosky, E. Jensen, J.K. Jensen, J. Johnson, M. Johnson, S. Johnstone, A. Jones, J. Jones, J. Joseph, I. Jun, L. Kah, H. Kahanpää, M. Kahre, N. Karpushkina, W. Kasprzak, J. Kauhanen, L. Keely, O. Kemppinen, D. Keymeulen, M.-H. Kim, K. Kinch, P. King, L. Kirkland, G. Kocurek, A. Koefoed, J. Köhler, O. Kortmann, A. Kozyrev, J. Krezoski, D. Krysak, R. Kuzmin, J.L. Lacour, V. Lafaille, Y. Langevin, N. Lanza, J. Lasue, S. Le Mouélic, E.M. Lee, Q.-M. Lee, D. Lees, M. Lefavor, M. Lemmon, A.L. Malvitte, L. Leshin, R. Léveillé, É. Lewin-Carpintier, K. Lewis, S. Li, L. Lipkaman, C. Little, M. Litvak, E. Lorigny, G. Lugmair, A. Lundberg, E. Lyness, M. Madsen, P. Mahaffy, J. Maki, A. Malakhov, C. Malespin, M. Malin, N. Mangold, G. Manhes, H. Manning, G. Marchand, M. Marín Jiménez, C. Martín García, D. Martin, M. Martin, J. Martínez-Frías, J. Martín-Soler, F.J. Martín-Torres, P. Mauchien, A. McAdam, E. McCartney, T. McConnochie, E. McCullough, I. McEwan, C. McKay, S. McNair, N. Melikechi, P.-Y. Meslin, M. Meyer, A. Mezzacappa, H. Miller, K. Miller, M. Minitti, M. Mischna, I. Mitrofanov, J. Moersch, M. Mokrousov, A. Molina Jurado, J. Moores, L. Mora-Sotomayor, R. Mueller-Mellin, J.-P. Muller, G. Muñoz Caro, M. Nachon, S. Navarro López, R. Navarro-González, K. Nealson, A. Nefian, T. Nelson, M. Newcombe, C. Newman, S. Nikiforov, P. Niles, B. Nixon, E. Noe Dobrea, T. Nolan, D. Oehler, A. Ollila, T. Olson, T. Owen, M.Á. de Pablo Hernández, A. Paillet, E. Pallier, M. Palucis, T. Parker, Y. Parot, K. Patel, M. Paton, G. Paulsen, A. Pavlov, B. Pavri, V. Peinado-González, R. Pepin, L. Peret, R. Perez, G. Perrett, J. Peterson, C. Pilorget, P. Pinet, J. Pla-García, I. Plante, F. Poitrasson, J. Polkko, R. Popa, L. Posiolova, A. Posner, I. Pradler, B. Prats, V. Prokhorov, S.W. Purdy, E. Raaen, L. Radziemski, S. Rafkin, M. Ramos, F. Raulin, M. Ravine, G. Reitz, N. Rennó, M. Richardson, F. Robert, K. Robertson, J.A. Rodriguez Manfredi, J.J. Romeral-Planelló, S. Rowland, D. Rubin, M. Saccoccio, A. Salamon, J. Sandoval, A. Sanin, S.A. Sans Fuentes, L. Saper, V. Sautter, H. Savijärvi, J. Schieber, M. Schmidt, W. Schmidt, D. “Dan” Scholes, M. Schoppers, S. Schröder, S. Schwenzer, E. Sebastian Martinez, A. Sengstacken, R. Shterts, K. Siebach, T. Siili, J. Simmonds, J.-B. Sirven, S. Slavney, R. Sletten, M. Smith, P. Sobrón Sánchez, J. Spray, S. Squyres, F. Stalport, A. Steele, T. Stein, J. Stern, N. Stewart, S.L.S. Stipp, K. Stoiber, B. Sucharski, R. Sullivan, R. Summons, V. Sun, K. Supulver, B. Sutter, C. Szopa, F. Tan, C. Tate, S. Teinturier, I. ten Kate, P. Thomas, L. Thompson, R. Tokar, M. Toplis, J. Torres Redondo, M. Trainer, V. Tretyakov, R. Urqui-O’Callaghan, J. Van Beek, T. Van Beek, S. VanBommel, A. Varenikov, A. Vasavada, P. Vasconcelos, E. Vicenzi, A. Vostrukhin, M. Voytek, M. Wadhwa, J. Ward, C. Webster, E. Weigle, D. Wellington, F. Westall, R.C. Wiens, M.B. Wilhelm, A. Williams, R. Williams, R.B. “Mouser” Williams, M. Wilson, R. Wimmer-Schweingruber, M. Wolff, M. Wong, J. Wray, M. Wu, C. Yana, A. Yingst, C. Zeitlin, R. Zimdar, M.-P. Zorzano

Mier, Mineralogy of a Mudstone at Yellowknife Bay, Gale Crater, Mars, Science. 343 (2014) 1243480.
[51] W. Rapin, P.-Y. Meslin, S. Maurice, D. Vaniman, M. Nachon, N. Mangold, S. Schröder, O. Gasnault, O. Forni, R.C. Wiens, G.M. Martínez, A. Cousin, V. Sautter, J. Lasue, E.B. Rampe, D. Archer, Hydration state of calcium sulfates in Gale crater, Mars: Identification of bassanite veins, Earth and Planetary Science Letters. 452 (2016) 197–205.
[52] F.M. Lea, Chemistry of Cement and Concrete, 4th ed., Arnold, London, 1998.
[53] G. Tzouvalas, G. Rantis, S. Tsimas, Alternative calcium-sulfate-bearing materials as cement retarders: Part II. FGD gypsum, Cement and Concrete Research. 34 (2004) 2119–2125.
[54] R.L. Myers, The 100 most Important Chemical Compounds: A Reference Guide, Greenwood Press, 2007.
[55] T. Le Dantec, Gypsum external renderings of Paris: History and fabrication. Further Studies in the history of Construction., Proceedings of the Third Conference of the Construction History Society. (2016).
[56] D. Freyer, W. Voigt, Crystallization and Phase Stability of CaSO4 and CaSO4 – Based Salts, Monatshefte Für Chemie / Chemical Monthly. 134 (2003) 693–719.
[57] P. Ballirano, E. Melis, Thermal behaviour of β-anhydrite CaSO4 to 1,263 K, Phys Chem Minerals. 34 (2007) 699–704.
[58] F.C. Hawthorne, R.B. Ferguson, Anhydrous sulphates; II, Refinement of the crystal structure of anhydrite, The canadian mineralogist. 13 (1975) 289–292.
[59] A. Kirfel, G. Will, Charge density in anhydrite, $CaSO_4$, from X-ray and neutron diffraction measurements, Acta Crystallogr B Struct Sci. 36 (1980) 2881–2890.
[60] H. Morikawa, I. Minato, T. Tomita, S. Iwai, Anhydrite: a refinement, Acta Crystallogr B Struct Sci. 31 (1975) 2164–2165.
[61] G.A. Lager, T. Armbruster, J.D. Jorgensen, D.G. Hinks, A crystallographic study of the low-temperature dehydration products of gypsum, CaSO4 · 2H2O: hemihydrate, CaSO4 · 0.50H2O, and γ-CaSO 4, American Mineralogist. 69 (1984) 910–919.
[62] K. Momma, F. Izumi, *VESTA 3* for three-dimensional visualization of crystal, volumetric and morphology data, J Appl Crystallogr. 44 (2011) 1272–1276.
[63] N.N. Bushuev, V.M. Borisov, X-ray diffraction investigation of CaSO4· 0, 67 H2O, Russ. J. Inorg. Chem. 27 (1982) 341–343.
[64] H.-J. Kuzel, M. Hauner, Chemische und kristallographische Eigenschaften von Calciumsulfat-Halbhydrat und Anhydrit III, Zement-Kalk-Gips. 40 (1987) 628–632.
[66] T. Schmid, R. Jungnickel, P. Dariz, Insights into the CaSO4–H2O System: A Raman-Spectroscopic Study, Minerals. 10 (2020) 115.
[67] A.J. Lewry, J. Williamson, The setting of gypsum plaster: Part I The hydration of calcium sulphate hemihydrate, J Mater Sci. 29 (1994) 5279–5284.
[68] D. Aquilano, F. Otálora, L. Pastero, J.M. García-Ruiz, Three study cases of growth morphology in minerals: Halite, calcite and gypsum, Progress in Crystal Growth and Characterization of Materials. 62 (2016) 227–251.
[69] J.C.A. Boeyens, V.V.H. Ichharam, Redetermination of the crystal structure of calcium sulphate dihydrate, CaSO4· 2H2O, Zeitschrift Für Kristallographie-New Crystal Structures. 217 (2002) 9–10.
[70] C. Fan, H.H. Teng, Crystallization and dissolution of gypsum. Gypsum: Properties, Production and Applications, (2011) 111–129.
[71] S. Follner, A. Wolter, K. Helming, C. Silber, H. Bartels, H. Follner, On the Real Structure of Gypsum Crystals, Cryst. Res. Technol. 37 (2002a) 207–218.
[72] M. Rubbo, M. Bruno, F.R. Massaro, D. Aquilano, The Five Twin Laws of Gypsum ($CaSO_4 \cdot 2H_2O$): A Theoretical Comparison of the Interfaces of the Contact Twins, Crystal Growth & Design. 12 (2012) 264–270.
[73] A.M. Cody, R.D. Cody, Evidence for micro-biological induction of {101} montmartre twinning of gypsum (CaSO4 ⋯ 2H2O), Journal of Crystal Growth. 98 (1989) 721–730.

[75] A.E. Van Driessche, M. Kellermeier, L.G. Benning, D. Gebauer, New perspectives on mineral nucleation and growth: from solution precursors to solid materials, Springer, 2016.
[76] M. Poggiale, Memoire sur la solubilite des sels dans l'eau, Ann Chim Phys. 3 (1843) 463–478.
[77] C. Marignac, Ueber die Löslichkeit des schwefelsauren kalkes in wasser, Z Anal Cam. 13 (1874) 57–59.
[78] H. Droeze, Solubility of gypsum in water and in saline solutions, Bericht d. deutsch, chem. Ges. in Berlin. 10 (1877) 330–343.
[79] W.A. Tilden, W.A. Shenstone, On the solubility of salts in water at high temperatures, Philos Trans R Soc. 175A (1984) 31.
[80] G.A. Raupenstrauch, Uber die Bestimmungder loslichkeit einiger salze in wasser bei verschiedenen temperaturen, Monatsh Chem, 1885.
[81] M. Boyer-Guillon, Etude sur la solubilite du sulfate de chaux. Extrait des Annales du Conservatoire des Arts et Metiers, 3e serie, tome II (1900).
[82] F.K. Cameron, Solubility of gypsum in aqueous solutions of sodium chloride, J Phys Chem. 5 (1901) 556–576.
[83] G.A. Hulett, L.E. Allen, The solubility of gypsum., J Am Chem Soc. 24 (1902) 667–679.
[84] A.C. Melcher, The solubility of silver chloride, barium sulphate, and calcium sulphate at high temperatures, J Am Chem Soc. 32 (1910) 50–66.
[85] R.E. Hall, J.A. Robb, C.E. Coleman, The solubility of calcium sulfate at boiler-water temperatures, J Am Chem Soc. 48 (1926).
[86] A.E. Hill, The transition temperature of gypsum to anhydrite, J Am Chem Soc. 59 (1937) 2242–2244.
[87] A.E. Hill, J.H. Wills, Ternary systems. XXIV. Calcium sulfate, sodium sulfate and water., J Am Chem Soc. 60 (1938) 1647–1655.
[88] E. Patridge, A.H. White, The solubility of calcium sulfate from 0 to 200ıC, J. Am. Chem. Soc. 51 (1929) 360–370.
[89] P.S. Roller, Chemical activity and particle size. The rate of solution of anhydrite below 70 microns, J Phys Chem. 35 (1931) 1132–1142.
[90] J. D'Ans, Die Losungsgleichgewichte der Systeme der Salze ozeanischer Salzablagerungen, Verlagsgesellschaft fur Ackerbau, Berlin. (1933) 5.
[91] J. D'Ans, Der Ubergangspunkt Gips-Anhydrit, Kali Steinsalz. 5 (1968) 109–111.
[92] H.S. Booth, R.M. Bidwell, Solubilities of salts in water at high temperatures, J Am Chem Soc. 72 (1950) 2567–2575.
[93] W.M. Madgin, D.A. Swayles, Solubilities in the system CaSO4-NaCl-H2O at 25ı and 35ı C., J Appl Chem. 6 (1956) 482–487.
[94] E. Bock, On the solubility of anhydrous calcium sulphate and of gypsum in concentrated solutions of sodium chloride at 25 ıC, Can. J. Chem. 39 (1961) 1746–1751.
[95] F.W. Dickson, C.W. Blount, G. Tunell, Use of hydrothermal solution equipment to determine the solubility of anhydrite in water from 100 ıC to 275 ıC and from 1 bar to 1000 bars pressure., Am. J. Sci. 261 (1963) 61–78.
[96] W.L. Marshall, R. Slusher, E.V. Jones, Aqueous systems at high temperature. XIV. Solubility and thermodynamic relationships for CaSO4 in NaCl-H2O solutions from 40 ıC to 200 ıC, 0 to 4 molal NaCl, J Am Chem Eng Data. 9 (1964) 187.
[97] E. Zen, Solubility measurements in the system CaSO4– NaCl–H2O at 35ı 50ı and 70ıC and one atmosphere pressure, J Petrol. 6 (1965) 124–164.
[98] W.L. Marshall, R. Slusher, Thermodynamics of Calcium Sulfate Dihydrate in Aqueous sodium chloride solutions, 0– 110ı., J Phys Chem. 70 (1966) 4015–4027.
[99] W.H. Power, B.M. Fabuss, C.N. Satterfield, Transient solubilities in the calcium sulfate-water system., J Am Chem Eng Data. 9 (1964) 437.

[100] W.H. Power, B.M. Fabuss, C.N. Satterfield, Transient solute concentrations and phase changes of calcium sulfate in aqueous sodium chloride, J Chem Eng Data. 11 (1966) 149–154.
[101] J. Block, O.B. Waters, The CaSO4-Na2SO4-NaCl –H2O system at 25 to 100 ıC., J Am Chem Eng Data. 13 (1968) 336–344.
[102] C.W. Blount, F.W. Dickson, The solubility of anhydrite (CaSO4) in NaCl–H2O from 100 to 450ıC and 1 to 1000 bars., Geochimica et Cosmochimica Acta. 33 (1969) 227–245.
[103] C.W. Blount, F.W. Dickson, Gypsum-anhydrite equilibria in systems CaSO4 –H2O and CaSO4 –NaCl–H2O., Am Mineral. 58 (1973) 323–331.
[104] C.H. Culberson, G. Lathman, R.G. Bates, Solubilities and activity coefficients of calcium and strontium sulfate in synthetic seawater at 0.5 and 25 ıC, J Phys Chem. 82 (1978) 2693–2699.
[105] G. Innorta, E. Rabbi, L. Tomadin, The gypsum-anhydrite equilibrium by solubility measurements, Geochimica et Cosmochimica Acta. 44 (1980) 1931–1936.
[106] J. Kontrec, D. Kralj, L. Brečević, Transformation of anhydrous calcium sulphate into calcium sulphate dihydrate in aqueous solutions, Journal of Crystal Growth. 240 (2002) 203–211.
[107] G. Azimi, V.G. Papangelakis, The solubility of gypsum and anhydrite in simulated laterite pressure acid leach solutions up to 250 ıC., Hydrometallurgy. 102 (2010) 1–13.
[108] J.H. Van't Hoff, E.F. Armstrong, W. Hinrichsen, F. Weigert, G. Just, Gips und anhydrit, Z Phys Chem. 45 (1903) 257.
[109] E. Posnjak, The system CaSO4–H2O, Am. J. Sci. 35 (1938) 247–272.
[110] G. Azimi, V.G. Papangelakis, J.E. Dutrizac, Modelling of calcium sulphate solubility in concentrated multi-component sulphate solutions, Fluid Phase Equilibria. 260 (2007) 300–315.
[111] E.F. Cruft, P.C. Chao, Nucleation kinetics of the gypsum-anhydrite system, 3rd Symp. on Salt. 1 (1970) 109–118.
[112] M. Ossorio, A.E.S. Van Driessche, P. Pérez, J.M. García-Ruiz, The gypsum–anhydrite paradox revisited, Chemical Geology. 386 (2014) 16–21.
[113] S. Karthika, T.K. Radhakrishnan, P. Kalaichelvi, A Review of Classical and Nonclassical Nucleation Theories, Crystal Growth & Design. 16 (2016) 6663–6681.
[114] D. Kashchiev, Nucleation, Elsevier, 2000.
[115] S.-T. Liu, G.H. Nancollas, Linear crystallization and induction-period studies of the growth of calcium sulphate dihydrate crystals, Talanta. 20 (1973) 211–216.
[116] A. Packter, The precipitation of calcium sulphate dihydrate from aqueous solution, Journal of Crystal Growth. 21 (1974) 191–194.
[117] J.A. Christiansen, A.E. Nielsen, The interplay between nucleus formation and crystal growth, Z Elektrochem. (1952) 465.
[118] P.G. Klepetsanis, P.G. Koutsoukos, Precipitation of calcium sulfate dihydrate at constant calcium activity, Journal of Crystal Growth. 98 (1989) 480–486.
[119] S.K. Hamdona, R.B. Nessim, S.M. Hamza, Spontaneous precipitation of calcium sulphate dihydrate in the presence of some metal ions, Desalination. 94 (1993) 69–80.
[120] S. He, J.E. Oddo, M.B. Tomson, The Nucleation Kinetics of Calcium Sulfate Dihydrate in NaCl Solutions up to 6 m and 90°C, Journal of Colloid and Interface Science. 162 (1994) 297–303.
[121] P.G. Klepetsanis, E. Dalas, P.G. Koutsoukos, Role of Temperature in the Spontaneous Precipitation of Calcium Sulfate Dihydrate, Langmuir. 15 (1999) 1534–1540.
[122] A. Lancia, D. Musmarra, M. Prisciandaro, Measuring induction period for calcium sulfate dihydrate precipitation, AIChE J. 45 (1999) 390–397.
[123] M. Prisciandaro, A. Lancia, D. Musmarra, Calcium Sulfate Dihydrate Nucleation in the Presence of Calcium and Sodium Chloride Salts, Ind. Eng. Chem. Res. 40 (2001) 2335–2339.
[124] M. Prisciandaro, A. Lancia, D. Musmarra, Gypsum nucleation into sodium chloride solutions, AIChE J. 47 (2001) 929–934.

[125] F. Alimi, H. Elfil, A. Gadri, Kinetics of the precipitation of calcium sulfate dihydrate in a desalination unit, Desalination. 158 (2003) 9–16.
[126] M. Prisciandaro, A. Lancia, D. Musmarra, The Retarding Effect of Citric Acid on Calcium Sulfate Nucleation Kinetics, Ind. Eng. Chem. Res. 42 (2003) 6647–6652.
[127] M.M. Rashad, M.H.H. Mahmoud, I.A. Ibrahim, E.A. Abdel-Aal, Crystallization of calcium sulfate dihydrate under simulated conditions of phosphoric acid production in the presence of aluminum and magnesium ions, Journal of Crystal Growth. 267 (2004) 372–379.
[128] C. Fan, A.T. Kan, G. Fu, M.B. Tomson, D. Shen, Quantitative Evaluation of Calcium Sulfate Precipitation Kinetics in the Presence and Absence of Scale Inhibitors, SPE Journal. 15 (2010) 977–988.
[129] Y.-W. Wang, Y.-Y. Kim, H.K. Christenson, F.C. Meldrum, A new precipitation pathway for calcium sulfate dihydrate (gypsum) via amorphous and hemihydrate intermediates, Chemical Communications. 48 (2012) 504–506.
[130] A.E.S. Van Driessche, L.G. Benning, J.D. Rodriguez-Blanco, M. Ossorio, P. Bots, J.M. García-Ruiz, The role and implications of bassanite as a stable precursor phase to gypsum precipitation, Science. 336 (2012) 69–72.
[131] A. Saha, J. Lee, S.M. Pancera, M.F. Bräeu, A. Kempter, A. Tripathi, A. Bose, New Insights into the transformation of calcium sulfate hemihydrate to gypsum using time-resolved cryogenic transmission electron microscopy, Langmuir. 28 (2012) 11182–11187.
[132] F. Jones, Infrared investigation of barite and gypsum crystallization: Evidence for an amorphous to crystalline transition, CrystEngComm. 14 (2012) 8374.
[133] T.M. Stawski, A.E.S. van Driessche, M. Ossorio, J. Diego Rodriguez-Blanco, R. Besselink, L.G. Benning, Formation of calcium sulfate through the aggregation of sub-3 nanometre primary species, Nat Commun. 7 (2016) 11177.
[134] U. Tritschler, M. Kellermeier, C. Debus, A. Kempter, H. Cölfen, A simple strategy for the synthesis of well-defined bassanite nanorods, CrystEngComm. 17 (2015) 3772–3776.
[135] K. He, A. Nie, Y. Yuan, S.M. Ghodsi, B. Song, E. Firlar, J. Lu, Y. Lu, T. Shokuhfar, C.M. Megaridis, R. Shahbazian-Yassar, In Situ Transmission Electron Microscopy Explores a New Nanoscale Pathway for Direct Gypsum Formation in Aqueous Solution, ACS Appl. Nano Mater. 1 (2018) 5430–5440.
[136] G. Jiang, J. Mao, H. Fu, X. Zhou, B. Guan, Insight into Metastable Lifetime of α-Calcium Sulfate Hemihydrate in $CaCl_2$ Solution, J. Am. Ceram. Soc. 96 (2013) 3265–3271.
[137] T.M. Stawski, R. Besselink, K. Chatzipanagis, J. Hövelmann, L.G. Benning, A.E.S. Van Driessche, Nucleation Pathway of Calcium Sulfate Hemihydrate (Bassanite) from Solution: Implications for Calcium Sulfates on Mars, J. Phys. Chem. C. 124 (2020) 8411–8422.
[138] C. Fan, A.T. Kan, G. Fu, M.B. Tomson, D. Shen, Quantitative Evaluation of Calcium Sulfate Precipitation Kinetics in the Presence and Absence of Scale Inhibitors, SPE Journal. 15 (2010) 977–988.
[139] U. Tritschler, A.E.S. Van Driessche, A. Kempter, M. Kellermeier, H. Cölfen, Controlling the Selective Formation of Calcium Sulfate Polymorphs at Room Temperature, Angew. Chem. Int. Ed. 54 (2015) 4083–4086.
[140] M. Enayetallah, A.A. Khalil, A.M. Gadalla, THE DEHYDRATION OF GYPSUM AND OF MOULDS FABRICATED FROM PREVIOUSLY DEHYDRATED GYPSUM BY DRY AND STEAM CALCINATION, (1977).
[141] K.-M. Song, J. Mitchell, L.F. Gladden, Observing microstructural evolution during plaster hydration, (2009).
[142] N. Kondratieva, M. Barre, F. Goutenoire, M. Sanytsky, Study of modified gypsum binder, Construction and Building Materials. 149 (2017) 535–542.
[143] J. de Brito, I. Flores-Colen, Gypsum Plasters, in: M.C. Gonçalves, F. Margarido (Eds.), Materials for Construction and Civil Engineering: Science, Processing, and Design, Springer International Publishing, Cham, 2015: pp. 123–184.

[144] R. Malinowski, Durable ancient mortars and concretes, 1982.
[145] G. Frigione, Gypsum in Cement, in: Advances in Cement Technology, Elsevier, 1983: pp. 485–535.
[146] Taylor Harry FW, Cement chemistry, London, 1997.
[147] U. Ludwig, N.B. Singh, Hydration of hemihydrate of gypsum and its supersaturation, Cement and Concrete Research. 8 (1978) 291–299.
[148] W. Michaelis, THE BEHAVIOUR OF PORTLAND CEMENT IN SEA-WATER., Minutes of the Proceedings of the Institution of Civil Engineers. 107 (1892) 370–376.
[149] W.C. Hansen, The setting a~d hardening of gypsum plasters, Mater. Res. and Stand. 3 (1963) 359.
[150] P. Haubert, W. Kronert, Tests on the first stages of gypsum setting, Tonind-Ztg. 2 (1977) 28.
[151] W. Kronert, P. Haubert, Mechanism of setting of gypsum hemihydrates in the early stage, Tonind-Ztg. 99 (1975) 238.
[152] W.A. Cunningham, R.M. Dunham, L.L. Antes, Hydration of gypsum plaster, Industrial & Engineering Chemistry. 44 (1952).
[154] A.C. Lasaga, A. Luttge, Variation of Crystal Dissolution Rate Based on a Dissolution Stepwave Model, Science. 291 (2001) 2400–2404.
[155] A.C. Lasaga, Chapter 2. FUNDAMENTAL APPROACHES IN DESCRIBING MINERAL DISSOLUTION AND PRECIPITATION RATES, in: A.F. White, S.L. Brantley (Eds.), Chemical Weathering Rates of Silicate Minerals, De Gruyter, 1995: pp. 23–86.
[156] P. Aagaard, H.C. Helgeson, Thermodynamic and kinetic constraints on reaction rates among minerals and aqueous solutions; I, Theoretical considerations, American Journal of Science. 282 (1982) 237–285.
[157] J. Cama, L. Zhang, J.M. Soler, G.D. Giudici, R.S. Arvidson, A. Lüttge, Fluorite dissolution at acidic pH: In situ AFM and ex situ VSI experiments and Monte Carlo simulations, Geochimica et Cosmochimica Acta. 74 (2010) 4298–4311.
[158] E.H.H. Chow, D.-K. Bučar, W. Jones, New opportunities in crystal engineering – the role of atomic force microscopy in studies of molecular crystals, Chem. Commun. 48 (2012) 9210.
[159] E. Ruiz-Agudo, M. Urosevic, C.V. Putnis, C. Rodríguez-Navarro, C. Cardell, A. Putnis, Ion-specific effects on the kinetics of mineral dissolution, Chemical Geology. 281 (2011) 364–371.
[160] D. Bosbach, G. Jordan, W. Rammensee, Crystal growth and dissolution kinetics of gypsum and fluorite: An in situ Scanning Force Microscope study, Ejm. 7 (1995) 267–276.
[161] C. Hall, D.C. Cullen, Scanning force microscopy of gypsum dissolution and crystal growth, AIChE J. 42 (1996) 232–238.
[162] C.-A. McGeouch, M. Peruffo, M.A. Edwards, L.A. Bindley, R.A. Lazenby, M.M. Mbogoro, K. McKelvey, P.R. Unwin, Quantitative Localized Proton-Promoted Dissolution Kinetics of Calcite Using Scanning Electrochemical Microscopy (SECM), J. Phys. Chem. C. 116 (2012) 14892–14899.
[163] M.P. Asta, J. Cama, J.M. Soler, R.. S. Arvidson, A. Luttge, Interferometric study of pyrite surface reactivity in acidic conditions, American Mineralogist. 93 (2008) 508–519.
[164] A. Kumar, J. Reed, G. Sant, Vertical Scanning Interferometry: A New Method to Measure the Dissolution Dynamics of Cementitious Minerals, J. Am. Ceram. Soc. 96 (2013) 2766–2778.
[165] A.S. Brand, P. Feng, J.W. Bullard, Calcite dissolution rate spectra measured by in situ digital holographic microscopy, Geochimica et Cosmochimica Acta. 213 (2017) 317–329.
[166] A.P. Abbott, M. Azam, K.S. Ryder, S. Saleem, In Situ Electrochemical Digital Holographic Microscopy; a Study of Metal Electrodeposition in Deep Eutectic Solvents, Anal. Chem. 85 (2013) 6653–6660.
[167] G. Artioli, T. Cerulli, G. Cruciani, M.C. Dalconi, G. Ferrari, M. Parisatto, A. Rack, R. Tucoulou, X-ray diffraction microtomography (XRD-CT), a novel tool for non-invasive mapping of phase development in cement materials, Anal Bioanal Chem. 397 (2010) 2131–2136.

[168] G. Artioli, L. Valentini, M. Voltolini, M.C. Dalconi, G. Ferrari, V. Russo, Direct Imaging of Nucleation Mechanisms by Synchrotron Diffraction Micro-Tomography: Superplasticizer-Induced Change of C–S–H Nucleation in Cement, Crystal Growth & Design. 15 (2015) 20–23.
[169] F. Claret, S. Grangeon, A. Loschetter, C. Tournassat, W. De Nolf, N. Harker, F. Boulahya, S. Gaboreau, Y. Linard, X. Bourbon, A. Fernandez-Martinez, J. Wright, Deciphering mineralogical changes and carbonation development during hydration and ageing of a consolidated ternary blended cement paste, IUCrJ. 5 (2018) 150–157.
[170] Y. Hayashi, Y. Hirose, Y. Seno, Polycrystal orientation mapping using scanning three-dimensional X-ray diffraction microscopy, J Appl Crystallogr. 48 (2015) 1094–1101.
[171] Y. Hayashi, Y. Hirose, D. Setoyama, *In Situ* Three-Dimensional Orientation Mapping in Plastically-Deformed Polycrystalline Iron by Three-Dimensional X-Ray Diffraction, MSF. 777 (2014) 118–123.
[172] H.F. Poulsen, 3DXRD-a new probe for materials science, Risø National Laboratory, 2004a.
[173] J. Hektor, S. Hall, N. Henningsson, J. Engqvist, M. Ristinmaa, F. Lenrick, J. Wright, Scanning 3DXRD Measurement of Grain Growth, Stress, and Formation of Cu6Sn5 around a Tin Whisker during Heat Treatment, Materials. 12 (2019) 446.
[174] N.A. Henningsson, S.A. Hall, J.P. Wright, J. Hektor, Reconstructing intragranular strain fields in polycrystalline materials from scanning 3DXRD data, J Appl Crystallogr. 53 (2020) 314–325.
[175] Y. Hayashi, D. Setoyama, Y. Hirose, T. Yoshida, H. Kimura, Intragranular three-dimensional stress tensor fields in plastically deformed polycrystals, Science. 366 (2019) 1492–1496.
[176] L. Nicoleau, A.E.S. Van Driessche, M. Kellermeier, A kinetic analysis of the role of polymers in mineral nucleation. The example of gypsum, Cement and Concrete Research. 124 (2019) 105837.
[177] W. Chen, W. Zhao, Y. Wu, Y. Wang, B. Zhang, F. Li, Q. Chen, Z. Qi, Z. Xu, Origin of gypsum growth habit difference as revealed by molecular conformations of surface-bound citrate and tartrate, CrystEngComm. 20 (2018) 3581–3589.
[178] O. Furat, T. Leißner, R. Ditscherlein, O. Šedivý, M. Weber, K. Bachmann, J. Gutzmer, U. Peuker, V. Schmidt, Description of Ore Particles from X-Ray Microtomography (XMT) Images, Supported by Scanning Electron Microscope (SEM)-Based Image Analysis, Microsc Microanal. 24 (2018) 461–470.
[179] O. Furat, M. Wang, M. Neumann, L. Petrich, M. Weber, C.E. Krill, V. Schmidt, Machine Learning Techniques for the Segmentation of Tomographic Image Data of Functional Materials, Front. Mater. 6 (2019) 145.
[180] D. Paganin, T.E. Gureyev, K.M. Pavlov, R.A. Lewis, M. Kitchen, Phase retrieval using coherent imaging systems with linear transfer functions, Optics Communications. 234 (2004) 87–105.
[181] K. Akhtar, S.A. Khan, S.B. Khan, A.M. Asiri, Scanning Electron Microscopy: Principle and Applications in Nanomaterials Characterization, in: S.K. Sharma (Ed.), Handbook of Materials Characterization, Springer International Publishing, Cham, 2018: pp. 113–145.
[182] K.D. Vernon-Parry, Scanning electron microscopy: an introduction, III-Vs Review. 13 (2000) 40–44.
[183] D. Rugar, P. Hansma, Atomic force microscopy, Physics today. 43 (1990) 23–30.
[184] I. Horcas, R. Fernández, J.M. Gómez-Rodríguez, J. Colchero, J. Gómez-Herrero, A.M. Baro, WSXM : A software for scanning probe microscopy and a tool for nanotechnology, Review of Scientific Instruments. 78 (2007) 013705.
[185] H. Poulsen, Three-Dimensional X-Ray Diffraction Microscopy, Springer Berlin Heidelberg, Berlin, Heidelberg, 2004b.
[186] D.J. Jensen, H.F. Poulsen, The three dimensional X-ray diffraction technique, Materials Characterization. 72 (2012) 1–7.

[187] A. Snigirev, I. Snigireva, M. Grigoriev, V. Yunkin, M. Di Michiel, S. Kuznetsov, G. Vaughan, Silicon planar lenses for high-energy x-ray nanofocusing, in: A.M. Khounsary, C. Morawe, S. Goto (Eds.), San Diego, CA, 2007: p. 670506.
[188] J. Wright, C. Giacobbe, M. Majkut, New opportunities at the Materials Science Beamline at ESRF to exploit high energy nano-focus X-ray beams, Current Opinion in Solid State and Materials Science. 24 (2020) 100818.
[189] C. Dejoie, M. Coduri, S. Petitdemange, C. Giacobbe, E. Covacci, O. Grimaldi, P.-O. Autran, M.W. Mogodi, D. Šišak Jung, A.N. Fitch, Combining a nine-crystal multi-analyser stage with a two-dimensional detector for high-resolution powder X-ray diffraction, J Appl Crystallogr. 51 (2018) 1721–1733.
[190] J.P. Wright, G.B.M. Vaughan, A.N. Fitch, Merging data from a multi-detector continuous scanning powder diffraction system, Comm. Crystallogr. Comput. 1 (2003) 92.
[191] E.S. Ameh, A review of basic crystallography and x-ray diffraction applications, Int J Adv Manuf Technol. 105 (2019) 3289–3302.
[192] C. Giacovazzo, H.L. Monaco, G. Artioli, D. Viterbo, M. Milanesio, G. Gilli, P. Gilli, G. Zanotti, G. Ferraris, M. Catti, Fundamentals of Crystallography, Oxford University Press, 2011.
[193] G. Ashiotis, A. Deschildre, Z. Nawaz, J.P. Wright, D. Karkoulis, F.E. Picca, J. Kieffer, The fast azimuthal integration Python library: *pyFAI*, J Appl Crystallogr. 48 (2015) 510–519.
[194] A.A. Coelho, *TOPAS* and *TOPAS-Academic* : an optimization program integrating computer algebra and crystallographic objects written in C++, J Appl Crystallogr. 51 (2018) 210–218.
[195] R.E. Dinnebier, S.J.L. Billinge, eds., Powder diffraction: theory and practice, Royal Society of Chemistry, Cambridge, 2008.
[196] H.M. Rietveld, A profile refinement method for nuclear and magnetic structures, J Appl Crystallogr. 2 (1969) 65–71.
[197] B. van Laar, H. Schenk, The development of powder profile refinement at the Reactor Centre Netherlands at Petten, Acta Crystallogr A Found Adv. 74 (2018) 88–92.
[198] H.F. Poulsen, W. Ludwig, E.M. Lauridsen, S. Schmidt, W. Pantleon, U.L. Olsen, P. Reischig, A. Lyckegaard, J. Wright, G. Vaughan, 4D characterization of metals by 3DXRD, Proceedings of the Risø International Symposium on Materials Science. 31 (2010) 101–119.
[199] J.P. Wright, ImageD11, (2017). https://github.com/FABLE-3DXRD/ImageD11 (accessed March 1, 2023).
[200] H.O. Sørensen, S. Schmidt, J.P. Wright, G.B. Vaughan, S. Techert, E.F. Garman, J. Oddershede, J. Davaasambuu, K.S. Paithankar, C. Gundlach, Multigrain crystallography, (2012).
[201] W.R. Busing, H.A. Levy, Angle calculations for 3- and 4-circle X-ray and neutron diffractometers, Acta Cryst. 22 (1967) 457–464.
[202] A. Alpers, H.F. Poulsen, 3DXRD and TotalCryst Geometry, Lehrstuhl für Angewandte Geometrie und Diskrete Mathematik, 2009.
[203] B. Beausir, J.J. Fundenberger, Analysis Tools for Electron and X-ray diffraction, ATEX-Software, Www. Atex-Software. Eu, Université de Lorraine-Metz. (2017).
[204] V. Cnudde, M.N. Boone, High-resolution X-ray computed tomography in geosciences: A review of the current technology and applications, Earth-Science Reviews. 123 (2013).
[205] L. Salvo, P. Cloetens, E. Maire, S. Zabler, J.J. Blandin, J.Y. Buffière, W. Ludwig, E. Boller, D. Bellet, C. Josserond, X-ray micro-tomography an attractive characterisation technique in materials science, Nuclear Instruments and Methods in Physics Research Section B: Beam Interactions with Materials and Atoms. 200 (2003) 273–286.
[206] L.A. Shepp, B.F. Logan, The Fourier reconstruction of a head section, IEEE Trans. Nucl. Sci. 21 (1974) 21–43.
[207] A. Kostenko, H. Sharma, E.G. Dere, A. King, W. Ludwig, W.V. Oel, S.E. Offerman, S. Stallinga, L.J. van Vliet, In-line x-ray phase-contrast tomography and diffraction-contrast tomography study of the ferrite-cementite microstructure in steel, in: Campinas, Brazil, 2012: pp. 63–68.

[208] Abramoff M. D., Magalhães Paulo J., Ram Sunanda J., Image processing with ImageJ, Biophotonics International. 11 (2004) 36–42.
[209] I. Goodfellow, Y. Bengio, A. Courville, Deep Learning. Adaptive Computation and Machine Learning series, MIT Press, 2016.
[210] J. Bensted, S.P. Varma, Infrared Spectra of Calcium Sulphate Hemihydrate, Nature Physical Science. 232 (1971) 174–175.
[211] M. Pons-Jiménez, R. Hernández-Altamirano, R. Cisneros-Dévora, E. Buenrostro-González, R. Oviedo-Roa, J.-M. Martínez-Magadán, L.S. Zamudio-Rivera, Theoretical and experimental insights into the control of calcium sulfate scales by using random copolymers based on itaconic acid, Fuel. 149 (2015) 66–77.
[212] S. Parsons, Introduction to twinning, Acta Crystallogr D Biol Crystallogr. 59 (2003) 1995–2003.
[213] H.D. Bellamy, E.H. Snell, J. Lovelace, M. Pokross, G.E.O. Borgstahl, The high-mosaicity illusion: revealing the true physical characteristics of macromolecular crystals, Acta Crystallogr D Biol Crystallogr. 56 (2000) 986–995.
[214] K. Harrison, Z. Wu, D.H. Juers, A comparison of gas stream cooling and plunge cooling of macromolecular crystals, J Appl Crystallogr. 52 (2019) 1222–1232.
[215] Godinho, Ma, Chai, Storm, Burnett, Mineral Precipitation in Fractures and Nanopores within Shale Imaged Using Time-Lapse X-ray Tomography, Minerals. 9 (2019) 480.
[216] J.R.A. Godinho, K.M. Gerke, A.G. Stack, P.D. Lee, The dynamic nature of crystal growth in pores, Sci Rep. 6 (2016) 33086.
[217] C. Anduix-Canto, M.A. Levenstein, Y. Kim, J.R.A. Godinho, A.N. Kulak, C.G. Niño, P.J. Withers, J.P. Wright, N. Kapur, H.K. Christenson, F.C. Meldrum, Exploiting Confinement to Study the Crystallization Pathway of Calcium Sulfate, Adv. Funct. Mater. 31 (2021) 2107312.
[218] C. Noiriel, D. Daval, Pore-Scale Geochemical Reactivity Associated with CO_2 Storage: New Frontiers at the Fluid–Solid Interface, Acc. Chem. Res. 50 (2017) 759–768.
[219] Y. He, J.J. Jonas, Maximum disorientation angles between crystals of any point groups and their corresponding rotation axes, J Appl Crystallogr. 41 (2008) 803–807.
[220] H. Grimmer, The distribution of disorientation angles if all relative orientations of neighbouring grains are equally probable, Scripta Metallurgica. 13 (1979) 161–164.
[221] J.K. Mackenzie, SECOND PAPER ON STATISTICS ASSOCIATED WITH THE RANDOM DISORIENTATION OF CUBES, Biometrika. 45 (1958) 229–240.
[222] J.K. Mackenzie, The distribution of rotation axes in a random aggregate of cubic crystals, Acta Metallurgica. 12 (1964) 223–225.
[223] D.C. Handscomb, On the Random Disorientation of two Cubes, Can. j. Math. 10 (1958) 85–88.
[224] R. Hellmann, S. Cotte, E. Cadel, S. Malladi, L.S. Karlsson, S. Lozano-Perez, M. Cabié, A. Seyeux, Nanometre-scale evidence for interfacial dissolution–reprecipitation control of silicate glass corrosion, Nature Mater. 14 (2015) 307–311.
[225] E. Rufe, M.F. Hochella, Quantitative Assessment of Reactive Surface Area of Phlogopite During Acid Dissolution, Science. 285 (1999) 874–876.
[226] P.M. Dove, F.M. Platt, Compatible real-time rates of mineral dissolution by Atomic Force Microscopy (AFM), Chemical Geology. 127 (1996) 331–338.
[227] R.S. Arvidson, I.E. Ertan, J.E. Amonette, A. Luttge, Variation in calcite dissolution rates:, Geochimica et Cosmochimica Acta. 67 (2003) 1623–1634.
[228] N.A. Christensen, M. Olesen, Y. Cerenius, T.R. Jensen, Formation and transformation of five different phases in the $CaSO_4$-H_2O system: crystal structure of the subhydrate beta-CaSO4 center dot 0.5H(2)O and soluble anhydrite $CaSO_4$, Chemistry of Materials 20. 6 (2008) 2124-2132.

[229] M. Theobald, J. Plank, β-Naphthalene sulfonate formaldehyde-based nanocomposites as new seeding materials for Portland cement, Construction and Building Materials. 264 (2020) 120240.